Using synchrotron radiation to determine the oxidation state of uranium in magmas

Helen Ruth Halse

Department of Earth Science and Engineering
Imperial College London

Department of Earth Sciences
The Natural History Museum

Diamond Light Source Ltd

Submitted in fulfilment of the requirements for the degree of Doctor of Philosophy

Declaration

Unless otherwise referenced or acknowledged, the work presented in this thesis is my own.

The copyright of this thesis rests with the author and is made available under a Creative Commons Attribution Non-Commercial No Derivatives licence. Researchers are free to copy, distribute or transmit the thesis on the condition that they attribute it, that they do not use it for commercial purposes and that they do not alter, transform or build upon it. For any reuse or redistribution, researchers must make clear to others the licence terms of this work.

Abstract

Young igneous rocks from a range of tectonic settings exhibit various Uranium-series (U-series) disequilibria. The U-series systematics of Mid-ocean-ridge basalts (MORBs) have been attributed to mantle melting, while those of arc basalts are widely thought to be slab-fluid signatures. Mid-ocean-ridge and arc U-series models generally assume that U^{4+} is the only oxidation state relevant to mantle melting processes, however the potential for the stabilisation of U^{5+} and/or U^{6+} has recently been proposed for some arc lavas.

To determine the oxidation state of U in geological melts, and to assess the relative stabilities of U^{4+}, U^{5+}, and U^{6+} under mantle conditions, X-ray absorption near edge structure (XANES) spectra were recorded from synthetic analogues, including an Fe-bearing MORB composition. Spectra were collected from quenched glasses equilibrated at 1400 °C and oxygen fugacities (fO_2s) between $\log fO_2$ = -18 and +4.7 (QFM-11.7 to QFM+11), and from equivalent high temperature melts using a custom designed XAS furnace. Spectra were collected at both the U L_3- and M_4-edges, as the variation of the M_4-edge spectral line-shape could be unambiguously linked to oxidation state changes in the glasses, while the higher energy of the L_3-edge was better suited to *in situ* studies.

The variation of the XANES spectra as a function of fO_2 allowed U^{5+} to be identified as a major component in both the MORB glasses and their original melts, and a methodology was developed to accurately quantify their U oxidation state proportions. The proportion of U^{4+} was found to be highly sensitive to fO_2 at conditions relevant to mantle melting, with $U^{5+}/\sum U$ varying between ~0.1 and 0.5 between QFM-1 and QFM+2 and pressures equivalent to mantle depths of ≥ 15 km. U-series models assuming melting of a variably oxidised mantle wedge can produce a wide range of U-series signatures that are consistent with many arc basalts. In contrast, the stability of even small proportions of U^{5+} in the melt may present a problem for those models currently attributing the ^{230}Th excesses of MORBs to mantle melting in the spinel lherzolite field.

Table of Contents

Chapter 1 Introduction

1.1 The importance of oxidation state in geological melts 11

1.2 U-series disequilibria and U-series models 13

1.2.1 Introduction to U-series disequilibria 13

1.2.2 U-series element partition coefficients and proxies 15

1.2.3 U-series disequilibria in Mid-Ocean-Ridge Basalts 16

1.2.4 U-series disequilibria in arcs 22

1.3 Controls on melt redox equilibrium 26

1.3.1 Temperature and pressure 27

1.3.2 Composition 28

1.4 Quantifying the oxidation state of U in silicate melts 30

Chapter 2 Methods

2.1 Background 34

2.1.1 Absorption spectroscopy 34

2.1.2 X-ray absorption spectroscopy 36

2.1.3 XANES as a tool for oxidation state quantification 39

2.2 Experimental Methods 42

2.2.1 Sample synthesis 42

2.2.1.1 1 atm glasses 43

2.2.2.2 High pressure glasses 46

2.2.2 Electron probe microanalysis (EPMA) 49

2.2.2.1 Basic principles 49

2.2.2.2 Analysis of U glasses 51

2.2.2.3 Results 52

2.2.3 XANES spectroscopy 56

2.2.3.1 Synchrotron source 56

2.2.3.2 Beamline setup 59

2.2.3.3 XANES spectral energy resolution 64

2.2.4 HERFD XANES spectroscopy 64

Chapter 3 U M_4-edge XANES spectroscopy of silicate glasses

3.1 Introduction 68

3.2 Experimental methods ……. 69
3.3 Results ……. 72
3.3.1 Beam damage ……. 74
3.3.2 XANES spectra normalisation …… 79
3.3.3 Analysis of the XANES spectra of MORB glasses …… 83
3.3.4 Analysis of the XANES spectra of AD glasses …….. 91
3.4 Preliminary conclusions …….. 93
Chapter 4 U L_3-edge XANES spectroscopy of silicate glasses
4.1 Introduction ……. 96
4.2 Experimental methods ……. 97
4.3 Results ……. 98
4.3.1 Beam damage …….. 100
4.3.2 XANES analysis ……. 103
4.4 Preliminary discussion and conclusions ……. 112
Chapter 5 Quantification of U oxidation states in silicate glasses using L_3- and M_4-edge XANES spectra
5.1 Introduction ……. 115
5.2 Modelling U oxidation state proportions in MORB glasses ……... 115
5.2.1 MORB Model Part 1 ……... 117
5.2.1.1 Methodology ……... 117
5.2.1.2 Results ……. 118
5.2.1.3 Conclusions ……. 120
5.2.2 MORB Model Part 2 ……... 121
5.2.2.1 Methodology ……... 121
5.2.2.2 Results ……. 122
5.2.2.3 Conclusions ……. 122
5.2.3 MORB Model Part 3.1 …… 123
5.2.3.1 Methodology ……... 123
5.2.3.2 Results ……. 125
5.2.4 MORB Model Part 3.2 …… 129
5.2.4.1 Methodology ……... 129
5.2.4.2 Results ……. 131
5.2.5 Discussion on the L_3- and M_4-edge XANES spectra of U^{5+} ….. 132

5.2.6 Final fits …….. 135
5.3 U oxidation state proportions in AD glasses ……... 137
5.3.1 Summary of observations …… 137
5.3.2 AD model Part 1 …… 138
5.3.2.1 Methodology ……... 138
5.3.2.2 Results ……. 139
5.3.2.3 Discussion ……... 140
5.3.3 AD model Part 2 …… 141
5.3.3.1 Methodology ……... 141
5.3.3.2 Results ……. 143
5.3.4 Discussion ……... 145
5.4 Conclusions ……. 145
Chapter 6 U L_3-edge XANES spectroscopy of silicate melts
6.1 Introduction ……. 146
6.2 XAS furnace …… 146
6.3 Experimental methods ……. 150
6.4 Results ……. 151
6.4.1 XANES analysis …… 153
6.4.1.1 Glasses vs. melts ……. 153
6.4.1.2 Effect of temperature …….. 160
6.5 Discussion ……... 161
6.5.1 Temperature …… 161
6.5.2 Melt composition …… 168
6.6 Conclusions ……. 170
Chapter 7 Geological Implications
7.1 Introduction ……. 172
7.2 U-series at MORs ……... 173
7.3 U-series at Arcs …….. 173
7.4 Modelling U-series in arcs: Part 1 ……... 175
7.4.1 Methodology ……... 175
7.4.2 Results ……. 180
7.5 Modelling U-series in arcs: Part 2 ……... 184
7.5.1 Methodology ……... 184

7.5.2 Results ……. 180
7.6 Discussion ……... 186
7.7 Conclusions ……. 190
Chapter 8 Concluding remarks and future work
8.1 Conclusions ……. 191
8.2 Future work ……. 194
Acknowledgements …… 200
References …….. 203
Appendix 1: List of high pressure experiments ……. 223
Appendix 2: List of glasses and their compositions (determined by EPMA) …… 225
Appendix 3: An assessment of the oxidation state line-shape extraction method using Cr K-edge XANES spectra of glasses ……... 240
Appendix 4: Calibration of the XAS furnace …… 249
Appendix 5: Ce L_3-edge XANES spectroscopy of silicate glasses and melts ……... 254
Appendix 6: Eu L_3-edge XANES spectroscopy of silicate melts ……..... 258
Appendix 7: Confocal laser scanning microscopy of U glasses …… 291

List of Figures

1.1 Lattice strain model parabolae ……..... 12
1.2 U-series decay chains ……. 14
1.3 MORB U-series data ……..... 17
1.4 U and Th clinopyroxene-melt partition coefficients ……... 18
1.5 Diagram of U-series disequilibria generation by two-phase flow ……..…….. 20
1.6 Arc basalt U-series data ……...…….. 23
1.7 Relationship between oxidation state and fO_2 ……..……..… 27
1.8 Structural components of a silicate glass …… 29
1.9 U oxidation state proportions in silicate glasses ……...……..… 31
2.1 Element absorption edges ……...… 35
2.2 Electronic transitions and emission lines ……..... 36
2.3 X-ray absorption spectrum of FeO ……. 37
2.4 Eu L_3-edge XANES spectra of Eu^{2+} and Eu^{3+} compounds and glasses ……. 39
2.5 Ce L_3-edge XANES spectra of Ce^{3+} and Ce^{4+} compounds …… 40
2.6 Diagram of a piston cylinder assembly …….. 48

2.7 Pressure dependence of the fO_2 of selected solid-state buffers …….. 49
2.8 Diagram of a synchrotron showing bending magnets and insertion devices ……. 57
2.9 Diagram of a XANES beamline ……. 60
2.10 Diagram of a crystal monochromator ……. 60
2.11 X-ray reflection profiles for different mirror surfaces/coatings ……. 62
2.12 Transferred vs. incident energy around the U Mβ emission line for UO_2 …….. 65
2.13 Diagram of a XANES experimental setup using a Rowland circle geometry …… 66
2.14 U L_3-edge HERFD XANES spectra of UO_2 …….. 67
3.1 Experimental setup for U M_4-edge XANES experiments at ID26 of the ESRF … 70
3.2 U M_4-edge XANES spectra of MORB and AD 1 atm glasses ……...…...…. 73
3.3 Successive U M_4-edge XANES scans of AD 1 atm glasses ……..……..... 75
3.4 Successive U M_4-edge XANES scans of MORB 1 atm glasses ……..….... 76
3.5 U M_4-edge beam damage scans of MORB and AD+Fo glasses ……..….. 77
3.6 U M_4-edge 40 s beam damage scan of AD+Fo glass ($\log fO_2$ = -12, 1400 °C) 79
3.7 Edge-step normalised U M_4-edge XANES spectra of MORB 1 atm glasses ..…... 80
3.8 Spectrometer energy scan around the U Mβ emission line ……..….. 81
3.9 Emission line normalised U M_4-edge spectra of MORB glasses ……..... 82
3.10 Two-component fits of U M_4-edge XANES spectra of MORB 1 atm glasses 84
3.11 Intermediate U component line-shapes from M_4-edge spectra of MORB glasses . 86
3.12 Three-component fits of U M_4-edge XANES spectra of MORB 1 atm glasses …. 88
3.13 Estimated proportions of three U components in 1 atm MORB glasses ……..... 89
3.14 U M_4-edge XANES spectra of MORB piston cylinder glasses ……..... 90
3.15 Intermediate U component line-shapes from M_4-edge spectra of AD glasses ….. 92
3.16 Four-component fits of U M_4-edge XANES spectra of AD 1 atm glasses ……..... 94
3.17 Estimated proportions of four U components in 1 atm AD glasses ……... 95
4.1 U L_3-edge XANES spectra of MORB and AD glasses ……..... 99
4.2 U L_3-edge beam damage scans of MORB and AD glasses ……...…. 101
4.3 Successive L_3-edge XANES white-line scans of AD+En glass ……..... 102
4.4 U L_3-edge XANES spectra showing features selected for XANES analysis ..…... 105
4.5 Intensity variations of glass L_3-edge XANES spectra as a function of fO_2……. 106
4.6 Edge- and post-white-line energy variations of glass L_3-edge XANES spectra … 107
4.7 U L_3-edge XANES spectra white line-crest intensity vs. white-line energy ..…… 111
4.8 logK´ vs. optical basicity for single-sigmoid fits to L_3-edge spectral features ….. 114

5.1 Intensity of U L_3-edge XANES spectra of MORB glasses at 17172.3 eV ……..... 118
5.2 Two-sigmoid model curves of MORB L_3-edge spectral intensities at 17172.3 eV 119
5.3 U L_3-edge XANES spectra showing energies selected for XANES analysis …… 121
5.4 Two-sigmoid model curves of U L_3-edge spectral intensities at selected energies 126
5.5 Two-sigmoid model of U M_4-edge spectral intensities at selected energies …….. 127
5.6 U L_3-edge XANES oxidation state end-member line-shapes ……. 128
5.7 U M_4-edge XANES oxidation state end-member line-shapes …… 129
5.8 U^{5+} M_4-edge XANES line-shapes extracted from 1 atm MORB spectra ……... 131
5.9 U M_4-edge HERFD XANES spectra of various U oxides ……. 134
5.10 U oxidation state proportions of MORB glasses as a function of fO_2 …… 136
5.11 U L_3-edge oxidation state line-shapes from AD glass three-sigmoid models …… 140
5.12 Four-component fits of U M_4-edge XANES spectra of AD 1 atm glasses …… 143
5.13 Estimated proportions of four U components in 1 atm AD glasses ……... 144
6.1 Diagram of the XAS furnace …….. 147
6.2 Photographs of the XAS furnace …… 148
6.3 Normalisation protocol for U L_3-edge XANES spectra ……. 152
6.4 U L_3-edge XANES spectra of MORB and AD melts ……. 153
6.5 U L_3-edge XANES spectra of MORB and AD melts vs. glasses…… 154
6.6 White-line intensities of U L_3-edge XANES spectra of glasses and melts …… 155
6.7 Relative white-line intensities of U L_3-edge XANES spectra of glasses and melts 156
6.8 U L_3-edge XANES edge-energy at a normalised intensity of 0.7 …….. 158
6.9 U L_3-edge XANES post-white-line energy at a normalised intensity of 1.1 …….. 159
6.10 U L_3-edge XANES spectra of MORB melts temperature series …… 160
6.11 Comparison of U L_3-egde spectral features of MORB melts temperature series 162
6.12 U L_3-edge XANES spectra of logfO_2 = -11 MORB and AD melts and glasses … 166
6.13 Intensity of U L_3-edge XANES spectra of MORB and AD melts at 17172 eV …. 170
6.14 logK_A' as a function of optical basicity …….. 170
7.1 U oxidation state proportions of MORB melts as a function of fO_2 ……..... 174
7.2 Diagram showing the key parameters of the Usercalc 2.0 U series model …… 176
7.3 Example of the results output by the Usercalc 2.0 model ……..... 179
7.4 U-series disequilibria generated by Usercalc 2.0 for two melting mineralogies..... 183
7.5 Comparison of the results of U-series oxidised melting models and arc data …… 188
8.1 Vanadium K-edge XANES spectra of glasses ……..…….. 198

8.2 Vanadium L-edge XANES spectra of vanadiniferous minerals ……..…… 199

List of Tables

2.1 Furnace gas mixing ratios at 1400 °C ……..… 46
2.2 Average glass compositions determined by EPMA ……...…… 53
2.3 Key statistics for the ESRF and the DLS synchrotron facility ……...… 58
2.4 X-ray emission lines of different U absorption edges …… 67
4.1 Beam induced decreases in the U L_3-edge white-line intensity of AD glasses ….. 102
4.2 Single-sigmoid fit parameters for L_3-edge XANES spectral features of glasses ... 108
5.1 Two-sigmoid fit parameters for MORB L_3 spectral intensities at 17172.3 eV ….. 120
5.2 Two-sigmoid fit parameters for MORB L_3 spectral intensities at five energies … 123
5.3 logK´ values from two-sigmoid models of MORB L_3 and M_4 spectra …… 125
5.4 Calculated U^{4+}, U^{5+}, and U^{6+} proportions of MORB glasses ……. 130
5.5 logK´ values from three-sigmoid models of AD L_3 spectral intensities ……..... 140
6.1 Absorption lengths of XAS furnace window materials and gases ……. 150
7.1 Partition coefficients and mineral melting modes used in U-series models ……... 178
7.2 U-series disequilibria calculated by Usercalc 2.0 for a 60 km melting column …. 181
7.3 U-series disequilibria calculated by Usercalc 2.0 for a 90 km melting column …. 182
7.4 ($^{230}Th/^{238}U$) ratios calculated by incremental “dynamic” melting model …….. 187

Chapter 1:

Introduction

1.1 The importance of oxidation state in geological melts

During magmatic processes trace elements are partitioned based on their differing affinity for the phases involved, which results in characteristic geochemical signatures. The preservation of such geochemical "fingerprints" in igneous rocks erupted and/or exposed at the surface can be used to infer their formation and differentiation histories. For example, depletion of the heavy rare earths elements (HREE) relative to the light (L) and middle (M) REE is characteristic of garnet, whilst amphibole preferentially incorporates the MREE over the HREE (Davidson *et al.*, 2007). Similarly fractionation of element pairs which have similar solid/melt distribution coefficients but differing fluid mobilitys (e.g. Ba/Th) have been used as indicators of slab-fluid addition at subduction zones (Becker *et al.*, 2000).

The compatibility of an ion, *i*, in a mineral phase relative to the melt phase, described by its mineral-melt partition coefficient (D_i), is strongly controlled by its radius (r_i) and charge ($n+$). As shown in Fig. 1.1, plotting the log of the partition coefficients against the atomic radii for a series of cations of the same charge entering a mineral site describes a parabola with a maximum corresponding to the size of the crystal lattice site on which substitution occurs (originally reported by Onuma *et al.*, 1986). The lattice strain model of Blundy and Wood (1994) gives a functional form to this experimental observation:

$$D_i = D_0^{n+} \exp\left\{\frac{4\pi N_A E^{n+}\left[\frac{1}{2}r_0^{n+}(r_i - r_0^{n+})^2 + \frac{1}{3}(r_i - r_0^{n+})^3\right]}{RT}\right\} \qquad (1.1)$$

where r_0 is the size of the substitutional site, E is the elastic response of that site to lattice strain (effective Young's Modulus) caused by ions that are bigger or smaller than r_0, D_0 is the partition coefficient of an ideally sized fictive cation that would enter the crystallographic site without strain, R is the ideal gas constant, N_A is Avogadro's number, and T is temperature (in Kelvin). The high sensitivity of partitioning behaviour to charge is also illustrated in Fig. 1.1, where the partitioning parabolae become tighter (E increases) and displaced to lower r_0 as charge increases.

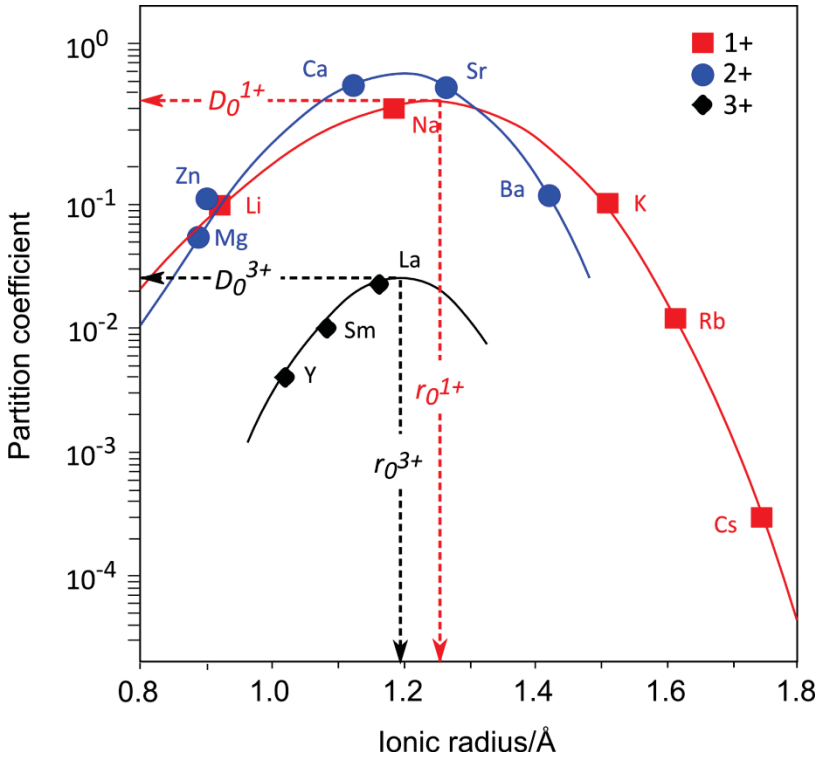


Figure 1.1: Fits of the lattice strain model to experimental plagioclase-melt partition coeffcients of different valence cations. The position of the maximum of the lattice strain parabola gives the size of the substitutional site (r_0) and the partition coefficient (D_0) of an ideally sized fictive cation that would enter the crystallographic site without strain (Figure adapted from: Blundy and Wood, 2003, Fig. 3 and 4(a), p. 69 and 70).

An important variable that has at times been neglected in experimental partitioning studies is oxygen fugacity (fO_2), which is a measure of the "availability" or chemical potential of

oxygen in a system. In the case of elements with more than one valence state, fO_2 is fundamental in controlling what oxidation states will be stabilised in a melt and in what proportions. The dependence of partitioning behaviour on ionic size and charge means that ions of the same element but having different oxidation states may behave entirely differently. For example Fe^{2+} strongly partitions into olivine, whilst Fe^{3+} behaves incompatibly (Bézos and Humler, 2005). Similarly, extreme positive Eu anomalies in the REE patterns of feldspars are attributed to its occurrence as Eu^{2+}, in contrast to the other REE, which are present as 3+ ions (Schnetzler and Philpotts, 1970).

1.2 U-series disequilibria and U-series models

1.2.1 Introduction to U-series disequilibria

U has received particular attention in igneous petrology due to its position as the initial parent in two radioactive decay chains (Fig. 1.2). A key characteristic of these U-series chains is that the initial U parent nuclides have much longer half-lives than all their intermediate radioactive daughter nuclides. This leads to the phenomenon of secular equilibrium, where, in an undisturbed system, the activity of a parent will be equal to that of its daughter (i.e. the parent-daughter activity ratio is 1: Bourdon *et al*., 2003). However, when the parent and daughter elements are partitioned from each other during processes that discriminate chemical behaviour, such as melting, fractional crystallization, fluid-melt partitioning, and magma degassing, U-series disequilibria are produced (Lundstrom *et al*., 2003). The magnitude and sense of a particular disequilibrium are dependent on the relative partitioning behaviour of the parent and daughter nuclides concerned. After the event causing parent-daughter disequilibrium the system returns to essentially secular equilibrium after 6 half-lives of the relevant daughter (^{230}Th = 76 kyr, ^{226}Ra = 1599 yr, ^{210}Pb = 22.6 yr, and ^{231}Pa = 33 kyr) (Bourdon *et al*., 2003). The preservation of various U-series disequilibria in volcanic rocks

from a range of tectonic settings has thus become a major focus for constraining the timescales of magmatic processes (Lundstrom *et al.*, 2003; Turner *et al.*, 2003). However, these timescales are only meaningful if the processes responsible for generating the disequilibria preserved at the surface can be assigned correctly. For example, interpreting U-series disequilibria actually generated at crustal levels to be derived from mantle processes could lead to magma transport times being significantly underestimated. To have any hope of making these assignments, the aim of U-series models, the partitioning behaviour of the parent relative to that of the daughter must be known.

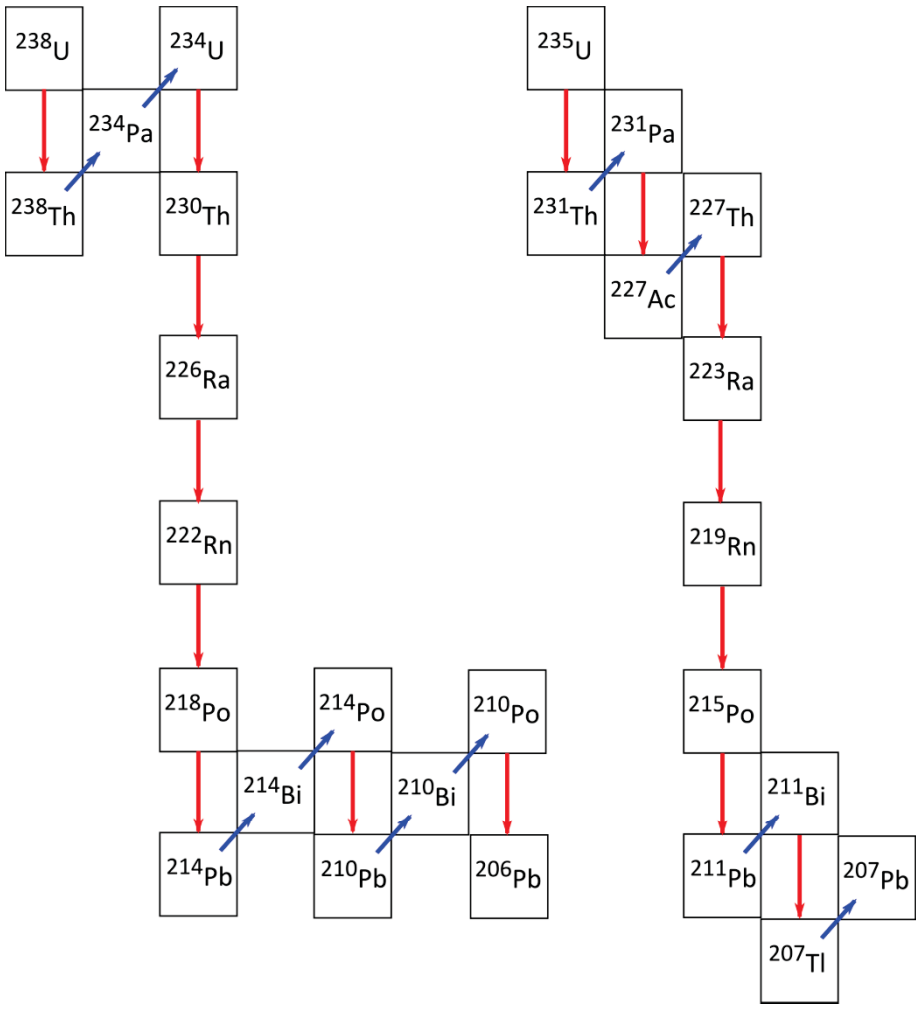


Figure 1.2: The ^{238}U and ^{235}U decay chains. Red and blue arrows represent α and β decay, respectively.

1.2.2 U-series element partition coefficients and proxies

Models that attempt to reproduce the U-series systematics of volcanic rocks are heavily reliant on the values of their input parameters, and the mineral-melt partition coefficients of key U-series elements (U, Th, Pa, and Ra) are fundamental to the models discussed in the following sections. Whilst many experimentally determined mineral-melt partition coefficients have been reported for U and Th (e.g. Beattie, 1993a and b; Wood *et al.*, 1999; Salters *et al.*, 2002; Salters and Longhi, 1999; Aigner-Torres and Blundy, 2007), experimental partition coefficients for Ra and Pa are extremely limited (Schmitt, 2007; Miller *et al.*, 2007; Fabbrizio *et al.*, 2009). This dearth of experimental data for Ra and Pa is largely due to their extreme incompatibility and high radioactivity, which makes doping to levels required to measure partition coefficients problematic. The partitioning behaviour of Pa and Ra are thus almost entirely derived from modelling and extrapolation of the partition coefficients measured for other elements (Blundy and Wood, 2003).

Since the parameters E and r_0 of Eq. 1.1 have physical meaning and exhibit systematic variations as a function of cation charge, their values can be estimated, and in turn be used to estimate the partition coefficient of a U-series element, a, based on the partition coefficient of a proxy, b (Blundy and Wood, 2003). The proxy must be of the same charge and similar radius to the element of interest, and its partitioning behaviour must be known under appropriate conditions. The U-series element partition-coefficient can then be obtained using Eq. 1.1 to write an expression for D_a, which when divided by the analogous expression for D_b and rearranged gives:

$$D_a = D_b \exp\left\{\frac{4\pi N_A E^{n+}\left[\frac{1}{2}r_0^{n+}(r_b^2 - r_a^2) - \frac{1}{3}(r_b^3 - r_a^3)\right]}{RT}\right\} \qquad (1.2)$$

1.2.3 U-series disequilibria in Mid-Ocean-Ridge Basalts

The U-series disequilibria observed in Mid-Ocean-Ridge Basalts (MORBs) have underpinned the development of the "standard" magmatic U-series models. As shown in Fig. 1.3, MORB samples from many ocean-ridges settings exhibit ($^{230}Th/^{238}U$), ($^{226}Ra/^{230}Th$) and ($^{231}Pa/^{235}U$) > 1 (where the parentheses denote activity), also referred to as Th, Ra and Pa excesses (Volpe and Goldstein, 1993; Sims *et al*., 2002; Rubin *et al*., 2005; Russo *et al*., 2009). Samples with ^{238}U excesses have rarely been reported, and these excesses are relatively small, with ($^{230}Th/^{238}U$) > 0.94 (Tepley *et al*., 2004; Elkins, 2009). The lack of ^{234}U-^{238}U disequilibria in these samples, and the fact that older basalts collected further from the ridge axis have ($^{226}Ra/^{230}Th$) = 1, suggests that the observed disequilibria do not result from post-eruptive alteration, and therefore represent magmatic processes (Volpe and Goldstein, 1993; Russo *et al*., 2009, Sims *et al*., 2002).

The U-series disequilibria observed in MORBs show correlations with features of magma differentiation, magma enrichment, and each other (Volpe & Goldstein, 1993; Sims *et al*., 2002; Rubin *et al*., 2005; Russo *et al*., 2009; Zhang *et al*., 2010). An inverse correlation between Th and Ra excesses is common, and has been confirmed as an eruptive feature of age constrained samples from the East Pacific Rise (EPR: Zhang *et al*., 2010; Rubin *et al*, 2005; Sims *et al*, 2002). The correlations of ($^{226}Ra/^{230}Th$) and ($^{230}Th/^{238}U$) with indices of differentiation, including SiO_2, Mg number (Mg# = Mg/(Mg + Fe)), and incompatible element enrichments, indicate that the most differentiated samples exhibit the largest Th excesses and lowest Ra excesses (Sims *et al*. 2002; Rubin *et al*., 2005).

The general requirement to produce Th excess in a melt, either by equilibrium partial melting or fractional crystallization, is that U is more compatible in the solid mineral assemblage than

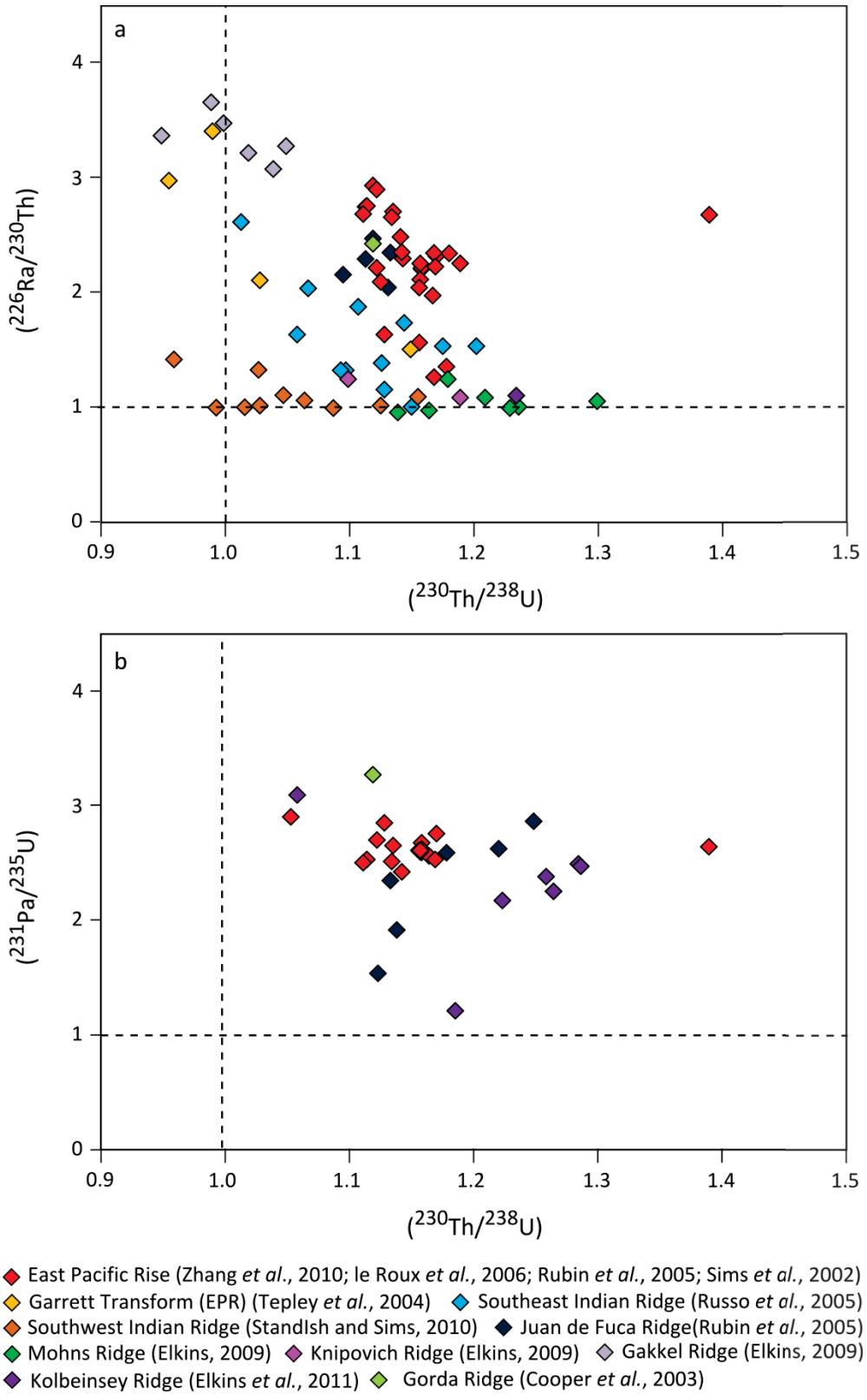


Figure 1.3: (a) ($^{226}Ra/^{230}Th$) and (b) ($^{231}Pa/^{235}U$) vs. ($^{230}Th/^{238}U$) for MORB samples from a range of settings, compiled from the literature.

Th (i.e. $D_U > D_{Th}$). U and Th are extremely incompatible in the major mantle minerals (Beattie, 1993a and b; Wood *et al.*, 1999; Salters *et al.*, 2002; Salters and Longhi, 1999; Blundy and Wood, 2003); however, U and Th mineral-melt partition coefficients for garnet and clinopyroxene are at least an order of magnitude larger than those for olivine and orthopyroxene and thus dominate the partitioning behaviour of U and Th in the upper mantle. U is more compatible than Th in garnet (Beattie, 1993a and b; Lundstrom *et al.*, 1994), whilst there is a strong pressure dependence on the relative preference of clinopyroxene for U over Th (Fig. 1.4: Wood *et al*,. 1999; Lanwehr *et al.*, 2001; Blundy and Wood, 2003). With increasing pressure along the mantle solidus clinopyroxene becomes poorer in Ca, decreasing the size of the M2 substitutional site, causing the clinopyroxene to increasingly favour the incorporation of the smaller U^{4+} ion over Th^{4+} (Blundy and Wood, 2003).

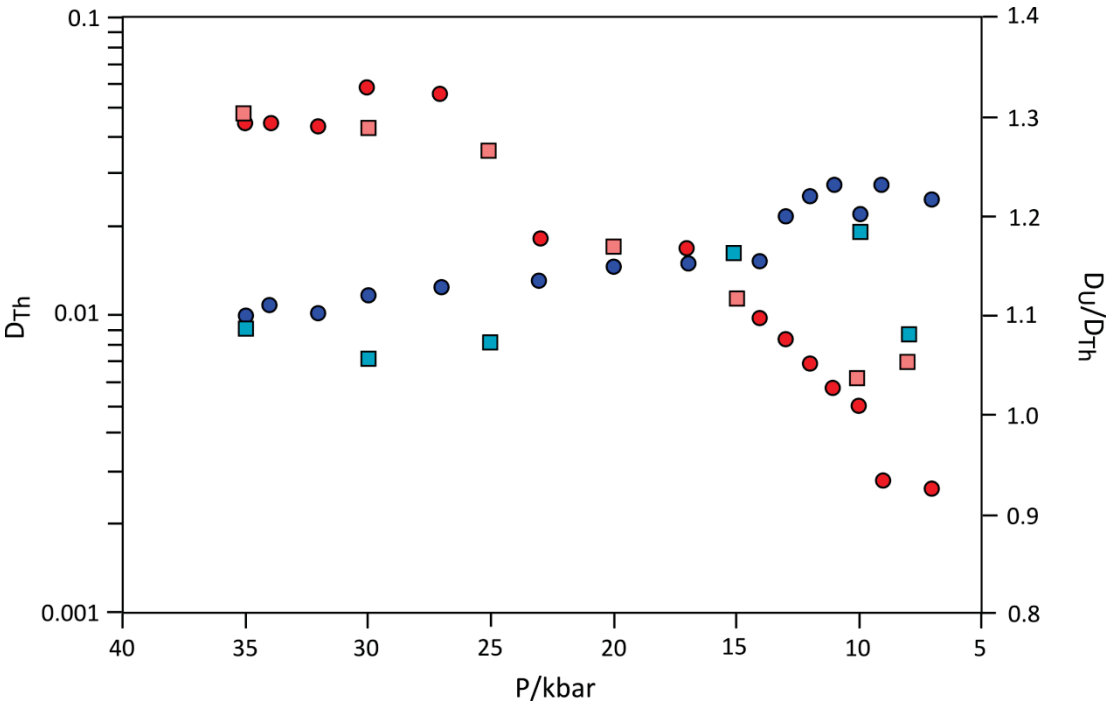


Figure 1.4: Calculated variation in D_U/D_{Th} (red symbols) and D_{Th} (blue symbols) along the mantle solidus (Figure Source: Blundy and Wood, 2003, Fig. 2, p. 67). Solidus clinopyroxene compositions were taken from experiments on natural compositions (squares: Falloon and Green, 1987) and synthetic systems (circles: - Walters and Presnall, 1994) and partition coefficients were calculated using the model of Landwehr *et al.* (2001).

The highly incompatible nature of U, Th, Ra, and Pa means that MORB U-series disequilibria cannot be attributed to simple fractional crystallization. Similarly, in simple batch or fractional melting models chemical fractionation will only occur when the degree of melting is comparable to the bulk partition coefficients. As such, attempts to reproduce the magnitudes of disequilibria observed in MORBs have resulted in the development of time-dependent melting models that are built on the concept of parent-daughter residence times (McKenzie, 1985 and 2000; Spiegelman and Elliot, 1993). For example, significant radioactive disequilibrium can be generated due to the U-series nuclides spending different times within a melting column during two phase flow by a "chromatographic" effect (Spiegelman and Elliot, 1993). As shown in Fig. 1.5, during mantle upwelling and melting, elements that do not partition into the solid (perfectly incompatible) move at the velocity of the melt, whereas perfectly compatible elements move at the velocity of the solid matrix through which the melt percolates. In fact, elements are expected to travel at some intermediate velocity governed by their mineral-melt partitioning behaviour. For a radioactive nuclide, the time spent in the column dictates how much of the nuclide entering the column will undergo radioactive decay and how much will survive to the top of the column. In the case of the radioactive intermediate daughter ^{230}Th and its parent ^{238}U, the amount of ^{230}Th leaving the column is equal to the sum of the amount of Th entering the column that does not undergo decay during transport (dependent on the residence time and half-life of daughter Th), and the amount of Th generated by decay of its radioactive parent U within the column (dependent on residence time and half-life of parent U). If the parent is more compatible, and therefore spends more time in the column, than the daughter it has more time to decay, and this may result in large excesses of the daughter nuclide at the top of the column (Bourdon *et al*., 2003; Spiegelman and Elliot, 1993).

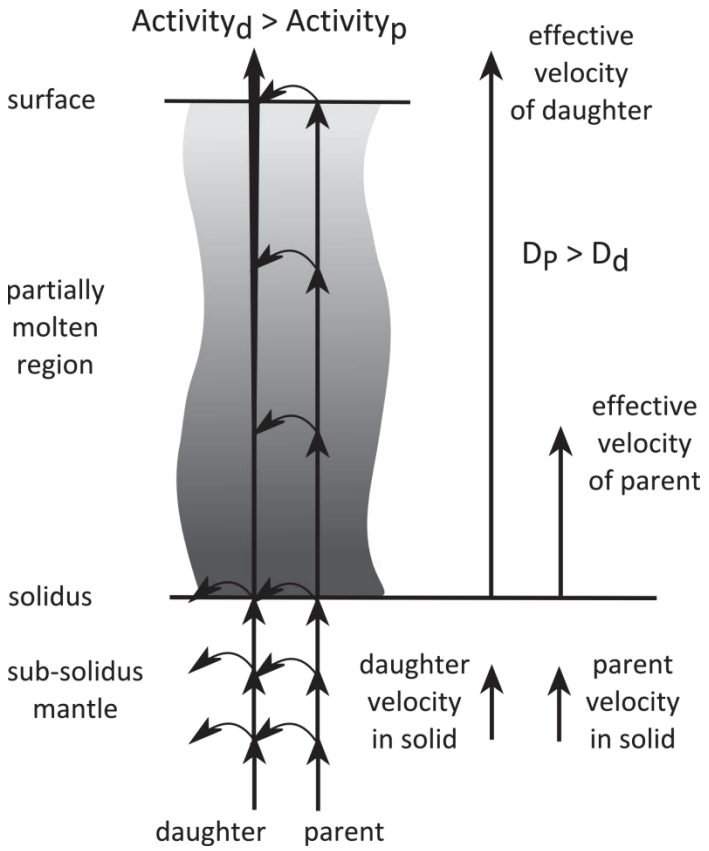


Figure 1.5: Schematic diagram showing the effect of melt transport with continuous melt-solid interaction on parent (p) and daughter (d) activities (Figure source: Spiegelman and Elliot, 1993, Fig.2, p.2). The vertical arrows show the distance each element travels before a fixed percentage decays (curved arrows denote decay). In the melting column the daughter is less compatible (i.e. smaller mineral-melt bulk partition coefficient, D) and travels faster than the parent. The total concentration of the daughter at the surface is enriched relative to the concentration at the base by decay of its slower moving parent.

Two end-member types of time-dependent models are often used: dynamic melting models (McKenzie, 1985; Stracke *et al*., 2003) and equilibrium transport models (also known as reactive porous flow models: Spiegelman and Elliot, 1993). In the case of dynamic melting models, melt is continually extracted from the melting region to maintain a critical threshold porosity, and melt transport occurs in chemical isolation from the surrounding solid mantle. This means that residence time differences, and hence disequilibria, can only be generated at the initiation of melting where a more compatible element will spend longer in the solid

before it is "pushed" into the liquid by melting (Spiegelman and Elliott, 2003). In dynamic melting models the U-series disequilibria start to decay as soon as the melt and matrix separate, and magmas must be transported rapidly to the surface (relative to the shortest daughter half-life) to prevent significant decay during transport (McKenzie, 1985). On the other hand, equilibrium transport models allow melt to continuously re-equilibrate with the surrounding solid during transport and residence time differences can be generated throughout the melting column.

The fact that MORBs are not in chemical equilibrium with abyssal peridotites (harzburgite and lherzolite) or mantle peridotites in ophiolites, either in terms of their trace element contents or orthopyroxene saturation (Kelemen *et al*., 1995; Batanova and Savelieva, 2009) has lent support to dynamic melting models. In addition, the contact relations of abyssal and ophiolitic dunites with surrounding mantle rocks, and the fact that they are close to being in chemical equilibrium with MORBs, has led to the conclusion that they represent pathways of focused melt migration (Kelemen *et al*., 1995; Batanova and Savelieva, 2009). However, the negative correlation between ^{230}Th and ^{226}Ra excesses seems to be inconsistent with either a dynamic or an equilibrium transport model alone. Melts produced by dynamic melting should show a positive correlation, whereas melts produced by reactive porous flow to shallow levels should not preserve a Th excess, since $D_U < D_{Th}$ in the shallow mantle (Sims *et al*., 2002). These conflicting observations have led to the development of models that lie somewhere between the "dynamic melting" and "equilibrium transport" end-members, which are termed "two-porosity models" (Jull *et al.*, 2002; Lundstrom, 2000; Iwamori, 1994).

The two-porosity models require that some melt produced at the base of the column ascends through high porosity conduits, where it does not react with shallower mantle material (as in

dynamic melting models), and the rest travels through a low porosity matrix where it continues to react with the surrounding solid (as in equilibrium transport models). The "deep" melt signature includes a Th excess (caused by garnet or Ca-poor clinopyroxene), a lower Mg#, higher incompatible element contents, and sometimes a slight enrichment of MREE over HREE (Lundstrom, 2003). In contrast, the "shallow" melt has a low Th excess (or U excess) and high Ra excesses (Lundstrom, 2003). Mixing of these melts generates the required negative correlation between Th and Ra excesses.

1.2.4 U-series disequilibria in arcs

In contrast to MORBs, arc basalts exhibit far more variable U-series ratios (Fig. 1.6); large ^{238}U excesses are common, though many arc basalts are close to ($^{230}Th/^{238}U$) equilibrium and some exhibit similar ^{230}Th excesses to MORBs. The near equilibrium ($^{230}Th/^{238}U$) ratios are generally accompanied by ^{231}Pa and ^{226}Ra excesses suggesting that they are not a result of melt/rock ageing (Reubi *et al.*, 2014). In contrast to their differing U-Th systematics, the Pa excesses reported for arc lavas are of a similar magnitude to those of MORBs, although the average Pa excess of arcs is slightly lower. The Tongan arc represents a rare exception with lavas exhibiting small ^{231}Pa deficits (Bourdon *et al.*, 1999). Similarly to the ^{231}Pa-^{235}U system, most of the measured arc ^{226}Ra excesses are within the range reported for MORBs, however they extend to higher values and extreme excesses have been recorded for individual samples from some arc settings (Caulfield *et al.*, 2012; Beier *et al.*, 2010; Turner *et al.*, 2003). In addition to a broadly positive correlation between arc ($^{231}Pa/^{235}U$) and ($^{230}Th/^{238}U$) (Pickett and Murrell, 1997; Turner *et al*., 2006), a negative correlation between ^{231}Pa excess and convergence rate has been noted (Turner *et al.*, 2006).

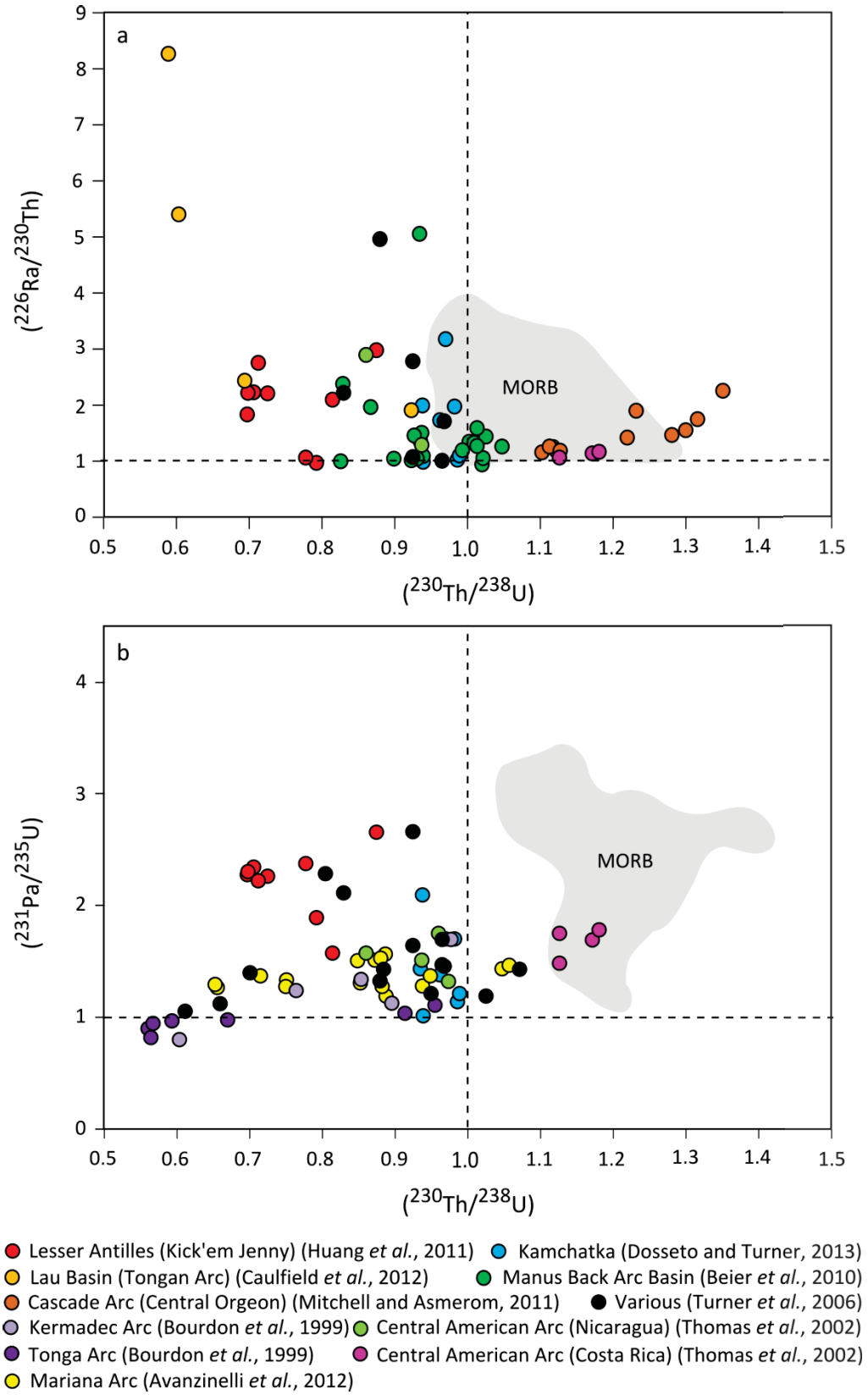


Figure 1.6: (^{230}Th/^{238}U) vs. (a) (^{226}Ra/^{230}Th) and (b) (^{231}Pa/^{235}U) for arc basalts and basaltic andesites from a range of settings, compiled from the literature. Fields of MORB data (from Fig. 1.3) are shown for comparison.

Whilst ^{238}U excesses relative to ^{230}Th may be generated by partial melting in the spinel lherzolite field at sufficiently low pressures that $D_U < D_{Th}$, this cannot cause sufficient U-Th fractionation to generate the large U excesses observed in arc magmas (Landwehr *et al*., 2001). Thus, arc ^{238}U excesses have widely been attributed to the addition of U-enriched slab-derived fluids (i.e. with ($^{238}U/^{230}Th$) > 1) to the mantle wedge prior to melting (Turner *et al.*, 2003). Excesses of ^{226}Ra in some arc lavas that are greater than any reported for MORB, and strong correlations between ^{226}Ra excesses and slab fluid indicators, such as Ba/Th and Sr/Th, have been used as evidence that the ^{226}Ra excesses of arc lavas are also a slab-derived signature (Turner *et al.*, 2001; Dosseto and Turner, 2013). This model requires that the time between slab dehydration and the final eruption of lavas is < 8 kyr, requiring rapid mantle melting, melt transport, and differentiation. However, the relative timing of U addition to the mantle wedge has been inferred to be between 10 and 200 kyr from arc suite U-Th equiline diagrams (Turner *et al.*, 2003). Multiple or continuous dehydration events, where the first fluids carry both U and Ra and the last carry only Ra, which is replenished in the slab by ingrowth from the fluid-immobile Th, have been suggested as a means of reconciling the conflicting U-Th and Ra-Th timescales.

In contrast to ^{238}U and ^{226}Ra excesses, ^{231}Pa excesses in arc lavas represent the opposite sense of disequilibria to that expected from fluid addition. They have thus been attributed to time-dependent melting signatures (Pa excess over U), similar to those observed in MORBs, overprinting fluid addition (U excess over Pa) (Turner *et al*,. 2006; Pickett and Murrell, 1997; Dosseto and Turner, 2013). The generation of Pa excesses requires that melts are derived from the mantle during upwelling or downwelling that lasts hundreds to thousands of years, which is again in conflict with the inference of slab-derived Ra-Th disequilibria (Huang *et al.*, 2011). More recently ^{231}Pa excesses have been attributed to the addition of sediment

melts from the subducting plate to the mantle wedge (Avanzinelli *et al.*, 2012). In this case, the sense and magnitude of disequilibria carried by sediment melts is expected to be strongly controlled by the stability of accessory phases (e.g. zircon, apatite, allanite, monazite: Hermann and Rubatto, 2009), which may explain the varied nature of U-series disequilibria in arc lavas (Avanzinelli *et al.*, 2012).

The U-series models outlined above have been built around the assumption that U^{4+} is the only oxidation state relevant to melt generation and differentiation, with the exception of U^{6+} carried by slab-derived aqueous fluids (Bali *et al.*, 2011). The U mineral-melt partition coefficients utilised by these models are based on high-pressure experiments (> 10 kbar) performed in graphite (unsealed) or graphite-lined capsules (Beattie, 1993a; Wood *et al.*, 1999; Landwehr *et al.*, 2001), which places a maximum limit on fO_2 of < QFM-1.3 (where QFM is the quartz-fayalite-magnetite solid-state buffer and QFM-1.3 is the C-CO_2 buffer), but does not define a minimum (Holloway *et al.*, 1992). Furthermore, the lattice strain derived U mineral-melt partition coefficients reported by Blundy and Wood (2003) explicitly assume that U is present as U^{4+} only. However, U is a multivalent element and the values of mineral-melt partition coefficients for U^{5+} and U^{6+} in the major mantle phases are expected to be considerably smaller than those of U^{4+} (Blundy and Wood, 2003; Lundstrom *et al.*, 1994). As such, it has recently been hypothesised that melting of an oxidised mantle, where U^{5+} and/or U^{6+} are stabilised in the melt, could produce large ^{238}U excesses (Beier *et al.*, 2010; Huang *et al.*, 2011). Indeed, such a model has been suggested as a means of producing the U-Th-Pa-Ra systematics of lavas from various arc settings that exhibit a wide range of U-series activity ratios (Beier *et al.*, 2010; Huang *et al.*, 2011; Reubi *et al.*, 2011 and 2014). Since in this scenario all disequilibria are generated during melting, by a similar mechanism hypothesised for MORBs, the time constraint on mass transfer from the slab to final eruption

is relaxed. Clearly the viability of such a model is entirely dependent on the oxidation state of U at conditions relevant to the sub-arc mantle.

1.3 Controls on melt redox equilibrium

Equilibrium between the oxidation states of a particular multivalent element in silicate melts is controlled by temperature, pressure, fO_2, and the composition of the liquid (Lauer and Morris, 1977). The reaction describing the oxidation of a metal, M, as an oxide component in a melt and the equilibrium constant for this reaction can be described by (Berry and O'Neill, 2004):

$$M^{n+}O_{n/2} + \frac{a}{4}O_2 = M^{(n+a)+}O_{(n+a)/2} \quad (1.3)$$

$$K = \frac{X_{M^{(n+a)}O_{(n+a)/2}}\gamma_{M^{(n+a)+}O_{(n+a)/2}}}{X_{M^{n+}O_{n/2}}\gamma_{M^{n+}O_{n/2}}(fO_2)^{a/4}} \quad (1.4)$$

where a is the number of electrons involved in the oxidation, X, is the mole fraction, and γ is the activity coefficient. Taking the log of Eq. 1.4 and rearranging leads to:

$$\log\frac{X_{M^{(n+a)}O_{(n+a)/2}}}{X_{M^{n+}O_{n/2}}} = \frac{a}{4}\log fO_2 + \log K - \log\frac{\gamma_{M^{(n+a)+}O_{(n+a)/2}}}{\gamma_{M^{n+}O_{n/2}}} \quad (1.5)$$

At low concentrations the behaviour of the element is independent of its concentration (Henry's Law) and for this case $\gamma_{M^{(n+a)+}O_{(n+a)/2}}$ and $\gamma_{M^{n+}O_{n/2}}$ can be assumed to be constant for a particular melt composition. For convenience we can define a new parameter:

$$\log K' = \log K - \log\frac{\gamma_{M^{(n+a)+}O_{\frac{n+a}{2}}}}{\gamma_{M^{n+}O_{\frac{n}{2}}}} = \frac{-\Delta G^0_{(T,\ P)}}{RT\ln 10} - \log\frac{\gamma_{M^{(n+a)+}O_{(n+a)/2}}}{\gamma_{M^{n+}O_{n/2}}} \quad (1.6)$$

Combining Eq. 1.4 and 1.5, and assuming:

$$M^{n+} + M^{n+a} = \sum M \quad (1.7)$$

the fO_2 dependence of oxidation state is given by:

$$\frac{M^{n+}}{\sum M} = \frac{1}{1 + 10^{\left(\frac{a}{4}\log fO_2 + \log K'\right)}} \quad (1.8)$$

which has a sigmoidal form, where logK´ controls the position, and *a* the steepness, of the redox transition in fO_2 space (Fig. 1.7).

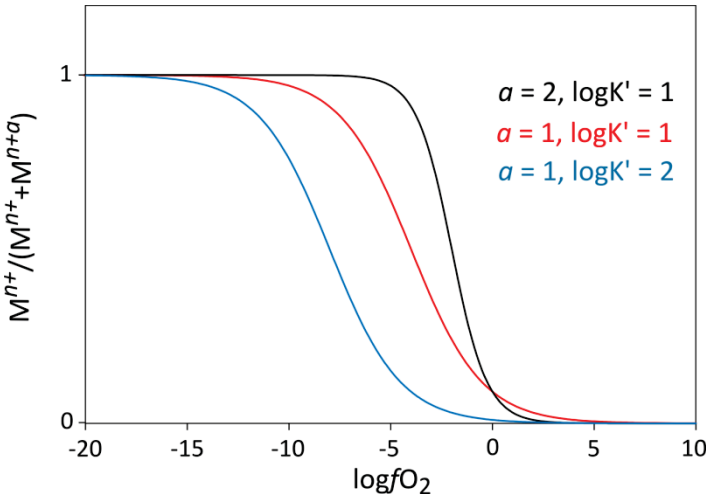


Figure 1.7: The theoretical relationship between oxidation state ratio and fO_2 in a melt.

1.3.1 Temperature and pressure

From Eq. 1.6 logK´, and hence the log of the redox ratios, is expected to have a linear relationship with 1/T, assuming that the temperature dependent variation of ΔG is negligible. For SiO_2-Na_2O-Fe_2O_3-FeO glasses quenched from melts equilibrated above the liquidus, log(Fe^{3+}/Fe^{2+}) vs. 1/T was found to be approximately linear over ~600 °C (Lange and Carmichael, 1989). A similar dependence has also been reported for Ce^{4+}-Ce^{3+}, although over a smaller temperature range (1300-1500 °C: Burnham and Berry, 2014). At constant fO_2, high temperature generally favours the reduced ion as has been reported for Fe^{2+}-Fe^{3+} (Kress and Carmichael, 1991), Ce^{3+}-Ce^{4+} (Burnham and Berry, 2014), Cr^{2+}-Cr^{3+}, Ti^{3+}-Ti^{4+} and Eu^{2+}-Eu^{3+}(Schreiber, 1977); notably, this is not the case for Cr^{3+}-Cr^{6+} (Schreiber, 1977).

The effect of pressure on the free energy term in Eq. 1.6 is given by:

$$\Delta G^{0}_{(T,\ P)} = \Delta G^{0}_{(T,\ 1\ bar)} + \int_{1\ bar}^{P} \Delta \bar{V} melt_{(T,\ P)} \cdot dP \qquad (1.9)$$

where $\Delta \bar{V} melt_{(T,\ P)}$ is the change in molar volume of the condensed components in the reaction. Increasing pressure is expected to favour smaller molar volumes and has been shown to cause a slight decrease in the Fe^{3+}/Fe^{2+} (Mysen and Virgo, 1985; Kress and Carmichael, 1991; O'Neill *et al.*, 2006) and Ce^{4+}/Ce^{3+} (Burnham and Berry, 2014) ratios in glasses. It has been suggested that the pressure induced reduction of Fe^{3+} to Fe^{2+} might be reversed at very high pressures (>> 3 GPa) due to the greater compressibility of Fe_2O_3 relative to FeO causing a switch in the volume change of the redox reaction (Kress and Carmichael, 1991).

1.3.2 Composition

The effect of composition on oxidation state has been reported using various compositional parameterisations. Silicate melts consist of a network of SiO_4 tetrahedra in which Si^{4+} may be partially replaced by other cations that have a similar ionic radius and charge (network formers, e.g. Al^{3+}); these tetrahedra are linked by bridging oxygens (BO: see Figure 1.8). The melt network is disrupted by the addition of network modifying cations (including alkalis and alkali earths) that generate non-bridging oxygens (NBO). As such, melt composition is commonly parameterised as the ratio of non-bridging oxygens to tetrahedral oxygens (NBO/T: Mysen *et al.*, 1982), which essentially describes the degree of melt polymerisation, whereby NBO/T increases as polymerisation decreases. However, oxidation state ratios do not always exhibit strong correlations with NBO/T (Berry *et al.*, 2006), which is perhaps unsurprising as it does not account for the differing chemical behaviour of elements within the same group.

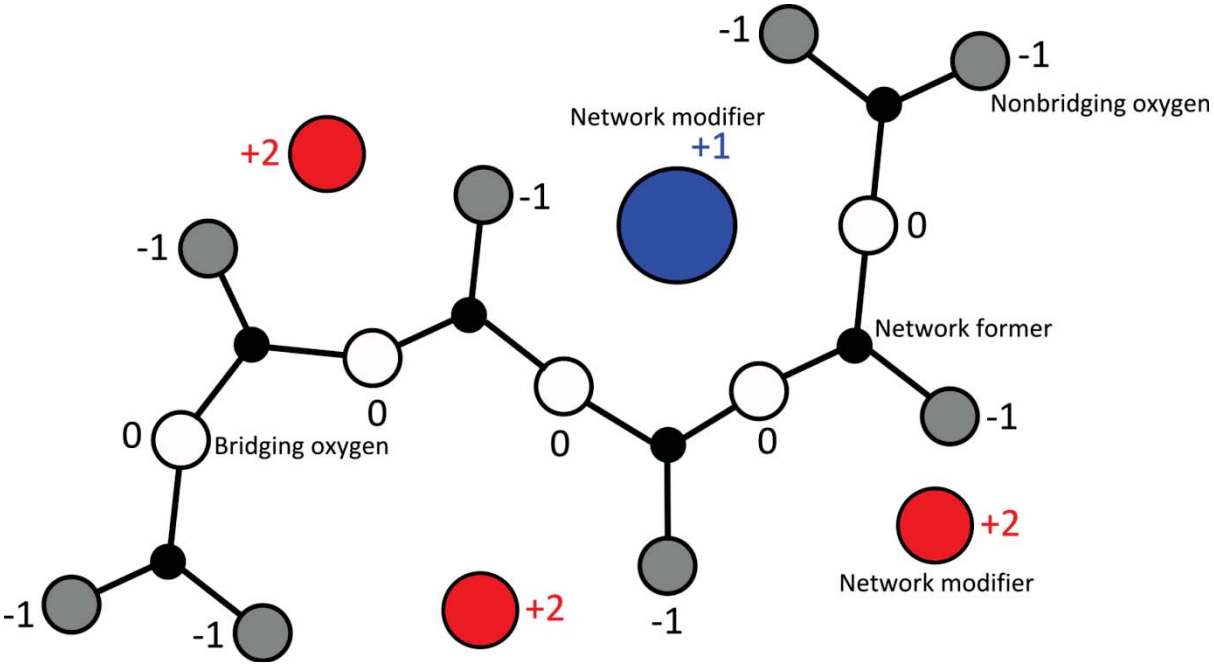


Figure 1.8: Structural components and their charges in a silicate glass.

An alternative approach is to express melt composition as a linear combination of the mole fractions of the constituent oxides with weightings applied to each term. Such a parameterisation has been derived for calculating Fe^{3+}/Fe^{2+} ratios in silicate melts based on a large dataset (Kress and Carmichael, 1991). A convenient compositional index, is optical basicity (Λ: Duffy, 1993), which can be thought of as either a measure of the average electron density around an oxygen atom, or the electron donor power of the medium; increasing basicity accompanies increasing negative charge on the oxygen atom. It is calculated as a summation of the proportion of oxygen atoms contributed by each oxide with a basicity weighting applied to each term:

$$\Lambda_{total} = \sum_i \Lambda_i X_i \qquad (1.11)$$

The basicity weighting/scaling terms of individual oxides have been experimentally determined using glasses containing a metal "probe" (Pb^{2+} or Tl^{+}) ion which exhibits an intense UV absorption peak. The extent of negative charge the metal ions receive depends on

the state of polarisation of the oxygen atoms and the position of the absorption peak shifts accordingly (Duffy and Ingram, 1976). More ionic network modifiers (e.g. Na^{+}, Ca^{2+}, Mg^{2+}) produce a larger negative charge on the oxygen atom, and thus have higher basicity weightings, than the network formers (Si^{4+} and Al^{3+}) (Duffy and Ingram, 1976). Excellent correlations of Λ with Ce^{3+}/Ce^{4+} (Burnham and Berry, 2014), Cr^{2+}/Cr^{3+} (Berry *et al.*, 2006), and Fe^{2+}/Fe^{3+} (Duffy, 1993) ratios have been reported, with higher basicity compositions favouring the more oxidised ion. These correlations have been attributed to the greater ability of O atoms in higher basicity melts to donate electron density and stabilise higher oxidation states (Duffy and Ingram, 1976).

1.4 Quantifying the oxidation state of U in silicate melts

Quantification of multivalent oxidation states in silicate melts has largely relied upon analyses of their quenched products at ambient temperature. Accurate quantification of U oxidation state as a function of the fO_2 of melt equilibration ($\log fO_2$ = 0 to -10 at 1450 °C) has previously been attempted for four silicate glass compositions by redox titrations in conjunction with visible to near IR absorption spectroscopy (Fig. 1.9: Schreiber, 1983). Redox titration measures the total reducing power of the sample by dissolving the glass in a solution containing excess Fe^{3+}. This solution reacts with the reduced U species to form U^{6+} and Fe^{2+}, and the resulting Fe^{2+} can be subsequently measured. The absorption spectra indicated the stability of three U oxidation states: U^{4+}, U^{5+}, and U^{6+}, and in order to quantify the relative amounts of the two reduced species (U^{4+} and U^{5+}) from redox titrations successive approximations were required. At the highest and lowest fO_2s it was assumed that only two states were stable (U^{5+} and U^{6+} at high fO_2s, and U^{4+} and U^{5+} at low fO_2s); the total U content and the total reduced U (as given by the titrations) were then used to quantify the proportions of each valence state. Finally the U^{4+} and U^{5+} proportions at intermediate fO_2s

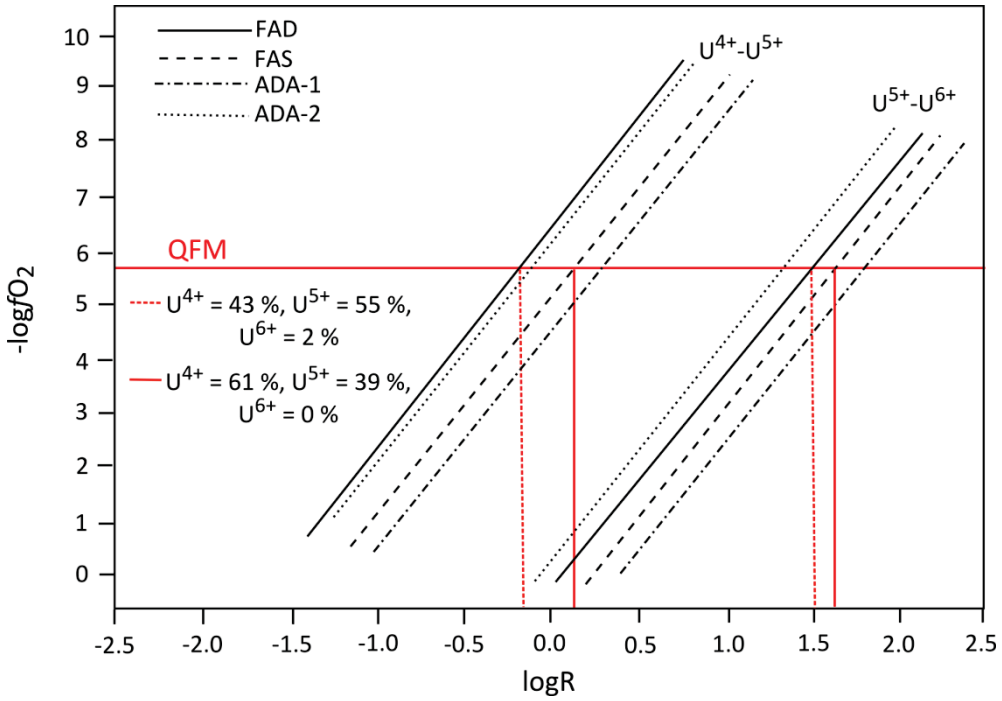


Figure 1.9: Uranium redox equilibria as a function of the imposed oxygen fugacity for U-doped glasses of various Fe-free compositions: FAD, FAS, ADA-1, and ADA-2 (FAS and FAD are Ca-Mg-Al-Si compositions, while ADA-1 and 2 include Na), at a melt temperature of 1450 ^{0}C and total U content of ~1 wt %. R = $[U^{4+}]/[U^{5+}]$ or $[U^{5+}]/[U^{6+}]$ (Figure Source: Schreiber, 1983, Fig. 4, p. 136). The U oxidation state proportions in FAS and FAD glasses at a fO_2 value equivalent to the QFM buffer are shown.

---

were estimated based on the relationships defined at low and high fO_2s and the expected thermodynamic relationships for two one electron oxidation reactions (Eq. 1.5 for U^{4+} to U^{5+} and U^{5+} to U^{6+}: Fig. 1.9). Redox titration is not element specific making it unsuitable for quantification of U redox ratios in glasses containing more than one multivalent species such as Fe- or Ti- bearing compositions.

Mineral-melt partitioning studies provide an indirect means of estimating the oxidation state ratios of elements in melts, as the measured partitioning of an element will represent an average of the partition coefficients of all its stable oxidation states weighted to their relative proportions. Results of a systematic study of the partitioning of U between zircon and a

andesitic melt composition as a function of fO_2 (over 15 log units) at 1300 °C and 1 atm were consistent with the oxidation of U^{4+} to U^{5+} in the melt with increasing fO_2, and indicated that this transition occurs at geologically relevant fO_2s (Burnham and Berry, 2014). Similarly, a decrease in the measured U clinopyroxene-melt partition coefficient with increasing fO_2 has been attributed to an increase in U oxidation state (Lundstrom, 1994), although this study neglected intermediate fO_2s.

Characterisation, including oxidation state quatification, of various U oxide compounds has been achieved by spectroscopic techniques including X-ray photoelectron spectroscopy (XPS), and X-ray absorption near-edge structure (XANES) spectroscopy (e.g. Belai *et al.*, 2008; Ilton and Bagus, 2011; Kvashnina *et al.*, 2013). Oxidation state assignment using XPS is based on shifts of core-electron binding energy peaks and associated satellite peaks (Ilton and Bagus, 2011), but this has proven ambigous even for relatively simple stoichiometric compounds. For example, XPS studies have attributed the mixed valence oxide U_3O_8 to a mixture of U^{4+} and U^{6+} ions in a 1:2 ratio (Idriss, 2010; Pireaux *et al.*, 1977); a conclusion that has been entirley undermined by a recent XANES study of U_3O_8, where the contribution of U^{5+} was clearly distinguishable ($2 \times U^{5+} + 1 \times U^{6+}$: Kvashnina *et al.*, 2013).

XANES spectroscopy offers a direct means of probing oxidation state that is both element specific and highly sensitive; U can be studied even as a minor component in samples containing high concentrations of elements such as Fe. In addition, hard X-ray spectroscopy does not require a high vacuum environment, as is the case for XPS, and samples can be studied in almost any state making it ideal for *in situ* studies of high temperature melts under controlled atmospheres (Polovov *et al.*, 2008; Berry *et al.*, 2006; Berry *et al.*, 2003a). U L_3-edge XANES spectroscopy and the intrinsically linked Extended X-ray Absorption Fine

Structure (EXAFS) spectroscopy has already supported the conclusion that three oxidation states occur in U-bearing silicate glasses (Farges *et al*., 1992). U^{4+} and U^{5+} were reported to occur in 6-fold coordination sites, with U-O distances of 2.26-2.29 Å and 2.19-2.24 Å, respectively, whilst U^{6+} was present as uranyl groups with two short axial bonds (~1.77-1.85 Å) and four to five longer equatorial bonds (~2.21-2.25 Å) to oxygen (Farges *et al.*, 1992). However, Farges *et al.* (1992) made no attempt to quantify redox ratios, or study Fe-bearing compositions. The aim of this thesis is to address these gaps and use XANES spectroscopy as a means of quantifying U redox ratios in analogues of geological melts. This work not only explores the U redox equilibrium of quenched glasses but also extends the study of U oxidation state to high temperature melts *in situ*. The implications of the multivalent nature of U on current U-series models are then discussed.

Chapter 2:

Methods

2.1 Background

2.1.1 Absorption spectroscopy

The experimental techniques used in this research are outlined individually in the following sections of this chapter; they are reliant on the principles of absorption spectroscopy, where energy from a beam of radiation is transferred to matter. The radiation may be in the form of electromagnetic radiation or elementary particles. When the energy of the incident radiation is sufficient to eject a core-level electron from an atom there is a sharp rise in absorption (absorption edge) caused by the excitation of this electron to the continuum (photoelectron) leaving a core-hole. Following the absorption event the atom is in an excited (unstable) state and will decay by an electron from an outer orbital dropping to fill the core-hole resulting in either emission of a fluorescent photon, or ejection of another bound electron (Auger effect). This decay from the excited state occurs on the femtosecond timescale. For heavy elements fluorescence is the dominant process, whilst Auger emission is more probable for light elements (Heald, 1988).

Absorption edges are named according to the principal quantum number, n, of the excited electron. Whilst there is a single K-edge representing excitation of a 1s electron, there are three L-edges where the L_1-edge corresponds to the excitation of a 2s electron and the L_2- and L_3-edge to excitation of 2p electrons. The L_2 and L_3-edges correspond to the $2p_{1/2}$ and $2p_{3/2}$ states, respectively, which have different binding energies due to spin-orbit splitting. Similarly, there are five M-edges corresponding to excitation of 3s (M_1-edge), 3p (M_2- and

M_3-edge) and 3*d* ($3d_{3/2}$ and $3d_{5/2}$: M_4- and M_5-edges) electrons. The energy of each of these absorption edges is element specific (Fig. 2.1).

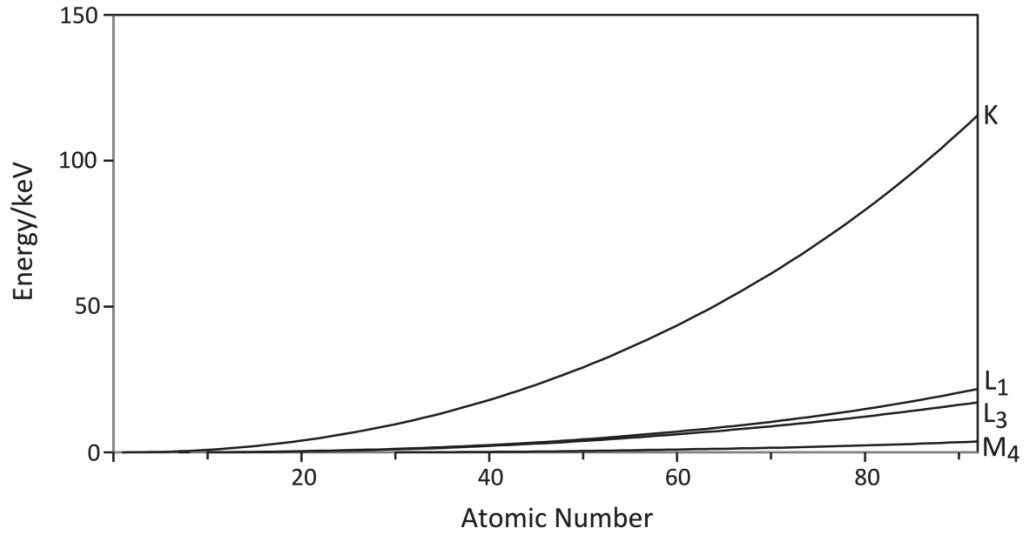


Figure 2.1: Edge energies as a function of atomic number (Thompson, 2009).

Electron orbital transitions are controlled by the dipole selection rules; the Laporte or parity selection rule states that electric dipole transitions may only occur between states differing in their orbital angular momentum quantum number, *l*, by 1 ($\Delta l = \pm 1$). For a given quantum number, *n*, *l* has a value between 0 and *n*-1; *s*-orbitals have *l* = 0, *p*-orbitals *l* = 1, *d*-orbitals *l* = 2 and so forth. Accordingly, the K- , L_1-, and M_1-edges provide information about the unoccupied *p* states, the $L_{2,3}$- and $M_{2,3}$-edges probe the unoccupied *s* and *d* states, and the $M_{4,5}$-edges probe the unoccupied *p* and *f* states. It is clear that there cannot be a transition between the K and L_1 shells as $\Delta l = 0$. However, the above statement is somewhat simplified as dipole forbidden transitions may occur under certain circumstances. For example, the Laporte selection rule is relaxed for transition metals in asymmetric coordination environments due to orbital mixing (Wildner *et al.*, 2004). Decay of an atom from a particular excited state may occur by numerous possible transitions, which are governed by the same

selection rules that apply to absorption, resulting in multiple discrete fluorescence lines, as shown in Fig. 2.2.

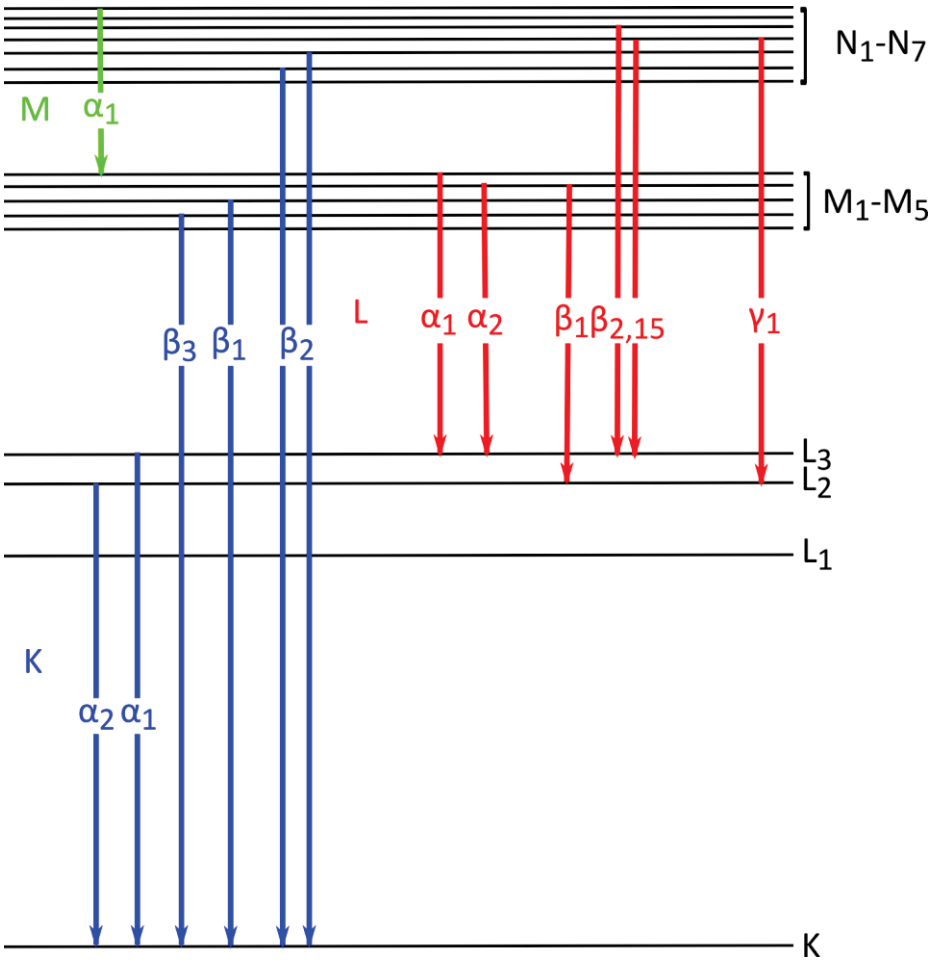


Figure 2.2: Transitions that give rise to various emission lines (Figure Source: Thompson, 2009, Fig. 1.1, p.1-14).

2.1.2 X-ray absorption spectroscopy

X-ray absorption spectroscopy (XAS) is the study of features around an X-ray absorption edge. An X-ray absorption spectrum consists of a sequence of structures (or features, or peaks) that, for data collection and analysis purposes, are generally divided into two regions, as shown in Fig. 2.3. Although the exact division of these regions is somewhat arbitrary and varies depending on the element/compound being probed, in a simplified view, the X-ray Absorption Near Edge Structure (XANES) region corresponds to a few eV below to ~50 eV

above the absorption edge, whilst the Extended X-ray Absorption Fine Structure (EXAFS) region occurs at energies > 50 eV (Brown *et al.*, 1988).

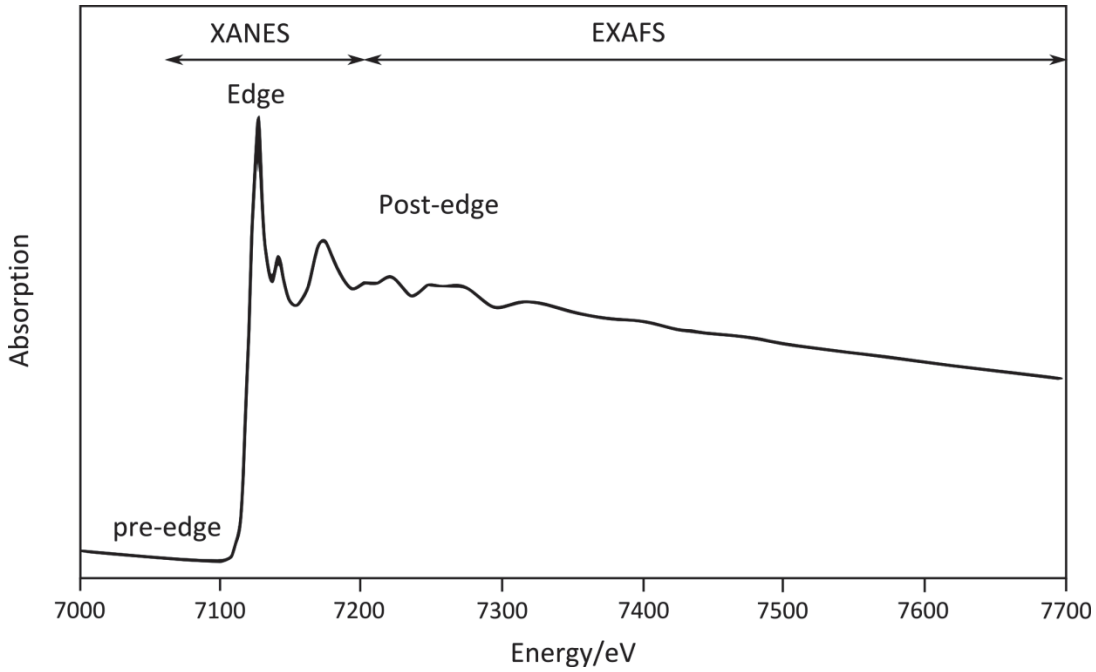


Figure 2.3: X-ray absorption spectrum of FeO (Newville, 2004).

The features of a X-ray absorption spectrum can also be divided based on the value of the incident X-ray energy, E_0, relative to the binding energy of the core-level electron, E_b. This division separates regions of different physical origin (Calas *et al.*, 1987). The pre-edge corresponds to the region below the main absorption jump ($E_0 < E_b$) where electronic transitions have low probabilities. The pre-edge may contain features representing electronic transitions to partially filled or empty bound states. The sharp rise in absorption corresponds to the edge region ($E_0 \sim E_b$) where there is a high probability of electronic transitions to unoccupied bound states or continuum states. This region includes the sharp intense peak or white-line, characteristic of many XANES spectra. The post-edge corresponds to $E_0 > E_b$ where electronic transitions occur with lower probability than at the edge, and the excited

photoelectrons remain in the sample for a short time with an excess kinetic energy (Brown *et al*., 1988).

The EXAFS region or far post-edge ($E_0 >> E_b$) is characterised by low frequency and low amplitude oscillations. These oscillations arise from weak backscattering of photoelectrons by single scattering processes (Brown *et al.*, 1988). The absorption of X-rays is given quantum mechanically by a matrix element between the initial state (electron in the atomic core) and final state (core-hole caused by the escaping photoelectron). When the ejected photoelectron has a high kinetic energy its interaction with the atoms surrounding the absorber atom can be treated to a good approximation as a perturbation of the final state about an isolated atom. The photoelectron is emitted from the core-level of the atom as an outgoing wave, which is then scattered by the surrounding atoms. The resulting final state is a superposition of the outgoing and scattered waves (Stern, 1988). The two wave functions will interfere constructively and destructively depending on their relative phase, which varies as a function of the photoelectron energy, thus producing the oscillations of the EXAFS region. The amplitude of the EXAFS oscillations depends on the number and type of atoms surrounding the absorber atom, while the frequencies depend on the absorber-scatterer distances (Calas *et al.*, 1987; Stern 1988). As the photoelectron's kinetic energy is lowered into the XANES region multiple scattering becomes more and more important. This is expressed in the XANES post-edge or near post-edge region, which is characterised by sharp features relative to the EXAFS oscillations. These multiple-scattering processes may extend beyond the nearest neighbour shell making XANES a sensitive probe of the local geometry and bonding characteristics around the absorbing atom (Brown *et al.*, 1988, Stern 1988).

2.1.3 XANES as a tool for oxidation state quantification

The multiple-scattering nature of the XANES spectral features make them complex to model. However, XANES may be used relatively straightforwardly as a fingerprinting technique. XANES spectral features are sensitive to oxidation state, for example, it is well established that features around the edge and pre-edge shift to higher energy with increasing oxidation state (e.g. for multivalent glasses: Fe-Berry *et al.*, 2003b; V-Sutton *et al*., 2005; Cr-Berry *et al.*, 2006; Eu-Karner *et al.*, 2010; Ce-Burnham and Berry, 2014). Indeed the energy shift of the Eu L_3-edge white-line between Eu^{2+} and Eu^{3+} is so large, that XANES spectra of mixed valence samples exhibit two peaks, as shown in Fig. 2.4, whose relative intensities vary as a function of redox ratio (Karner *et al.*, 2010). These energy shifts can be easily understood in

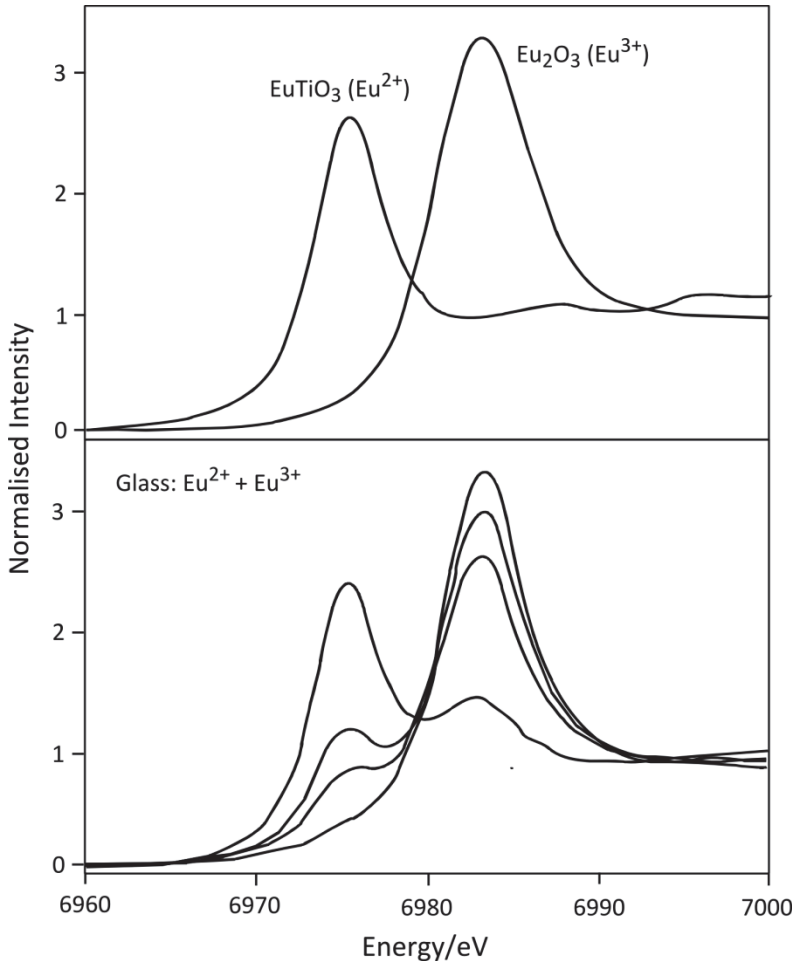


Figure 2.4: Eu L_3-edge XANES spectra of (a) Eu^{2+} and Eu^{3+} compounds, and (b) mixed Eu^{2+} + Eu^{3+} glasses (Karner *et al*., 2010).

terms of reduced nuclear shielding as electrons are removed from the outer shells, such that more energy is required to excite a core level electron in the higher oxidation state species (Brown *et al.*, 1988; Mottana, 2004).

However, oxidation state assignments must be made with caution as edge-energy is controlled by coordination environment as well as oxidation state, and a XANES spectrum may exhibit further features controlled by more complicated transitions and interactions, which may confuse oxidation state quantification. The Ce L_3-edge XANES spectra of various Ce^{3+} and Ce^{4+} compounds provides one example of the complexity of interpreting XANES spectral features (Fig. 2.5). The spectra of Ce^{3+} species are made up of a single intense

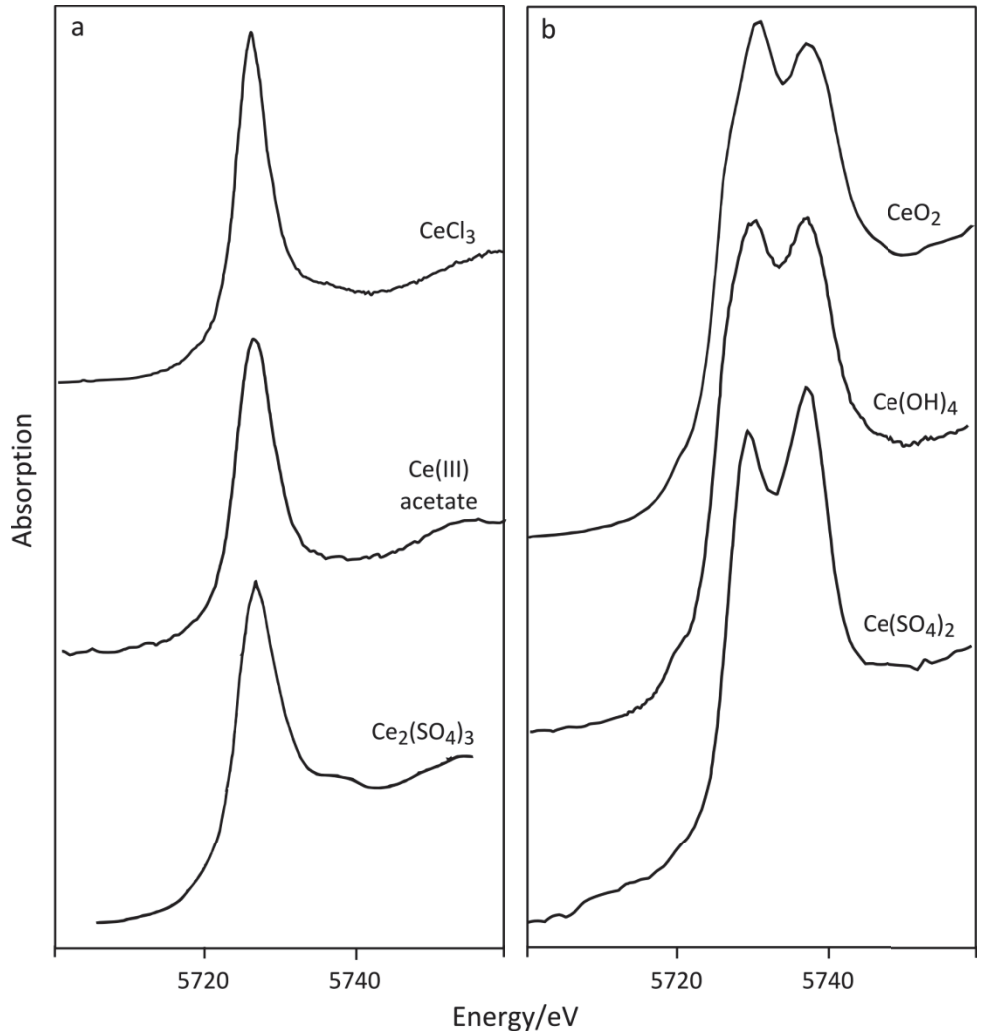


Figure 2.5: Ce L_3-edge XANES spectra of various (a) Ce^{3+}, and (b) Ce^{4+} species (Takahashi *et al*., 2002).

absorption peak at ~5726 eV, which is straightforwardly assigned to the $2p_{3/2} \rightarrow 5d$ transition using the dipole selection rules. In contrast the spectra of Ce^{4+} compounds have two distinct peaks at ~5730 and 5738 eV. The low energy peak of the Ce^{4+} spectrum results from mixing between the localized Ce 4*f* and the delocalised O 2*p* level (Soldatov *et al*., 1994). Thus, the higher energy peak is attributed to the $2p_{3/2} \rightarrow 5d$ transition and the lower energy peak to $2p_{3/2} \rightarrow (4f\underline{L})5d$ transition, which corresponds to simultaneous excitation of the Ce 2*p* electron to the 5*d* band and transfer of an electron from a ligand oxygen 2*p* orbital to the 4*f* orbital of Ce ("shake-down" transition) (Soldatov *et al*., 1994; Takahashi *et al*., 2002). The variation in Ce L_3-edge spectral shape with changing fO_2 (Burnham and Berry, 2014) is similar to that observed at the Eu L_3-edge for mixed valence glasses. As such, without knowledge of the pure Ce^{4+} line-shape, the XANES spectra and hence Ce redox ratios of glasses could easily be misinterpreted.

One approach to oxidation state quantification of mixed valence samples is by comparison or fitting of the unknown spectra with reference spectra collected from crystalline compounds for which the valence state is known. However, since XANES spectral features are strongly controlled by coordination geometry this approach is unlikely to be accurate for unknowns where the coordination environment is significantly different from the standards. This is a major limitation when comparing mineral standards with amorphous materials, including glasses and melts (Berry *et al.*, 2003b; Wilke *et al.*, 2004). An alternative approach is to prepare sets of samples such that the conditions of equilibration are known and the oxidation state ratios are expected to vary in a systematic way that can be predicted by thermodynamics. Preparing a suite of glasses over a large fO_2 range and fitting the relationship between spectral features and $\log fO_2$ using the redox equation (Eq. 1.8) has proven a highly successful methodology for oxidation state quantification of various elements

in glasses and melts (Cr: Berry *et al.*, 2006; Berry and O'Neill, 2004; Fe: Berry *et al.*, 2003b; Eu: Burnham *et al*., in preparation: see Appendix 6 of this thesis), although so far its application has been limited to divalent systems. The aim of this PhD is to use a similar approach to quantify the oxidation state of U in glasses and melts *in situ*.

2.2 Experimental Methods

2.2.1 Sample synthesis

A large number of epoxy mounted, synthetic U-doped silicate glasses, of different compositional sets, made by Dean Scott and Guil Mallmann at the Research School of Earth Sciences, Australian National University, Canberra, were provided for this research. In addition, further glasses were synthesised to supplement these sets during the course of the project. A full sample list is provided in the tables of Appendix A.2; samples made by persons other than the author are specified in the relevant tables. For room-temperature (RT) XANES spectroscopy studies seven compositional sets of U-bearing glasses, six in the system CaO-MgO-Al_2O_3-SiO_2 (CMAS), and the seventh a synthetic Fe-Ti-bearing Mid-Ocean-Ridge Basalt (MORB), were prepared at atmospheric pressure, 1400 °C, and a range of fO_2s ($\log fO_2$ = 0 to -18 or QFM+6.3 to QFM-11.7 for CMAS and $\log fO_2$ = 0 to -11 for MORB). CMAS compositions included the anorthite-diopside eutectic (AD), and four variants on this saturated in forsterite (AD+Fo), enstatite (AD+En), wollastonite (AD+Wo), and quartz (AD+Qz) as described in O'Neill and Eggins (2002). The final composition has previously been described and referred to as CMAS-7A (O'Neill and Eggins 2002; O'Neill and Mavrogenes 2002; Berry *et al*., 2006). Note that whilst CMAS-7A refers to a specific composition, the Fe-free glasses are referred to collectively as CMAS throughout this work. Further AD and MORB composition glasses were prepared at a range of pressures and fO_2s using piston cylinder apparatus. AD glasses were made at 1400 °C and 5-15 kbar buffered by

C-CO_2, Re-ReO_2, Ru-RuO_2, Ir-IrO_2, and Pt-PtO_2 (corresponding to log$f$$O_2$ = -7.7, -3.9, -0.4, +1.9, and +4.7 at 10 kbar), whilst MORB glasses were made at 5-25 kbar buffered by C-CO_2, Re-ReO_2 (10 kbar only), Ru-RuO_2, and Pt-PtO_2. For *in situ* XANES studies using the XAS furnace (see Chapter 6), MORB and AD composition glasses on Pt and Re loops were pre-equilibrated at 1400 °C, and a range of $f$$O_2$s (log$f$$O_2$ = -3 to -12).

Sample mixtures were prepared from reagent grade powders of SiO_2, MgO, Al_2O_3, and TiO_2 dried at 1000 °C, and $CaCO_3$ and Fe_2O_3 dried at 300 °C, weighed out in the required proportions. To these mixtures was added ~0.4 wt % UO_2. Alternatively, U was added to the powder mixtures in the form of nitrate solution as 1000 ppm U atomic absorption standard solution (1000 ppm U in 1 wt % HNO_3); ~3.5 ml of solution were added per gram of powder to give a U concentration of ~0.35 wt %. Dried powders were mixed under acetone using an agate mortar and pestle for at least 30 min. U-solution slurries were mixed at RT until dry.

2.2.1.1 1 atm glasses

For the most reduced samples, log$f$$O_2$ ≤ -16, the powder mix was pressed into pellets and loaded into wells drilled into a graphite block. For samples equilibrated at > log$f$$O_2$ = -16, a small amount of sample powder (~100 mg) was mixed with polyethylene oxide and water to form a paste, which was mounted onto a loop of either Pt or Re metal. Several samples, of different compositions, were equilibrated in a single experiment by hanging multiple sample loops from a Pt or ceramic chandelier. Sample loop and chandelier materials were dependent on the log$f$$O_2$ of the furnace gas mixture of each experiment. For Fe-free compositions at log$f$$O_2$ ≥ -12 the loops and chandelier were made of Pt; for lower log$f$$O_2$s Re loops and a ceramic chandelier were used. For Fe-bearing samples, Re loops were used for experiments where log$f$$O_2$ ≤ -8, as Fe alloys with Pt at these conditions (Sugawara, 1999). Fe-bearing

experiments were limited to logfO_2s ≥ -11 due to the precipitation of increasing amounts of Fe metal with decreasing fO_2 below the Iron-Wüstite (IW) buffer (logfO_2 = -9.7 at 1400 °C, O'Neill and Pownceby, 1993) causing significant changes in melt composition at lower fO_2s. Pt loops were used for experiments where logfO_2 > -8; although there is still some alloying between Fe and Pt at logfO_2 = -7 and -6, Re loops cannot be used as it is volatile at these conditions (Borisov and Jones, 1999). The removal of a small proportion of Fe from the original mix at logfO_2 = -7 and -6 does not change the resulting glass composition sufficiently to change its optical basicity, and is therefore not expected to impact oxidation state ratios.

The chandeliers or graphite blocks were suspended at the end of an alumina rod in the hot zone of a 1 atm, vertical, gas-mixing furnace at 600 °C, heated to 1400 ˚C, and equilibrated with gas mixtures of CO/Ar, CO_2/CO, O_2/Ar or O_2/CO_2, and O_2 to impose values of logfO_2 between 0 and -18. Most of the CMAS samples were equilibrated for > 20 h, however, experiments in the most oxidising atmospheres were limited to ~8 h to prevent excessive U loss due to volatilisation. Time series experiments for Eu- (Burnham *et al*., in preparation: experiment durations of 8 to 42 hours) and S-bearing melts (O'Neill and Mavrogenes, 2002: experiment durations of 1 to 50 hours) indicated that 8 h was sufficient for CMAS melts to equilibrate with the imposed gas mix at 1400 ^{0}C. MORB samples were equilibrated for between 8 (oxidised experiments) and 88 h, with the exception of a selection of fO_2s (logfO_2 = 0, -3, -5, -7), which had short equilibration times of ~4 h. It has been shown that 4 h is sufficient to achieve equilibrium in S solubility studies of Fe-bearing melts (O'Neill and Mavrogenes, 2002); however, whether or not the short-experiment samples of this study reached equilibrium is not taken for granted during the XANES data analysis discussed in Chapter 5 of this thesis. At the end of an experiment the samples were drop quenched, either into the base of the furnace (for *in situ* furnace loops) or into water (for RT studies), to

produce glasses. Samples for RT studies were mounted in epoxy, exposed, and polished. For *in situ* studies at least two loops of each composition were made in each pre-equilibration experiment so that one could be mounted for compositional analysis leaving the other for *in situ* XAS experiments.

The large sample preparation furnace (Gero HTRV 70-250/18) was heated using three U-shaped $MoSi_2$ elements. Temperature was measured by a type B ($Pt_{70}Rh_{30}$-$Pt_{94}Rh_6$) thermocouple and monitored by a Eurotherm controller (model 2416) that controlled the power supply (RETTH-E 400/6). The gas atmosphere imposed upon the samples was separated from the heating elements by a gas tight alumina tube cooled by water at both ends. The gas inlet was at the base of the furnace and the exhaust at the top. The gas mixing ratios required for each fO_2 were calculated following the methodology of Deines *et al.* (1974) using the NIST-JANAF thermochemical tables (Chase, 1998). Gas flow rates, measured in standard cubic centimetres per minute (sccm), were controlled using Celerity FC2900 CO and CO_2 calibrated mass flow controllers (MFCs). There were two flow rate channels for each gas, one slow (up to 10 sccm) and one fast (up to 200 sscm). For gases other than CO_2 and CO a gas correction factor was applied to achieve the desired flow rate of the alternate gas using the CO or CO_2 calibrated MFC. The flow rates used for each fO_2 condition at 1400 °C are given in Table 2.1. As it is the gas-mixing ratio that defines the fO_2, the actual values in Table 2.1 are arbitrary; however, the flow-rates on each channel were chosen so that the total flow rate was approximately constant across the whole fO_2 series to minimise any effect of gas flow rate on temperature. A value of $\log fO_2 = -0.7$ was achieved by disconnecting the gas lines and allowing air to flow freely through the furnace.

Table 2.1: Gas mixing ratios at 1400 °C. Values are reported as a percentage of the maximum flow rate 10 or 200 sccm), and represent actual flow rates. When using CO and CO_2 calibrated MFCs correction factors must be applied for other gases: multiply by 0.7 for O_2 on the CO_2 controller, 0.7 for Ar on the CO controller, 1.0 for O_2 on the CO controller, and 0.5 for Ar on the CO_2 controller.

logfO_2	CO 10 sccm	CO 200 sccm	CO_2 10 sccm	CO_2 200 sccm	O_2 10 sccm	O_2 200 sccm	Ar 200 sccm	O_2 10 sccm	O_2 200 sccm	CO_2 200 sccm
0	-	-	-	-	-	40.0	-	-	-	-
-1	-	-	-	-	99.0	-	45.2	-	5.5	50
-2	-	-	-	-	10.4	-	51.4	10	-	50
-3	-	-	-	51.0	-	-	-	-	-	-
-4	5.1	-	-	51.0	-	-	-	-	-	-
-5	16.0	-	-	51.0	-	-	-	-	-	-
-6	40.0	-	-	40.0	-	-	-	-	-	-
-7	-	6.3	-	40.0	-	-	-	-	-	-
-8	-	13.0	-	27.0	-	-	-	-	-	-
-9	-	31.0	-	20.0	-	-	-	-	-	-
-10	-	33.4	-	6.7	-	-	-	-	-	-
-11	-	47.0	60.0	-	-	-	-	-	-	-
-12	-	50.0	20.0	-	-	-	-	-	-	-
-14	-	100.0	4.0	-	-	-	-	-	-	-
-16	-	40.0	-	-	-	-	-	-	-	-
-18	94.4	-	-	-	-	-	36.8	-	-	-

2.2.1.2 High pressure glasses

U-doped glasses were equilibrated between 5 and 25 kbar using a piston cylinder apparatus. The sample powder (30-70 mg) was loaded into a Pt capsule along with a redox buffer powder (PtO_2, or mixtures of Ir-IrO_2, Ru-RuO_2, or Re-ReO_2), with the exception of C-CO_2 buffered experiments, where the sample powder was packed into a graphite capsule. The graphite capsule was machined to fit snuggly inside the outer Pt capsule, into which it was then loaded. The buffer powder was equally distributed between the top and base of the capsule, in a sandwich-like arrangement, and made up to ~40 % of the total capsule load material by mass; metal-metal oxide buffer mixtures were approximately 25 % metal and 75 % oxide by mass. Powders were densely packed using a drill bit to remove excess space. All starting mixtures, with the exception of those for C-CO_2 buffered experiments, were fully

decarbonated prior to loading by heating to ~1000 °C. The maximum fO_2 for graphite-lined capsules is that of the C-CO_2 buffer, which is achieved if vapour saturation is reached (i.e. the melt is CO_2 saturated: Holloway *et al.*, 1992). Powders for C-CO_2 buffered experiments were thus at least partially carbonated to provide a source of CO_2 in the melt (in addition to the reaction of graphite and Fe_2O_3 for MORB samples).

The ends of the Pt capsules were welded shut and flattened. The capsule was then placed at the centre of a piston cylinder assembly, as shown in Fig. 2.6. This consisted of a rod of MgO with a recess machined at its centre to accommodate the Pt capsule, which was then placed in a cylindrical graphite heater, surrounded by a pyrex cylinder; all of this was contained within an outer sleeve of NaCl wrapped with a rectangular piece of teflon. A 4 mm (OD) Pt capsule and a ½ inch assembly size were used for most experiments. However, to improve the pressure control at the lowest pressures a combination of a smaller capsule size (2.7 mm for powder buffers, and 3.5 mm for experiments using an inner graphite capsule), and a larger assembly size ($^5/_8$ inch) was used; full details of sample syntheses are given in Appendix A.1.

The assemblies were run in an end-loaded piston cylinder apparatus. Pressure was monitored by the piston pressure gauge, and temperature was measured using a Type B thermocouple. Prior to heating the assemblage was placed under a confining pressure of 4-5 bar and the internal pressure was taken up to about 70 bar. Samples were then heated to 1400 °C (or 1500 °C for the highest pressure experiments, to ensure they were above the liquidus) at a ramp rate of ~6000 °C/hr and held at temperature. The remaining pressure requirement was slowly applied during heating. Equilibration times were between 6 and 24 h, at the end of which samples were quenched by cutting the power supply to the heater. The low friction NaCl assembly used for these experiments does not require a pressure correction (i.e. the pressure

on the gauge corresponds directly to the pressure on the sample), and the uncertainties in pressure and temperature for this assembly have previously been estimated to be ~0.3 kbar and up to ±15 °C, respectively (Klemme and O'Neill, 1997).

The fO_2s of piston cylinder experiments were calculated from Ulmer and Luth (1991), O'Neill and Nell (1997), and Pownceby and O'Neill (1994), for the C-CO_2, Ru-RuO_2 and Ir-IrO_2, and Re-ReO_2 buffers, respectively. Under the pressure and temperature conditions of these experiments, PtO_2 breaks down to Pt and sufficient O_2 to produce a partial pressure equal to the confining pressure (Mallmann and O'Neill, 2009); the resulting fO_2 at each pressure was calculated from the equation of state of pure O_2 given by Belonoshko and Saxena (1991). Although the absolute value of fO_2 of each buffer changes with pressure, the fO_2 relative to the Quartz-Fayalite-Magnetite (QFM) buffer only varies by ~0.5 log units

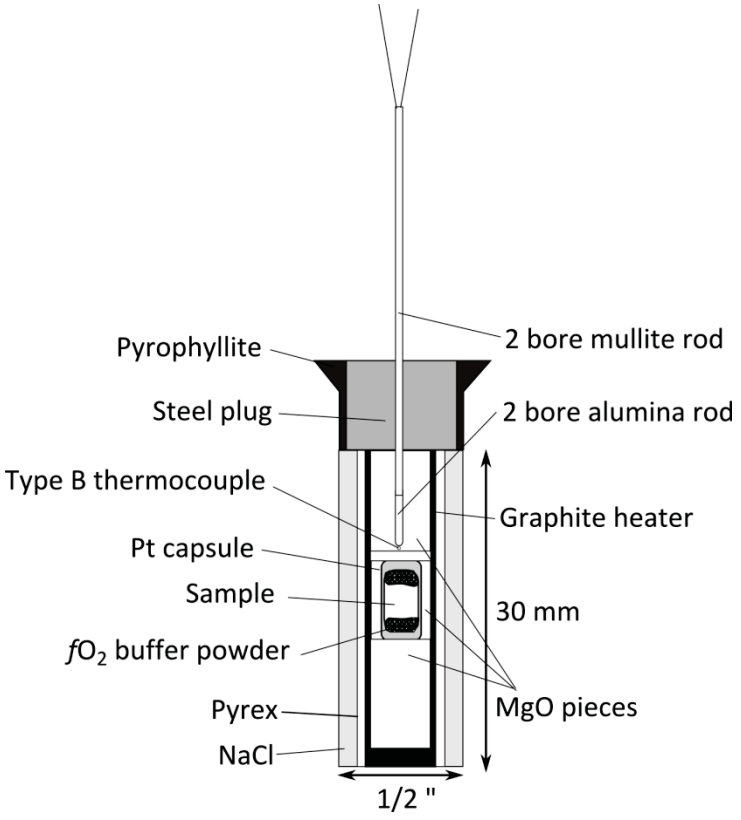


Figure 2.6: Schematic diagram of a piston cylinder assembly.

(with the exception of Pt-PtO_2 which varies by ~0.9 log units) between 5 and 25 kbar at 1400 °C, as shown in Fig. 2.7. The fO_2 values of QFM were calculated using the temperature dependent equation of O'Neill (1987), with an extra term that included the volume change of the reaction to account for the effect of pressure. The volume change was calculated using the data of Holland and Powell (1998).

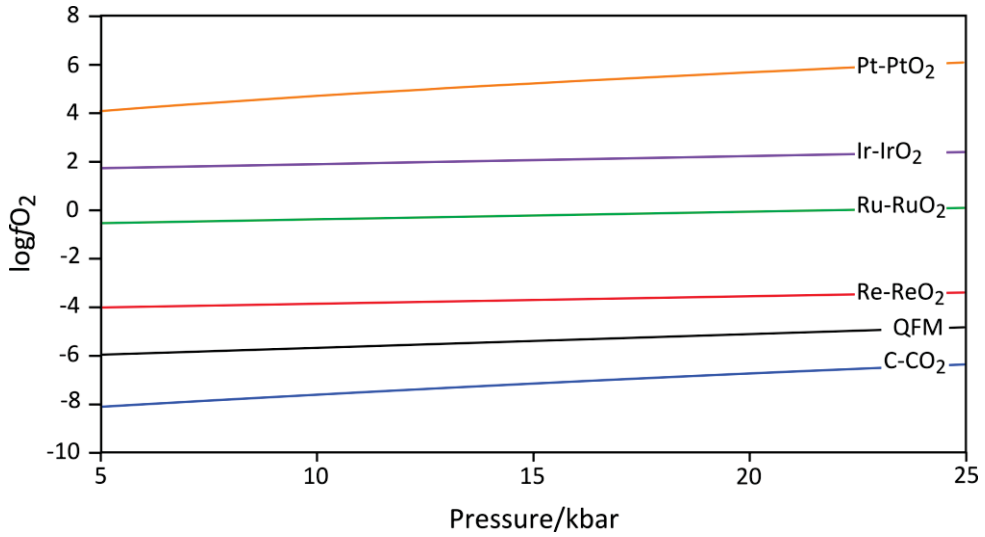


Figure 2.7: fO_2s of piston cylinder buffers and the QFM buffer at 1400 °C as a function of pressure, calculated from the equations of Ulmer and Luth (1991), O'Neill and Nell (1997), Pownceby and O'Neill (1994), O'Neill (1987) and Belonoshko and Saxena (1991).

2.2.2 Electron probe microanalysis (EPMA)

2.2.2.1 Basic principles

Electrons produced by thermionic emission from a W filament or sharpened LaB_6 crystal tip are accelerated and focused in vacuum onto the sample. This results in a variety of elastic and inelastic interactions between the source electrons and the atoms of the sample. Some of the incident electrons are backscattered as a result of elastic collisions with the sample atoms; the direction of travel of an electron is changed but it loses little energy. The fraction of back-scattered electrons (BSE) varies directly as a function of atomic number (Z), and BSE images can be used to show compositional differences of the near surface region of a sample. Some

electrons transfer energy to the electrons of the sample atoms causing electron excitation into the conduction or valence bands or induce inner shell ionization producing secondary electrons. Secondary electrons have much lower energies (average of a few electron volts) than backscattered electrons and only those produced close to the surface escape. Thus, secondary electron images are generally employed to show the topography of samples. Following excitation or ionization the atom will decay from the excited state resulting in the emission of X-rays characteristic of the element. By measuring the intensity of X-rays emitted from a particular element in the sample to that emitted by a standard the concentration of the element in the sample can be determined (Reed, 2005).

Quantitative compositional analysis commonly uses wavelength dispersive spectrometry (WDS). In WDS a crystal analyser is used to select the X-ray energy of interest (i.e. the peak of a particular element's emission line). Only X-rays with a wavelength that satisfies the Bragg equation:

$$n\lambda = 2dsin\theta \qquad (2.1)$$

where d is the distance between lattice planes in the crystal, θ is the angle of the incident X-ray beam on the lattice planes, and λ is the X-ray wavelength, will reach the detector. Since WD spectrometers only allow the selection and recording of one wavelength at a time electron microprobes are usually equipped with several spectrometers. Using different crystals (with different d spacings) in each spectrometer also allows them to access different X-ray energy ranges (Reed, 2005). This means that individual crystals do not have to be changed to measure different elements in a sample.

The measured peak intensity includes a contribution from the background (X-ray continuum resulting from deceleration of the impinging electrons in the strong electric field of the target

atoms nucleus) (Reed, 2005). The true peak intensity is generally determined by recording the count rate at the maximum of the peak, and at two background positions, on each side of the peak; the background intensity can then be interpolated and subtracted. To estimate the proportion of the element in the sample the X-ray intensity from the sample is normalised to that emitted from a reference standard for which the concentration of the element of interest is known. To obtain "true" concentrations from these estimates, corrections must be applied for any peak overlaps and matrix effects. Matrix corrections account for factors such as the volume of sample that is being excited and the loss of X-ray intensity due to electron backscattering (dependent on the average atomic number of the sample), the reduction in X-ray intensity caused by absorption in the sample, and the enhancement of some elements emission lines at the expense of others due to secondary fluorescence (i.e. elements may emit characteristic X-rays due to excitation by higher energy X-rays emitted by other elements) (Reed, 2005).

2.2.2.2 Analysis of U glasses

The major and trace element compositions of the U-bearing glasses were determined using the Cameca SX-100 electron probe at the Natural History Museum. The accelerating voltage was 20 keV and the beam current was 20 nA. The spot size aimed for on the sample surface was ~10-20 μm. In addition to the elements of the original starting mixtures the glasses were analysed for the possible contaminants Na, K, P, and Cl. The standards used were forsterite for Mg, corundum for Al, fayalite for Fe, wollastonite for Ca and Si, rutile or $MnTiO_3$ for Ti, UO_2, Th metal, albite or jadeite for Na, orthoclase for K, vanadite for Cl, and $ScPO_4$ for P. The analysing crystals were LTAP (Si Kα, Al Kα, Mg Kα, Na Kα), PET (Ca Kα, Ti Kα, K Kα), LLIF (Fe Kα), and LPET (Cl Kα, P Kα, U Mβ, Th Mα). Selected piston cylinder glasses were also analysed for the element used for fO_2 buffering: Pt (LLIF, Lα), Re (LLIF, Lα), Ir

(LLIF, Lα). Accurate quantification of the Ru concentrations of Ru-RuO_2 buffered glasses was prevented by the lack of an appropriate standard. However, the presence of significant concentrations of Ru in the glasses was checked by scanning across the full wavelength range of the crystal spectrometers (LLIF, LTAP, LPET) producing sets of WDS spectra.

2.2.2.3 Results

CMAS samples are typically optically transparent and homogeneous. The glasses vary systematically in colour with fO_2 from brown (highly reduced), to blue (reduced), to colourless (oxidised), to yellow (highly oxidised). AD+En composition glasses equilibrated at almost all fO_2s contain enstatite crystals up to 40 μm in size. Wollastonite crystals up to ~100 μm in size occur in some of the AD+Wo glasses, with no relationship between crystal occurrence and the fO_2 of equilibration. AD+Qz composition glasses are cloudy and are characterised by heavily pitted surfaces even after polishing due to the high concentration of bubbles trapped in the high viscosity melt. None of the crystal phases contain U MORB glasses vary in colour from green (reduced) to black/brown (oxidised).

Average 1 atm glass compositions are given in Table 2.2; EPMA data for all samples are reported in Appendix A.2. It was not necessary to apply any corrections for peak overlaps as samples did not contain significant amounts of the contaminant K whose Kα (~3312 eV) peak overlaps the U Mβ (~3340 eV) peak. For some of the sets of glasses a large proportion of the compositional totals fall below an acceptable value for an anhydrous glass (~98 wt %). The reasons for these low totals, and the magnitudes of the deviations from 100% vary depending on the specific sample set. An assessment of the data for 1 atm samples is given in Appendix A.2; discussion here will be limited to the glasses prepared using piston cylinder apparatus, where the low totals are thought to reflect additional compositional components.

Table 2.2: Average 1 atm glass compositions (wt % oxide) determined by EPMA, and resulting optical basicity values (Duffy, 1993). Compositions are averaged from 80 analyses (total) of 15 glasses (AD), 76 analyses of 14 glasses (AD + Fo), 68 analyses of 14 glasses (AD + Wo), 71 analyses of 14 glasses (AD + En), 71 analyses of 14 glasses (AD + Qz), 73 analyses of 14 glasses (CMAS-7A), and 181 analyses of 16 glasses (MORB). Values in parentheses represent one standard deviation. Dashes indicate that the element concentration is below detection.

Comp.	SiO_2	Al_2O_3	MgO	CaO	FeO	TiO_2	UO_2	Total	Optical basicity
AD	49.0 (7)	14.8 (3)	10.7 (1)	23.2 (3)	-	-	0.37 (8)	98.0 (20)	0.607 (1)
AD+Fo	47.9 (7)	12.5 (2)	17.4 (2)	19.7 (3)	-	-	0.38 (5)	98.0 (20)	0.610 (1)
AD+Wo	49.5 (9)	6.0 (2)	4.3 (1)	37.3 (5)	-	-	0.41 (5)	98.0 (20)	0.634 (1)
AD+En	53.0 (6)	9.1 (2)	21.2 (4)	14.3 (2)	-	-	0.36 (9)	98.0 (20)	0.595 (1)
AD+Qz	65 (1)	9.7 (3)	7.0 (2)	15.1 (4)	-	-	0.4 (1)	97.0 (20)	0.559 (2)
CMAS-7A	54 (1)	15.3 (3)	12.3 (1)	15.5 (3)	-	-	0.36 (9)	98.0 (20)	0.583 (2)
MORB*	51.7 (5)	15.7 (2)	8.17 (7)	12.2 (1)	9.6 (5)	1.27 (2)	0.4 (1)	99.0 (20)[1]	0.588 (3)[2]

*10 of the MORB glasses also contain ~0.5 wt % ThO_2, but for averaging ThO_2 was not included and the composition s were re-normalised.

(1) Totals corrected for FeO-Fe_2O_3 contents.

(2) Assumes basicity of Fe^{3+} is the same as Fe^{2+}.

The solubility of Re and Pt in CMAS melts is expected to be on the order of ~2 wt % and 0.5 wt %, respectively (H. St. C. O'Neill: personal communication 19/08/2014). The U-bearing Re-ReO_2 buffered glasses of this thesis were found to contain Re at concentrations of 2-4 wt %, and analyses of Pt-PtO_2 buffered samples gave Pt concentrations of 0.1-0.9 wt %; these concentrations are strongly correlated with the pressure of equilibration (increasing with increasing pressure). It is not clear whether the high concentrations of Re measured by EPMA in the glasses represent the concentrations of Re dissolved in the melt, or result from the presence of sub-microscopic metallic particles (micro/nano-nuggets) such as those that

have been identified by LA-ICP-MS studies of similar glasses (Mallmann and O'Neill, 2007). In contrast, Ir concentrations were below the limit of detection (~1000 ppm) for all of the Ir-IrO_2 buffered glasses, and no evidence of peaks at the wavelengths of the Ru emission lines were observed in the WDS spectra of Ru-RuO_2 buffered glasses. The WDS spectra of Ru-RuO_2 buffered glasses also did not indicate the presence of any other contaminants in spite of the fact that many of these glasses exhibit by far the lowest compositional totals (~94.5 % compared to a minimum value of ~96.5 % for the other buffers).

All of the piston cylinder glasses are expected to contain some water due to diffusion of H_2 into the capsules; which is consistent with low EPMA totals. Glasses buffered by C-CO_2 are also expected to contain ~0.3-1.6 wt % dissolved CO_2 (increasing as a function of the pressure of equilibration between 5 kbar and 20 kbar: see Ni and Keppler, 2013 for a review of CO_2 solubility in melts). Early studies of quenched glasses concluded that carbon is dissolved primarily as CO_3^{2-} in basaltic compositions. However, recent *in situ* high temperature/pressure studies and molecular dynamic simulations indicate that molecular CO_2 is also likely to be significant in the original melts (Ni and Keppler, 2013; Guillot and Sator, 2011). The speciation of water also appears to be temperature dependent, with increasing molecular H_2O being converted to hydroxyl groups with increasing temperature (Kohn, 2000). Dissolution of CO_2 and H_2O are expected to result in changes to the melt structure; carbonate is thought to increase melt polymerisation (Mysen and Virgo, 1980), whilst it is well known that H_2O causes a decrease in viscosity (Kohn, 2000). As such the addition of volatiles to the piston cylinder glasses might be expected to cause a shift in the U redox ratio that is not related to pressure. The optical basicities of CO_2 and H_2O are small (Lebouteiller and Courtine, 1998) and the addition of several wt % of theses volatiles to the melt significantly decreases its calculated optical basicity. For example, the change in the basicity

values for MORB glasses is ~0.01 when 2 wt % H_2O is added, and ~0.03 for 2 wt % CO_2. However, it has been reported that as much as ~4.7 wt % dissolved water (i.e. higher concentrations than are anticipated for any of the glasses of this study) has negligible impact on $Fe^{3+}/\sum Fe$ in basaltic glasses (Botcharnikov *et al.*, 2005). In spite of its relatively large impact on the calculated melt basicity values, experiments modelling partial melting of spinel lherzolite in the CMAS system at 11 kbar found that the presence of saturation amounts of CO_2 had no effect on the temperature of the solidus or the composition of the melt produced relative to CO_2-free experiments (Liu *et al.*, 2006).

To ensure that the piston cylinder glasses had been equilibrated at fO_2s defined by the Ir-IrO_2, Ru-RuO_2, and Re-ReO_2 buffers the buffer was checked afterwards for the presence of both metal and oxide phases using reflected light microscopy; both phases were present for all of the Ru-RuO_2 and Ir-IrO_2 buffered experiments (see far right column of Table A1.1). In contrast, no evidence of Re metal was observed during examination of the remaining buffer for capsules loaded with Re-ReO_2. Unbuffered experiments using this apparatus typically have a fO_2 around Ni-NiO (Burnham and Berry, 2014), as such, Re-ReO_2 buffered glasses may have equilibrated at more reduced fO_2s, than their target values (~1.5 log units lower: O'Neill and Pownceby, 1993). For C-CO_2 buffered samples the fO_2 defined by the buffer represents the maximum attainable value and is dependent on whether CO_2 saturation was reached. However, there is a large range of dissolved CO_2 contents for which the fO_2 is expected to be within < 1 log unit of the C-CO_2 buffer (Holloway *et al.*, 1992; Fig. 4 of Peach and Mathez, 1993). If the capsules were to leak in the PtO_2 experiments, where PtO_2 breaks down to O_2, the fO_2 would be ~11 log units lower than expected; such a large decrease in fO_2 relative to the target value is expected to be clearly distinguishable in the U XANES spectra of these samples.

2.2.3 XANES spectroscopy

A XANES spectrum is collected by placing the sample in a monochromatic beam of X-rays and measuring the absorption of the sample as a function of X-ray energy. As the probability of emission of fluorescence photons is proportional to the probability of absorption, spectra can be recorded either in transmission, where the absorption is measured directly by measuring what is transmitted through the sample, or in fluorescence mode, where the refilling of a core-hole is detected by measuring the sample fluorescence (Heald, 1988). Transmission is appropriate for concentrated samples (i.e. the element of interest is a major component), and the sample must be of an appropriate thickness to collect a spectrum but not attenuate all the X-rays. In contrast, fluorescence mode is employed for thick or low concentration samples (Newville, 2004). In this study XANES spectra of glasses and *in situ* melts were collected in fluorescence mode at the U L_3- and M_4-edges using both standard and high-energy-resolution setups; the details of each experimental setup are described in Chapters 3,4, and 6. The purpose of the following sections of this chapter is to define and describe the major spectroscopic components and terms that will appear in later chapters.

2.2.3.1 Synchrotron source

XANES spectra are collected at synchrotron facilities that provide high intensity tuneable X-ray beams covering a broad range of energies. Synchrotron radiation is produced using a high energy storage ring, where electrons are deflected by magnetic fields. As the electrons travel in a curved trajectory they emit electromagnetic radiation (Motanna, 2004; Brown *et al.*, 1988). A synchrotron is composed of several key components, shown in Fig. 2.8. The electrons are produced by an electron gun and are accelerated using a linear accelerator (linac) to ~ 100 MeV. They are then injected into a booster ring where they are accelerated further until they reach the energy of the electrons in the storage ring. Electrons from the

booster ring are periodically injected into the storage ring, where they are maintained on a closed path by arrays of magnets. The storage ring consists of curved sections, containing bending magnets, joined by straight sections, containing insertion devices. Beamlines run off tangentially to the storage ring, along the axes of the insertion devices and tangentially to the bending magnets. As the circulating electrons loose energy by emitting radiation, their kinetic energy is replenished by giving them a small boost at every turn as they pass through a radio frequency cavity (Willmott, 2011).

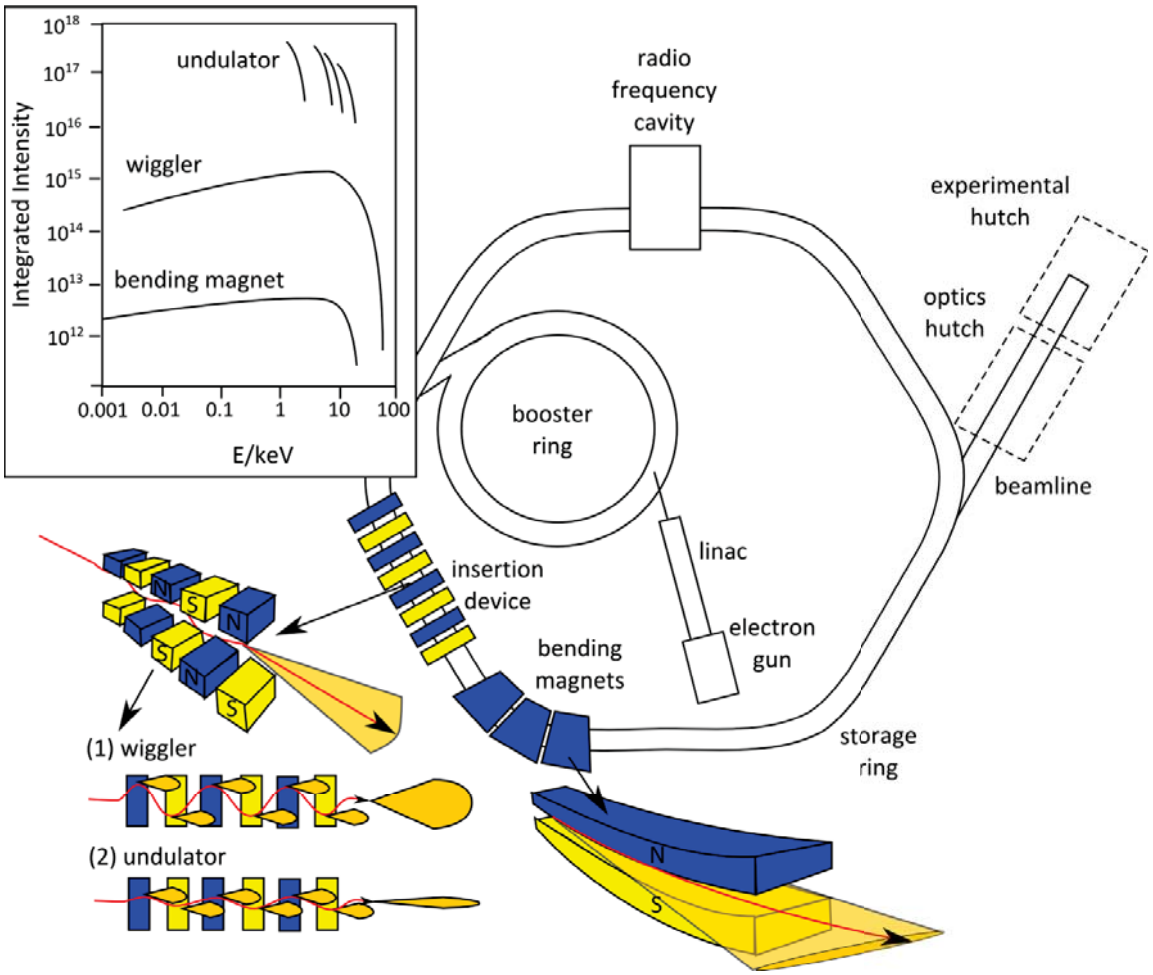


Figure 2.8: Schematic diagram showing the key components of a synchrotron source. Coloured illustrations show how the direction of travel of the electron beam (red) is changed by insertion devices and bending magnets, and the resulting angular spread of the emitted radiation (dark yellow). Insert shows the spectral distribution of synchrotron radiation emitted from a source by different insertion devices and bending magnets. (Figure adapted from: Willmott, 2011, Fig. 3.1, 3.13, 3.15, and 3.16 p. 41, 56, 57 and 58; Motanna, 2004, Fig. 6b, p. 490).

Bending magnets circulate the electron beam in the storage ring by deflecting them from their straight paths. They produce bending magnet radiation in a flattened cone with a fan angle equal to the angular change of the path of the electrons. The large subtended angle of bending magnet radiation means it is possible to position more than one "bending magnet" (BM) beamline at a single bending magnet using two or more apertures (Willmott, 2011). The energy spectrum from a bending magnet is a smooth continuum, see insert in Fig. 2.8 (Motanna, 2004). The spectral distribution is described by the critical energy, E_c, given by:

$$E_c = 2.2\mathcal{E}^3 R \tag{2.2}$$

where R is the bending radius (m) at the emitting point, and $\mathcal{E}$ is the energy of the electrons (GeV) in the storage ring, (Willmott, 2011; Brown *et al.*, 1988). The bending radius is related to the magnetic field (Tesla), B, by:

$$R = 3.3\mathcal{E}/B \tag{2.3}$$

At $E > E_c$ the flux decreases exponentially as $exp(-E/E_c)$; for $E < E_c$ it decreases smoothly as $(E/E_c)^{2/3}$ (Brown *et al.*, 1988). The normal operating conditions of the synchrotron facilities used in this project are listed in Table 2.3.

Table 2.3: Key statistics for the Diamond Light Source and European Synchrotron Radiation facilities.

Machine	Energy (GeV)	Bending radius (m)	Critical energy (keV)	Bending magnet field (T)	Storage ring orbit (m)
DLS	3	7.1	8.4	1.4	560
ESRF	6	24.8	19.2	0.8	844

Insertion devices produce synchrotron radiation with significantly higher intensities than bending magnets. They are made up of two rows of magnets with alternately arranged poles, which cause the electrons to oscillate. There are two types of insertion devices, which are differentiated by the degree to which the electrons are forced to deviate from a straight path.

Wiggler insertion devices cause large angular excursions, so that the radiation cones from each oscillation do not overlap and therefore the intensities are added. This results in high power X-rays over a broad spectral range. In contrast, undulator insertion devices cause more gentle oscillations of the electrons, where the beam displacement is comparable to the beam size, and the radiation cones emitted by the electrons interfere. As only certain wavelengths interfere constructively the energy spectrum from an undulator is discontinuous, but with very high intensities, see Fig. 2.8 insert (Willmott, 2011; Motanna 2004). The horizontal spread of the insertion device radiation is given by:

$$\theta_h = 2\varphi_{max} \tag{2.4}$$

where φ_{max} is the maximum angular deviation of the electron oscillations. Thus, the radiation beam divergence from an insertion device is small, and is approximately an order of magnitude smaller for an undulator than for a wiggler (Willmott, 2011).

2.2.3.2 Beamline setup

A XANES beamline is composed of several key components, as shown in Fig. 2.9. The monochromator uses Bragg's Law ($n\lambda = 2dsin\theta$) to filter a narrow energy band pass from the continuous spectrum of X-ray energies produced at the source. The *n* term in the Bragg equation is an integer (*n* = 1, 2, 3 etc). Thus, not only the wavelength of interest is selected by the monochromator, but also multiples of this wavelength (harmonics). The lattice spacing, *d*, needs to be comparable to the wavelengths that are being diffracted. Monochromators for hard X-rays are usually perfect crystals of silicon or germanium that have been cut parallel to a particular crystallographic plane (Willmott, 2011). X-rays are diffracted from the monochromator's crystal lattice and peaks of scattered intensity are observed at the wavelengths that obey Bragg's law. By changing the angle of the monochromator, or the crystal plane used (Fig. 2.10(a)) different X-ray wavelengths can be selected.

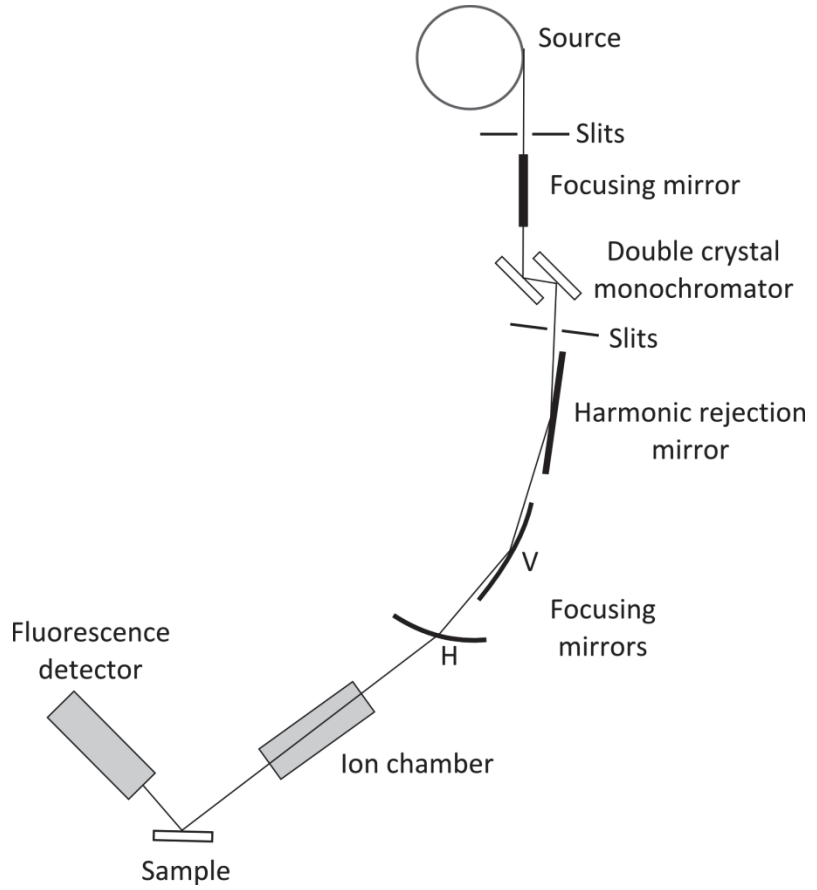


Figure 2.9: Simplified diagram of a XANES beamline running in fluorescence mode. The sample is mounted at 45 ° to the incident beam, and the fluorescence detector is perpendicular to the incident beam.

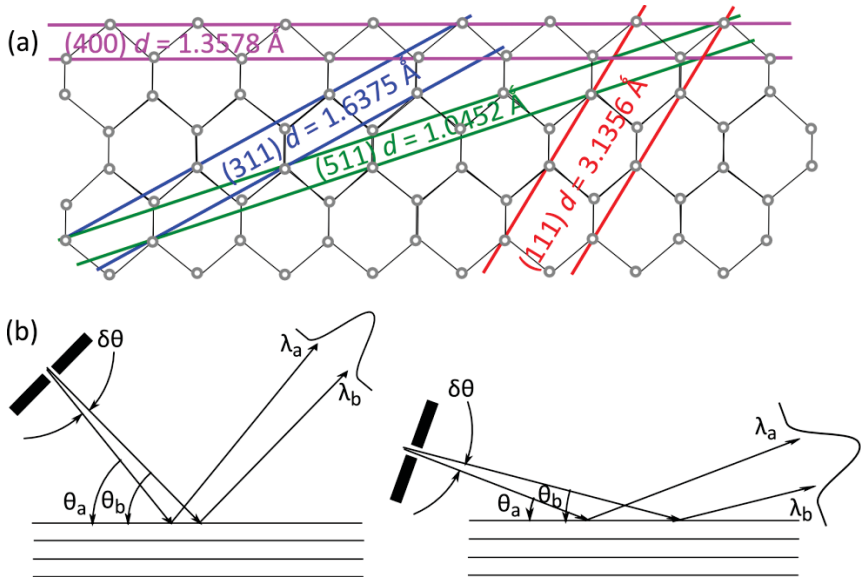


Figure 2.10: Schematic diagram showing (a) some of the lattice planes of silicon and their *d* spacing, and (b) the impact of beam divergence on the energy bandwidth selected by a monochromator for steep and shallow incident beam angles (Figure adapted from: Willmott, 2011, Fig. 4.14, p. 98).

Although Bragg's Law ideally states that the energy bandwidth of the selected radiation should be infinitely narrow, a real crystal monochromator diffracts the beam within a finite angular interval around the theoretical angle. The profile of the diffracted intensity as a function of the crystal rotation angle at a set X-ray energy is the crystal rocking curve and the width of this curve is known as the Darwin width (Mottana, 2004). Thus, the total energy resolution of a monochromator is dependent on its Darwin width and the angular divergence of the X-ray beam. The effect of beam divergence is shown in Fig. 2.10(b); according to Bragg's Law, the crystal will select longer wavelengths from the part of the beam that impinges more steeply on it than the part of the beam that strikes the crystal at a shallower angle (Willmott, 2011). The energy bandwidth caused by a given beam divergence is larger for shallower X-ray incidence angles.

In XAS experiments a double-crystal monochromator is typically used, which consists of two separate crystals cut parallel to the same lattice plane. This maintains a constant beam position during energy scanning. They may also be used to suppress harmonics by slight detuning of the two crystals. Such detuning takes advantage of the fact that the Darwin width is always greater for the fundamental reflection than for the harmonics (Brown *et al.*, 1988; Mottana, 2004).

XANES beamlines use various types of X-ray mirrors to focus the beam. X-rays can be efficiently reflected by low angle mirrors where the reflectivity of different X-ray energies varies with mirror coating and X-ray incidence angle (Fig. 2.11). Whilst theoretically the perfect focusing element is a parabolic mirror, such surfaces are hard to engineer and a toroidal mirror, which approximates a parabolic surface, can provide acceptable focusing. Focusing may also be achieved by separate horizontal and vertical focusing using two

cylindrical mirrors; these are known as Kirkpatrick-Baez (KB) mirrors (Willmott, 2011). Focusing mirrors or additional dedicated harmonic rejection mirrors may also be used to remove higher order harmonics from the X-ray beam. Harmonics are removed by choosing a mirror material/angle with a high reflectivity at the desired X-ray energy but low reflectivity at the energies of the higher order harmonics. A single mirror may have stripes of different coatings to extend its operational energy range.

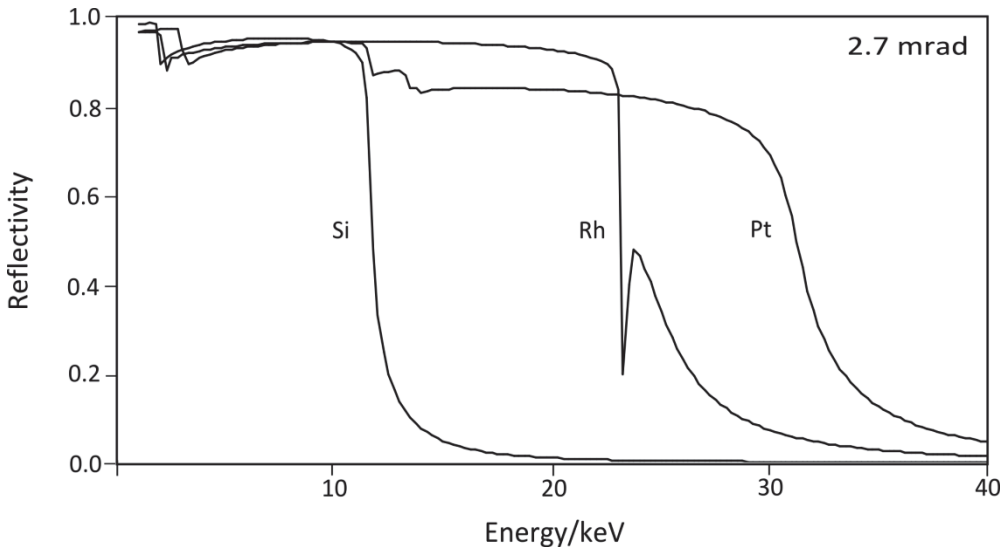


Figure 2.11: X-ray reflectivity curves for different mirror coatings at an incident X-ray angle of 2.7 mrad (Figure Source: Rabedeau, 2010, p.7, Slide 13).

In order to determine the photon flux at the sample, an ion chamber is placed upstream of the sample. An ion chamber consists of a gas filled chamber to which an external electric field is applied. When the X-ray beam passes through the chamber it causes ionisation events resulting in ion-electron pairs ("ion pairs"), which move under the applied electric field generating a current. The size of this current is used to determine the number of ionisation events (Knoll, 2010). The average energy required to produce an ionisation event is dependent on the gas type, whilst the percentage of the beam absorbed over the path length of

the ion chamber is dependent on the properties of the gas and the energy of the incident beam. Since these are known, the number of photons contributing to the ion chamber current and the total number of incident photons can be calculated. The fluorescence counts (I_f) measured from the sample are normalised to this flux (I_0).

XANES fluorescence spectra are typically recorded using an Energy Dispersive (ED) solid-state detector. The X-ray detection medium is a semiconductor, usually silicon or germanium, which has a small energy gap between its valence and conduction bands. At low temperatures few valence band electrons can gain sufficient energy to be elevated to the conduction band. However, when X-rays are absorbed by the semiconductor electrons are raised from the valence to the conduction band producing electron-hole pairs. If an electric field is applied to the semiconductor material the electrons in the conduction band will migrate in a direction parallel to the applied field; the holes representing a net positive charge will move in the opposite direction. This generates a pulse of current, the size of which depends on the number of electron-hole pairs produced, which is dependent on the energy of the incident radiation (Knoll, 2010; Reed, 2005). In reality the number of electron-hole pairs generated at a given X-ray energy is a mean value, and a spread of pulse heights of Gaussian distribution is produced. This is a major controlling factor on the resolution of the detector. The energy resolution of a solid-state detector is dependent on the incident X-ray energy, but is on the order of 100 eV (Reed, 2005).

A solid-state detector takes a finite amount of time to process each current pulse, and any further pulses that arrive during that time interval are not recoded, the system is "dead" (Reed, 2005; Knoll, 2010). These "dead-time" losses become increasingly severe with higher counting rates and limit the amount of signal that can be processed (Knoll, 2010). Detection

systems at XAS beamlines are thus commonly based on an array of solid-state detectors (multi-element detector) to increase the total count-rate limit (Cramer *et al*., 1988).

2.2.3.3 XANES spectral energy resolution

The energy resolution of standard XAS experiments is limited by the natural lifetime broadening of the core-hole. By the Heisenberg uncertainty principle, the energy width of a state is inversely proportional to its lifetime; this uncertainty in the inner-shell energy makes it possible to detect "fluorescence radiation" with incident photon energies below the absorption edge (Hämäläinen *et al*., 1991). For example, the U L_3-edge energy resolution is limited by a natural lifetime broadening of ~7.4 eV (Krause and Oliver, 1979). Added to the intrinsic (core-hole) width is the resolution of the beamline optics (i.e. the monochromator energy resolution controlled by its Darwin width and the beam divergence). Thus, a typical XANES spectrum has a spectral energy resolution controlled by a combination of the monochromator resolution, which imparts a Gaussian broadening, and the core-hole width, which imparts a Lorentzian broadening (de Groot *et al.*, 2002); the total energy resolution is obtained by adding these values in quadrature.

2.2.4 HERFD XANES spectroscopy

When fluorescence radiation is measured with a solid-state detector, the accepted bandwidth due to the detector resolution (> 100 eV) is generally much wider than the natural energy width (~0-10 eV) of the core-hole. However, specialist experimental setups, where the energy of the fluorescence photons is analysed with a better resolution than the core-hole lifetime width, can be used to produce XANES spectra with a better resolution than the core-hole broadening (Hämäläinen *et al*., 1991; Glatzel *et al.*, 2009; 2013). By tuning the spectrometer to the maximum of a particular emission line the spectral broadening is controlled by the

lifetime broadening of the final state rather than the intermediate state (de Groot *et al.*, 2002). In this case a high-energy resolution fluorescence detected (HERFD) (or partial fluorescence yield-PFY) XANES spectrum is collected. The lifetime broadening of a HERFD XANES spectrum relative to the equivalent spectrum collected in total fluorescence yield (TFY) is illustrated in Fig. 2.12, which shows the spectral landscape as a 2D contour map of the incident and transferred energies over the U M_4-edge and the Mβ emission line (Kvashnina *et al.*, 2013). The HERFD XANES spectrum corresponds to the diagonal cut through this plane at the maximum of the emission line resulting in a significantly reduced spectral broadening (dashed arrow) relative to the TFY broadening (solid arrow) (de Groot *et al.*, 2002).

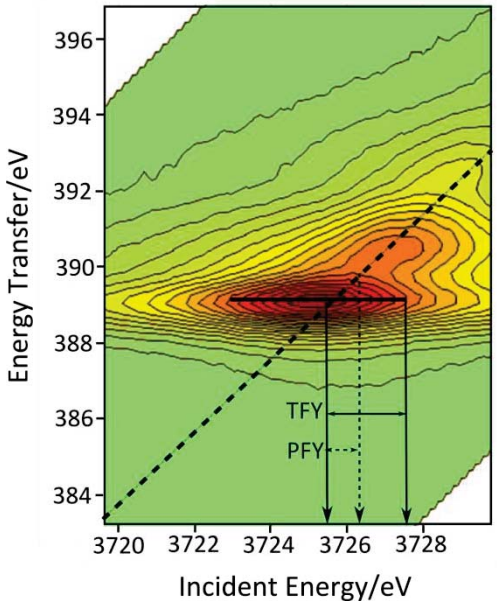


Figure 2.12: Contour map with axes corresponding to incident and transferred energies over the U M_4 absorption edge and U Mβ emission line for UO_2 (Kvashnina *et al.*, 2013). Colour variation in the plot relates to the different scattering intensity (red = maximum, green = minimum). A HERFD/PFY spectrum corresponds to a diagonal cut (dashed line) through the plane at the maximum of the Mβ emission line. Arrows indicate the projection from the same intensity contour onto the X-ray absorption axis for the PFY and TFY experiments.

HERFD XAS setups are similar to standard fluorescence experiments, except that only fluorescence photons of a specific energy (i.e. maximum of the emission line) are detected. This can be achieved by using a crystal analyser to choose the energy of the fluorescence

photons that reach the detector. An experimental setup for this purpose is shown in Fig. 2.13. The sample, crystal analysers, and detector are located on an imaginary "Rowland circle", and the crystal lattice planes are curved to twice the radius of this circle so that the bragg angle is the same at all points (Reed, 2005). The same principles are employed for the WD spectrometers of EPMA.

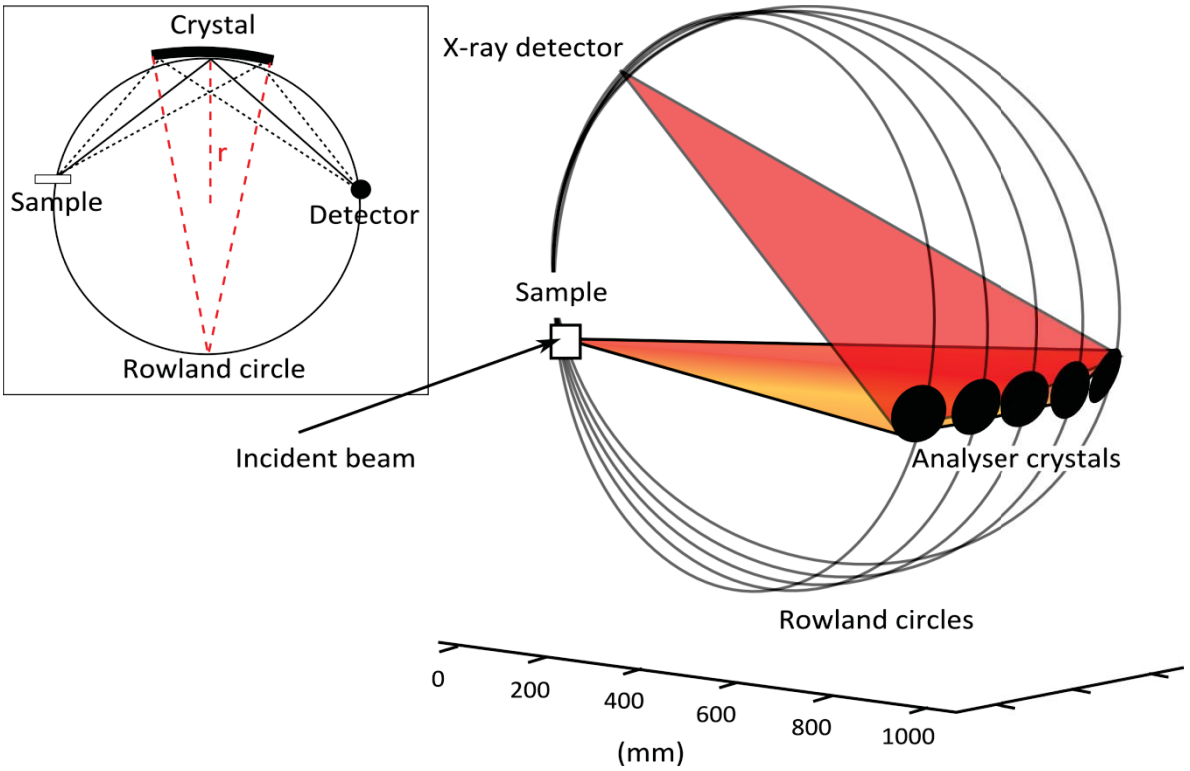


Figure 2.13: Schematic diagram of an experimental setup for HERFD XAS (Figure Source: Glatzel *et al*., 2009, Fig. 2, p.14) using a point-to-point Rowland geometry with five spherically bent crystals. Insert illustrates the Rowland circle geometry (Figure source: Reed, 2005, Fig. 5.14, p.89).

The intermediate and final state lifetime widths of various U $L_{1\text{-}3}$ and $M_{3\text{-}5}$ edge emission lines are listed in Table 2.4 (Campbell and Papp, 2001). Fig. 2.14 illustrates that the smaller lifetime width of the 5*d* core-hole improves the spectral broadening of the L_3-edge when measuring the $L\beta_5$ emission line, thus revealing additional structures compared to measurements tuned to other emission lines (Glatzel *et al.*, 2013). In practice getting sufficient signal from dilute systems will limit the choice of emission lines that can be used.

Table 2.4: X-ray emission lines resulting from core electron excitation at different U absorption edges including their intermediate and final state lifetime broadenings (Campbell and Papp, 2001). Shaded rows correspond to emission lines for which HERFD XANES spectra are shown in Fig. 2.14.

Edge	Edge energy/eV[(1)]	Emission Line	Emission line energy/eV[(1)]	Transition	Intermediate state broadening/eV	Final state broadening/eV
L_1	21757	$L\beta_3$	17454	L_1-M_3	16	7.9
L_1	21757	$L\beta_4$	16575	L_1-M_2	16	14.1
L_1	21757	$L\gamma_2$	20486	L_1-N_2	16	9.6
L_1	20948	$L\gamma_3$	20714	L_1-N_3	16	8
L_2	20948	$L\beta_1$	17220	L_2-M_4	10	3.5
L_2	20948	$L\gamma_1$	20170	L_2-N_4	10	4.5
L_2	20948	$L\gamma_6$	20845	L_2-O_4	10	0.9 [(3)]
L_3	17166	$L\alpha_1$	13614	L_3-M_5	8.2 [(2)]	3.5
L_3	17166	$L\alpha_2$	13438	L_3-M_4	8.2 [(2)]	3.5
L_3	17166	$L\beta_2$	16388	L_3-$N_{4,5}$	8.2 [(2)]	4.5, 4.25
L_3	17166	$L\beta_5$	17063	L_3-$O_{4,5}$	8.2 [(2)]	0.9, 1.1 [(3)]
M_3	4303	$M\gamma$	3567	M_3-N_5	7.9	4.25
M_4	3728	$M\beta$	3337	M_4-N_6	3.5	0.37
M_5	3552	$M\alpha$	3164	M_5-$N_{6,7}$	3.5	0.37, 0.31

[(1)]From tables contained within Hephaestus software: Ravel and Newville (2005).

[(2)]Value of 7.43 eV reported by Krause and Oliver (1979).

[(3)]From Fuggle and Alvarado (1980).

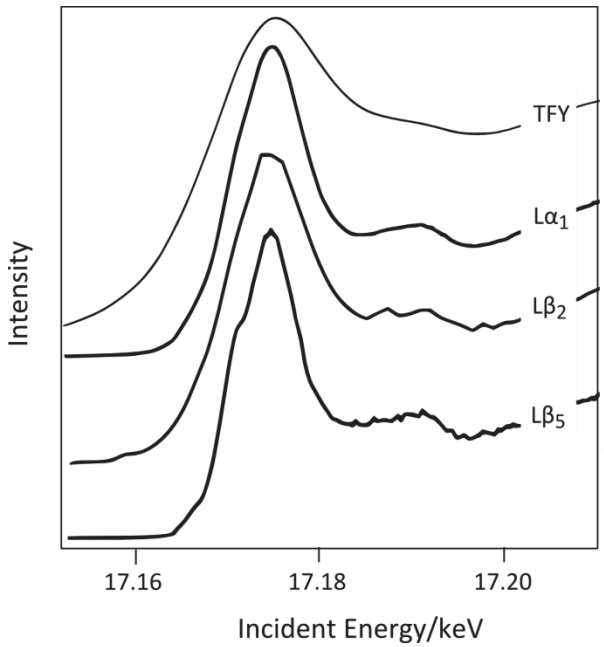


Figure 2.14: HERFD U L_3-edge XANES spectra of UO_2 recorded with the emission spectrometer set to different X-ray emission lines, and using a standard XANES setup (TFY) (Figure Source: Glatzel *et al.*, 2013, Fig. 4, p.20).

Chapter 3:

U M_4-edge XANES spectroscopy of silicate glasses

3.1 Introduction

Most U XAS studies are performed at the U L_3 ($2p_{3/2}$) edge (e.g. Kosog *et al*., 2012; Polovov *et al.*, 2008; Soldatov *et al.*, 2007; Hu *et al*.,1998), which according to the dipole selection rules provides information about the unoccupied 6*d* states. U L_3-edge XANES spectra exhibit a simple white-line that varies in intensity, broadness, and asymmetry. The energy shift of the absorption edge between different U oxidation states was found to be ~3.0 eV between U^{4+} and U^{6+} (Kosog *et al*., 2012; Belai *et al*., 2008; Soldatov *et al.*, 2007; Hu *et al*.,1998; Hudson *et al*., 1995; Kalkowski *et al.*, 1987). The spectral line broadening at the L_3-edge is ~8 eV due to the short core-hole life time of the U $2p_{3/2}$ level (Krause and Oliver 1979; Campbell and Papp, 2001). Further, U compounds of the same valence may show edge energy shifts of a similar magnitude to those observed between different valence states due to different U chemical environments (Kosog *et al*., 2012; Soldatov *et al.*, 2007; Petiau *et al.*, 1986).

L_3-edge spectral broadening can be significantly reduced by using high energy resolution fluorescence detected (HERFD) XANES spectroscopy where an emission spectrometer selects an emission line with a small final state lifetime (Glatzel *et al.*, 2013; Kvashnina and Butorin, 2014), as discussed in Chapter 2. However, most of the unique properties of U compounds originate from the localized 5*f* states, which can be probed at the U $M_{4,5}$ ($3d_{3/2}$, $3d_{5/2}$) absorption edges (Kvashnina *et al*., 2013). The U $M_{4,5}$-edges have the benefit of relatively small lifetime broadenings, which can be improved still further by fluorescence detection at the Mβ (M_4) or $M\alpha_1$ (M_5) emission lines (Table 2.4). Experimentally the M_4-edge is favoured over the M_5-edge due to its slightly higher energy (loss of signal due to X-ray

absorption is significant at these energies) and the better energy resolution of the crystal spectrometer for detection of the Mβ emission line (Kvashnina and Butorin, 2014). In this case the width of the spectral features is no longer limited by the $3d_{3/2}$ core-hole lifetime of ~3.5 eV, but by the sharper $4f_{5/2}$ lifetime broadening of ~0.37 eV (Campbell and Papp, 2001).

3.2 Experimental methods

U M_4-edge HERFD XANES spectra of U bearing AD and MORB composition glasses were recorded at ID26 of the European Synchrotron Radiation Facility (ESRF). Spectra were collected in two separate sessions, in April 2011 and October 2012. The excitation energy was selected using a water cooled Si(111) double crystal monochromator providing an energy bandwidth of ~0.53 eV. Higher harmonics were suppressed by three low angle Si mirrors. The photon flux was ~10^{12} photons/sec. The X-ray beam size on the sample was ~0.5 × 0.1 mm (H × V), with some variation during and between sessions. The energy of the detected fluorescent photons was selected using an X-ray emission spectrometer, consisting of five spherically bent Si(220) crystals in a one-to-one focusing Rowland geometry, tuned to the U M_β ($4f_{5/2}$-$3d_{3/2}$, 3337 eV) fluorescence line, and recorded using a Si drift detector. The spectrometer crystals and detector were enclosed in a helium bag with an opening close to the sample, as shown in Figure 3.1, to minimise the emitted X-ray path through air and reduce loss in intensity due to absorption (absorption length in air at 3337 eV is 5.8 cm: Ravel and Newville, 2005). A combined instrumental energy resolution (the incident energy bandwidth, controlled by the monochromator, convoluted with the emission energy bandwidth, controlled by the emission spectrometer) of ~0.88 eV was obtained. This was determined by measuring the full width at half maximum (FWHM) of the elastic peak, which is obtained by fixing the emission spectrometer at a particular energy and scanning the monochromator about that energy.

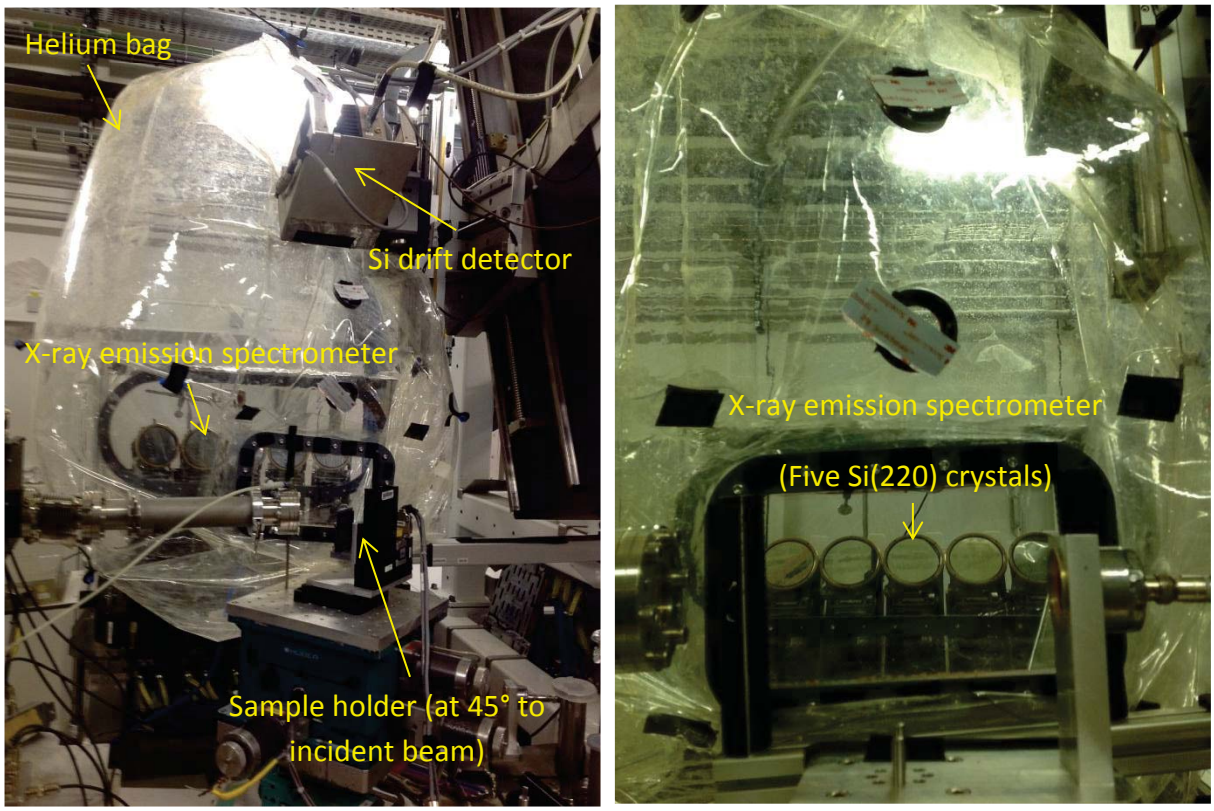


Figure 3.1: Experimental setup for U M_4-edge measurements at beam line ID26 of the ESRF.

The overall spectral broadening was calculated following the methodology of Swarbrick *et al*. (2009) (also summarised by Glatzel *et al.,* 2013), outlined below. The core-hole lifetime broadenings of the intermediate and final states determine the overall peak broadening of HERFD spectra, as determined from the formula given by de Groot *et al.* (2002) as

$$\Gamma_{app} = \frac{1}{\sqrt{\frac{1}{(\Gamma_{INT})^2} + \frac{1}{(\Gamma_{FIN})^2}}} \qquad (3.1)$$

where Γ_{app} is the apparent peak broadening and , Γ_{INT} and Γ_{FIN} are the peak broadening due to the intermediate state ($3d_{3/2}$ = ~3.5 eV) and final state ($4f_{5/2}$ = ~0.37 eV) core-hole lifetimes (from Campbell & Papp, 2001), respectively. It is necessary to combine the core-hole lifetime broadening and the instrumental broadening. The total experimental energy bandwidth, E_{TOT}, was 0.7 eV, a combination of the incident (E_{INC} = 0.53) and emission (E_{EMI}) energy bandwidths,

$$E_{TOT} = \sqrt{E_{INC}^2 + E_{EMI}^2} \quad (3.2)$$

The formula for the approximate Voigt-profile broadening of the measured peak, f_V, obtained by convoluting the Gaussian-type broadening (due to the instrumental resolution), f_g , with the Lorentzian-type broadening (due to the core-hole lifetime broadening), f_L , is given by (Olivero, and Longbothum, 1977)

$$f_v = 0.5346 f_L + \sqrt{0.2169 f_L^2 + f_G^2} \quad (3.3)$$

First, the Lorentzian-profile final state lifetime broadening, Γ_{FIN}, was convoluted with the Gaussian-profile emission energy bandwidth E_{EMI} (0.7 eV; determined from Eq. 3.2) using Eq. 3.3, giving a new value for Γ_{FIN} of 0.94 eV. The intermediate state core-hole lifetime broadening, Γ_{INT}, was then accounted for by applying Eq. 3.1, to determine Γ_{app} = 0.92 eV. Finally the effect of the Gaussian-profile incident energy bandwidth, E_{INC}, was included by again using Equation 3.3 (f_L = 0.92 and f_G = 0.53). The estimated overall peak broadening was 1.2 eV.

In the first M_4-edge session (April 2011) spectra were recorded from ~3710-3780 eV with a step size of 0.1 eV taking a total of 180 s to record each spectrum. At least 25 scans were recorded in immediate succession for each sample, with the beam remaining at a fixed position on the sample. Scan parameters were altered for the second session (October 2012), reducing the energy range to ~3718-3741 eV with a step size of 0.05 eV. Based on the observation of beam damage in AD composition glasses (discussed in the Results section of this chapter), a slightly different data collection method was used for the AD relative to MORB composition glasses. For MORB glasses a single scan time of 60 s was used and multiple scans were recorded with the beam at a fixed position on the sample. Again, a minimum of 25 scans were recorded for all MORB samples, although for the majority of

glasses between 50 and 100 spectra were collected. For AD glasses shorter single scan duration of 40 s were used and the beam position was moved to a new spot on the glass before each scan. Starting at the centre of the sample a set of unique beam positions, based on a beam movement of 0.9 mm horizontally and 0.3 mm vertically (beam size ~0.5 × 0.1 mm),were calculated for a circle with a diameter approximately equal to that of the sample. In some cases a further set of positions was calculated by offsetting the centre of the circle by 0.2 mm in the horizontal and vertical and repeating the calculation. Between 25 and 50 spectra were collected from each glass using this approach. For initial comparison spectra were simply normalised to their maximum intensity. It was not necessary to extract a linear baseline before crest normalisation as the background fluorescence intensity in the pre-edge range was so low.

3.3 Results

M_4-edge spectra recorded from both MORB and AD composition glasses exhibit systematic changes in shape as a function of the fO_2 of sample equilibration, as shown in Fig. 3.2. Spectra have several features that vary in relative intensities; as samples become more oxidised a lower energy white-line peak at ~3725.1 eV (2) shrinks and a higher energy peak grows. The higher energy peak shifts in energy from ~3726.2 to 3726.7 eV (3) as its crest first broadens and then narrows with increasing fO_2 suggesting that this feature represents two poorly resolved peaks. Spectra from the most oxidised glasses also have two intense post-edge peaks at 3728.4 eV (4) and 3731.5 eV (5), which are identical to features reported for, and thought to be characteristic of, the uranyl ion (Kvashnina *et al.*, 2013). In addition, a pre-edge peak at ~3723.5 eV (1) is observed in spectra collected from AD composition glasses equilibrated under relatively reducing conditions, this feature was not observed in the spectra collected from any of the MORB glasses.

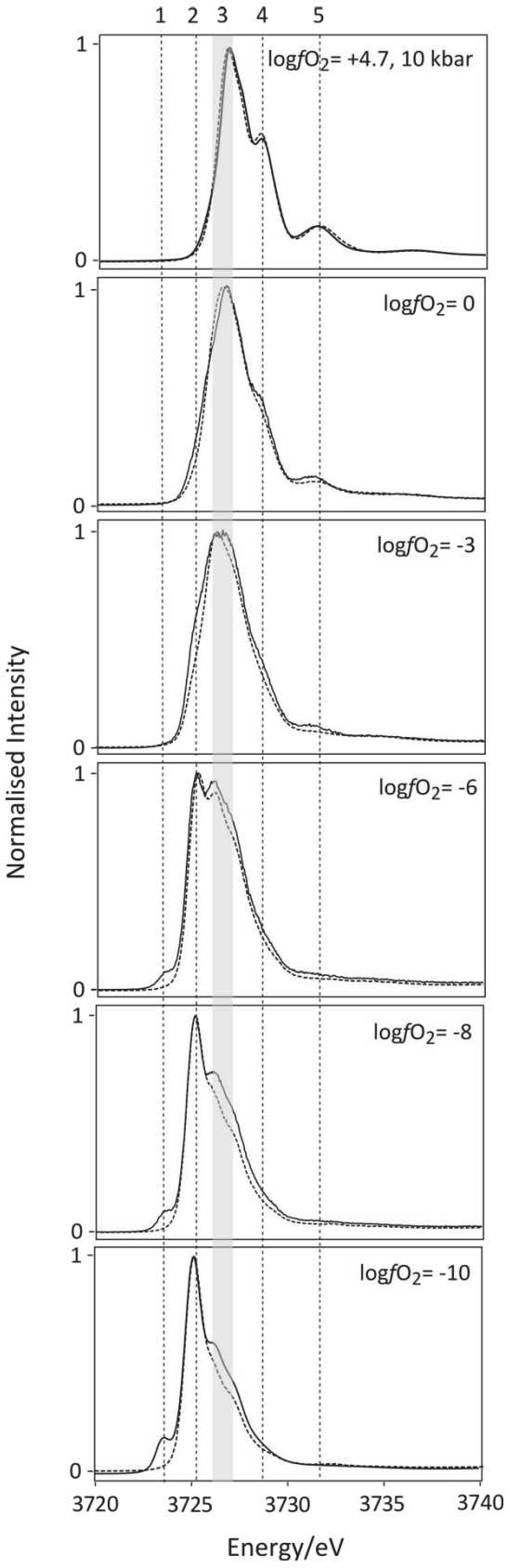


Figure 3.2: U M_4-edge XANES spectra of MORB (dashed lines) and AD (solid lines) composition glasses quenched from 1400 °C and the fO_2s indicated. Major spectral features are indicated at (1) 3723.5, (2) 3725.1, (3) 3726.2-3726.7 eV (shaded), (4) 3728.4, and (5) 3731.5 eV.

3.3.1 Beam damage

Comparison of the first and last scans recorded from each glass during the April 2011 beamtime showed a time-dependent change in the spectral shape for the AD composition glasses. In spectra collected from the most reduced AD glasses (logfO_2 = -9, -10, and -12 in Fig. 3.3) there was a decrease in the pre-edge shoulder intensity at 3723.5 eV (1) and a corresponding growth of the higher energy white-line peak, appearing as a shoulder at ~3726.5 eV (3). No change was observed in spectra collected from MORB glasses regardless of the fO_2 or pressure of equilibration (Fig. 3.4). The impact of beam damage was most clearly observed in the spectra from AD glasses equilibrated under the most reduced gas atmospheres at 1 atm, and samples equilibrated at 5-15 kbar at the C-CO_2 buffer (logfO_2 ~ -7.7).

The rate at which beam damage was occurring in the glasses was investigated by measuring the incident flux (I_0)-normalised fluorescence intensity as a function of time at a set incident X-ray energy from part of the sample not previously exposed to beam. This allowed beam damage to be observed at timescales shorter than the time taken to record a series of scans. Incident X-ray energies were selected based on the position of key spectral features, including the pre-edge peak (1) and the edge crests (2 and 3).

Fig. 3.5 shows that in 180 s the I_0-normalised fluorescence intensity recorded from a reduced (logfO_2 = -12) Fe-free (AD+Fo composition) glass at the pre-edge energy (3723.5 eV) exhibited a rapid decrease of ~15 %; this was mirrored by a fluorescence intensity increase at ~3726.5 eV of ~5 % (region 3 in Fig. 3.3). Further, the extent of damage was hardly reduced by defocusing the beam, which effectively doubled the beam size on the sample. Again, there was no evidence for the occurrence of beam damage in the MORB glasses.

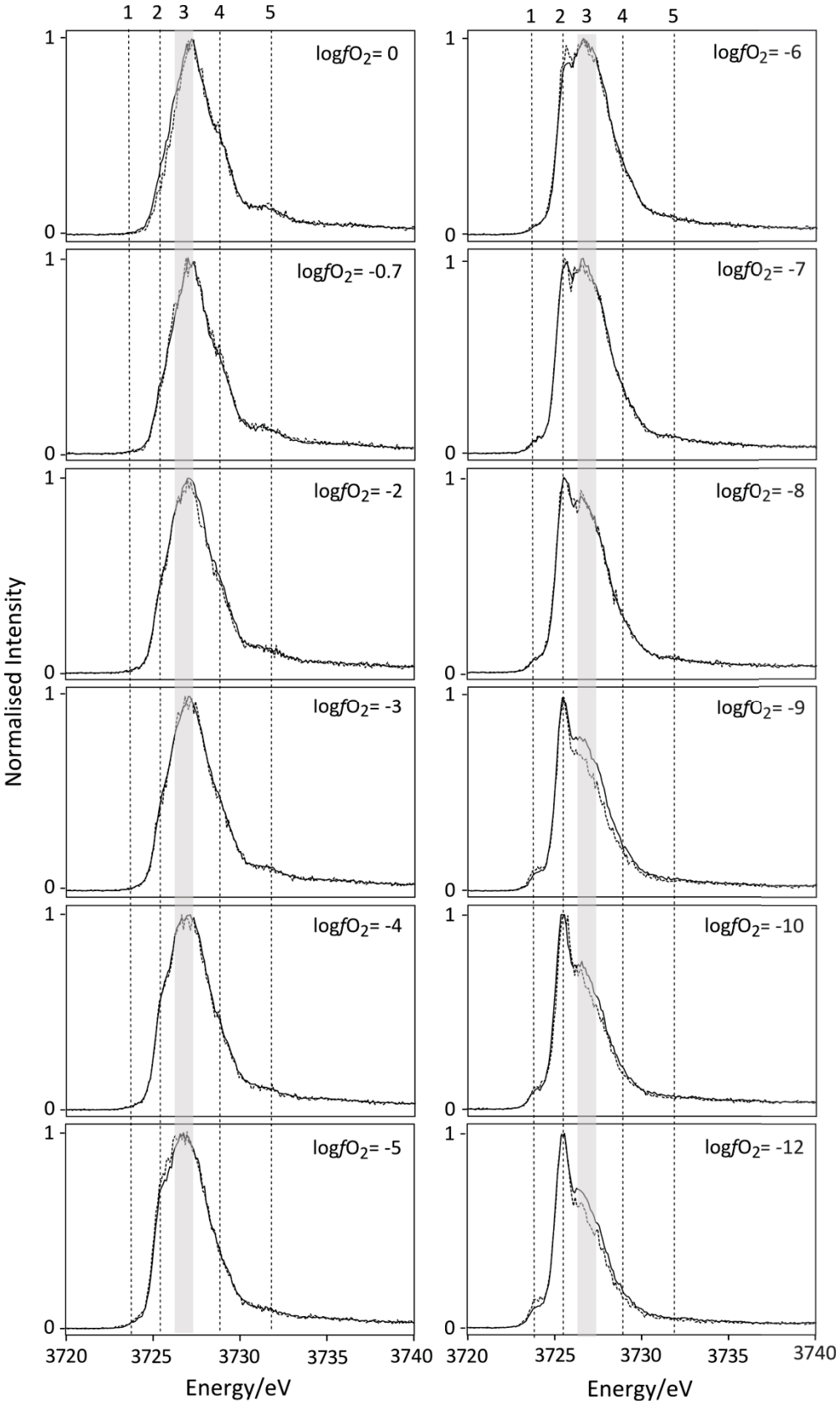


Figure 3.3: U M_4-edge XANES spectra of 1 atm AD composition glasses equilibrated at 1400 °C and the fO_2s indicated. Spectra were produced from the averages of the first three scans (dashed lines) and last ten scans (solid lines) of twenty-five 180 s scans collected with the beam at a fixed position on the glass. Major spectral features are indicated at (1) 3723.5, (2) 3725.1, (3) 3726.2-3726.7 eV (shaded), (4) 3728.4, and (5) 3731.5 eV.

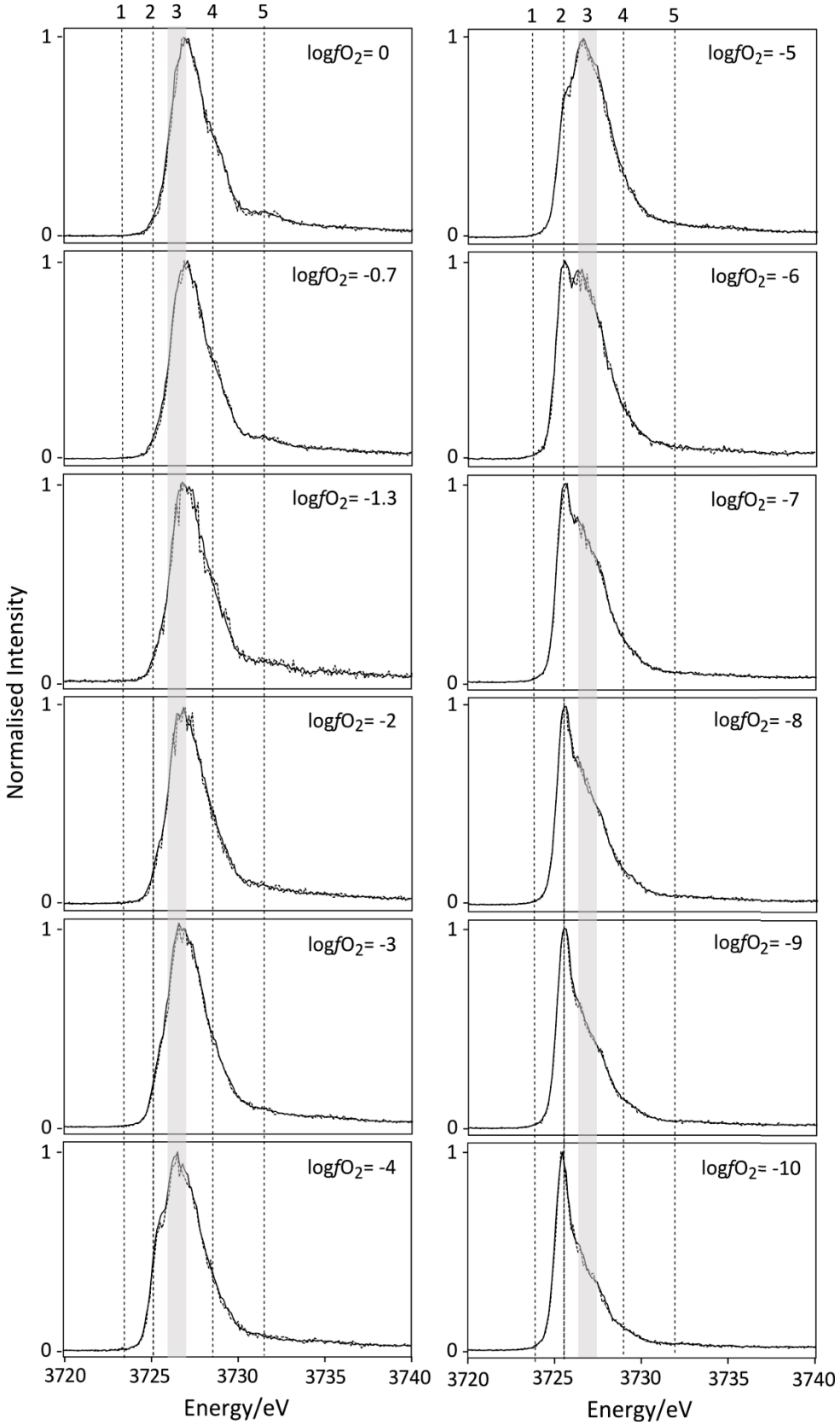


Figure 3.4: U M_4-edge XANES spectra of 1 atm MORB composition glasses equilibrated at1400 °C and the fO_2s indicated. Spectra were produced from the averages of the first three scans (dashed lines) and last ten scans (solid lines) of twenty-five 180 s scans collected with the beam at a fixed position on the glass. Major spectral features are indicated at (1) 3723.5, (2) 3725.1, (3) 3726.2-3726.7 eV (shaded), (4) 3728.4, and (5) 3731.5 eV.

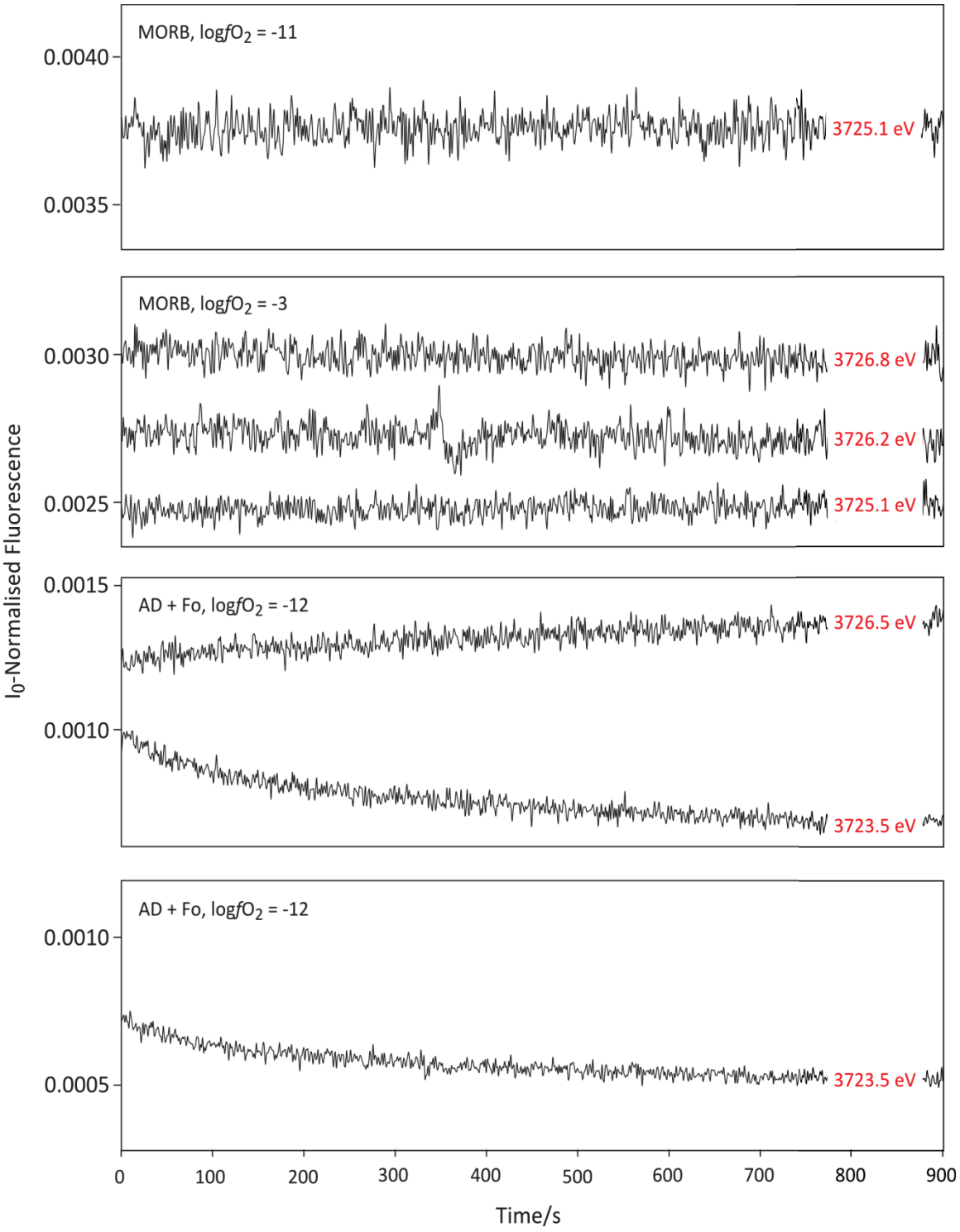


Figure 3.5: I_0-normalised fluorescence count rate time-scans of MORB and AD+Fo glasses at selected incident X-ray energies (red). At t = 0 the shutter was opened with the beam focused on a new spot of the glass. The scan in the lowest panel was collected with a defocused beam.

Interestingly, it was the pre-edge feature, which was not observed in MORB spectra, which appeared to represent the chemical state that was unstable in the beam. The change in spectral shape with time was consistent with a beam induced oxidation of the U state represented by the pre-edge feature. It was clear that even after a single 180 s scan the shape of the U M_4-edge spectra collected from reduced Fe-free composition glasses had changed significantly from that of the undamaged state.

Based on the observation of rapid beam damage in the Fe-free glasses a different scan regime was used in the second beamtime to reduce its impact of the recorded spectra (as described in the experimental methods section of this chapter: section 3.2). Using a shorter 40 s scan time the major spectral features were recorded at ~9-10 s, 12-13 s, and 14-16 s for the pre-edge (3723.5 eV), "low energy white-line crest" (3725.1 eV), and "high energy white-line crest" (3726.2-3726.7 eV) energies, respectively. The beam-induced decrease in the fluorescence intensity of the pre-edge in the time for these energies to be reached during scanning, and during a complete 40 s scan were estimated from the time-scan of the AD+Fo, logfO_2 = -12 glass. The relative change in the pre-edge intensity over the time taken to record the main spectral features, highlighted in Fig. 3.6, is ~4 % which includes ~1 % during scanning before the pre-edge feature was reached. With this new XANES data collection method the beam damage was expected to have a very small impact on the relative intensities of the main spectral features. In comparison, a decrease of ~25 % was measured for a scan duration of ~1000 s (Fig. 3.5), which represents a conservative data collection time if all twenty-five scans were recorded without moving the beam position on the sample.

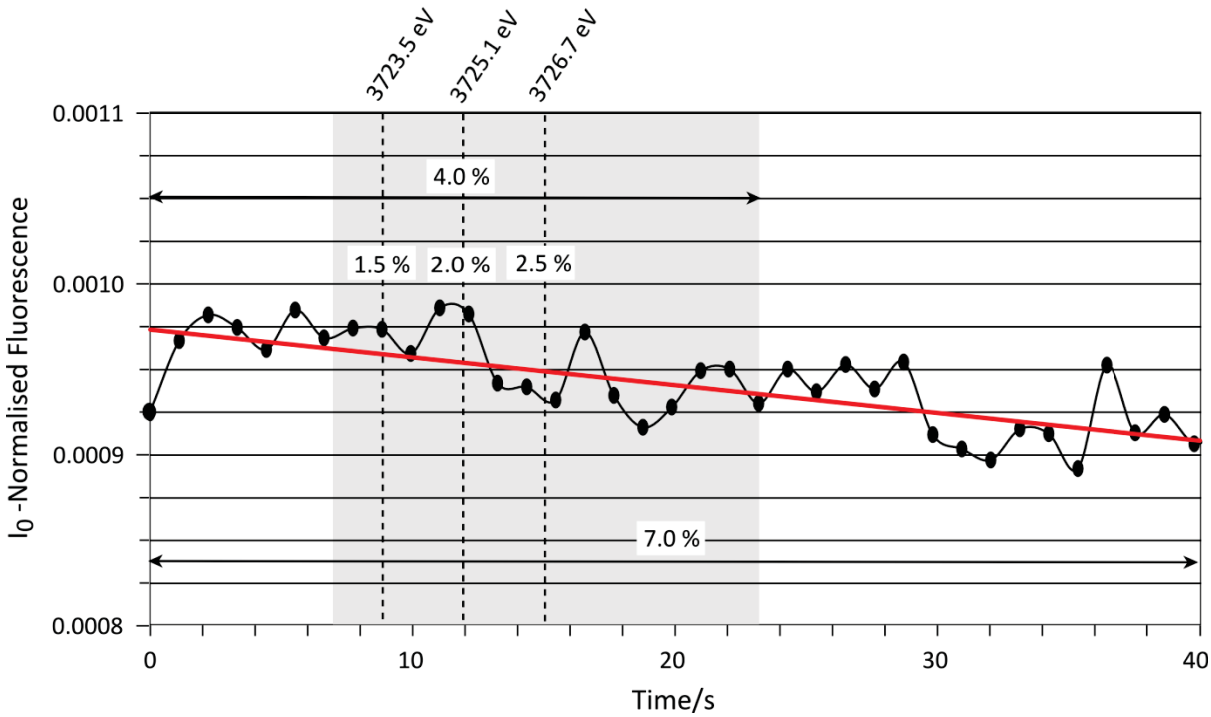


Figure 3.6: I_0-normalised fluorescence count rate-time scans from an AD+Fo composition glass equilibrated at 1400 °C and logfO_2 = -12, at an incident X-ray energy of 3723.5 eV. At t = 0 the shutter was opened with the beam focused on a new spot of the glass. The times at which the energies of the pre-edge peak (at 3723.5 eV) and low- and high-energy white-line crests (at 3725.1 eV and 3726.7 eV, respectively) would be reached during a 40 s XANES scan are indicated with dashed lines. Arrows indicate the data ranges corresponding to the times taken to record the main spectral features and a whole XANES spectrum from the time the shutter is opened at t = 0. Labels give the percentage changes in fluorescence intensity since the start of scanning using a linear best-fit to the data points (red line). The shaded region represents the time range that a XANES scan would be in the energy range of the main spectral features with the other energy ranges being in the pre- and post-edge regions.

3.3.2 XANES spectra normalisation

For XANES analysis the sets of multiple scans recorded from a single sample were averaged to produce a final spectrum. In the case of spectra collected from AD glasses, each scan was inspected and those exhibiting different spectral line-shapes or poor signal-to-noise when compared to the majority were removed. Anomalous spectral shapes were considered to be related to the glass having suffered more beam damage at some sample positions than others, for example, due to damage caused whilst locating the sample during setup.

When comparing U L_3-edge XANES spectra the general procedure is to correct for a baseline offset below the edge, and normalise using a function fitted to the fluorescence intensity above the edge, to give an "edge-step" of 1. However, this normalisation method was not very successful for the M_4-edge spectra of the U-bearing glasses, primarily due to the spectral shape and low fluorescence intensity in the post-edge energy range with respect to the background noise, i.e. a very small edge-step. This issue can be observed in Fig. 3.7, which shows XANES spectra from MORB composition glasses normalised to the average fluorescence intensity between 3769 and 3780 eV, and where the intensities of the spectral features do not change smoothly and/or systematically with fO_2. In particular the spectrum collected from the glass equilibrated at logfO_2 = -6 has an unexpectedly low normalised intensity. This is clearly a normalisation problem as the shapes of the spectra vary systematically with fO_2.

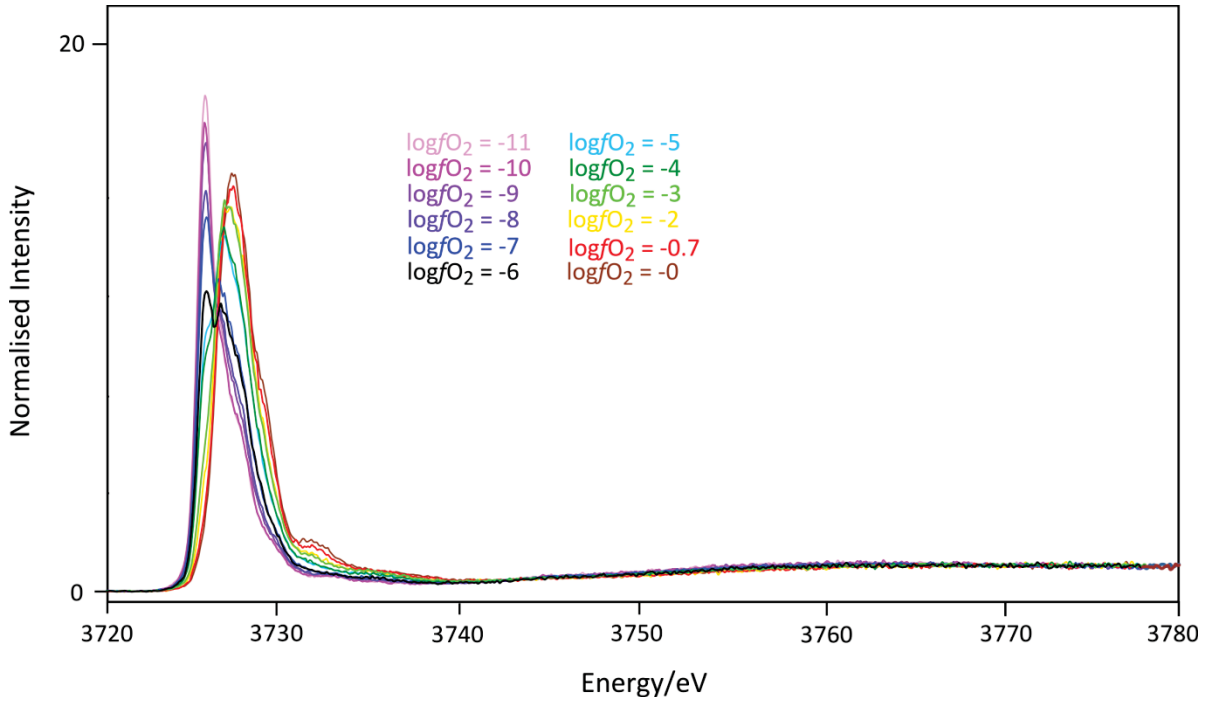


Figure 3.7: Edge-step normalised U M_4-edge XANES spectra of 1 atm MORB glasses equilibrated at 1400 °C and a series of logfO_2s ranging from reduced to oxidised.

Instead, a different approach was used to normalise the spectra of the MORB glasses. The monochromator energy was set to 3850.25 eV, ~125 eV above the edge, and the fluorescence intensity was measured as a function of spectrometer energy between 3330-3345 eV giving a peak profile, such as the ones shown in Fig. 3.8. The peak profile was fitted using a Pseudo-Voigt function whose maximum intensity was used as a normalisation factor. During XANES scanning the spectrometer was tuned to the crest of this peak (at 3337 eV) resulting in a single data point being collected at an incident energy of 3850.25 eV. Thus, the normalisation method was essentially the same as normalising to the intensity at the end of the XANES scan, but this intensity value was better defined.

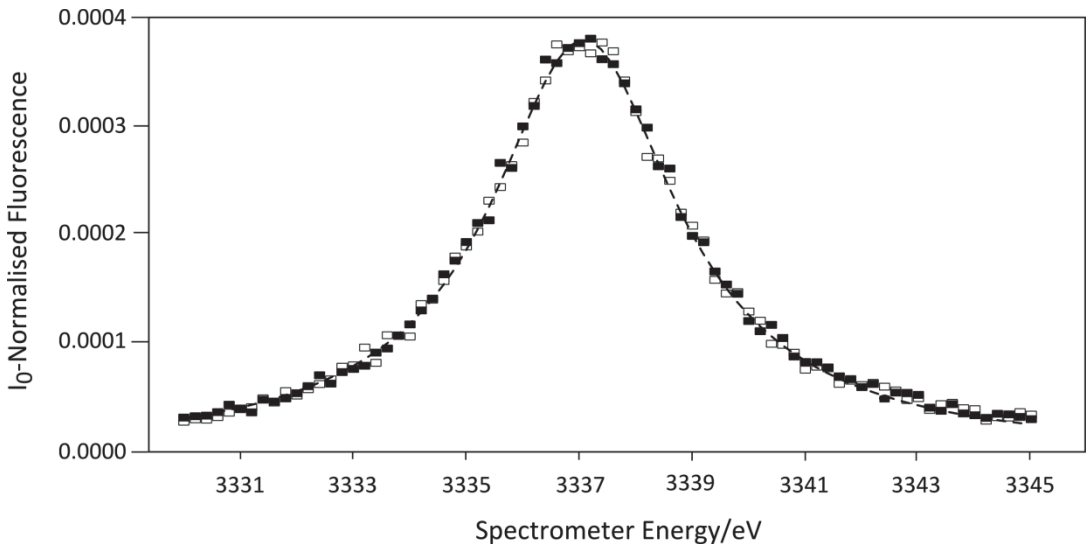


Figure 3.8: I_0-normalised fluorescence count rate as a function of detected photon energy from the MORB glass equilibrated at 1400 °C and $\log fO_2$ = -9, with the incident X-ray energy set to 3850.25 eV. Two scans were collected for each glass, represented as filled and unfilled points, one before and one after the XANES scans. The Pseudo-Voigt peak fitted to the data is also shown (dashed line).

Normalisation scans were recorded both before and after the XANES multiple scans from each glass. Comparison of the maximum intensities of the two scans showed that the average difference between the two values was 2 ± 2 %. The average maximum intensity of the two

scans was used to normalise the average XANES spectrum. The intensity of features of the spectra from the 1 atm MORB glasses normalised using this procedure varied systematically with fO_2, as shown in Fig 3.9. Due to beam damage and the data collection method (i.e. moving the beam to a new spot before each XANES scan) spectra collected from AD glasses could not be normalised in this way and were simply normalised to their maximum intensity.

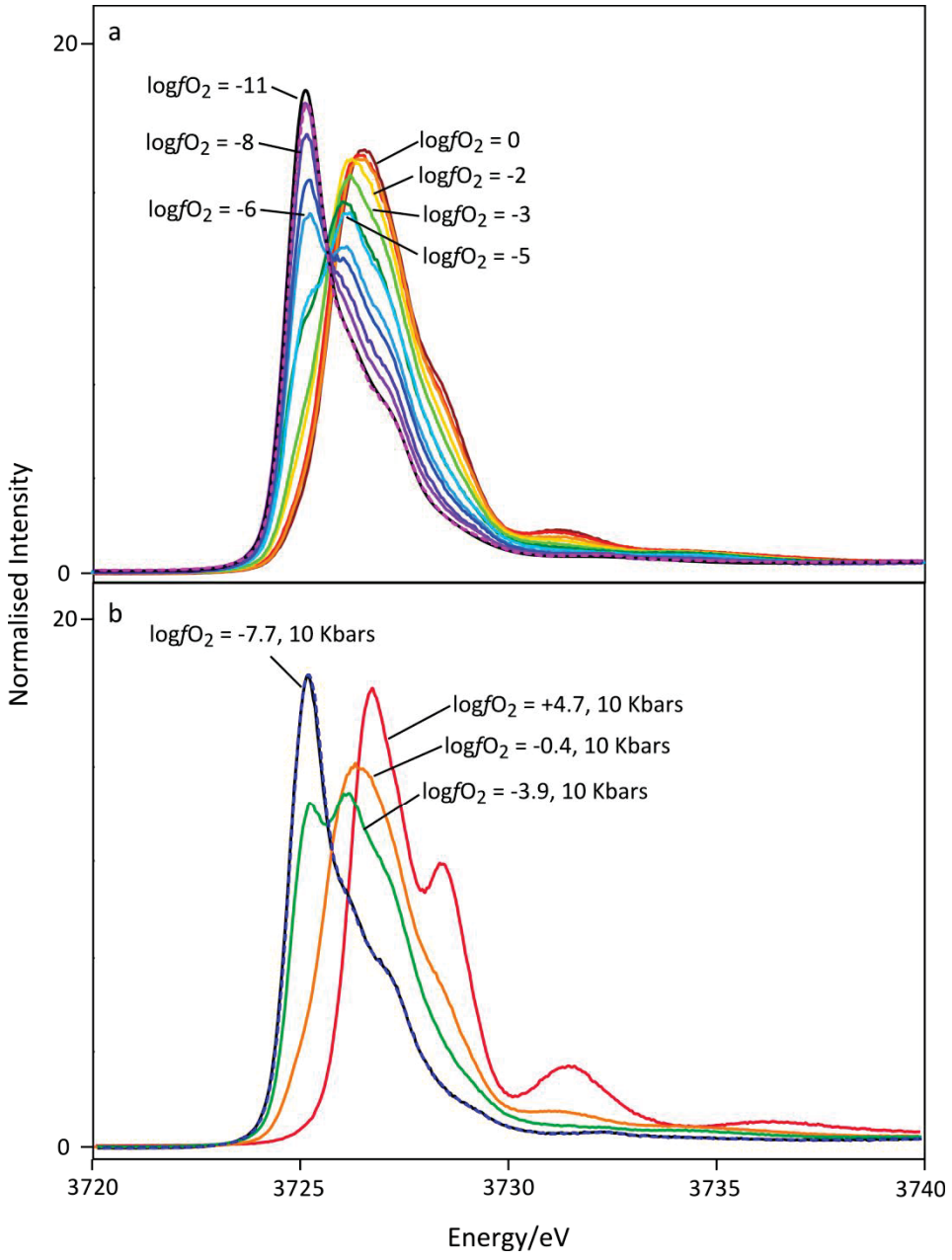


Figure 3.9: U M_4-edge XANES spectra of MORB glasses equilibrated at 1400 °C and (a) 1 atm and (b) 10 kbar, and a series of logfO_2s ranging from reduced to oxidised, normalised to the core emission line.

3.3.3 Analysis of the XANES spectra of MORB glasses

M_4-edge XANES spectra were recorded for MORB 1 atm glasses equilibrated over a range of fO_2s, and at pressures between 5 and 25 kbar at the Pt-PtO_2, Ru-RuO_2, Re-ReO_2 (10 kbar only), and C-CO_2 buffers. If the changing line-shape of the 1 atm U M_4-edge XANES spectra represents a change in the proportions of only two U oxidation states (i.e. U^{4+} and U^{6+}), and there is no change in the coordination environment of a particular U oxidation state with fO_2, then it should be possible to model the shapes of all the spectra by linear combination fits of the most reduced ($\log fO_2$ = -11) and oxidised ($\log fO_2$ = 0) sample line-shapes, which correspond to the largest percentages of U^{4+} and U^{6+}, respectively. Fig. 3.10 shows the best two-component fits to spectra of MORB samples prepared at intermediate fO_2s where the two "end-member" line-shapes were allowed to vary in intensity, but not in shape or energy; the difference between the spectra and the fits are also shown. Fitting was carried out using the freeware program Fityk (version 0.9.8; Wojdyr, 2010). Although the spectra could not be fitted well using this model the residuals had a similar shape in all cases.

The spectra were then fitted using the oxidised and reduced end-member line-shapes and a number of additional peaks. Various peak functions were tried including Lorentzians, Pseudo-Voigts (with a Lorentz fraction of 0.5) and Gaussians. These additional peaks did not have constrained widths. Both Lorentzians and Pseudo-Voigts could only provide satisfactory fits to the data when a large number of peaks were added to the fits, some of these peaks had very narrow widths, which were far below the energy resolution of the experiment. Gaussians were thus chosen to complete the fits. In some fits the energy of the end-members were fixed and in others they were allowed to shift slightly in the final stage of fitting (i.e. after the best zero-energy-shift fit had been obtained). The Gaussians were constrained to have a positive height, and the sum of the Gaussians was required to be continuous (i.e. non-zero) across the

active energy range (~3720-3740 eV). Some degree of trial and error was required to meet these criteria. The sum of the additional Gaussians was extracted to produce a third intermediate U component line-shape.

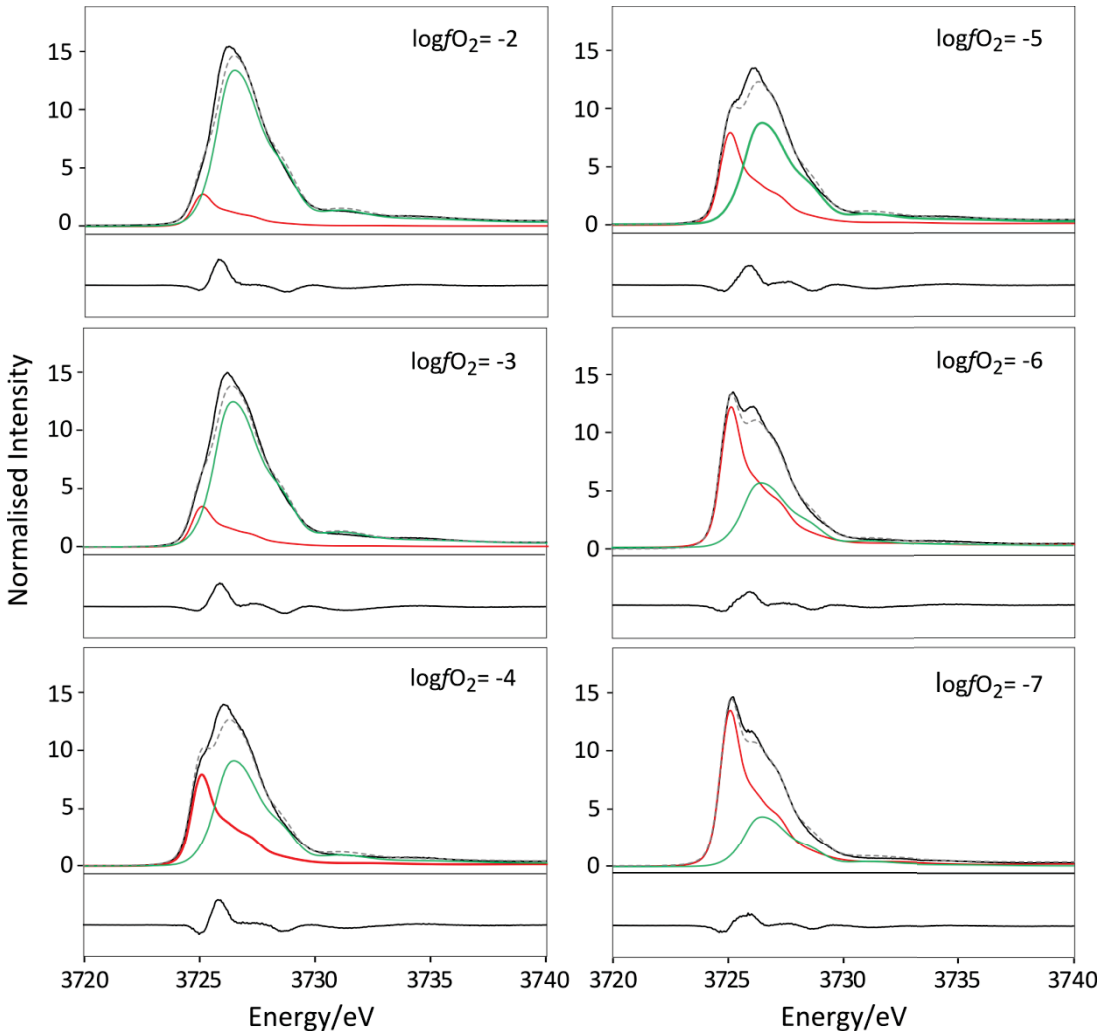


Figure 3.10: U M_4-edge XANES spectra of 1 atm MORB glasses, quenched from 1400 °C and the logfO_2 values indicated fitted (grey dashed lines) using a combination of the most oxidised (logfO_2 = 0: green) and most reduced (logfO_2 = -11: red) 1 atm MORB spectra. The difference between the recorded spectrum and the fit (residual) is shown below each spectrum.

It was expected that the number of Gaussians added to the original two-component fits should be the minimum required to produce a reasonable fit to the MORB spectra, so as to prevent the additional peaks also taking the place of the "U^{4+}" and "U^{6+}" components. The number of Gaussians added to each fit was first varied to determine the optimum number; five

Gaussians was found to be the minimum number required to produce a good fit, whilst being independent of slight changes in the energy range of the data included in the fit of a particular spectrum. The fitting process was repeated for all spectra where the residual component was large enough to distinguish a reasonable shape from the background. Allowing limited energy shifts of the "U^{4+}" and "U^{6+}" spectra in the final stage of fitting reduced the number of spectra from which a sensible intermediate line-shape could be extracted as the energy shifts became unrealistic as the amount of the missing component became small.

The above procedure used the most reduced and oxidised glasses as U^{4+} and U^{6+} end-members, respectively. However, extraction of the intermediate U state line-shape by this method does not require the end-members to be pure U^{4+} and U^{6+} line-shapes, only that the end-member sample has a larger percentage of the end-member component than the intermediate samples. The intermediate line-shapes extracted using the choice of $\log fO_2 = -11$ for the reduced end-member, and $\log fO_2 = 0$ for the oxidised end-member were checked by replacing them with other relatively reduced ($\log fO_2 = -10$, -9, pressure = 1 atm) and oxidised ($\log fO_2 = +4.1$, pressure = 5 kbar) spectra. The same methodology was also applied to MORB glasses equilibrated at 10 kbar. XANES spectra from glasses equilibrated at the Ru-RuO_2 ($\log fO_2 = -0.4$) and Re-ReO_2 ($\log fO_2 = -3.9$) buffers, were fitted using the line-shapes from glasses equilibrated at the C-CO_2 ($\log fO_2 = -7.7$) and Pt-PtO_2 ($\log fO_2 = +4.7$) buffers, as the U^{4+} and U^{6+} line-shapes, respectively.

All the extracted line-shapes are shown in Fig. 3.11. The average line-shapes were indistinguishable for all 1 atm end-member combinations and for the case where the spectra of the 5 kbar, Pt-PtO_2 buffered MORB glass was used as the oxidised end-member. The line-shape extracted from the spectra of glasses prepared at 10 kbar were also very similar to the

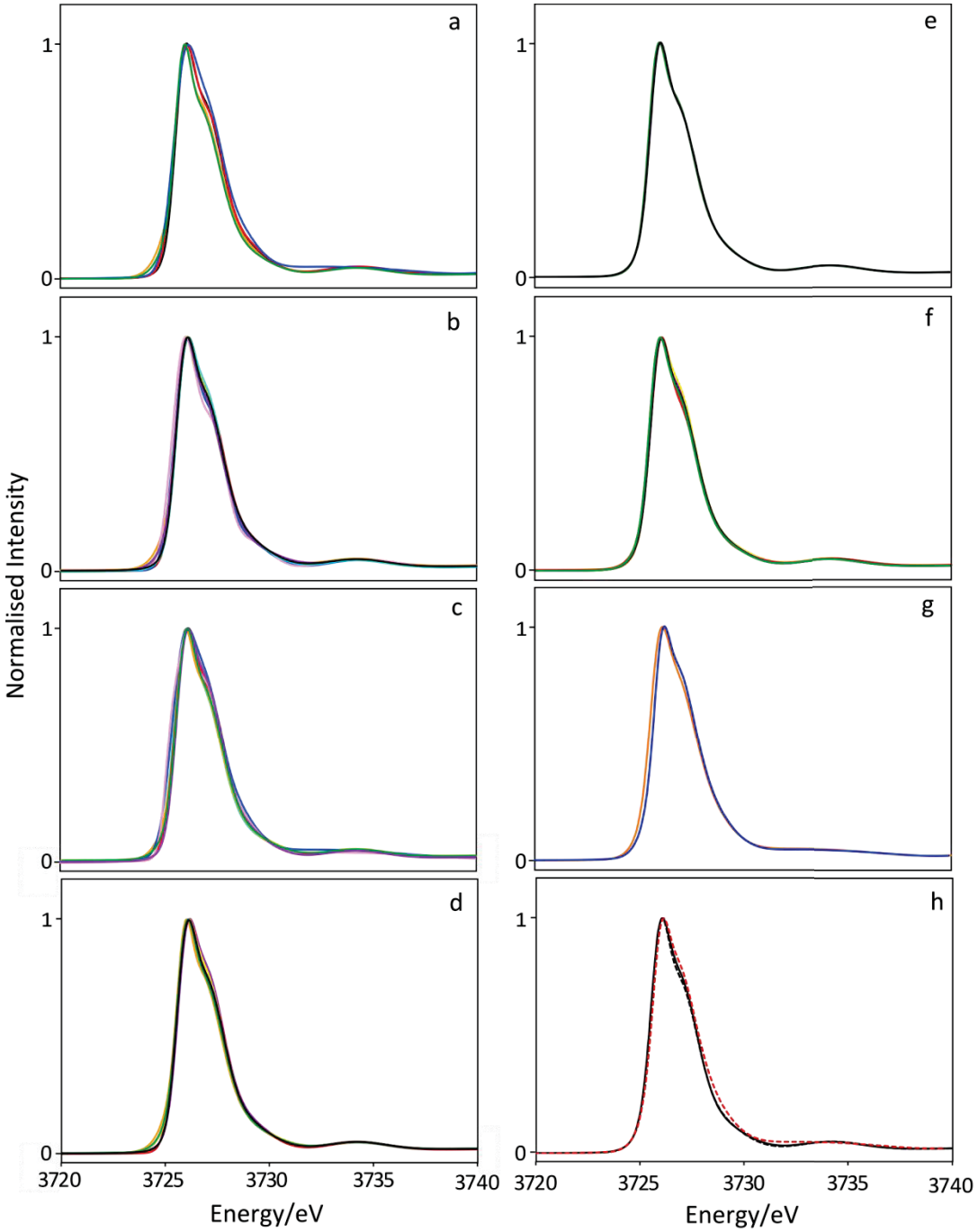


Figure 3.11: Intermediate line-shapes (sum of five Gaussians) extracted from MORB spectra (logfO_2 = 0 to -7) fitted using different oxidised- and reduced- end-member combinations and 5 Gaussians: (a) logfO_2 = -11 (1 atm) and 0 (1 atm) (five in panel), (b) logfO_2 = -11 (1 atm) and +4.1 (5 kbar) (nine in panel), (c) logfO_2 = -10 (1 atm) and +4.1 (5 kbar) (eight in panel), (d) logfO_2 = -9 (1 atm) and +4.1 (5 kbar) (seven in panel), (e) logfO_2 = -11 (1 atm) and 0 (1 atm) (two in panel), (f) logfO_2 = -11 (1 atm) and +4.1 (5 kbar) (six in panel), (g) logfO_2 = -7.7 (10 kbar) and +4.7 (10 kbar) (two in panel). End-member line-shapes were allowed to shift in energy during fitting for the line-shapes shown in (e) and (f). Panel (h) shows the average of the intermediate line-shapes extracted using different end-member combinations: logfO_2 = -11 (1 atm) and 0 (1 atm) (black), logfO_2 = -11 (1 atm) and +4.1 (5 kbar) (black dashed), and logfO_2 = -7.7 (10 kbar) and 4.7 (10 kbar) (red dashed).

average 1 atm line-shape (Fig 3.11(g) and 3.11(h)). This result was not necessarily expected, but it suggests that pressure does not significantly impact the M_4-edge spectral line-shapes of the different U oxidation states, and that the spectra of the Pt-PtO_2 buffered glasses can be used as a 1 atm line-shape much closer to 100 % U^{6+} than exists for the 1 atm glasses.

Using the average of the intermediate line-shapes produced from five Gaussians with the spectra of logfO_2 = -11 (1 atm) and logfO_2 = 0 (1 atm) as the reduced- and oxidised- end-members (Fig 3.11(h)), all of the 1 atm MORB spectra were finally fitted using three spectral components. Spectra were fitted using a combination of the logfO_2 = -11 and logfO_2 = +4.1 (5 kbar) spectra, and the average intermediate line-shape (Fig. 3.12). The proportions of each component in each spectrum as a function of logfO_2 are shown in Fig. 3.13; the proportions of the intermediate component was obtained by making the sum of all three components equal to 1. The energy of the white-line maximum of the intermediate component, which lies between the logfO_2 = -11 and logfO_2 = +4.1 spectra, and its variation in intensity with fO_2 suggests that it represents U^{5+}.

The intermediate line-shape extraction method is not necessarily expected to produce the full U^{5+} line-shape. This is discussed in Appendix A3 for a set of Cr-bearing glasses for which the oxidation state proportions in each glass are known. The closeness of the extracted line-shape to the true U^{5+} spectrum will depend on how much of the three U oxidation states' spectral line-shapes/features are shared. As such, whilst this method tells us the number of U oxidation states in the glasses, and gives us an estimate of their relative proportions, these estimates have a large uncertainty associated with them In fact, the U^{5+} proportions plotted in Fig. 3.13 represents the minimum possible values, as such, it is apparent that U^{5+} is a significant component in the MORB glasses, even at relatively reduced fO_2s.

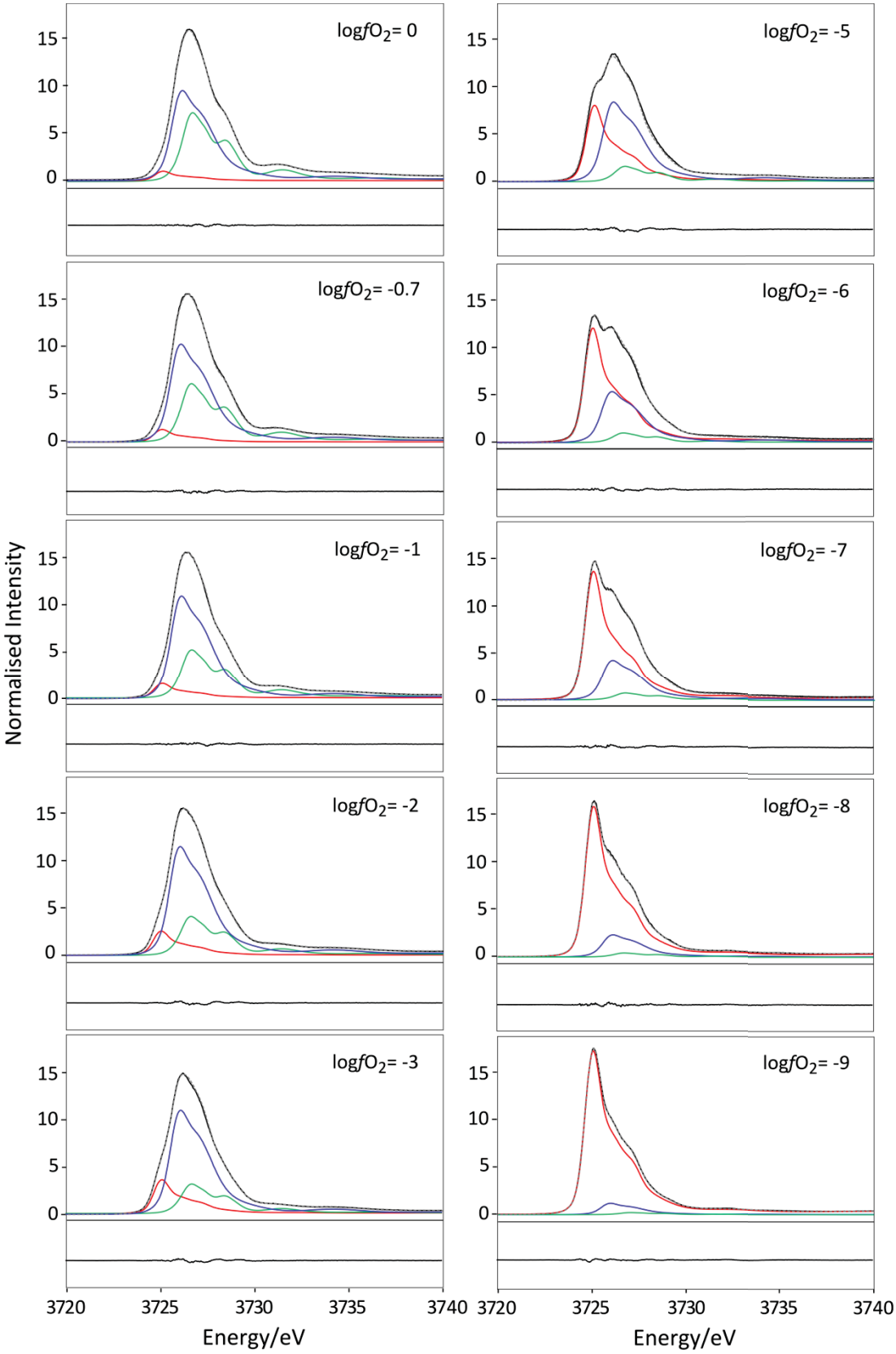


Figure 3.12: U M_4-edge XANES spectra of MORB 1 atm glasses quenched from 1400 °C and the logfO_2 values indicated fitted (grey dashed lines) using a combination of the most oxidised (logfO_2 = +4.1, P = 5 kbar: green) and reduced (logfO_2 = -11: red) spectra, and the average extracted intermediate line-shape (sum of five Gaussians: blue). The difference between the recorded spectrum and the fit is shown below each spectrum.

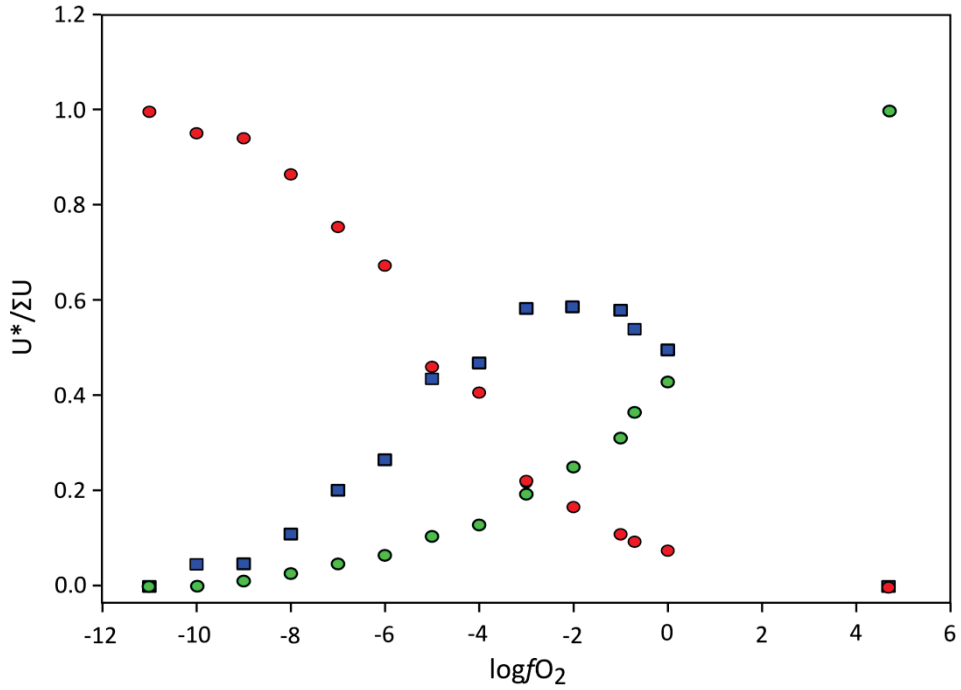
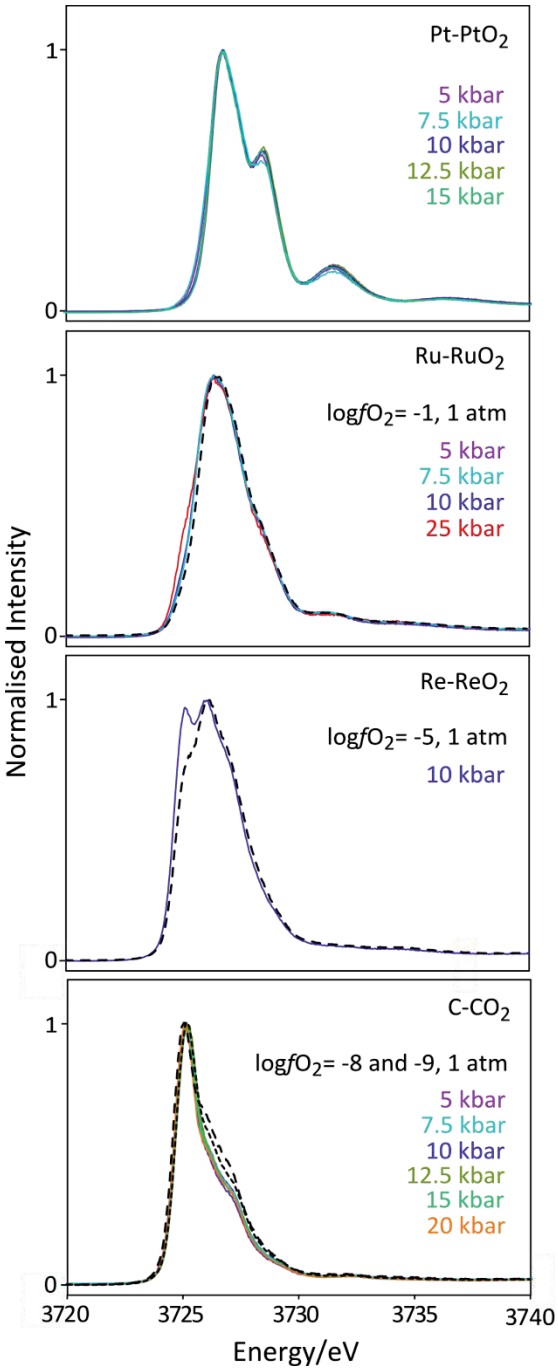


Figure 3.13: Proportions of the MORB logfO_2 = -11 (red circles) and logfO_2 = +4.1 (5 kbar) (green circles) line-shapes, and the average intermediate line-shape extracted from MORB spectra using five Gaussians (blue squares), in three-component fits of spectra of MORB 1 atm glasses equilibrated at 1400 °C.

As shown in Fig. 3.14, spectra from glasses synthesised at pressures ≥ 5 kbar at the C-CO_2 and Re-ReO_2 buffers exhibit significantly more reduced line-shapes to those of glasses equilibrated at approximately equivalent fO_2s at 1 atm (logfO_2 = -8 and -4, respectively). The presence of CO_2 and/or H_2O in these glasses may be capable of causing a shift in the U redox equilibria that is not pressure induced. However, the volatile contents of the 5 kbar C-CO_2 buffered glass must be small, as CO_2 solubility is expected to be ~0.3 wt % at this pressure for a basaltic melt (Ni and Keppler, 2013), and an EPMA total of 98.9 wt % suggests minimal H_2O (Table A2.1: C4318). In addition, spectra of Ru-RuO_2 buffered glasses synthesied at different pressures, which are expected to contain similar amounts of H_2O to glasses prepared at other buffers, are barely different from their 1 atm equilvalent (logfO_2 = -1). For C-CO_2 experiments the fO_2 defined by the buffer represents the maximum attainable value for these samples, which will only have been achieved if CO_2 saturation was reached and the CO_2 did

not leak from the capsule. However, any deviation from the buffer value is expected to be small, as it will be equal to the logarithm (base 10) of the CO_2 in the melt divided by the CO_2 content of the melt at saturation (i.e. if the melt only contained half as much dissolved CO_2 than at saturation logfO_2 = buffer value - log(1/2) = buffer value - 0.3). It is also possible that



Figures 3.14: U M_4-edge XANES spectra of MORB glasses equilibrated as a function of pressure at 1400 and 1500 °C, and buffered at Pt-PtO_2, Ru-RuO_2, Re-ReO_2, and C-CO_2.

the "Re-ReO_2 buffered" glass was in fact equilibrated at a more reduced fO_2 (~1.5 log units below Re-ReO_2). If the C-CO_2 and Re-ReO_2 buffered glasses were equilibrated at more reduced fO_2s the change in U oxidation state between 1 atm and higher pressure melts might be less than that suggested by the spectra shown in Fig. 3.14.

Spectra from glasses equilibrated between 5 and 25 kbar at the same fO_2 buffer exhibit little, if any, difference in spectral line-shape with the pressure of equilibration (Fig. 3.14). Whilst a role for dissolved CO_2 and/or H_2O in changing the U oxidation state cannot be ruled out, it seems unlikely that varying volatile concentrations are fortuitously cancelling out any pressure induced oxidation state change. There may be a systematic variation in the Ru-RuO_2 buffered glasses spectra with pressure, with the spectra from higher pressure glasses (in particular 25 kbar) exhibiting a slight shoulder on the edge-rise, consistent with a slight increase in the proportion of the reduced U^{4+} state. However, the change in spectral shape is extremely subtle, and is not observed for the C-CO_2 or Pt-PtO_2 buffered glasses. The fO_2 of the Ru-RuO_2 buffer relative to QFM is 0.5 log units more reduced at higher pressure (Ru-RuO_2 = QFM+5 and QFM+5.5 at 5 and 25 kbar, respectively); however, similar offsets also occur for the C-CO_2 and Pt-PtO_2 buffers as a function of pressure.

3.3.4 Analysis of the XANES spectra of AD glasses

When the methodology described for the MORB spectra was applied to the AD 1 atm spectra a single intermediate line-shape could not be produced, as shown in Fig. 3.15. This result was independent of the number of Gaussians added, the choices of oxidised and reduced end-member spectra, and whether or not end-member spectra energy shifts were allowed or forbidden. However, the extracted intermediate line-shapes varied systematically with fO_2. The line-shapes extracted from spectra exhibited two distinct peaks; those extracted from the

most reduced glasses were dominated by a peak at the same energy as the MORB "U^{4+}" end-member, whilst those extracted from the most oxidised glasses were dominated by a peak at

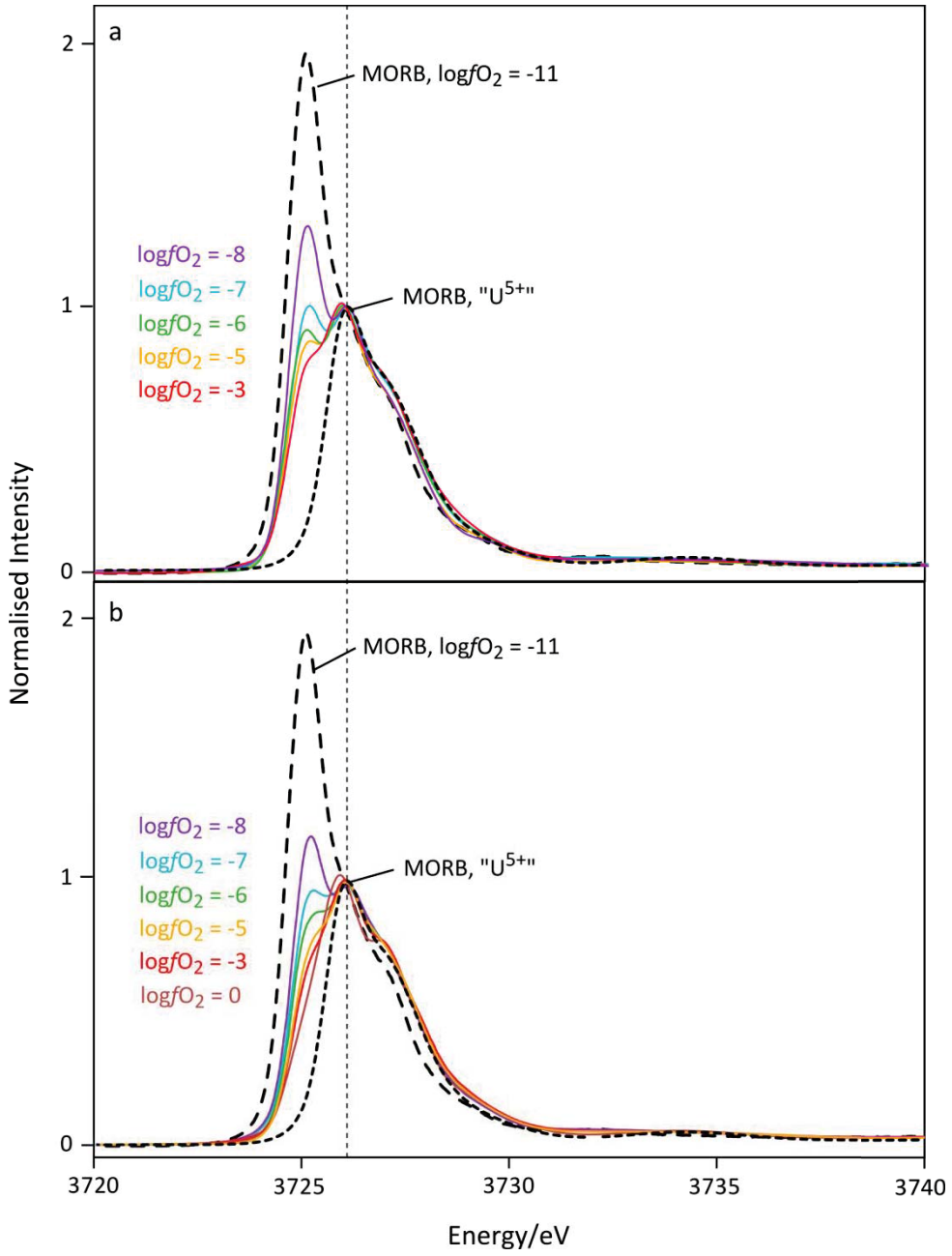


Figure 3.15: Intermediate line-shapes extracted from spectra of AD glasses equilibrated at 1400 °C and the fO_2s indicated. Spectra were fitted using a combination of reduced and oxidised end-member line-shapes (a) logfO_2 = -18 (1 atm) and 0 (1 atm), and (b) logfO_2 = -12 (1 atm) and +4.7 (10 kbar), and Gaussians. The spectrum of the MORB glass equilibrated at logfO_2 = -11 (1 atm), and the MORB intermediate component line-shape are also shown. Spectra are intensity normalised to 1 at an energy of 3726.2 eV (dashed vertical line).

energies consistent with the intermediate component extracted from MORB spectra, interpreted as representing U^{5+}.

With this in mind the AD spectra were fitted using four spectral components, a combination of the AD reduced and oxidised end-members spectra collected from glasses equilibrated at logfO_2 = -18 (1 atm) and logfO_2 = +4.7 (10 kbar), the MORB logfO_2 = -11 (1 atm) spectrum, and the average intermediate line-shape produced from fitting the MORB spectra. The relative intensities/proportions of the four components in these fits varied systematically with the fO_2 of sample equilibration, as shown in Fig. 3.16. As the AD spectra were not background-normalised the proportions of each component were compared by dividing the maximum intensity of each component in each spectrum by the sum of the maximum intensities of all four components in that spectrum, as shown in Fig. 3.17. Although this is not suitable for precise quantification, as it assumes that the four components have equivalent normalised maximum intensities, it is an internally consistent way to compare the relative variation of the four U components in the glasses.

3.4 Preliminary conclusions

To reproduce the U M_4-edge spectral variation as a function of fO_2 for MORB glasses requires three U components, whose white-line energies, spectral features, and relative contributions to each spectrum are consistent with U^{4+}, U^{5+}, and U^{6+}. Comparison of spectra collected from glasses synthesised at different pressures indicates a change in U oxidation state equilibria between 1 atm and 5 kbar, with increased pressure seemingly favouring U^{4+}. Increasing pressure above 5 kbar seems to have little effect, on U oxidation state proportions at a given fO_2 buffer, although the data were somewhat sparse, with only one sample buffered by Re-ReO_2.

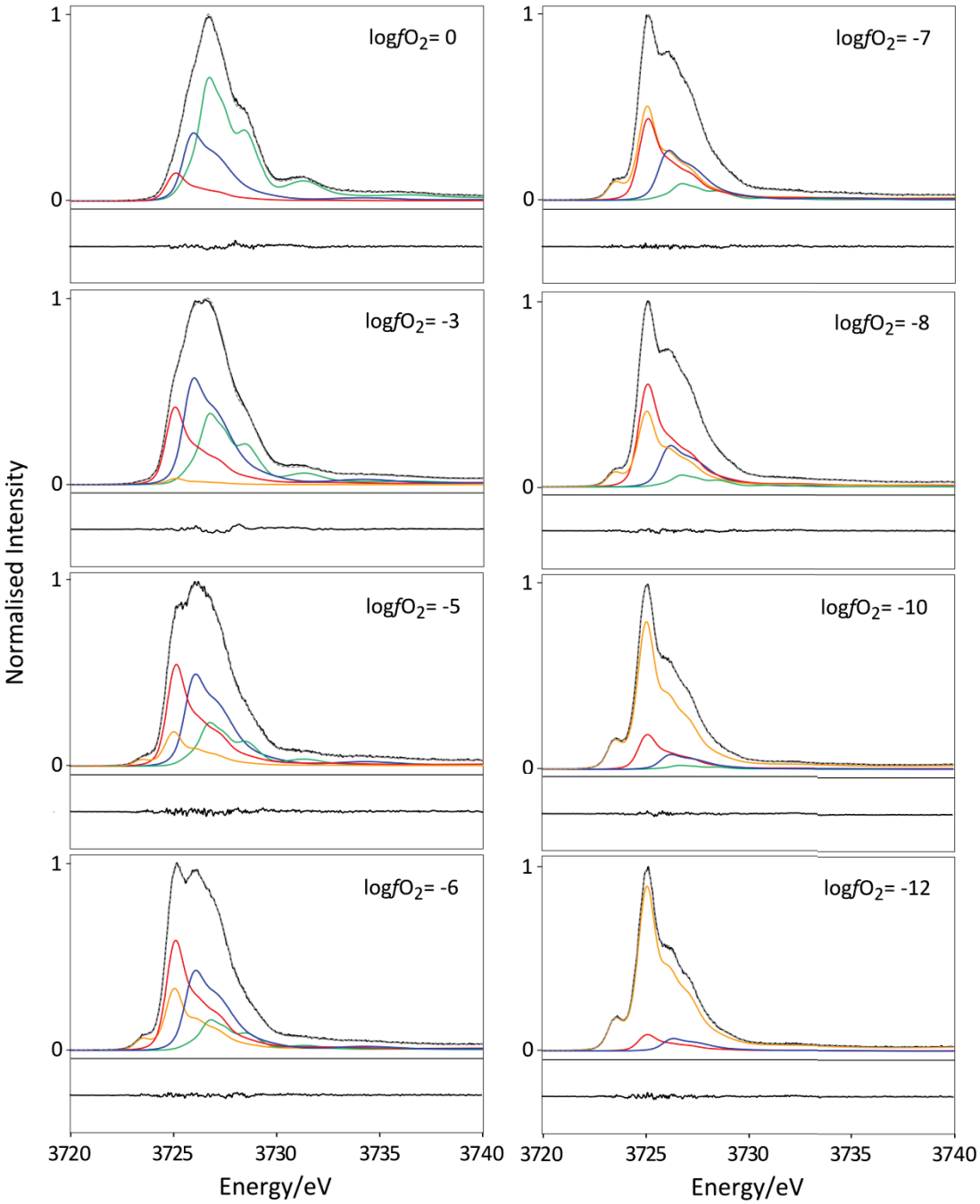


Figure 3.16: U M_4-edge XANES spectra of AD 1 atm glasses quenched from 1400 °C and the logfO_2 values indicated fitted (grey dashed lines) using a combination of the most oxidised (logfO_2 = +4.7, P = 10 kbar: green) and reduced (logfO_2 = -18: orange) AD spectra, the most reduced MORB spectrum (logfO_2 = -11: red), and the average intermediate line-shape (sum of five Gaussians: blue) extracted from MORB spectra. The difference between the recorded spectrum and the fit is shown below each spectrum.

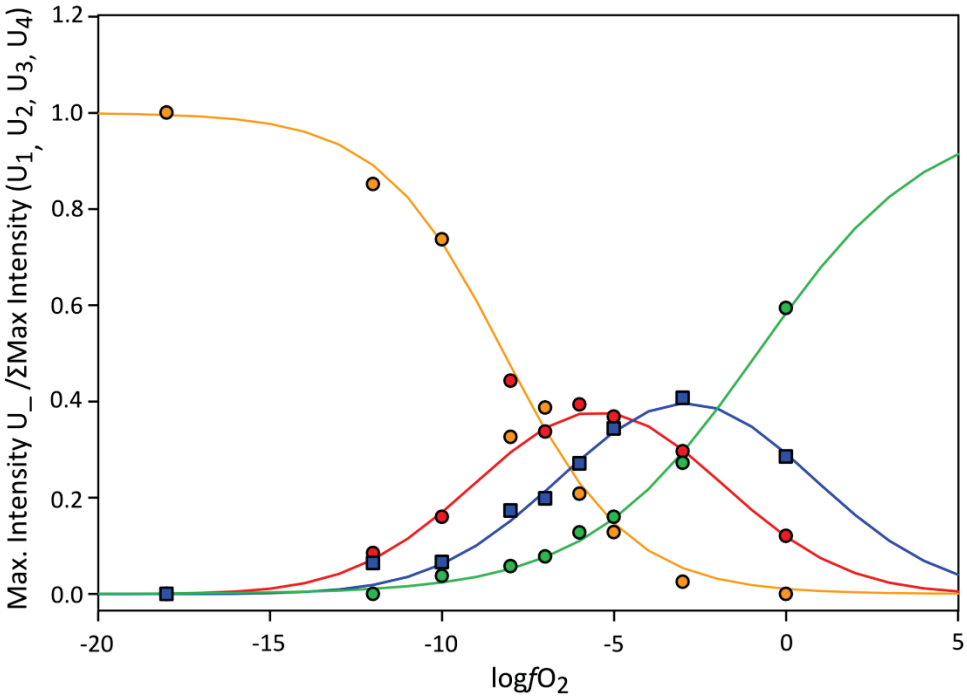


Figure 3.17: Relative maximum intensities of the AD logfO_2 = -18 (orange circles) and logfO_2 = +4.7 (10 kbar) (green circles) line-shapes, the MORB logfO_2 = -11 (red circles) line-shape, and the intermediate line-shape extracted from MORB spectra using five Gaussians (blue squares), in four-component fits of spectra from AD 1 atm glass. Sigmoidal and Gaussian curve fits to the component variations are shown for clarity.

The peak energies and variation in spectral and residual line-shapes of the spectra of the AD glasses indicates the presence of three U components with similar line-shapes to those in the MORB glasses (U^{4+}, U^{5+}, and U^{6+}). However, the pre-edge feature in the spectra of the AD glasses limited the reduced end-members ability to fit the full "U^{4+}" (3725.1 eV) peak. The AD glasses must contain a fourth U component that is stable under reducing conditions, which is represented by the beam sensitive pre-edge feature, and whose white-line maximum occurs at essentially the same energy as that of the U^{4+} component observed for both the MORB and AD glasses.

Chapter 4:

U L_3-edge XANES spectroscopy of silicate glasses

4.1 Introduction

Whilst glasses have commonly been used as analogues for melts, it has become apparent that the oxidation state and coordination environment of an element in a glass may not represent those of the original melt (Berry *et al.*, 2006; Wilke *et al.*, 2007). For example, Cr^{2+} has been shown to be the dominant oxidation state in Fe-free silicate glasses and in Fe-bearing basaltic melts at magmatic temperatures and terrestrial fO_2s ($Cr^{2+}/\sum Cr$ = ~0.5 at QFM at 1400 °C). However, this oxidation state was not observed in the equivalent Fe-bearing quenched glasses. The absence of Cr^{2+} in the synthetic Fe-bearing glasses, and indeed in terrestrial materials, where the redox variable Fe occurs in much higher concentrations than Cr, is an artefact of the quench caused by the electron exchange reaction $Cr^{2+} + Fe^{3+} \rightarrow Cr^{3+} + Fe^{2+}$ (Berry *et al*., 2006; Berry and O'Neill, 2004). This reaction goes to completion despite rapid quenching of the melts. It is thus critical for oxidation state quantification studies to be extended to melts *in situ*.

An advantage of using XANES spectroscopy to quantify oxidation states is the ability of the technique to take measurements directly from high temperature melts, rather than from their quenched products. Such studies can be carried out using a specialist XAS furnace. However, the U M_4-edge energy is too low for XANES measurements in conjunction with a furnace that also meets the temperature and gas atmosphere requirements of this work due to X-ray attenuation by the furnace windows and gas atmospheres. The furnace design along with its capabilities and limitations will be discussed in detail in Chapter 6. The collection of U XANES spectra from silicate melts is thus limited to the higher energy L_3-edge.

Changes in U L_3-edge XANES spectra with oxidation state are relatively subtle, and oxidation state assignment using this edge alone may be ambiguous (Petiau *et al.*, 1986; Hu *et al*., 1998; Kosog *et al*., 2012). In order to interpret the XANES spectra collected from *in situ* melts it was first necessary to understand how spectral line-shape changes at the L_3-edge relate to changes in U oxidation state. To this end, L_3-edge XANES spectra were first collected from U-bearing glasses. This allowed spectra collected at the L_3-edge to be compared with those collected at the M_4-edge, which is more "feature rich", from the same samples. Preliminary studies of glasses offered the additional advantages that a wider fO_2 coverage was possible than for *in situ* melts, where the fO_2 range is limited by the capabilities of the XAS furnace, and that data for a large number of glass compositions could be collected with relative ease.

4.2 Experimental methods

U L_3-edge XANES spectra of U glasses were recorded at beamlines I18 and B18 of Diamond Light Source (DLS); details in Mosselmans *et al*. (2009) and Dent *et al.* (2009). Spectra were recorded from all the 1 atm glasses resulting in seven fO_2 series (six CMAS and one MORB composition). Spectra were also recorded from MORB and AD composition glasses synthesised at various fO_2 buffers at 10 kbar and 5-15 kbar, respectively. The excitation energy was selected using a Si(111) double crystal monochromator. For spectra collected at I18 (insertion device) the spectral energy resolution is well approximated by a combination of the Darwin width of the monochromator (2.40 eV at 17172 eV) and the U L_3 core-hole width (7.43 eV, Krause & Oliver 1979; Hämäläinen *et al*., 1991) giving a value of 7.8 eV. At B18 (bending magnet) the effect of beam divergence at the monochromator is also significant at the shallow angle of incidence of the U L_3-edge (6.6° at 17170 eV). A maximum estimated divergence of 15 microradians corresponds to ~2.2 eV at 17100 eV, resulting in a total

resolution of 8.1 eV. The Rh coated toroidal mirror (I18) and Pt coated collimating mirror (B18) before the crystal monochromator rejected higher order harmonics. Fluorescence was recorded using a 9 element Ge detector. The X-ray beam size on the sample was ~0.3 × 0.3 mm (H × V). The photon flux at the sample was ~2×10^{11} photons/s at B18 and within an order of magnitude of this value at I18.

U spectra were recorded over the energy range 17000-17400 eV, with a step size of 10 eV in the pre-edge region (17000-17145 eV), 0.5 eV over the white-line (17145-17190 eV), 2 eV in the near post-edge region (17190-17250 eV), and 10 eV in the far post-edge region (17250-17400 eV), with a counting time of 1 s per point. The total acquisition time for a single spectrum was 7-9 minutes, varying between different sessions. Replicate spectra indicated a monochromator drift of < 0.25 eV during individual data collection sessions. To allow comparison between different beamtimes reference spectra were collected from several of the same glasses during each session.

The possibility of beam induced oxidation state changes in the glasses was also investigated. The monochromator energy was set to that of the white-line crest before moving to a new spot on the sample and recording the incident flux-normalised fluorescence as a function of time. The shutter was opened after the scan macro had been started so that no immediate effect would be missed in the seconds taken to open the shutter.

4.3 Results

All spectra were normalised by subtracting a linear base-line fitted to the pre-edge energy range, 17000-17070 eV, and then dividing by an energy dependent value obtained from a linear function fitted to the post-edge between 17230 and 17400 eV. The spectra of both

MORB and CMAS glasses equilibrated at all pressures varied systematically with the fO_2 of equilibration, as shown in Fig. 4.1. Spectra collected from AD glasses equilibrated at the same fO_2 buffer between 5 and 15 kbar were essentially identical regardless of the pressure of equilibration. The spectra consisted of an intense white-line that shifted to higher energy, broadened, and became increasingly asymmetric as the glasses became more oxidised. The spectra from the most oxidised samples exhibited a distinct shoulder on the high energy side of the white line crest. This shoulder is thought to be characteristic of uranyl (U^{6+}) (Petiau *et*

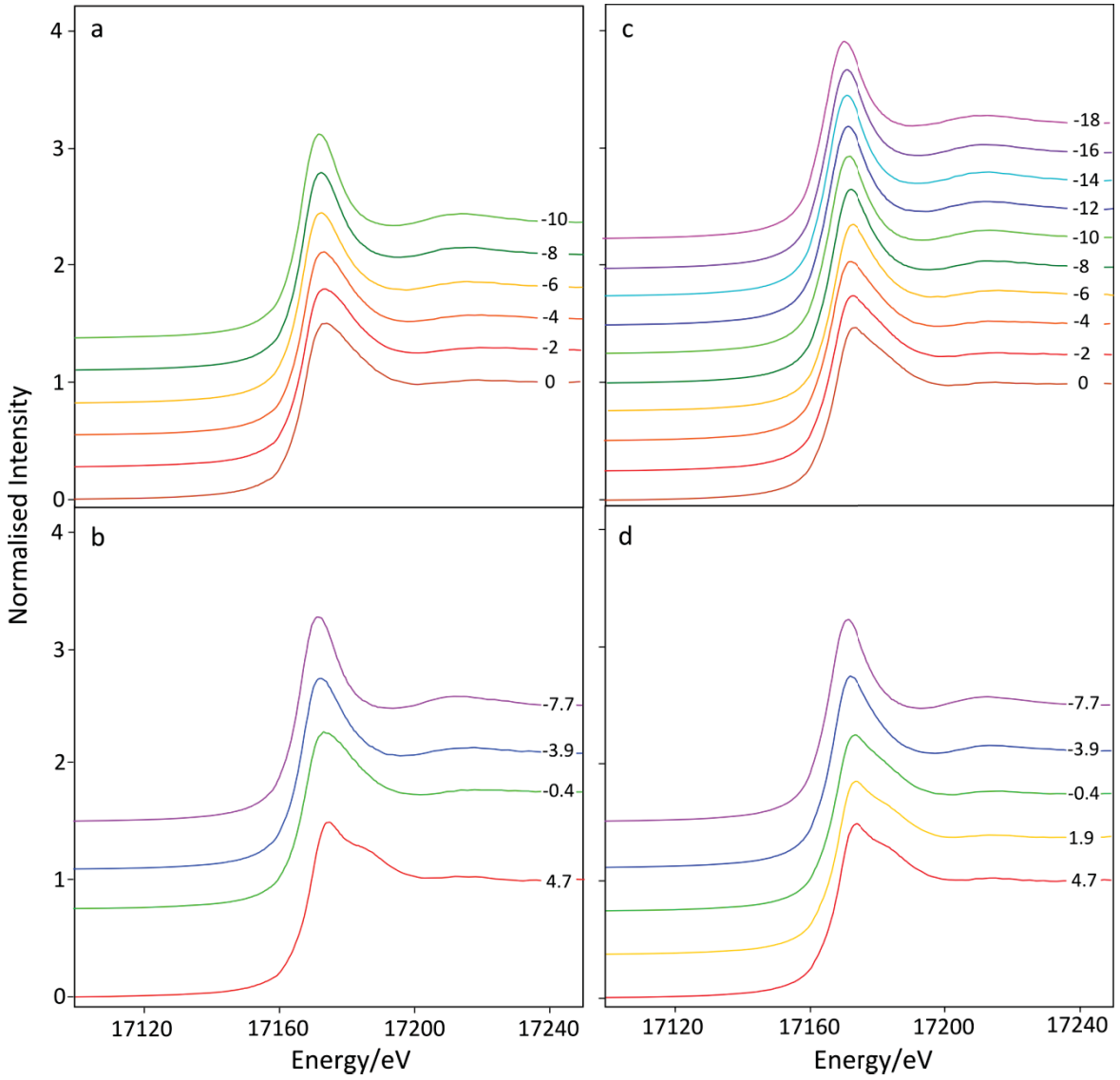


Figure 4.1: U L_3-edge XANES spectra of MORB (a) 1 atm and (b) 10 kbar, and AD (c) 1 atm and (d) 10 kbar composition glasses equilibrated at 1400 °C and the logfO_2 values indicated.

al., 1986; Hudson *et al*., 1995), and notably is not reported for all U^{6+} compounds (Kosog et al., 2012). The maximum normalised intensity of the white-line decreased with increasing fO_2.

The variation in spectral line-shape was small, even between samples that were expected to represent a large change in the proportions of U oxidation states. As such, attempting to calibrate features such as white-line intensity between different beamtimes is likely to be associated with a large uncertainty, comparable to the oxidation state induced spectral changes observed over a wide fO_2 range. To avoid this problem, XANES spectra were collected from complete sample sets during a single session. For example, spectra for all the MORB composition glasses were collected during one beamtime. Quantitative analysis was thus only applied to "sets" of data that were collected during the same session and are therefore expected to be internally consistent. Spectra from all the Fe-free glasses were also collected in a single session, but on a separate occasion to those from the MORB glasses.

4.3.1 Beam damage

A beam induced decrease in the intensity of the white-line crest as a function of time was clearly observed for reduced AD composition glasses, shown in Fig. 4.2, which exhibited a rapid drop in fluorescence intensity on opening of the shutter. Such an effect was not observed for more oxidised AD glasses, or for any of the MORB composition glasses. AD samples prepared at 10 kbar and various fO_2 buffers exhibited analogous beam damage behaviour to the 1 atm samples. The 10 kbar glass synthesised at C-CO_2 ($\log fO_2$ = -7.7), the most reducing condition, exhibited the largest drop in fluorescence intensity of ~2 % in 150 s, whilst the glass synthesised at the moderately oxidising Re-ReO_2 buffer ($\log fO_2$ = -3.9) showed a smaller decrease of ~1 % in the same time. In contrast, time-scans from 10 kbar

glasses buffered at Ru-RuO_2 (logfO_2 = -0.4) and Pt-PtO_2 (logfO_2 = +4.7) did not show any signs of damage.

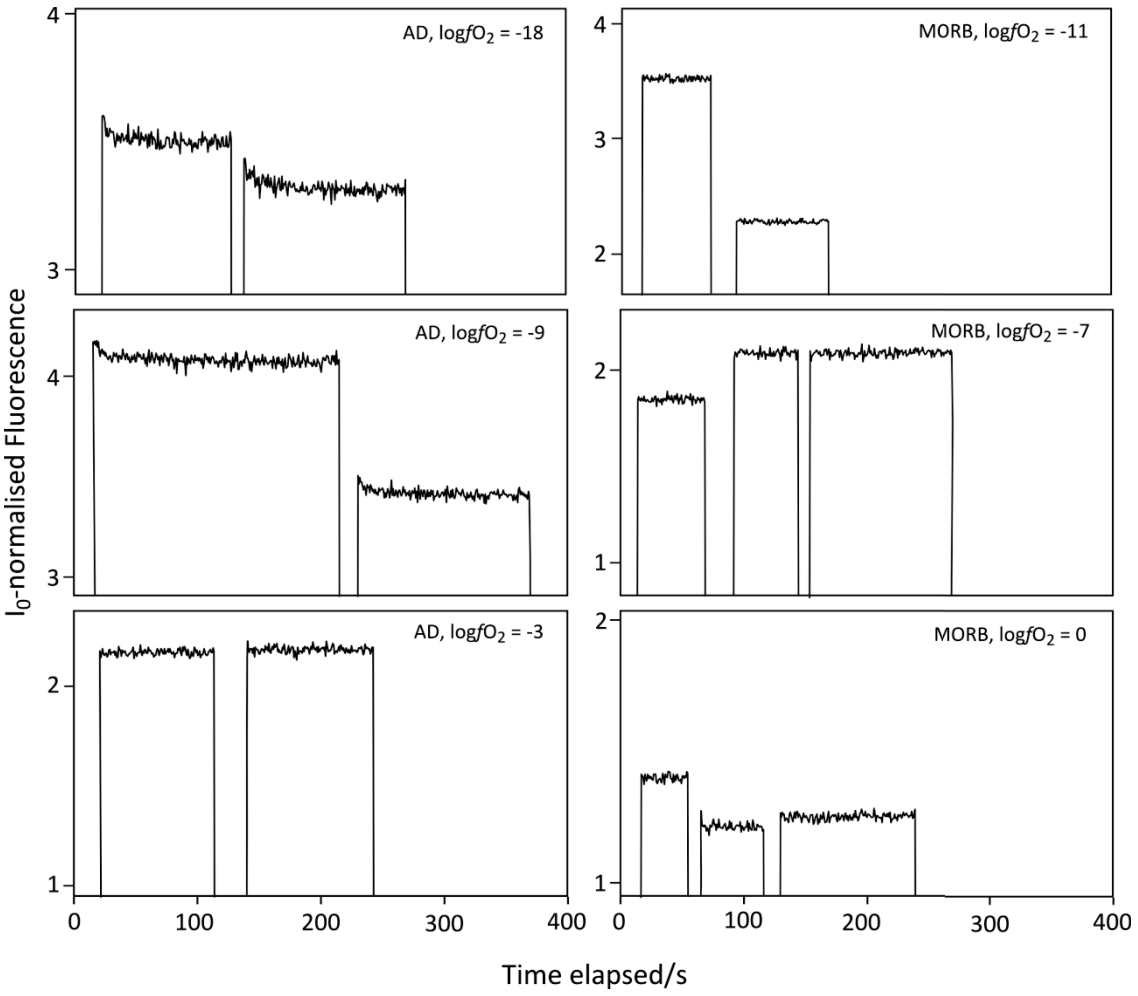


Figure 4.2: Fluorescence intensity, normalised to the beam intensity, as a function of time for U in AD and MORB glasses equilibrated at various fO_2s for excitation energies set to the U L_3-edge white-line crest. Insets show enlarged versions of regions indicated.

Fig. 4.3 shows three 9 minute scans recorded in immediate succession from the same spot of a reduced CMAS composition glass (AD+En logfO_2 = -10). The white-line crest intensity decreased by ~0.5 % between each scan. This is slower than the rate observed in the short time-scans, which are summarised in Table 4.1, and confirms that the worst damage occurs within tens of seconds. Beam induced changes are likely to have a significant impact on

XANES spectra analysis at the L_3-edge, as the reduction in the normalised white-line intensity between the spectra of the most reduced and most oxidised samples (Fig. 4.1) due to U oxidation state changes is only ~15 %. No evidence of beam damage was observed from multiple scans of MORB composition glasses. Unlike experiments at the M_4-edge (Chapter 3), there was no means of collecting XANES spectra fast enough to reduce the effect of beam damage and beam damaged spectra had to be included for XANES analysis.

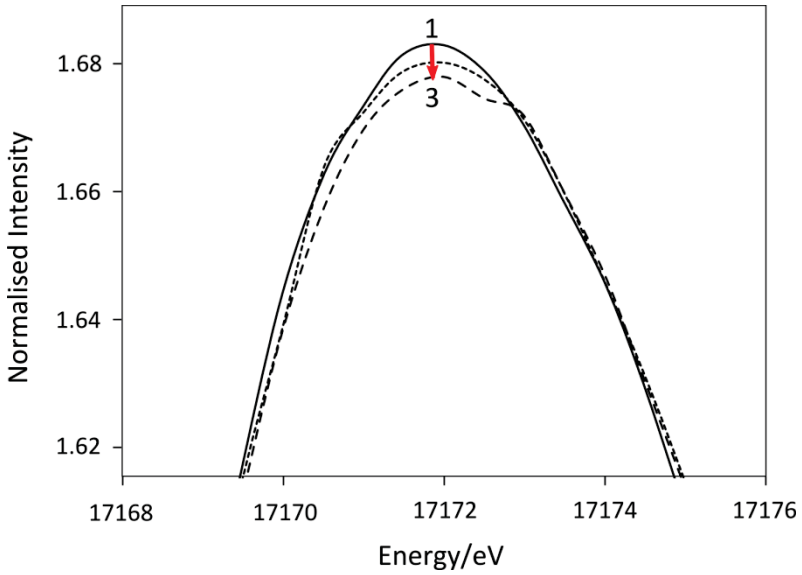


Figure 4.3: The white-line crest region of three U L_3-edge XANES scans recorded in immediate succession from an AD+En composition glass equilibrated at 1 atm, 1400 °C, and logfO_2 = -10. Each full XANES scan took 9 minutes to record.

Table 4.1: Summary of the beam induced decreases in the U L_3-edge white-line intensity as a function of time for AD composition glasses equilibrated at various fO_2s.

Beamline	logfO_2	Pressure	decrease	Time/s
B18	-18	1 atm	2.4 %	100
B18	-18	1 atm	3.4 %	120
B18	-14	1 atm	3 %	150
B18	-9	1 atm	2 %	270
B18	-9	1 atm	2.3	140
B18	-9	1 atm	2	100
I18	-7.7	10 kbar	~2 %	150
I18	-3.9	10 kbar	~1 %	150

4.3.2 XANES analysis

If there were only two U oxidation states present in the glasses, the expected thermodynamic relationship between the two states is given by:

$$\frac{U^{4+}}{\sum U} = \frac{1}{1 + 10^{\left(\frac{a}{4}\log fO_2 + \log K'\right)}} \quad (4.1)$$

where a is the number of electrons involved in the oxidation (e.g. $a = 2$ for $U^{4+} \rightarrow U^{6+}$), and logK′ is a parameter related to the melt composition, temperature, and pressure (Berry and O'Neill, 2004). This function has a sigmoidal form when $U^{4+}/\sum U$ are plotted against logfO_2, with $U^{4+}/\sum U$ varying between 0 and 1. The value of a controls the range of fO_2 over which the transition from reduced to oxidised occurs; the more electrons involved in the oxidation reaction the steeper the curve and the smaller the fO_2 range. The position of the curve relative to the fO_2 axis is controlled by logK′, where -4logK′ is the inflexion point of the sigmoid (i.e. $U^{4+}/\sum U = 0.5$). –logK′ has been defined as the electrochemical reduction potential (E_M') of a metal in a melt (Schreiber, 1987; Berry *et al*., 2006).

If the systematic changes in U L-edge spectral features result only from the changing proportions of the two valence states then they will be a linear function of $U^{4+}/\sum U$, resulting in the expression:

$$\frac{U^{4+}}{\sum U} = a_0 f + a_1 \quad (4.2)$$

where f is the spectral feature, and a_0 and a_1 are constants. Combining Equations 3.1 and 3.2 gives:

$$f = \frac{1}{a_0}\left(\frac{1}{1 + 10^{\left(\frac{a}{4}\log fO_2 + \log K'\right)}} - a_1\right) \quad (4.3)$$

For simplicity, equation 4.3 can be rewritten in the form:

$$f = \frac{b}{\left(1 + 10^{\left(\frac{a}{4}\log fO_2 + \log K'\right)}\right)} + c \qquad (4.4)$$

where $b = 1/a_0$ and $c = a_1/a_0$ are constants. The values c and b act to offset the sigmoid from zero on the y-axis, and as a stretching factor, respectively. That is, one limit of the sigmoid curve defined by Eq. 4.4 will be equal to c and the other to $c + b$.

The variation of certain features of the spectra recorded from CMAS and MORB 1 atm and 10 kbar glasses with the fO_2 of equilibration were fitted using Eq. 4.4. The spectral features were parameterised after smoothing the raw data by recreating each spectrum using a number of Gaussians functions. The purpose of this was only to remove the noise from each spectrum. Since the aim was to reproduce the spectral line-shape the number of Gaussians fitted to each spectrum was not fixed, and the choice of Gaussians over any other function for this purpose is not important. The selected features are illustrated in Fig. 4.4 and include the intensities at the energies interpreted as the U^{4+} and U^{6+} crests, the energy of the absorption edge, and the spectrum weighted average. The spectrum weighted average was defined as:

$$\bar{x} = \frac{\sum_{i=17100}^{17250} E_i I_i}{\sum_{i=17100}^{17250} I_i} \qquad (4.5)$$

where E is the incident X-ray energy, and I is the intensity of the spectrum at that energy. This was calculated using a step size of 0.5 eV over the energy range of interest.

Due to the small number of MORB 10 kbar data points across a large fO_2 range, the variation of a given spectral feature in the MORB 1 atm and 10 kbar spectra were fitted simultaneously with the constraint that the parameters b and c were the same for both datasets. This assumes that the sigmoid limits are the same, and by extension that the reduced and oxidised end-member spectra are the same, at 1 atm and 10 kbar. Simultaneous fitting was expected to have two advantages. First, it provided tighter constraints on the 10 kbar data, due to the

higher density of fO_2 values for the 1 atm samples. Second, it better constrained the oxidised limit of the 1 atm data due to the wider oxidised fO_2 coverage of the 10 kbar data points.

Simultaneous fitting of the AD 1 atm and 10 kbar data could not produce acceptable fits to the 10 kbar spectral intensity variations; the spectra of the most reduced 10 kbar samples had a white-line that was far too intense to fit concurrently with the 1 atm data. As it was not clear why this would be the case, the AD 1 atm and 10 kbar data were fitted separately. Fits to the CMAS 1 atm data were tried both including and excluding the AD 10 kbar Pt-PtO_2 ($\log fO_2$ = +4.7) data point to place some constraint on the oxidised limit of the fit. All of the resulting fit parameters are given in Table 4.2. The data points and resulting fits for most of the selected features are shown in Fig. 4.5 and 4.6.

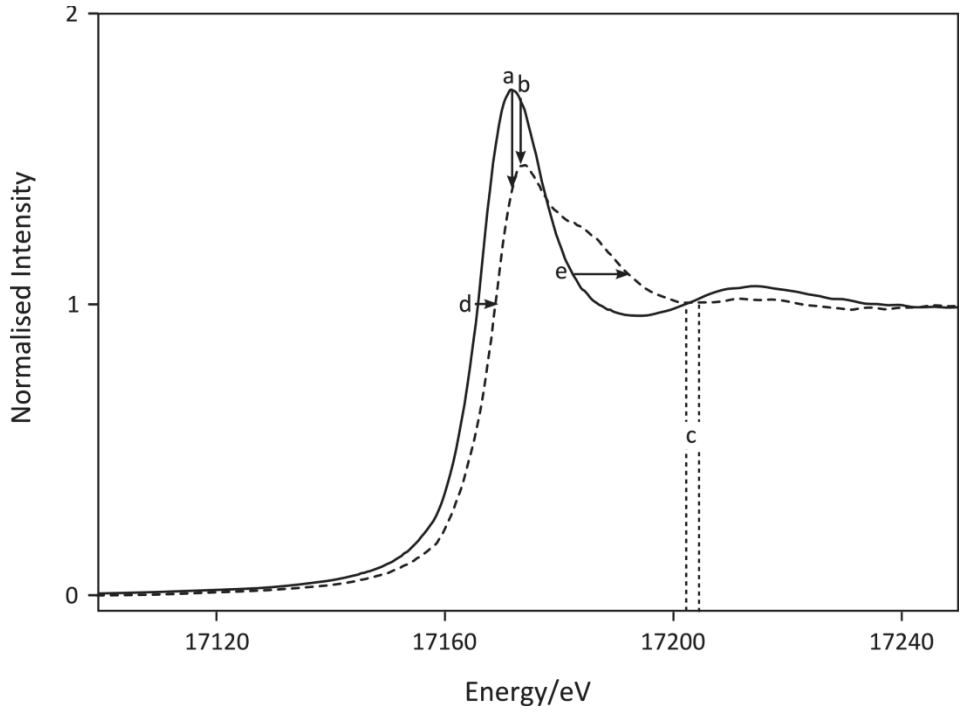


Figure 4.4: U L_3-edge XANES spectra of MORB glasses equilibrated at 1400 °C and $\log fO_2$ = -10 at 1 atm (solid line), and $\log fO_2$ = +4.7 at 10 kbar (dashed line). Key spectral features exhibit systematic variations as a function of fO_2, including (a) intensity at 17172.3 eV (approximate U^{4+} crest energy), (b) intensity at 17174.7 eV (approximate U^{6+} crest energy), (c) spectra weighted averages (calculated between 17100 and 17250 eV), (d) edge energy at a normalised-intensity of 1, and (e) post white-line energy at a normalised-intensity of 1.1.

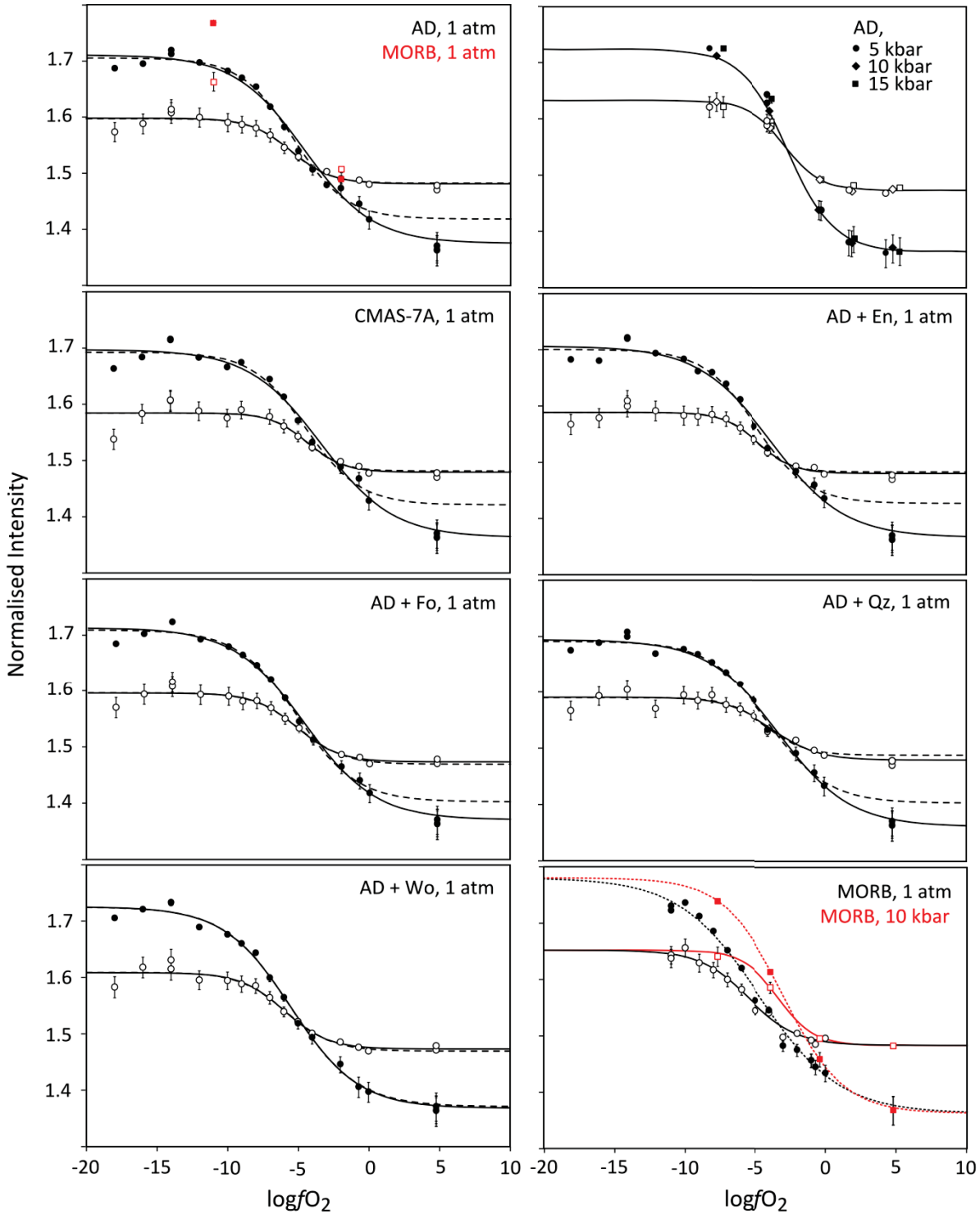


Figure 4.5: Intensity of CMAS and MORB XANES spectra at the U^{4+} (filled symbols) and U^{6+} (open symbols) crest energies (markers a and b in Fig. 4.4) as a function of fO_2 of sample equilibration. Plots show best-fit sigmoid curves (Eq. 4.4) to the 1 atm CMAS data when the AD 10 kbar Pt-PtO_2 data point was included (solid lines) and excluded (dashed lines) in the fit. Sigmoid fits to MORB U^{4+} (dotted lines) and U^{6+} (solid lines) intensities are shown in the bottom right panel. For comparison the 1 atm AD panel (top left) also shows data points for MORB 1 atm glass spectra (red squares) collected during the same session as the AD data.

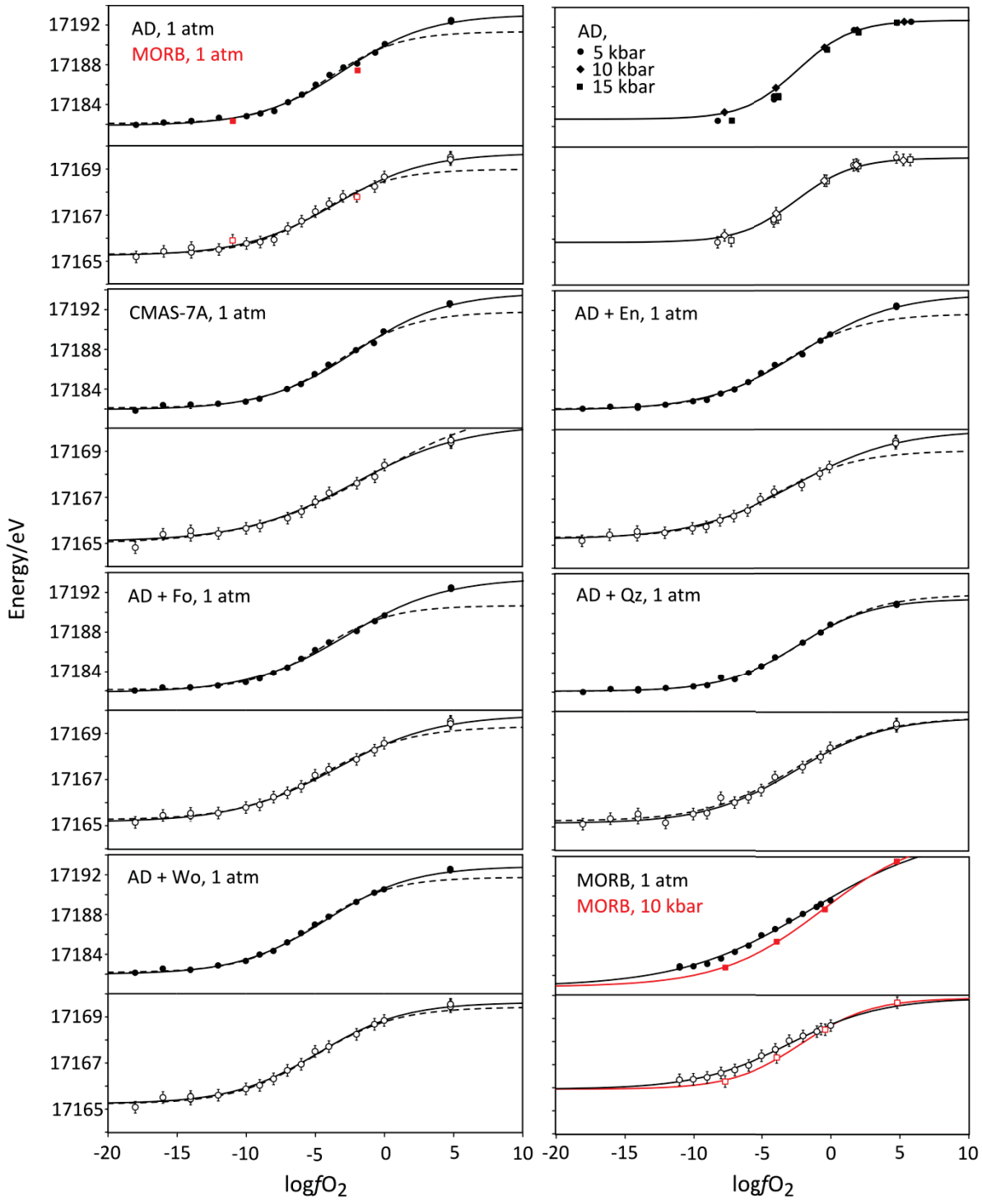


Figure 4.6: Energy of CMAS and MORB XANES spectra at a normalised intensity of 1.1 on the post white-line drop (filled symbol), and a normalised intensity of 1 on the edge rise (open symbols) (markers d and e in Fig. 4.4) as a function of fO_2 of sample equilibration. Plots show best-fit sigmoid curves (Eq. 4.4) to the 1 atm CMAS data when the AD 10 kbar Pt-PtO_2 data point was included (solid lines) and excluded (dashed lines) in the fit. For comparison the 1 atm AD panel (top left) also shows data points for MORB 1 atm glass spectra (red squares) collected during the same session as the AD data.

Table 4.2: Parameters of the single-sigmoid fits to the variation of selected spectral features as a function of $\log fO_2$ (shown in Fig. 4.4). CMAS fits both including(1) and excluding(2) the oxidised 10 kbar AD $\log fO_2 = +4.7$ data point are summarised. Values in parentheses indicate the standard error on parameters output by the fitting program (Fityk: version 0.9.8; Wojdyr, 2010).

	b	logK´	*a*/4	*c*
AD (1)				
Intensity at 17172 eV ("U^{4+} crest")	0.33 (2)	0.8 (1)	0.18 (2)	1.38 (1)
Intensity at 17174.4 eV ("U^{6+} crest")	0.12 (1)	1.7 (4)	0.31 (7)	1.48 (6)
Energy at intensity of 1 on edge rise	-4.4 (3)	0.5 (1)	0.13 (2)	17169.7 (0.2)
Energy at intensity of 1.1, post white-line	-11.1 (5)	0.42 (6)	0.14 (1)	17193.1 (4)
Weighted average	-2.1 (1)	0.7 (1)	0.15 (2)	17203.6 (1)
AD (2)				
Intensity at 17172 eV ("U^{4+} crest")	0.29 (2)	1.3 (2)	0.24 (3)	1.42 (1)
Intensity at 17174.4 eV ("U^{6+} crest")	0.11 (1)	1.8 (5)	0.32 (8)	1.482 (7)
Energy at intensity of 1 on edge rise	-3.7 (4)	0.8 (2)	0.17 (3)	17169.0 (4)
Energy at intensity of 1.1, post white-line	-9.2 (8)	0.7 (2)	0.17 (2)	17191.4 (7)
Weighted average	-1.7 (1)	1.1 (2)	0.20 (3)	17203.3 (1)
MORB				
Intensity at 17172.3 eV ("U^{4+} crest")	0.42 (2)	0.72 (7)	0.15 (1)	1.36 (1)
Intensity at 17174.7 eV ("U^{6+} crest")	0.17 (1)	1.4 (2)	0.25 (4)	1.483 (6)
Energy at intensity of 1 on edge rise	-4.0 (2)	0.39 (5)	0.13 (1)	17169.9 (2)
Energy at intensity of 1.1, post white-line	-16 (2)	0.13 (7)	0.09 (1)	17197 (1)
Weighted average	-2.1 (1)	0.56 (7)	0.14 (2)	17204.0 (1)
AD 10 kbar				
Intensity at 17172 eV ("U^{4+} crest")	0.36 (1)	0.71 (7)	0.27 (2)	1.365 (6)
Intensity at 17174.4 eV ("U^{6+} crest")	0.16 (1)	1.0 (3)	0.35 (7)	1.474 (6)
Energy at intensity of 1 on edge rise	-3.7 (2)	0.51 (8)	0.21 (3)	17169.5 (1)
Energy at intensity of 1.1, post white-line	-10.0 (2)	0.52 (2)	0.221 (7)	17192.7 (8)
Weighted average	-1.8 (1)	0.66 (8)	0.24 (3)	17203.70 (4)
MORB 10 kbar				
Intensity at 17172.3 eV ("U^{4+} crest")	0.42 (2)	0.61 (9)	0.21 (3)	1.36 (1)
Intensity at 17174.7 eV ("U^{6+} crest")	0.17 (1)	1.2 (3)	0.35 (9)	1.483 (6)
Energy at intensity of 1 on edge rise	-4.0 (2)	0.36 (7)	0.17 (2)	17169.9 (2)
Energy at intensity of 1.1, post white-line	-16 (2)	0.06 (8)	0.11 (2)	17197 (1)
Weighted average	-2.1 (1)	0.5 (1)	0.19 (3)	17204.0 (1)
CMAS-7A (1)				
Intensity at 17172 eV ("U^{4+} crest")	0.33 (3)	0.6 (1)	0.17 (3)	1.36 (2)
Intensity at 17174.4 eV ("U^{6+} crest")	0.11 (2)	1.5 (9)	0.3 (2)	1.48 (1)
Energy at intensity of 1 on edge rise	-5.1 (6)	0.2 (1)	0.11 (2)	17170.2 (5)
Energy at intensity of 1.1, post white-line	-11.7 (6)	0.27 (6)	0.13 (1)	17193.6 (5)
Weighted average	-2.3 (2)	0.4 (1)	0.12 (1)	17203.8 (1)
CMAS-7A (2)				
Intensity at 17172 eV ("U^{4+} crest")	0.27 (3)	1.0 (4)	0.23 (6)	1.42 (3)
Intensity at 17174.4 eV ("U^{6+} crest")	0.10 (2)	2 (1)	0.4 (2)	1.48 (2)
Energy at intensity of 1 on edge rise	-6 (4)	0.1 (6)	0.09 (4)	17171 (4)
Energy at intensity of 1.1, post white-line	-10 (1)	0.5 (2)	0.16 (2)	17192 (1)
Weighted average	-2.4 (8)	0.3 (4)	0.12 (4)	17203.9 (7)

	b	logK′	*a*/4	*c*
En (1)				
Intensity at 17172 eV ("U^{4+} crest")	0.34 (2)	0.6 (1)	0.17 (2)	1.37 (2)
Intensity at 17174.4 eV ("U^{6+} crest")	0.109 (8)	1.7 (5)	0.35 (9)	1.481 (7)
Energy at intensity of 1 on edge rise	-4.8 (3)	0.29 (8)	0.12 (1)	17170.0 (3)
Energy at intensity of 1.1, post white-line	-11.8 (5)	0.27 (5)	0.130 (8)	17193.7 (4)
Weighted average	-2.2 (1)	0.5 (1)	0.13 (1)	17203.7 (1)
En (2)				
Intensity at 17172 eV ("U^{4+} crest")	0.27 (2)	1.1 (3)	0.23 (4)	1.43 (2)
Intensity at 17174.4 eV ("U^{6+} crest")	0.11 (1)	1.8 (7)	0.4 (2)	1.484 (8)
Energy at intensity of 1 on edge rise	-3.8 (6)	0.6 (2)	0.15 (3)	17169.1 (5)
Energy at intensity of 1.1, post white-line	-10 (1)	0.5 (1)	0.15 (2)	17191.7 (9)
Weighted average	-1.7 (2)	0.8 (2)	0.17 (3)	17203.4 (1)
Fo (1)				
Intensity at 17172 eV ("U^{4+} crest")	0.34 (2)	0.8 (1)	0.17 (2)	1.37 (1)
Intensity at 17174.4 eV ("U^{6+} crest")	0.123 (9)	1.5 (4)	0.30 (7)	1.474 (7)
Energy at intensity of 1 on edge rise	-4.6 (3)	0.42 (7)	0.12 (1)	17169.8 (2)
Energy at intensity of 1.1, post white-line	-11.7 (6)	0.34 (6)	0.123 (9)	17193.5 (5)
Weighted average	-2.2 (1)	0.6 (1)	0.13 (1)	17203.7 (1)
Fo (2)				
Intensity at 17172 eV ("U^{4+} crest")	0.31 (2)	1.1 (2)	0.21 (3)	1.40 (2)
Intensity at 17174.4 eV ("U^{6+} crest")	0.13 (1)	1.4 (5)	0.28 (8)	1.47 (1)
Energy at intensity of 1 on edge rise	-4.0 (5)	0.6 (2)	0.14 (2)	17169.3 (4)
Energy at intensity of 1.1, post white-line	-8.6 (5)	0.8 (1)	0.17 (1)	17190.7 (4)
Weighted average	-1.9 (1)	0.9 (1)	0.16 (2)	17203.4 (1)
Qz (1)				
Intensity at 17172 eV ("U^{4+} crest")	0.33 (2)	0.56 (9)	0.17 (2)	1.36 (1)
Intensity at 17174.4 eV ("U^{6+} crest")	0.11 (1)	1.0 (4)	0.27 (8)	1.48 (1)
Energy at intensity of 1 on edge rise	-4.6 (4)	0.3 (1)	0.13 (2)	17169.8 (3)
Energy at intensity of 1.1, post white-line	-10.8 (4)	0.38 (5)	0.161 (9)	17193.1 (3)
Weighted average	-2.2 (1)	0.5 (1)	0.14 (1)	17203.8 (1)
Qz (2)				
Intensity at 17172 eV ("U^{4+} crest")	0.29 (3)	0.8 (2)	0.21 (3)	1.40 (3)
Intensity at 17174.4 eV ("U^{6+} crest")	0.10 (2)	1.3 (8)	0.3 (1)	1.49 (2)
Energy at intensity of 1 on edge rise	-5 (1)	0.4 (4)	0.14 (4)	17170 (1)
Energy at intensity of 1.1, post white-line	-11 (2)	0.3 (2)	0.16 (2)	17194 (2)
Weighted average	-2.2 (5)	0.5 (3)	0.14 (3)	17203.8 (4)
Wo (1)				
Intensity at 17172 eV ("U^{4+} crest")	0.36 (1)	1.0 (1)	0.18 (2)	1.37 (1)
Intensity at 17174.4 eV ("U^{6+} crest")	0.14 (1)	1.7 (4)	0.28 (6)	1.473 (7)
Energy at intensity of 1 on edge rise	-4.4 (2)	0.67 (8)	0.14 (1)	17169.6 (1)
Energy at intensity of 1.1, post white-line	-10.9 (3)	0.59 (5)	0.140 (7)	17192.8 (2)
Weighted average	-2.1 (1)	0.9 (1)	0.16 (2)	17203.6 (1)
Wo (2)				
Intensity at 17172 eV ("U^{4+} crest")	0.35 (2)	1.0 (2)	0.19 (2)	1.37 (2)
Intensity at 17174.4 eV ("U^{6+} crest")	0.14 (1)	1.6 (4)	0.27 (7)	1.47 (1)
Energy at intensity of 1 on edge rise	-4.2 (4)	0.7 (2)	0.15 (2)	17169.4 (3)
Energy at intensity of 1.1, post white-line	-9.6 (4)	0.81(7)	0.164 (9)	17191.7 (3)
Weighted average	-2.0 (1)	1.0 (2)	0.17 (2)	17203.5 (1)

The slopes (a/4) and logK′ values of sigmoid fits to the 1 atm data vary across the features fitted. The intensity variation at the "U^{6+} crest" energy produced the steepest curves with a/4 values within uncertainty of 0.25. The fits to the 10 kbar spectral variations were steeper than the equivalent 1 atm curves for both MORB and AD, and in the case of AD were close to a/4 = 0.25 for most of the features. MORB 10 kbar sigmoids were shallower (smaller values of a/4) than the equivalent AD sigmoids; this relationship was also observed for the MORB 1 atm fits relative to many of the CMAS 1 atm fits.

The values of b obtained from the 1 atm MORB "U^{4+}" and "U^{6+}" intensity fits are larger than those of the equivalent 1 atm AD (and other CMAS) fits; b = 0.42 and 0.17 for MORB, U^{4+} and U^{6+} intensities, respectively, compared to b = 0.33 and 0.12 for AD. These differences are significant when we consider that b represents the total range of intensity values between the reduced and oxidised end-members. Thus, the fit range of AD intensity values are reduced by ~ 20 % at the U^{4+} crest, and 30 % at the U^{6+} crest, compared to the MORB ranges.

The differences in magnitudes of the intensity ranges between 1 atm MORB and CMAS spectra does not appear to be an artefact of the slightly different constraints used to fit the MORB vs. CMAS data, i.e. that the MORB 1 atm and 10 kbar data were fitted simultaneously, and does result from the fact that the MORB and CMAS datasets were collected during different beamtimes. Data points from spectra collected from MORB composition glasses, equilibrated at log$f$O$_2$ = -11 and -2, during the same session as the Fe-free CMAS glasses are shown with the AD data in the top left panel of Fig. 4.5. The MORB log$f$O$_2$ = -11 points have significantly higher intensities than the most reduced AD data.

Figure 4.7 shows the correlation between the maximum intensity and corresponding energy of the white-line for samples equilibrated at different fO_2s. The energies of all the MORB

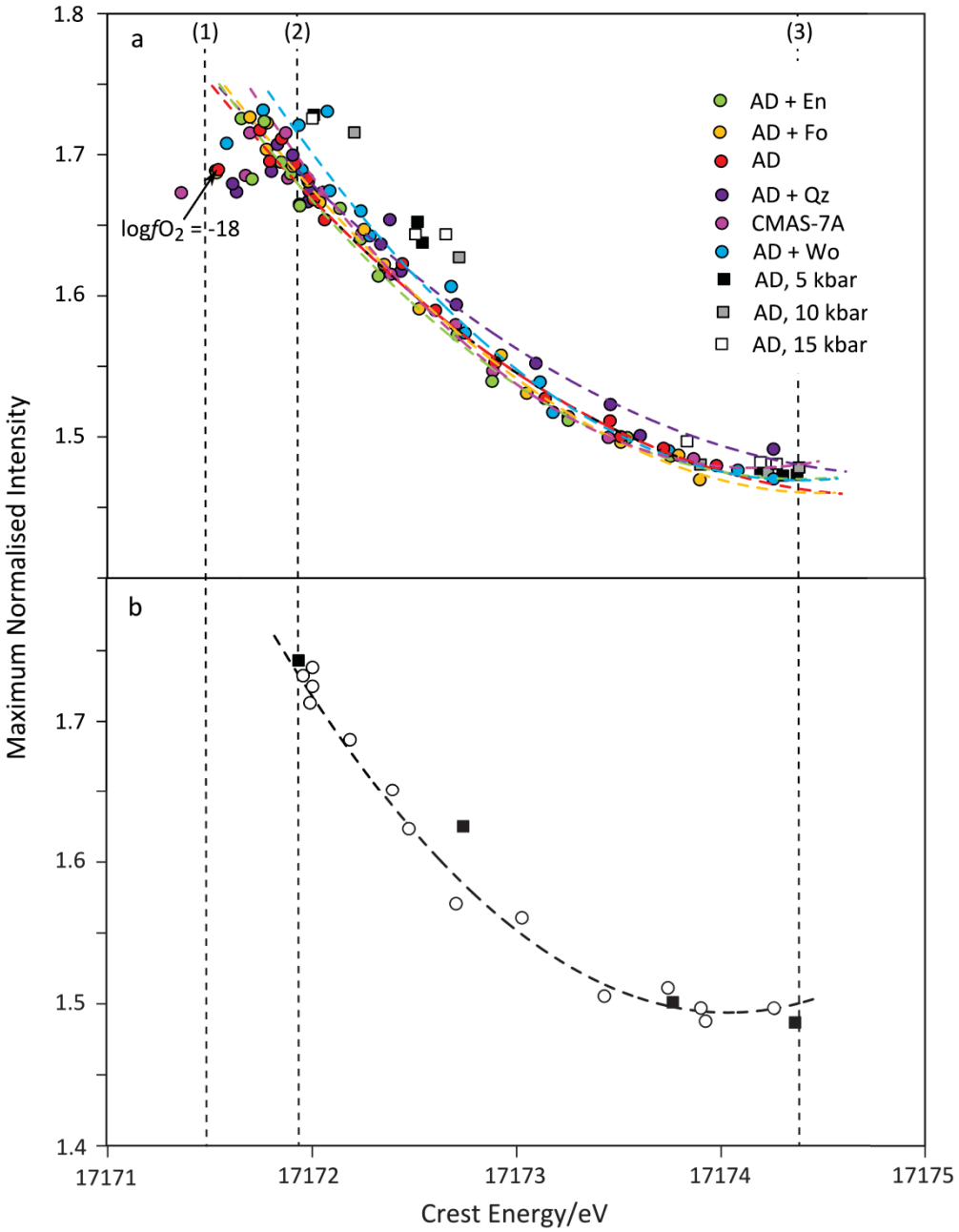


Figure 4.7: White-line crest intensity as a function of crest energy of U L_3-edge XANES spectra from (a) CMAS, and (b) MORB 1 atm (open circles) and 10 kbar (closed squares), glasses. Polynomial fits (of order 2) to data points that correspond to samples equilibrated between logfO_2 = 0 and -9 are shown. Dashed lines indicate (1) the reduced limit of the CMAS data, (2) the reduced limit of the MORB data, and (3) the oxidised limit of the CMAS and MORB data.

data points, whose spectra were collected during a different session to the CMAS compositions, were shifted by an equal amount so that the spectra of the calibration samples (those collected during both sessions) were aligned.

The energy spread of the CMAS 1 atm data is significantly larger than that of the MORB, with CMAS points extending to lower energy values relative to MORB (between dashed lines 1 and 2 in Fig. 4.7). This region of the plot corresponds to the most reduced AD glasses ($\log fO_2$ = -16 and -18), well beyond the $\log fO_2$ range of the MORB glasses. There is essentially no difference in the maximum energy values between MORB and CMAS data (dashed line 3). Excluding the reduced CMAS data points, MORB and CMAS data exhibit very similar curved trends (Fig. 4.7: between markers 2 and 3); a steep negative gradient at lower energy values which flattens out at higher energies. In other words, the spectra of the reduced samples are characterised by a relatively large decrease in crest intensity and increase in crest energy with increasing fO_2, whilst oxidised spectra continue to shift to higher energy with increasing fO_2, but with little change in crest intensity. The energy range of the most reduced CMAS spectra corresponds to an abrupt change in trend within the CMAS data, from a strongly negative to a broadly positive gradient. No such feature was observed in the MORB data.

4.4 Preliminary discussion and conclusions

The variation of the L_3-edge spectral features certainly does not indicate a two-electron reaction (i.e. $U^{4+} \rightarrow U^{6+}$), as we would expect sigmoid slopes of $a/4 = 0.5$. Sigmoid fits are also generally too shallow to be consistent with a simple one-electron process ($a/4 = 0.25$). The unexpectedly low values of $a/4$ in the 1 atm and 10 kbar fits, and the large variation of $a/4$ and logK´ values, suggests a non-linear relationship between different spectral features.

One reason for this may be the presence of more than two U oxidation states. In this case the slope of the single sigmoid fit to a particular spectral feature will be controlled by the variation of that feature between the three, or more, oxidation-state "end-member" components.

The curved correlations between spectra crest intensities and energies (Fig. 4.7) also indicate more complex systems than mixtures of two U end-member spectral line-shapes. The trends exhibited by all the datasets suggest at least three components, one with an intense white-line at lower energy, and two with less intense white-lines at higher energies. The two higher energy components must have similar intensities but be shifted relative to each other in energy.

The cause of the change in the crest intensity-energy trend for the most reduced CMAS glasses is unclear. A decrease in the crest intensity of the most reduced glasses is consistent with the observed beam damage. However, the offset in spectral intensities between reduced CMAS and MORB spectra (Fig. 4.5) could also be explained by the presence of an additional reduced U component in the Fe-free glasses, whose white-line crest has a lower intensity and lower energy than the other three components. The U M_4-edge data, discussed in the previous chapter, indicated that MORB and AD glasses must contain three and four components, respectively. The interpretation of spectra at the L_3-edge is consistent with these conclusions.

The variation of the single-sigmoid fits logK′ values for each spectral feature between the six CMAS compositions exhibit broadly positive correlations with optical basicity (Duffy, 1993), with the exception of the AD+Qz composition (Λ = 0.559), as shown in Fig. 4.8. This suggests that composition does influence U oxidation state equilibrium in melts, and that

higher basicity melts stabilise higher U oxidation states; this is consistent with the results of similar studies of Cr (Berry *et al.*, 2006) and Ce (Burnham and Berry, 2014). However, two-state models are not appropriate for the accurate quantification of the role of composition in these glasses.

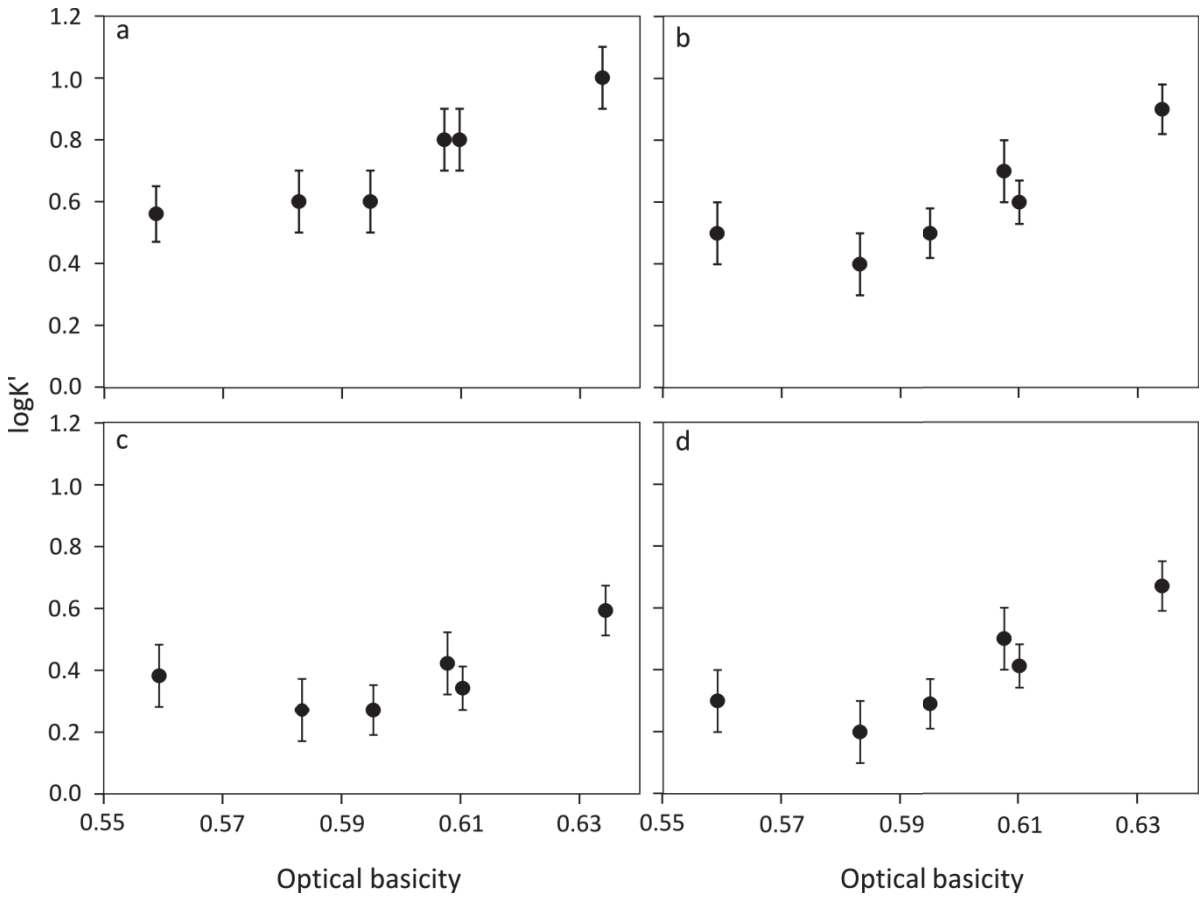


Figure 4.8: logK′ values as a function of optical basicity, from single-sigmoid fits to the variation of the (a) U^{4+} crest intensity, (b) spectrum weighted average (calculated between 17100 and 17250 eV), (c) post white-line energy at a normalised intensity of 1.1, and (d) edge-energy at a normalised intensity of 1, of U L_3-edge XANES spectra of CMAS composition glasses. Error bars indicate the uncertainties in logK′ values, as quoted in Table 4.2.

Chapter 5:

Quantification of U oxidation states in silicate glasses using L_3- and M_4-edge XANES spectra

5.1 Introduction

Both the U L_3- and M_4-edge XANES spectra of CMAS and MORB composition glasses show that the U oxidation state variation as a function of fO_2 does not correspond to a simple two-state system. MORB M_4-edge XANES spectra can be reproduced by linear combinations of three line-shapes, whose edge-energies, and relative proportions as a function of fO_2 are consistent with U^{4+}, U^{5+}, and U^{6+}. AD glasses are even more complex requiring at least four U components to explain the M_4-edge spectral variation over the whole fO_2 range; L_3-edge spectra suggest that this is the case for all Fe-free compositions. Quantifying U oxidation state proportions in reduced CMAS glasses may be further complicated by their susceptibility to significant beam damage.

5.2 Modelling U oxidation state proportions in MORB glasses

The MORB glasses were considered first, as they represent a simpler system than the CMAS glasses, and they did not exhibit any evidence of beam damage. If the variation of the MORB L_3- and M_4-edge spectral features with fO_2 results from both the $U^{4+} \rightarrow U^{5+}$ and $U^{5+} \rightarrow U^{6+}$ reactions then the data, rather than defining a single sigmoid, is expected to represent a combination of two sigmoid functions given by:

$$A = \frac{U^{4+}}{U^{4+} + U^{5+}} = \frac{1}{1 + 10^{(0.25\log fO_2 + \log K_A')}} \quad (5.1)$$

$$B = \frac{U^{5+}}{U^{5+} + U^{6+}} = \frac{1}{1 + 10^{(0.25\log fO_2 + \log K_B')}} \quad (5.2)$$

where:

$$U^{4+}+U^{5+}+U^{6+} = \Sigma U = 1 \tag{5.3}$$

Rearrangement of Eq. 5.1 and 5.2 gives expressions for U^{5+} in terms of *A* and U^{4+}, and U^{6+} in terms of U^{5+} and *B*. Substitution of the former into the latter gives expressions for U^{5+} and U^{6+} in terms of U^{4+}, *A*, and *B*, which can be substituted into Eq. 5.3. From the derived U^{5+}, U^{6+} and $\sum U$ expressions the proportion of each valence state can be expressed as a function of *A* and *B*:

$$U^{4+} = \frac{1}{\left(1 + \left(\frac{1-A}{A}\right) + \left(\frac{1-A}{A}\right)\left(\frac{1-B}{B}\right)\right)} \tag{5.4}$$

$$U^{5+} = \frac{\left(\frac{1-A}{A}\right)}{\left(1 + \left(\frac{1-A}{A}\right) + \left(\frac{1-A}{A}\right)\left(\frac{1-B}{B}\right)\right)} \tag{5.5}$$

$$U^{6+} = \frac{\left(\frac{1-A}{A}\right)\left(\frac{1-B}{B}\right)}{\left(1 + \left(\frac{1-A}{A}\right) + \left(\frac{1-A}{A}\right)\left(\frac{1-B}{B}\right)\right)} \tag{5.6}$$

which can be simplified to:

$$U^{4+} = \frac{1}{\left(1 + \frac{1}{AB} - \frac{1}{B}\right)} \tag{5.7}$$

$$U^{5+} = \frac{1-A}{\left(A + \frac{1}{B} - \frac{A}{B}\right)} \tag{5.8}$$

$$U^{6+} = \frac{(1-A)(1-B)}{(1+AB-A)} \tag{5.9}$$

Taking a spectral feature that is summed during end-member spectra mixing, such that:

$$i_{mixed} = U^{4+}I_{U^{4+}} + U^{5+}I_{U^{5+}} + U^{6+}I_{U^{6+}} \tag{5.10}$$

we obtain:

$$i_{mixed} = \left(\frac{I_{U^{4+}}}{\left(1+\frac{1}{AB}-\frac{1}{B}\right)}\right) + \left(\frac{(1-A)I_{U^{5+}}}{\left(A+\frac{1}{B}-\frac{A}{B}\right)}\right) + \left(\frac{(1-A)(1-B)I_{U^{6+}}}{(1+AB-A)}\right) \quad (5.11)$$

where i_{mixed} is the value of the feature in a particular spectrum, and I_{U^*} is the value of that feature in the pure U* spectrum. The values of $I_{U^{4+}}$ and $I_{U^{6+}}$ correspond to the reduced and oxidised limits of the two-sigmoid curve respectively.

5.2.1 MORB Model Part 1

5.2.1.1 Methodology

Accepting that the XANES spectra were normalised correctly, the variation of the spectral intensities as a function of logfO_2 at a single energy value is expected to be described by equation 5.11. The variation of L_3-edge spectral intensities at 17172.3 eV, interpreted as the energy of the U^{4+} crest, was taken as a trial case. This feature was previously fitted using a single sigmoid function, as discussed in Chapter 4 and shown in Fig. 5.1.

The values of $I_{U^{4+}}$, $I_{U^{5+}}$, and $I_{U^{6+}}$were defined prior to fitting. Values of $I_{U^{4+}}$ and $I_{U^{6+}}$ were chosen to match the limits of the combined 1 atm and 10 kbar single sigmoid fits to the same feature (Fig. 5.1), which were determined from the parameters *b* and *c* given in the MORB section of Table 4.2. Based on the continual decrease of spectra intensities at 17172.3 eV from the reduced to oxidised glasses, the intensity of the pure U^{5+} spectrum at this energy, $I_{U^{5+}}$, must lie somewhere between the $I_{U^{4+}}$ and $I_{U^{6+}}$ values. The average of $I_{U^{4+}}$ and $I_{U^{6+}}$ was considered to be a reasonable starting estimate. Thus, the I_{U^*} parameters of Eq. 5.11 were defined as:

$$I_{U^{4+}} = b + c = 1.78 \quad (5.12)$$

$$I_{U^{6+}} = c = 1.36 \quad (5.13)$$

$$I_{U^{5+}} = \frac{2c + b}{2} = 1.57 \tag{5.14}$$

The intensities of 1 atm and 10 kbar spectra at 17172.3 eV as a function of fO_2 were then fitted separately using Eq. 5.11, with Eq. 5.1 and 5.2 substituted for the parameters *A* and *B*, respectively. The I_{U^*} values were substituted for those given by Eq. 5.12-5.14 and the two logK′ values were free to vary. The impact of using different values of $I_{U^{5+}}$ in Eq. 5.11 was also investigated; values of $I_{U^{5+}}$ = 1.70 or $I_{U^{5+}}$ = 1.44, i.e. close to the values of $I_{U^{4+}}$ = 1.78 or $I_{U^{6+}}$ = 1.36, were trialled. The parameters $I_{U^{4+}}$ and $I_{U^{6+}}$ were not changed.

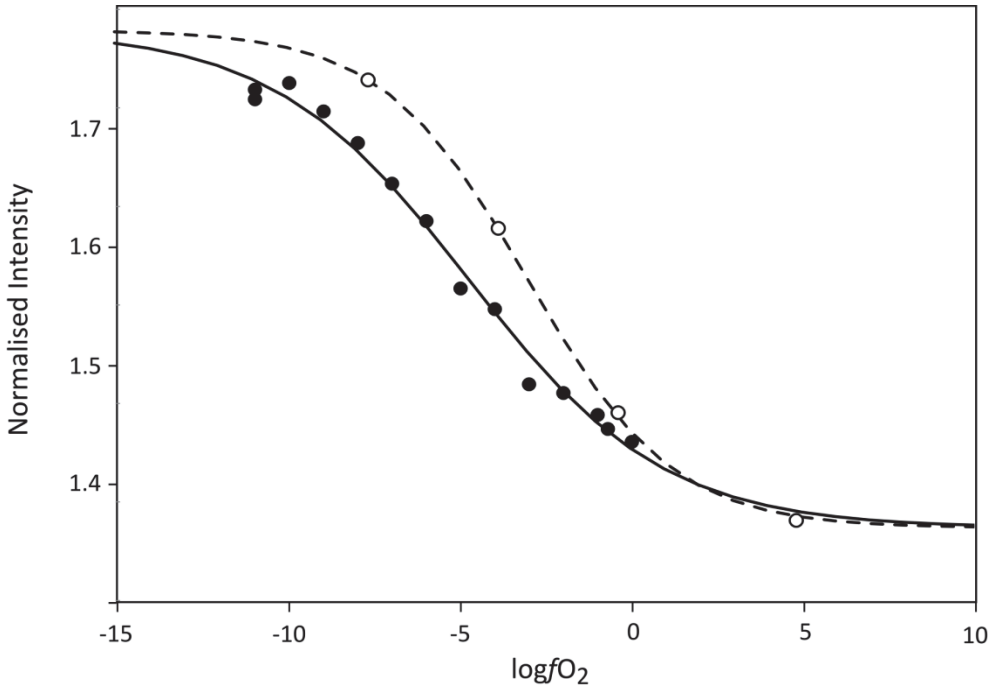


Figure 5.1: Normalised intensities at 17172.3 eV of U L_3-edge XANES spectra of MORB 1 atm (filled circles) and 10 kbar (open circles) glasses as a function of fO_2 at 1400 °C. The best-fit single-sigmoid curves (with *a*/4 as a variable) to 1 atm (solid line) and 10 kbar (dashed line) data are shown.

5.2.1.2 Results

The curves produced from various $logK_A'$ and $logK_B'$ combinations are shown in Fig. 5.2(a). The curves are for illustrative purposes only, and show how the model function may vary in shape; the hypothetical logK′ values are within the range reported for multivalent elements in

silicate melts (Schreiber, 1987). The best-fit curves to the 1 atm and 10 kbar data using the different $I_{U^{5+}}$ values are shown in Fig. 5.2(b), and the fit parameters are given in Table 5.1.

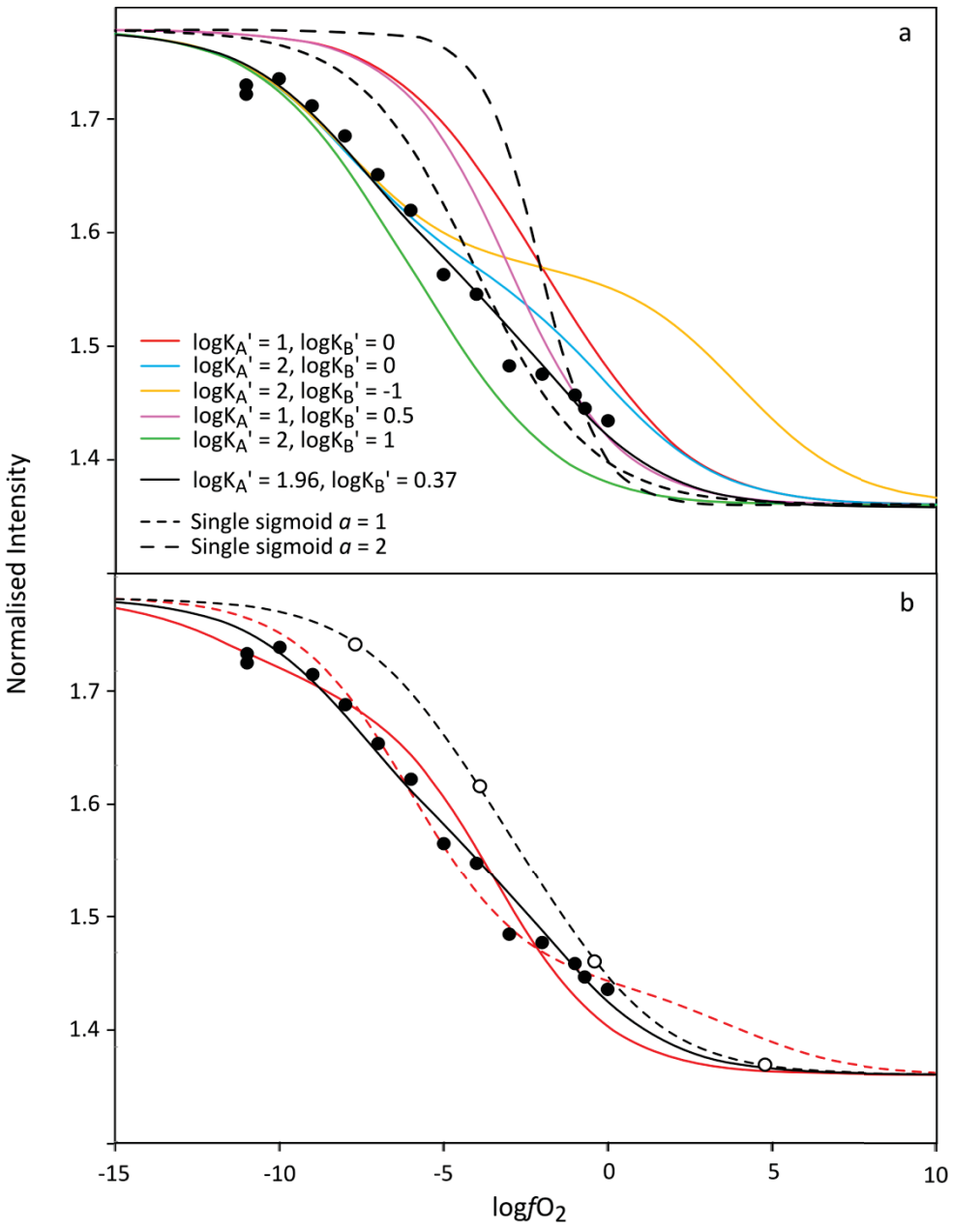


Figure 5.2: Two-sigmoid model curves ($U^{4+}\rightarrow U^{5+}$, $a/4$ = 0.25 and $U^{5+}\rightarrow U^{6+}$, $a/4$ = 0.25) of MORB L_3-edge spectra intensities at 17172.3 eV from (a) various $logK_A'$ and $logK_B'$ combinations, and (b) the best-fit logK′ values for 1 atm (filled circles) and 10 kbar (open circles) data, with $I_{U^{4+}}$ = 1.78 and $I_{U^{6+}}$ = 1.36, and $I_{U^{5+}}$ = 1.57 (black lines). Best-fit curves are also shown in (b) for 1 atm data when $I_{U^{5+}}$ = 1.70 (solid red line), or $I_{U^{5+}}$ = 1.44 (dashed red line).

Table 5.1: Parameters obtained from two-sigmoid fits to MORB spectral intensities at 17172.3 eV with $I_{U^{4+}}$ = 1.78, $I_{U^{6+}}$ = 1.36, and three different $I_{U^{5+}}$ values. *StDev* gives the standard deviation of the difference between the data points and fit values on the intensity/y-axis.

	MORB 1 atm				MORB 10 kbar			
$I_{U^{5+}}$	$\log K_A'$	$\log K_B'$	R^2	*StDev*	$\log K_A'$	$\log K_B'$	R^2	*StDev*
1.44	1.50 (5)	-1.0 (7)	0.976	0.0158	0.94 (3)	-0.4 (1)	0.999	0.0050
1.57	1.96 (5)	0.37 (5)	0.988	0.0132	1.25 (2)	0.22 (2)	1.000	0.0016
1.70	2.9 (3)	0.86 (6)	0.964	0.0228	1.9 (2)	0.54 (4)	0.998	0.0070

The logK′ values obtained from the three choices of $I_{U^{5+}}$ vary widely. This suggests that U proportions cannot be accurately quantified without more knowledge of the U^{5+} line-shape. However, certain choices of $I_{U^{5+}}$ provide better fits to the 1 atm data than others, for example, setting $I_{U^{5+}}$ =1.70 results in a relatively poor fit. Fits to the 10 kbar data are excellent in all cases.

5.2.1.3 Conclusions

Modelling the intensity data in this way was limited by the user defined values of $I_{U^{4+}}$, $I_{U^{5+}}$, and $I_{U^{6+}}$. Choosing different values changed the best-fit logK′s, and hence the U oxidation state proportions estimated. A poor fit to the 1atm data using pre-defined values indicates that the choice of one, or more, of the values was incorrect. This, in turn, suggests that the optimum values of $I_{U^{4+}}$, $I_{U^{5+}}$, and $I_{U^{6+}}$ can be obtained by allowing them all to vary freely during fitting; these optimum fit values are expected to correspond to the true values. Consistently good fits to the 10 kbar data, regardless of the choice of $I_{U^{5+}}$, are attributed to the small size of this dataset.

5.2.2 MORB Model Part 2

5.2.2.1 Methodology

The intensity variation of the MORB L_3-edge spectra at 17172.3 eV as a function of logfO_2 was re-fitted whilst allowing all parameters, $I_{U^{4+}}$, $I_{U^{5+}}$, $I_{U^{6+}}$, logK_A', and logK_B', to vary freely. Fitting was carried out using "Fityk" an open source curve fitting program (version 0.9.8; Wojdyr, 2010), which allows users to define their own functions for fitting data. Spectral intensity variations at four other energies, illustrated in Fig. 5.3, were also fitted. The energy values were chosen to cover the main spectral features and a range of relationships between the three oxidation state end-members (i.e. changes in intensity ordering, and different magnitudes of intensity offsets between end-members); this allowed comparison of the logK' values obtained from different spectral features.

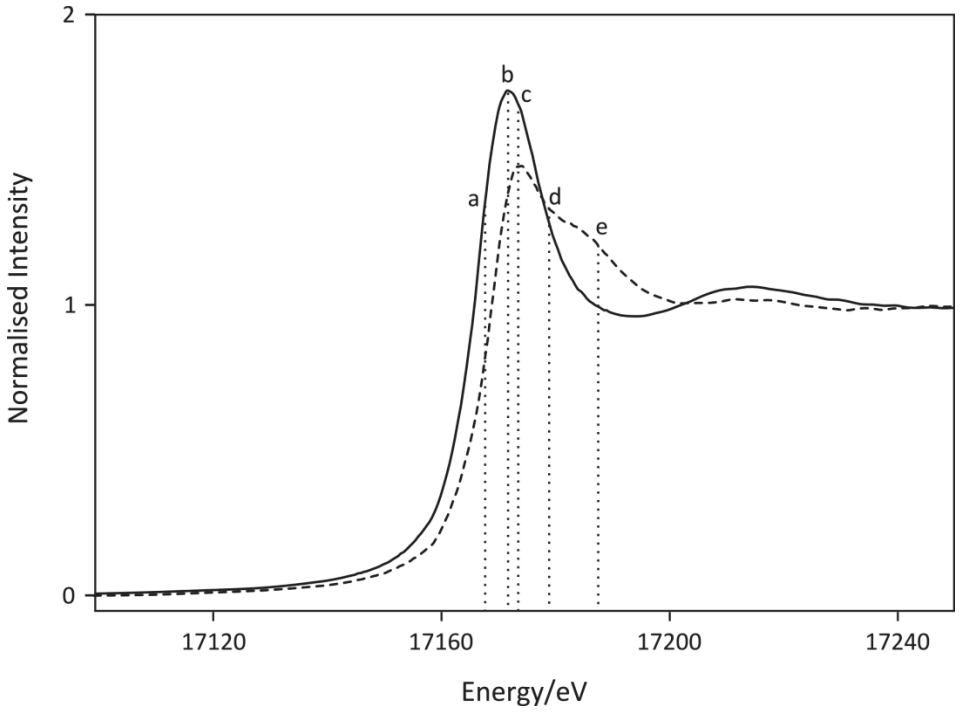


Figure 5.3: U L_3-edge XANES spectra of MORB glasses equilibrated at 1400 °C and logfO_2 = -10 at 1 atm (solid line), and logfO_2 = +4.7 at 10 kbar (dashed line). Energies are marked by dotted lines at (a) 17168 eV, (b) 17172.3 eV, (c) 17174.7 eV, (d) 17179.5 eV, and (e) 17187.5 eV.

The 1 atm and 10 kbar data were fit simultaneously with the constraint that:

$$I_{U^*\mathrm{E},\ 1\,\mathrm{atm}} = I_{U^*\mathrm{E},\ 10\,\mathrm{kbar}} \tag{5.15}$$

where E denotes the energy value of the intensity variation being fitted. This effectively states that the three pure U oxidation state spectra have the same shape at 1 atm and 10 kbar. This provided tighter constraints on the fit parameters, as there was a higher density of fO_2 values for the 1 atm samples, whilst the 10 kbar data increased the upper limit of the fO_2 coverage. Although this was an assumption it was considered to be a better approach than including a single 10 kbar data point ($\log fO_2 = +4.7$) in the 1 atm fits to constrain the oxidised limits, as this would have to include an additional assumption about at what $\log fO_2$ the U oxidation state proportions at 1 atm would be equal to those present in the 10 kbar glass.

5.2.2.2 Results

The fit parameters obtained from the spectral intensity variation at five energies are given in Table 5.2. The sets of four logK´ values, two for 1 atm data and two for 10 kbar data, are largely within uncertainty for all five energies. However, many of the logK´ values have a large uncertainty associated with them; the $\log K_B'$ values are particularly poorly defined.

5.2.2.3 Conclusions

Fitting the 1 atm and 10 kbar data in tandem placed some constraint on the oxidised limits of the 1 atm fits without assuming that the most oxidised ($\log fO_2 = +4.7$) 10 kbar glass is the U^{6+} end-member. The large uncertainties in the fit derived $\log K_B'$ values are interpreted to result from the low data coverage for extremely oxidising conditions, but may also reflect the relatively small differences in U oxidation-end-member intensities at some of the selected energy values. The consistency of the logK´ value sets between the two-sigmoid fits to the intensity variations of the L_3-edge spectra at different energies suggests that there is a set of

four logK′ values that can produce good fits to the spectral intensity variations at all energies for the 1 atm and 10 kbar data.

Table 5.2: Parameters obtained from two-sigmoid fits to MORB L_3-edge XANES spectral intensities as a function of logfO_2 at different set energies. Letters in parentheses correspond to the energy labels in Fig. 5.3.

Energy	$\log K_A'$	$\log K_B'$	$I_{U^{4+}}$	$I_{U^{5+}}$	$I_{U^{6+}}$
MORB 1 atm					
17168 eV (edge-rise, a)	1.35 (8)	-0.5 (3)	1.337 (7)	0.93 (3)	0.73 (1)
17172.3 eV (U^{4+} peak, b)	1.45 (8)	-0.3 (4)	1.751 (5)	1.46 (3)	1.36 (1)
17174.7 eV (U^{6+} peak, c)	1.5 (7)	1 (1)	1.651 (8)	1.6 (2)	1.485 (6)
17179.5 eV (post-edge shoulder, d)	1.3 (1)	-1 (1)	1.260 (4)	1.41 (2)	1.3 (1)
17187.5 (post-edge shoulder, e)	1.34 (6)	-0.5 (1)	0.991 (1)	1.123 (8)	1.250 (6)
MORB 10 kbar					
17168 eV (edge-rise, a)	0.89 (7)	-0.2 (2)	1.337 (7)	0.93 (3)	0.73 (1)
17172.3 eV (U^{4+} peak, b)	0.85 (8)	-0.2 (2)	1.751 (5)	1.46 (3)	1.36 (1)
17174.7 eV (U^{6+} peak, c)	0.6 (4)	1.0 (9)	1.651 (8)	1.6 (2)	1.485 (6)
17179.5 eV (post-edge shoulder, d)	0.9 (1)	-1 (2)	1.260 (4)	1.41 (2)	1.3 (1)
17187.5 (post-edge shoulder, e)	0.87 (6)	-0.5 (1)	0.991 (1)	1.123 (8)	1.250 (6)

5.2.3 MORB Model Part 3.1

5.2.3.1 Methodology

As in Part 2 (section 5.2.2), the intensity variation of the MORB L_3-edge spectra at set energies as a function of logfO_2 was fitted whilst allowing the parameters $I_{U^{4+}}$, $I_{U^{5+}}$, $I_{U^{6+}}$, $\log K_A'$, and $\log K_B'$ to vary, and with the constraint expressed by Eq. 5.15 linking 1 atm and 10 kbar fits. However, for a given fO_2 dataset, the values of $\log K_A'$ and $\log K_B'$ are expected to be constant regardless of the feature/energy being fitted. Therefore, rather than considering each energy point of the spectra separately, the $\log K_A'$ and $\log K_B'$ values were constrained to be the same for all fits of the same pressure set, such that:

$$\log K_{AE1,\ 1\ atm}' = \log K_{AE2,\ 1\ atm}' = \log K_{AE3,\ 1\ atm}' = \ldots\ldots \quad (5.16)$$

$$\log K_{BE1,\ 1\ atm}' = \log K_{BE2,\ 1\ atm}' = \log K_{BE3,\ 1\ atm}' = \ldots.. \quad (5.17)$$

Many single energy fits were then run simultaneously to obtain the optimum logK′ values. The intensity variations of MORB L_3-edge spectra as a function of logfO_2 were fitted at 45 different energy values; over the energy range 17168-17190 eV (between lines (a) and (e) in Fig. 5.3), with a step size of 0.5 eV. 1 atm and 10 kbar fits were run together, resulting in a total of 90 fits, 45 for 1 atm data and 45 for 10 kbar data, being run simultaneously to produce a total of four logK′ values, and 45 sets of three I_{U^*} values, which correspond to the intensities of the U^{4+}, U^{5+}, and U^{6+} spectra at each energy. The energy range was limited compared to the total data collection range to ensure that the differences between the intensities of the end-member spectra would be reasonably large.

The intensity variations of the MORB M_4-edge spectra at set energies were also fitted using the same methodology. 1 atm and 10 kbar fits were run simultaneously for 70 different energy values; over the energy range 3725-3728.45 eV, with a step size of 0.05 eV (a total of 140 fits), resulting in a total of four logK′ values and 70 sets of three I_{U^*} values. The constraint that the U oxidation state spectra have the same line-shape at 1 atm and 10 kbar (Eq. 5.15) was established as a reasonable assumption for the M_4-edge spectra in section 3.3.3 of this thesis.

In previous sections, the uncertainty associated with each logK′ has been quoted as the standard error output by the fitting program. However, these values represent the precision of the fits rather than the true uncertainty on logK′; they are a measure of how well the model fits the data, and do not account for uncertainty within the data or erroneous data points. In this section the logK′ values and their associated uncertainty were estimated by running the

same fitting procedure many times with different logfO_2 data points included/excluded. The average logK´s and their standard deviations are reported.

5.2.3.2 Results

The logK´ values determined from the multi-energy fits of the L_3- and M_4-edge spectral intensities are given in Table 5.3. A subset of the resulting fits to the L_3- and M_4-edge data are shown in Fig. 5.4 and Fig. 5.5; these fits effectively show the variation in the relative intensities of the three oxidation state end-members as a function of energy. Thus, the seemingly anomalous shape of the fits in panels 5.4(d) and 5.5(c) simply indicate that the intensity of the pure U^{5+} spectrum at this energy is greater than both the U^{4+} and U^{6+} spectra. The logK´ sets derived from fitting the L_3- and M_4-edge data are expected to be the same. In the case of the 1 atm data, the logK´ values are identical within uncertainty. For the 10 kbar data the $logK_A'$ values are almost within uncertainty, however, the $logK_B'$ exhibit a much larger variation, with values of -0.29 and -0.53. This is unsurprising given the small number of 10 kbar data points, and the poor data coverage in the oxidised limits of both the 1 atm and 10 kbar fits, which corresponds to most of the $U^{5+} \rightarrow U^{6+}$ transition. The inclusion/exclusion of various data point combinations, such as those samples that were allowed an exceptionally short time (~4 h) to equilibrate (logfO_2 = 0, -3, -5, -7: section 2.2.1.1), had little effect on the model-derived logK´ values.

Table 5.3: Parameters obtained from fits of MORB spectral intensities as a function of logfO_2 at 45 (L_3-edge) and 70 (M_4-edge) set energies using the two-sigmoid model, given by Eq. 5.11. Values of $logK_A'$ and $logK_B'$ correspond to the $U^{4+} \rightarrow U^{5+}$ and $U^{5+} \rightarrow U^{6+}$ reactions, respectively. 1 atm and 10 kbar data were fitted simultaneously to give separate logK´s for each pressure and three shared I_{U*} values at each energy.

	MORB 1 atm		MORB 10 kbar	
Edge	$logK_A'$	$logK_B'$	$logK_A'$	$logK_B'$
L_3	1.38 (3)	-0.44 (6)	0.90 (3)	-0.29 (3)
M_4	1.42 (3)	-0.40 (6)	0.98 (3)	-0.53 (6)

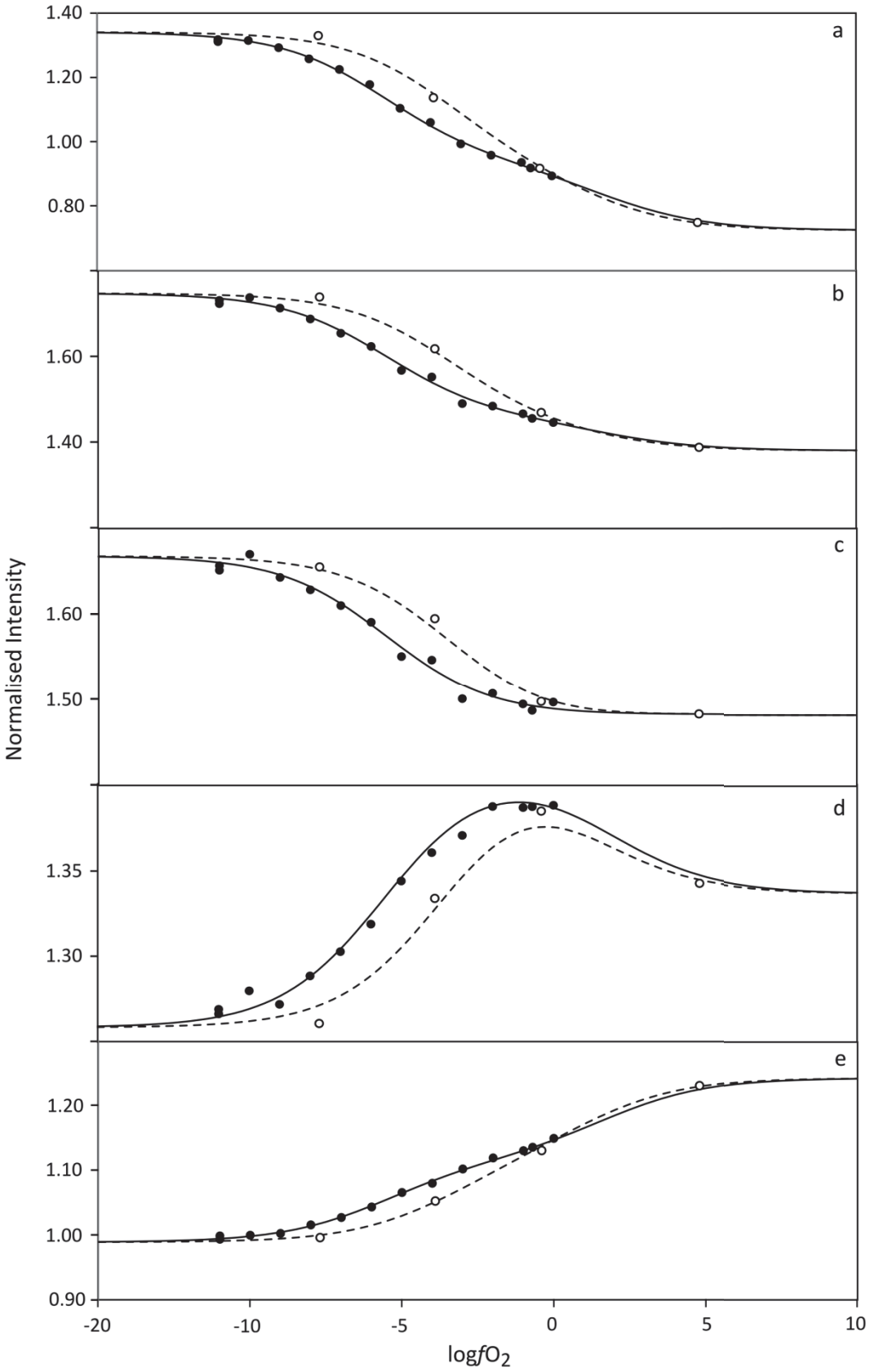


Figure 5.4: Two-sigmoid model curves of U L_3-edge XANES spectra intensities as a function of the logfO_2 of sample equilibration (1400 °C) at selected energies: (a) 17168 eV (b) 17173 eV, (c) 17175 eV, (d) 17180 eV, and (e) 17188 eV, for MORB 1 atm (filled circles) and 10 kbar glasses (open circles).

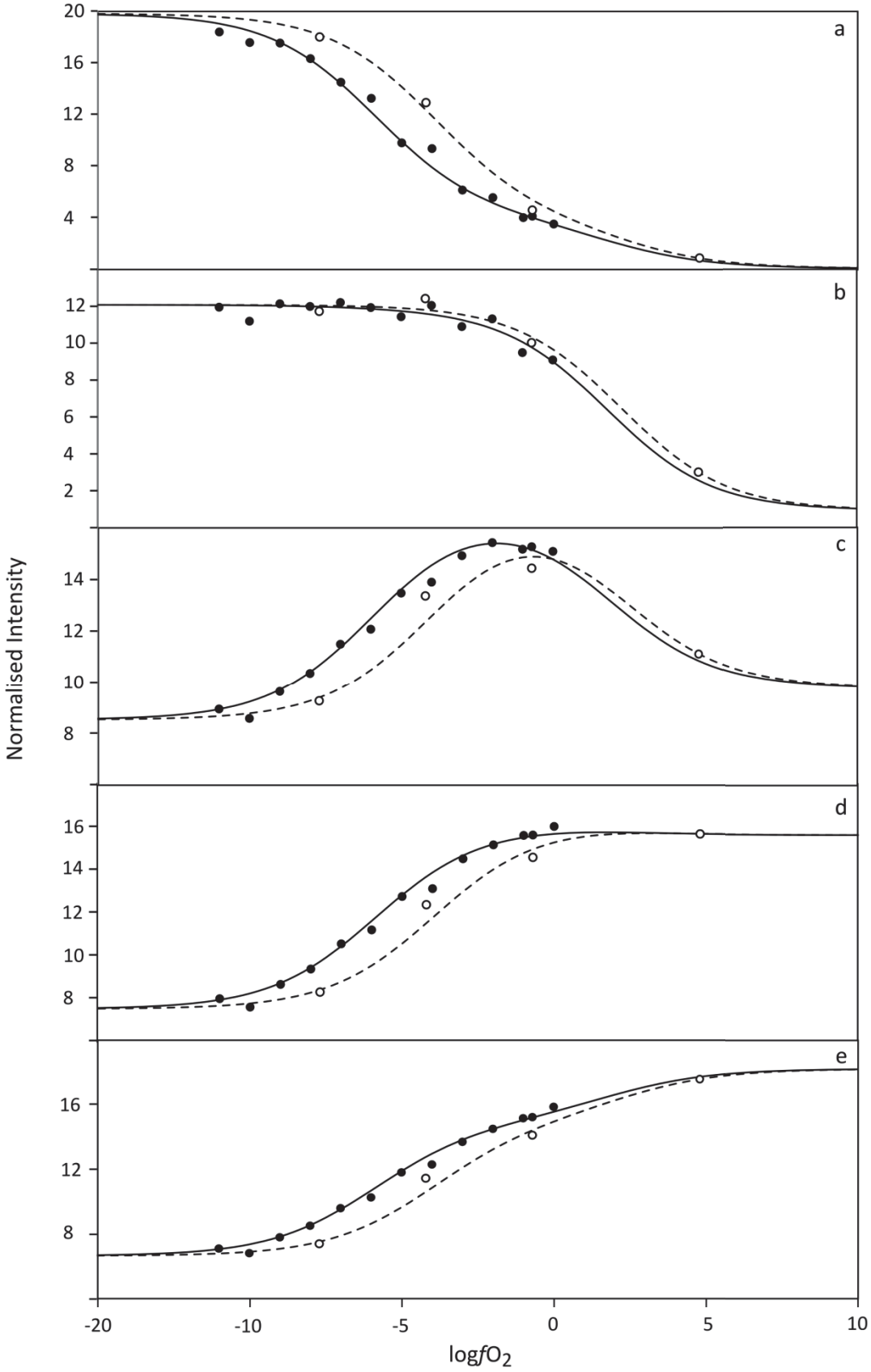


Figure 5.5: Two-sigmoid model curves of U M_4-edge XANES spectra intensities as a function of the logfO_2 of sample equilibration (1400 °C) at selected energies: (a) 3725.1 eV (b) 3725.65 eV, (c) 3726.2 eV, (d) 3726.45 eV, and (e) 3726.7 eV, for MORB 1 atm (filled circles) and 10 kbar glasses (open circles).

Since the fits not only produced sets of logK′ values, but also values of $I_{U^{4+}}$, $I_{U^{5+}}$, and $I_{U^{6+}}$ at each energy value, it was possible to map the model-derived three end-member U oxidation state line-shapes for the L_3- and M_4-edges across the selected energy ranges, as shown in Fig. 5.6 and Fig. 5.7, respectively. Notably, the U^{5+} and U^{6+} L_3-edge line-shapes had essentially the same intensities at ~17174.7 eV (the energy of the U^{6+} white-line crest). This implies that the variation in spectral intensities with fO_2 at 17174.7 eV was due only to the changing proportion of U^{4+}, which can be fitted using a single sigmoid with $a/4 = 0.25$ (the expected slope for a one-electron oxidation) representing the $U^{4+} \rightarrow U^{5+}$ reaction. The single sigmoid fits to this feature were reported in Chapter 4 (Table 4.2), and gave logK′ (actually representing $\log K_A'$) values of 1.4(2) and 1.2(3) for the 1 atm and 10 kbar data, respectively. These values are within uncertainty of those produced by the multi-energy two-sigmoid models.

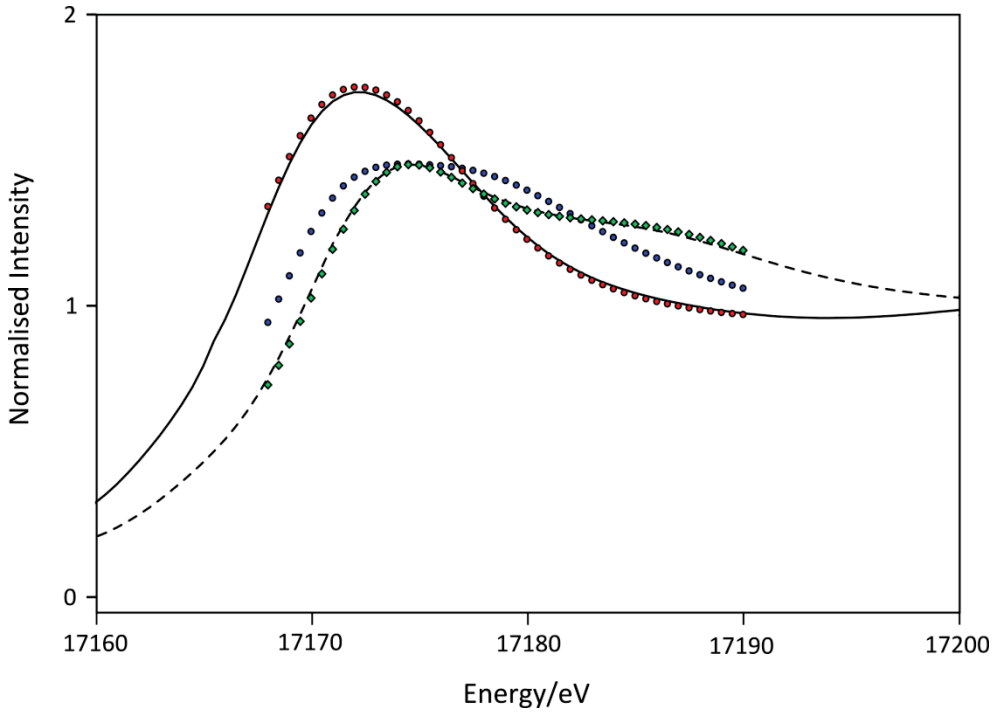


Figure 5.6: U^{4+} (red circles), U^{5+} (blue circles), and U^{6+} (green diamonds) L_3-edge line-shapes derived from the MORB two-sigmoid model, over the energy range 17168-17190 eV. U L_3-edge XANES spectra recorded from MORB glasses equilibrated at 1400 °C and $\log fO_2$ = -11 at 1 atm (solid line), and $\log fO_2$ = +4.7 at 10 kbar (dashed line) are shown for comparison.

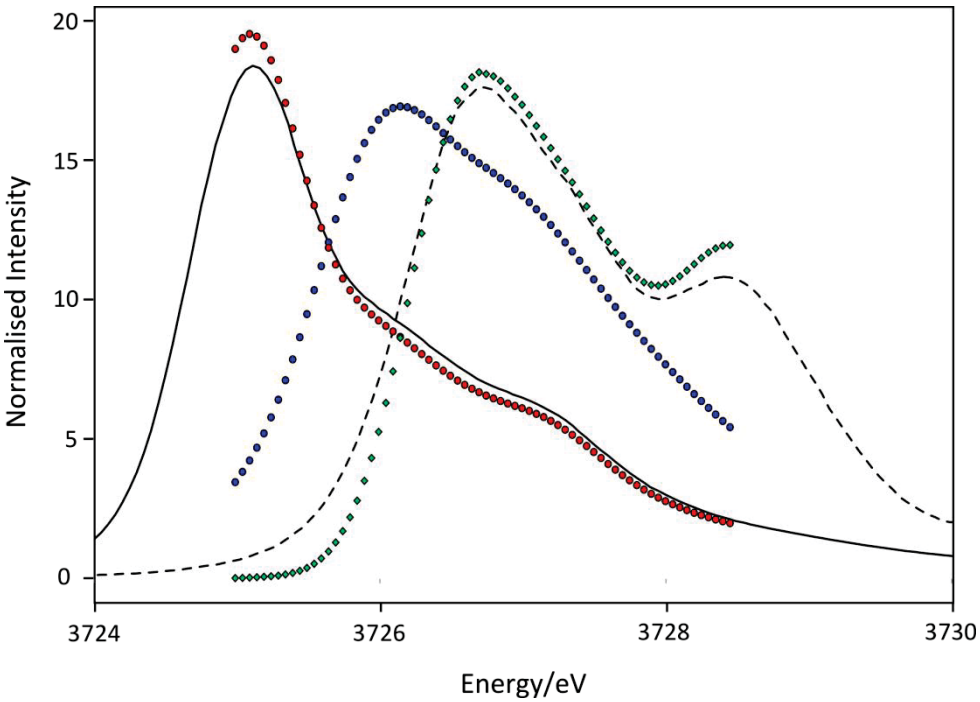


Figure 5.7: U^{4+} (red circles), U^{5+} (blue circles), and U^{6+} (green diamonds) M_4-edge line-shapes derived from the MORB two-sigmoid model, over the energy range 3725-3728.45 eV. U M_4-edge XANES spectra recorded from MORB glasses equilibrated at 1400 °C and log$f$O$_2$ = -11 at 1 atm (solid line), and log$f$O$_2$ = +4.7 at 10 kbar (dashed line) are shown for comparison.

5.2.4 MORB Model Part 3.2

5.2.4.1 Methodology

To check the two-sigmoid model for internal consistency the U^{5+} spectral line-shape was also extracted from the MORB M_4-edge spectra using the model derived logK´ values (Table 5.3). This was achieved by calculating the expected U oxidation state proportions in the spectrum of each glass using the two-sigmoid logK_A´ and logK_B´ values (columns 2-4 of Table 5.4). The percentage of the log$f$O$_2$ = -11 (1 atm) and log$f$O$_2$ = +4.7 (10 kbar) spectra required to remove all of the U^{4+} and U^{6+} contributions were then subtracted from each intermediate log$f$O$_2$ spectrum (columns 5 and 7 of Table 5.4), such that the remaining/residual component of the spectrum was expected to represent a pure U^{5+} line-shape. These residual line-shapes were then normalised to the intensity of a 100 % U^{5+} spectrum by dividing the whole line-shape by the proportion of U^{5+} that it was calculated to represent (column 9 of Table 5.4).

Table 5.4: Calculated U^{4+}, U^{5+}, and U^{6+} proportions in each MORB glass using the $logK_A'$ and $logK_B'$ values derived from the two-sigmoid modelling of the L_3- and M_4-edge XANES spectral intensities. The proportions of the spectra of the $log fO_2$ = -11 (1 atm) and +4.7 (10 kbar) glasses required to subtract the U^{4+} and U^{6+} components from each spectra, and the amount of U^{5+} represented by the resulting residual line-shape are given in shaded columns.

M_4-edge				1 atm: $logK_A'$ = 1.42 and $logK_B'$ = -0.40 10 kbar: $logK_A'$ = 0.98 and $logK_B'$ = -0.53				
$log fO_2$	$U^{4+}/\sum U$	$U^{5+}/\sum U$	$U^{6+}/\sum U$	Prop. $log fO_2$ = -11	$U^{5+}/\sum U$ (from $log fO_2$ = -11)	Prop. $log fO_2$ = 4.7 (1)	$U^{5+}/\sum U$ (from $log fO_2$ = 4.7 (1))	$U^{5+}/\sum U$ (residual)
-11	0.955	0.045	0.000	1.000	0.045	0.000	0.000	0.000
-10	0.923	0.077	0.000	0.966	0.043	0.000	0.000	0.034
-9	0.871	0.129	0.000	0.912	0.041	0.000	0.000	0.088
-8	0.791	0.208	0.001	0.828	0.037	0.001	0.000	0.171
-7	0.680	0.318	0.002	0.712	0.032	0.003	0.001	0.286
-6	0.543	0.451	0.006	0.568	0.025	0.007	0.001	0.425
-5	0.398	0.589	0.013	0.417	0.019	0.016	0.003	0.567
-4	0.268	0.704	0.028	0.280	0.013	0.034	0.006	0.685
-3	0.166	0.778	0.055	0.174	0.008	0.068	0.013	0.758
-2	0.096	0.802	0.101	0.101	0.005	0.124	0.023	0.775
-1	0.052	0.774	0.173	0.055	0.002	0.213	0.040	0.732
-0.7	0.043	0.756	0.201	0.045	0.002	0.247	0.046	0.708
0	0.026	0.696	0.277	0.028	0.001	0.340	0.063	0.632
+4.7(1)	0.001	0.184	0.814	0.000	0.000	1.000	0.184	0.000
L_3-edge				1 atm: $logK_A'$ = 1.38 and $logK_B'$ = -0.44 10 kbar: $logK_A'$ = 0.90 and $logK_B'$ = -0.29				
$log fO_2$	$U^{4+}/\sum U$	$U^{5+}/\sum U$	$U^{6+}/\sum U$	Prop. $log fO_2$ = -11	$U^{5+}/\sum U$ (from $log fO_2$ = -11)	Prop. $log fO_2$ = 4.7 (1)	$U^{5+}/\sum U$ (from $log fO_2$ = 4.7 (1))	$U^{5+}/\sum U$ (residual)
-11	0.959	0.041	0.000	1.000	0.041	0.000	0.000	0.000
-10	0.929	0.071	0.000	0.969	0.040	0.000	0.000	0.031
-9	0.881	0.119	0.000	0.919	0.038	0.000	0.000	0.081
-8	0.806	0.193	0.001	0.840	0.034	0.001	0.000	0.159
-7	0.700	0.298	0.002	0.729	0.030	0.002	0.000	0.268
-6	0.566	0.429	0.005	0.590	0.024	0.006	0.001	0.404
-5	0.421	0.568	0.012	0.439	0.018	0.013	0.002	0.548
-4	0.287	0.688	0.025	0.299	0.012	0.028	0.003	0.673
-3	0.180	0.770	0.050	0.188	0.008	0.056	0.007	0.756
-2	0.106	0.802	0.092	0.110	0.005	0.104	0.012	0.786
-1	0.058	0.782	0.160	0.060	0.002	0.181	0.021	0.759
-0.7	0.048	0.766	0.186	0.050	0.002	0.210	0.024	0.740
0	0.030	0.712	0.258	0.031	0.001	0.292	0.034	0.677
+4.7(1)	0.001	0.115	0.884	0.000	0.000	1.000	0.115	0.000

(1) Equilibrated at 10 kbar

5.2.4.2 Results

The U^{5+} line-shapes extracted from M_4-edge XANES spectra of MORB glasses equilibrated at 1400 °C between logfO_2 = 0 and -7 are shown in Fig. 5.8; the line-shapes extracted from more reduced glasses (logfO_2 < -7) were extremely noisy, as the U^{5+} component was small, and are not shown. Generally the extracted line-shapes are in good agreement with that derived directly from the M_4-edge two-sigmoid model, with the exception of the line-shapes extracted from the logfO_2 = -4, -6, and -7 spectra, which exhibit some deviation in shape

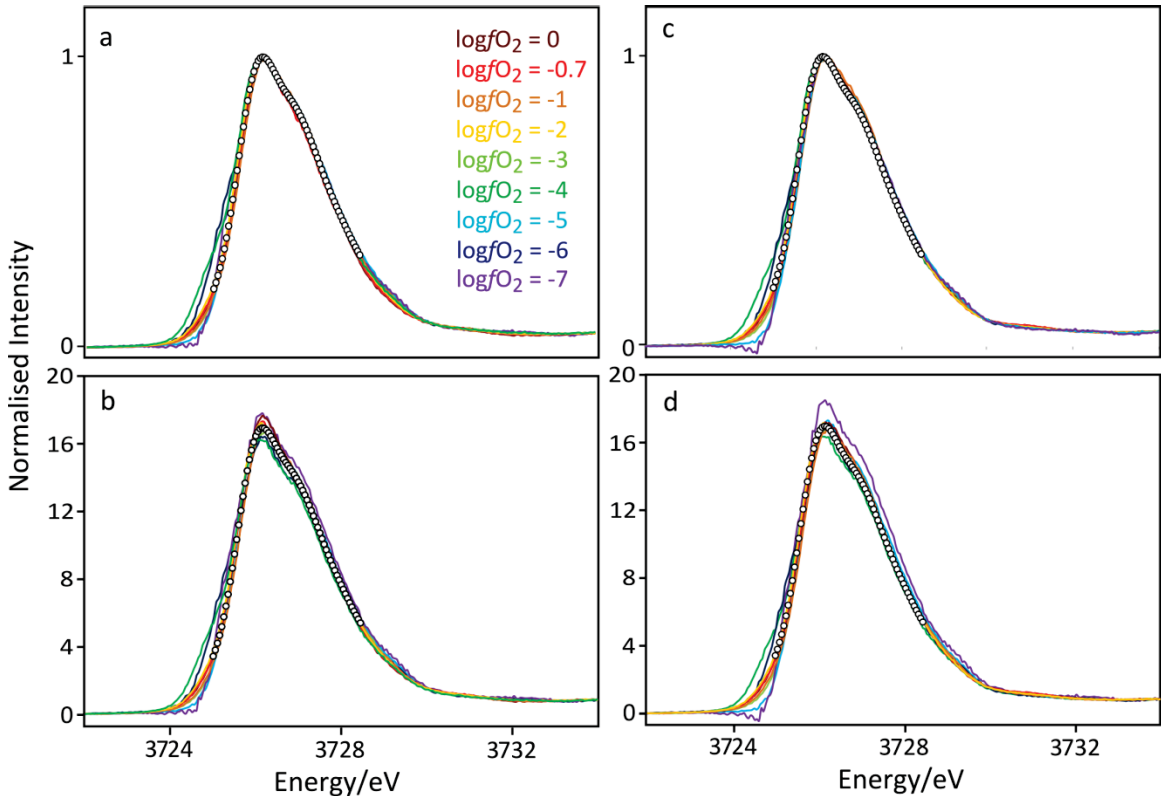


Figure 5.8: U^{5+} M_4-edge XANES line-shapes extracted from spectra of 1 atm MORB glasses equilibrated at 1400 °C and the logfO_2 values indicated. Spectra were fitted using the appropriate proportion of the reduced and oxidised end-member spectra, logfO_2 = -11 (1 atm) and +4.7 (10 kbar), to remove the U^{4+} and U^{6+} contributions. The U oxidation state proportions were calculated using the logK_A' and logK_B' values derived from two-sigmoid oxidation state models of (a,b) M_4- and (c,d) L_3-edge spectral intensities. In each case the residual between the two-end-member fit and the recorded spectrum was extracted as the U^{5+} line-shape. Line-shapes are divided by (a,c) their maximum intensities and (b, d) the U^{5+} proportion they were calculated to represent. The U^{5+} line-shape derived directly from the M_4-edge two-sigmoid model is shown for comparison (white circles).

and/or normalised intensity. However, for spectra where the proportion of U^{5+} is relatively small, such as logfO_2 = -7, the extracted line-shapes will be strongly affected by small variations/inconsistencies in processing, for example, in the estimated U oxidation state proportions, raw data normalisation, or energy drifts of the monochromator during the beam time. The discrepancy of the line-shape extracted from the logfO_2 = -4 spectrum is not unreasonable as this fO_2 (at 1400 °C) is achieved by a gas mixture comprising 0.995 % CO_2 and 0.005 % CO (logfO_2 = -3 is 100 % CO_2), as such even a small error in the CO flow-rate will significantly change the fO_2 of sample equilibration.

5.2.5 Discussion on the L_3- and M_4-edge XANES spectra of U^{5+}

The U line-shapes extracted from the two-sigmoid models are thought to represent the true U L_3- and M_4-edge XANES spectra of U^{4+}, U^{5+}, and U^{6+} for the MORB glasses (Fig. 5.6 and Fig. 5.7). The edge-energy of the U^{5+} L_3-edge end-member spectrum (17168.4 eV: measured at a normalised intensity of 1) lies ~2.1 eV above, and ~1.45 eV below, the U^{4+} (17166.3 eV) and U^{6+} edges (17169.85 eV), respectively. In comparison, a total edge-shift of 2.9 eV between U^{4+} ($U_{0.33}Na_{0.67}MoO_4$: 17159.5 eV) and U^{6+} ($C_2H_3O_7PU$: 17162.4 eV) compounds has been reported, with the edge of the mixed valence $U^{5+}(H_2O)_2(U^{6+}O_2)_2O_4(OH)(H_2O)_4$ compound lying slightly below that of U^{6+} (17162.0 eV) (Belai *et al.*; 2008). The U^{5+} L_3-edge was also found to lie between those of U^{4+} and U^{6+} for U alkali oxides (Soldatov *et al.*, 2007). Direct comparison of U oxidation state energy-shifts at the L_3-edge for MORB glasses with other studies of U compounds is somewhat complicated by the comparable effects of changes in U coordination environment and oxidation state on the L_3-edge XANES edge- and white-line maximum energy (Soldatov *et al.*, 2007; Schelter *et al.*, 2010).

The U^{5+} L_3-edge line-shape derived from the MORB glass spectra (Fig. 5.6) is characterised by an extremely broad and asymmetric white-line. Interestingly the white-line crest occurs at a similar energy, and has almost the same intensity as the U^{6+} line-shape for the same glasses. The similarity in the white-line position of the U^{5+} and U^{6+} spectra is consistent with previously reported L_3-edge spectra of silicate glasses, where no energy shift was observed with changing U^{5+} and U^{6+} proportions (Farges *et al*.; 1992). Significant asymmetry of the U^{5+} L_3-edge white-line is consistent with previous measurements of oxide compounds where a high intensity shoulder on the edge-rise was attributed to the U^{5+} ion (Soldatov *et al*., 2007).

Collection of HERFD U M_4-edge XANES spectra of the binary oxides U_4O_9 and U_3O_8 have resulted in the interpretation that they are U^{4+}/U^{5+} and U^{5+}/U^{6+} compounds, respectively (Kvashnina *et al.*, 2013), rather than the previously assumed U^{4+}/U^{6+}. Comparison of the two-sigmoid derived MORB U M_4-edge oxidation state line-shapes with those of U_4O_9, U_3O_8, UO_2 (U^{4+}), and $UO_2(acac)_2$ (U^{6+}: uranyl) are entirely consistent with these oxidation state assignments, with almost identical edge-energy shifts observed between the different U oxidation state line-shapes of the two studies, as shown in Fig. 5.9. The MORB glass U oxidation state line-shapes resulting from the two possible valence combinations of both U_3O_8 and U_4O_9 were calculated and are shown in Fig 5.9. The MORB mixed line-shapes corresponding to the correct oxidation state assignment (as reported by Kvashnina *et al.* 2013) are very similar to those obtained from the relevant oxide compound, whilst those of the alternative oxidation state combination are very different.

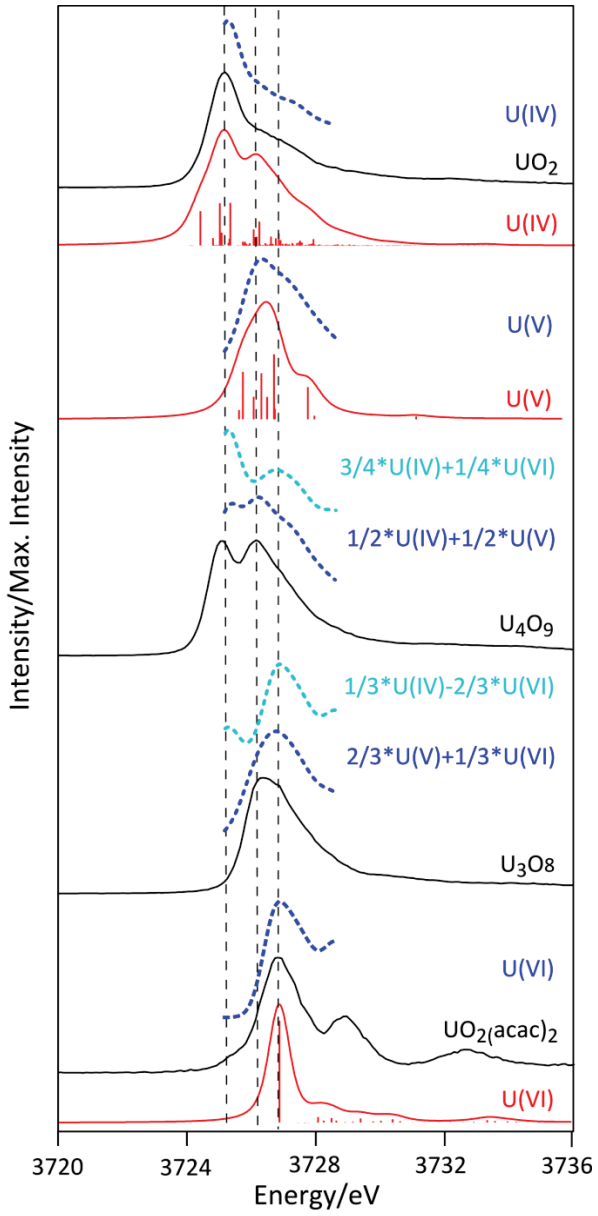


Figure 5.9: Published U M_4-edge HERFD XANES experimental (black lines) and calculated (red lines) spectra of various U oxides of differing valences (Kvashnina *et al.*; 2013) plotted with the U^{4+}, U^{5+}, U^{6+}, and mixed valence line-shapes determined from MORB glass spectra of this study (dashed blue-lines). Dark blue lines correspond to the MORB line-shapes of equivalent U valences to the oxides, and pale blue lines show the alternative hypothetical valence combination for U_3O_8 and U_4O_9. Dashed black vertical lines indicate the approximate energy positions of U^{4+}, U^{5+}, and U^{6+} white-line crests.

5.2.6 Final fits

The MORB 1 atm and 10 kbar M_4-edge spectra were finally fitted using a combination of the logfO_2 = -11 (1 atm) and logfO_2 = +4.7 (10 kbar) spectra, and the average U^{5+} spectrum. The U oxidation state proportions in each glass were calculated from these fits using a reverse approach to that of section 5.2.4. The calculated U proportions are shown in Fig. 5.10(a) and the resulting $U^{4+}/(U^{4+}+U^{5+})$ and $U^{5+}/(U^{5+}+U^{6+})$ ratios are shown in Fig. 5.10(b).

Data in Fig. 5.10 correspond to the calculated U oxidation state values when the proportions of the logfO_2 = -11 and logfO_2 = +4.7 (10 kbar) spectra were taken to be the average of the two sets of values reported in Table 5.4. Error bars resulting from the 7 % difference in the U^{5+}-U^{6+} values of the logfO_2 = +4.7 spectrum using the logK´s derived from the L_3-edge compared to the M_4-edge two-sigmoid models are smaller than the data points at all other logfO_2s (i.e. log$fO_2 \leq 0$). The variation of the U^{4+} and U^{6+} proportions as a function of logfO_2 in the 1 atm and 10 kbar glasses are fitted using sigmoid curves with limits of 1 and 0. The variation of U^{5+} in 1 atm glasses as a function of logfO_2 exhibits a Gaussian-like distribution, so $U^{5+}/\sum U$ are fitted using Gaussian curves (Fig. 5.10(a)). The sigmoid fit to the 10 kbar U^{4+} proportions is significantly steeper than predicted by the two-sigmoid model; it is not clear whether this is a true feature of the U oxidation states in MORB glasses at 10 kbar, or is due to an outlying data point having a significant effect due to the limited number of data.

Sigmoid fits to the $U^{4+}/(U^{4+}+U^{5+})$ and $U^{5+}/(U^{5+}+U^{6+})$ ratios, shown in Fig. 5.10(b), have slopes forced to the expected $a/4 = 0.25$, and give $logK_A'$ and $logK_B'$ values of 1.35(2) and -0.36(3), and 0.92(4) and -0.45(3) for the 1 atm and 10 kbar data, respectively. The U oxidation state proportions that each spectrum would represent if the logfO_2 = -11 and logfO_2 = +4.7 were instead taken as the true U^{4+} and U^{6+} end-members were also calculated, and are

shown by the error bars in Fig. 5.10. This illustrates that even a large uncertainty in the U^{6+} end-member will have a relatively small impact (<0.05) on the estimated U oxidation state proportions at $\log fO_2 \leq 0$.

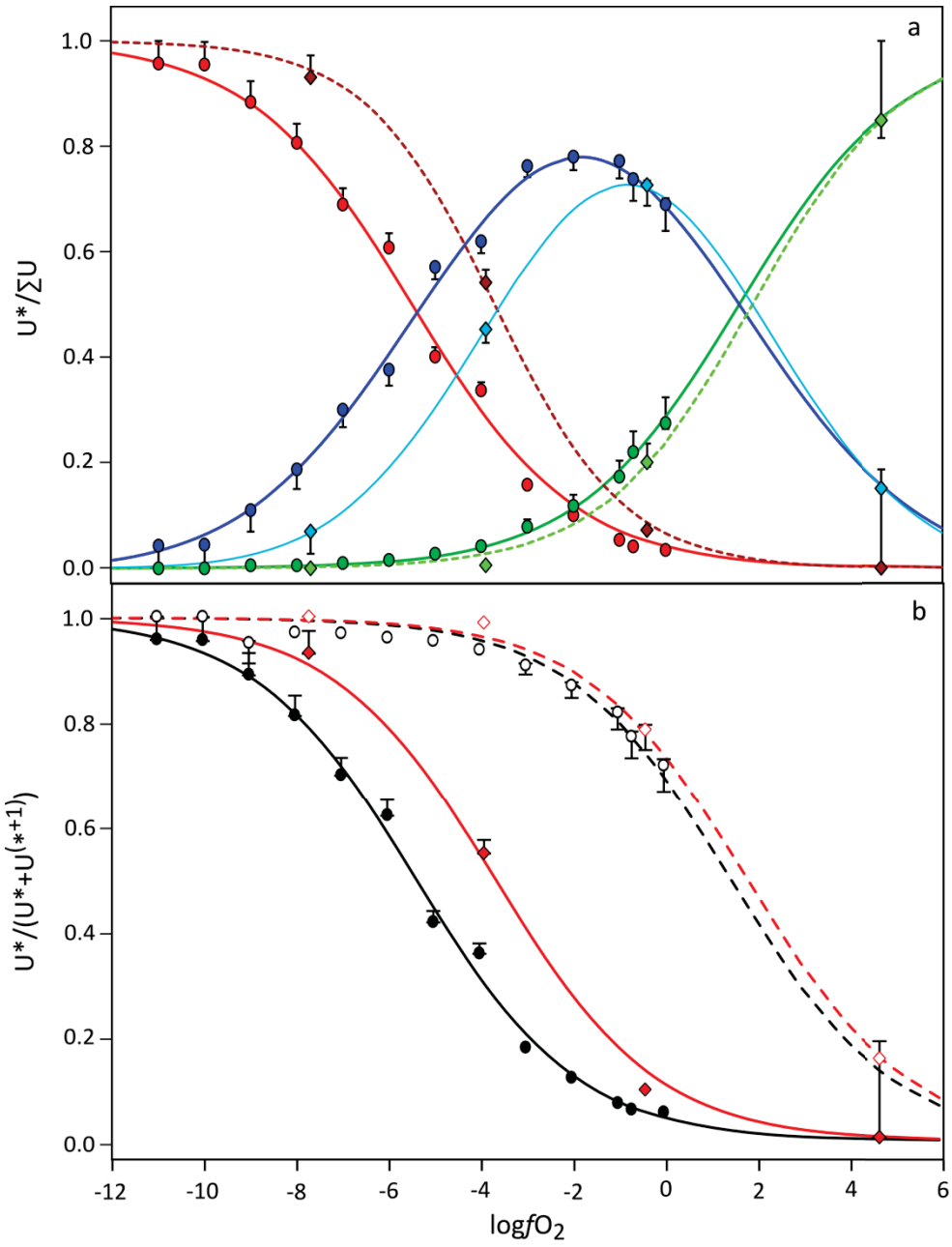


Figure 5.10: Calculated U oxidation state (a) proportions: U^{4+} (red), U^{5+} (blue) and U^{6+} (green), and (b) ratios: $U^{4+}/(U^{4+}+U^{5+})$ (filled data points) and $U^{5+}/(U^{5+}+U^{6+})$ (unfilled data points) of MORB 1 atm (circles) and 10 kbar (diamonds) glasses equilibrated at 1400 °C. Sigmoid and Gaussian (U^{5+}) curve fits to the data are shown. Error bars represent the change in the calculated U oxidation states of each glass if the $\log fO_2$ = -11 and +4.7 spectra were taken as the U^{4+} and U^{6+} end-members, respectively.

The U oxidation state proportions in the MORB glasses suggest that an increase in pressure from 1 atm to 10 kbar has little, if any, impact on the $U^{5+} \rightarrow U^{6+}$ reaction, although the oxidised limits of the U^{5+} and U^{6+} fits are associated with the largest uncertainty. In contrast, the $U^{4+} \rightarrow U^{5+}$ equilibrium shifts between 1 atm and 10 kbar to favour U^{4+} at higher pressure. Thus, the stability field of U^{5+} is significantly compressed for the high pressure glasses ($\geq$ 5 kbar) relative to the 1 atm glasses.

5.3 U oxidation state proportions in AD glasses

5.3.1 Summary of observations

CMAS glasses vary systematically in colour as a function of fO_2 from yellow (highly oxidised), to colourless (oxidised), to blue (reduced), to brown (very reduced). Reduced AD (and other CMAS composition) glasses exhibited time-dependent spectral changes consistent with beam-induced oxidation at both the L_3- and M_4-edges (see sections 3.3.1 and 4.3.1 of this thesis). In addition, the M_4-edge spectra of AD glasses contain a strong pre-edge feature that is not observed in any of the MORB spectra (section 3.3). The intensity of this pre-edge peak increases with decreasing fO_2, and is interpreted to represent an additional reduced U state. The dramatic decrease in pre-edge intensity with exposure to the beam suggests that it is this state that is sensitive to beam damage. At the L_3-edge the additional state appears to be characterised by a decrease in white-line intensity and energy, as the intensity of the white-line maximum of the most reduced CMAS spectra is significantly smaller than that of the most reduced MORB spectra. However, it is not clear to what extent beam damage also contributes to this intensity offset between CMAS and MORB spectra at the L_3-edge.

5.3.2 AD model Part 1

5.3.2.1 Methodology

It was shown in Chapter 3 that the M_4-edge XANES spectra from AD composition glasses can be reproduced by linear combinations of four spectral line-shapes. It is possible that these line-shapes represent four U oxidation states, including the three oxidation states observed in MORB glasses (interpreted as U^{4+}, U^{5+}, and U^{6+}), and an additional reduced state, perhaps U^{3+}. In this case, by analogy with the MORB glasses, the intensity variation of the AD XANES spectra at a set energy is expected to be a combination of three sigmoid functions, representing the $U^{4+} \rightarrow U^{5+}$ and $U^{5+} \rightarrow U^{6+}$ reactions given by Eq. 5.1 and 5.2, and an additional curve for the $U^{3+} \rightarrow U^{4+}$ reaction:

$$C = \frac{U^{3+}}{U^{3+} + U^{4+}} = \frac{1}{1 + 10^{(0.25\log fO_2 + \log K_C')}} \tag{5.18}$$

Using these three sigmoid functions, the proportions of each U oxidation can be derived and used to write a similar expression to Eq. 5.11, given by:

$$\begin{aligned} i_{mixed} = &\left(\frac{I_{U^{3+}}}{\left(\frac{1}{ABC} + \frac{1}{B} - \frac{1}{AB} - \frac{1}{BC} + \frac{1}{C}\right)}\right) + \left(\frac{(1-C)I_{U^{4+}}}{\left(\frac{1}{AB} + \frac{C}{B} - \frac{C}{AB} - \frac{1}{B} + 1\right)}\right) \\ &+ \left(\frac{(1-A)(1-C)I_{U^{5+}}}{\left(\frac{1}{B} + \frac{CA}{B} - \frac{C}{B} - \frac{A}{B} + A\right)}\right) \\ &+ \left(\frac{(1-A)(1-B)(1-C)I_{U^{6+}}}{(1 + CA - C - A + AB)}\right) \end{aligned} \tag{5.19}$$

This Equation has two additional parameters to account for the U^{3+} component, which are the intensity of the pure U^{3+} spectrum at the energy being fitted, $I_{U^{3+}}$, and the logK′ of the $U^{3+} \rightarrow U^{4+}$ reaction, $\log K_C'$.

The intensity variations of AD L_3-edge spectra as a function of $\log fO_2$ were fitted using the same methodology that was successfully applied to the MORB data. Fits were run at 45

different energy values; over the energy range 17168-17190 eV, with a step size of 0.5 eV. Fits to the 1 atm data were run both simultaneously with the 10 kbar data and alone; for the latter case, the 10 kbar ($\log fO_2$ = +4.7) data point was included as a "1 atm" data point to place some constraint on the oxidised limit. Because the AD fitting equation (Eq. 5.19) had many parameters (seven parameters compared to the five of the MORB fits: Eq. 5.11), the AD data were fitted in two ways. First, all the fits were run simultaneously, with no external constraints placed on any of the fitting parameters. Second, the AD fits were run with the values of $I_{U^{4+}}$ at each energy fixed to that of the MORB $\log fO_2$ = -11 spectrum, which was collected during the same beamtime. Based on the results of the MORB fitting, this spectrum was expected to represent an essentially pure U^{4+} line-shape. However, this constraint assumes that the 100 % U^{4+} line-shape was the same for MORB and AD glasses. It was impossible to fit the AD U M_4-edge data using the above methodology as the data could not be normalised appropriately, as discussed in Chapter 3.

5.3.2.2 Results

Simultaneous fits to the 1 atm and 10 kbar data could not produce sensible solutions to the 10 kbar data as $\log K_C'$ tended to unreasonably large values (> 20), this may be a result of the sparse data coverage. The U oxidation state line-shapes derived from the fits to the 1 atm data with both constrained and unconstrained $I_{U^{4+}}$ values are shown in Fig 5.11, and the resulting logK′ values are given in Table 5.5. The fit derived logK′ values and, by extension, the calculated U oxidation state proportions of each glass, are significantly different between the two fitting methodologies, in particular for U^{3+} and U^{4+}.

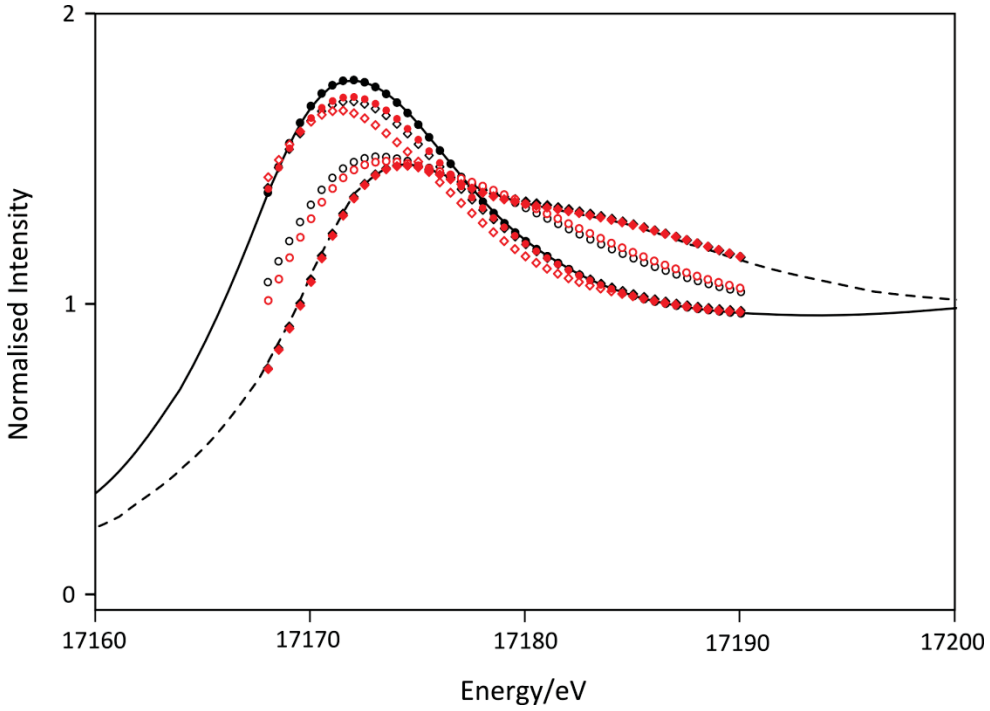


Figure 5.11 U^{3+} (open diamonds), U^{4+} (filled circles), U^{5+} (open circles), and U^{6+} (filled diamonds) L_3-edge line-shapes derived from the AD three-sigmoid models over the energy range 17168-17190 eV, with the U^{4+} line-shape free to vary (red) and fixed to that of the MORB log$f$O$_2$ = -11 spectrum (black). The U L_3-edge XANES spectra recorded from the MORB glass equilibrated at 1400 °C and log$f$O$_2$ = -11 at 1 atm (solid line), and the AD glass equilibrated at 1400 °C and log$f$O$_2$ = +4.7 at 10 kbar (dashed line) are shown for comparison.

Table 5.5: Parameters obtained from fits of AD L_3-edge spectral intensities as a function of log$f$O$_2$ at 45 set energies using the three-sigmoid model, given by Eq. 5.19, with the U^{4+} line-shape either free to vary or fixed to that of the MORB log$f$O$_2$ = -11 spectrum. Values of logK_A', logK_B' and logK_C' correspond to the $U^{4+} \rightarrow U^{5+}$, $U^{5+} \rightarrow U^{6+}$ and $U^{3+} \rightarrow U^{4+}$ reactions, respectively.

Fit	logK_A'	logK_B'	logK_C'
$I_{U^{4+}}$ free	1.53 (1)	-0.16 (3)	4.6 (2)
$I_{U^{4+}}$ fixed	1.86 (3)	0.04 (3)	2.00 (6)

5.3.2.3 Discussion

When the line-shape of U^{4+} was not fixed the three-sigmoid model produced a best-fit logK_C' of 4.6(2). In this case, the $U^{3+} \rightarrow U^{4+}$ transition occurs at extremely reduced fO$_2$s, and

$U^{3+}/\sum U$ is expected to increase from 0.07 to 0.44 between logfO_2 =-14 and logfO_2 = -18. A dramatic change in colour between these two glasses, from blue to brown, is certainly consistent with such an oxidation state change. Indeed, a study of the reduction of U^{4+} to U^{3+} in an alkali chloride melt reported that the melt colour changed from green to a deep purple (Polovov *et al.*, 2008). However, this logK_C' value also predicts that U^{3+} should have entirely oxidised to U^{4+} at logfO_2 > -9, which is entirely contradicted by the observation of a low intensity pre-edge in the M_4-edge spectra of AD glasses as oxidised as logfO_2 = -5.

In the case where the U^{4+} line-shape for AD glasses was forced to be identical to that for MORB glasses, an entirely different value of logK_C' = 2.00(6) was produced. This predicts that some U^{3+} ($U^{3+}/\sum U$ = 0.03) will be present in a glass equilibrated at logfO_2 = -5, although this proportion is too small to justify the observation of a distinct pre-edge shoulder in the M_4-edge spectrum. In addition, no significant oxidation state change is expected between the most reduced glasses with $U^{3+}/\sum U$ predicted to increase from 0.97 to 1.00 between logfO_2 = -14 and -18. This seems to be at odds with the varying colours of these glasses (if this is a result of changing U states) and the variation of U L_3-edge spectral intensity and energy across this fO_2 range.

5.3.3 AD model Part 2

5.3.3.1 Methodology

For comparison with the AD L_3-edge three-sigmoid models, the 1 atm AD M_4-edge spectra were again fitted using four spectral components (similarly to section 3.3.4): a combination of the MORB logfO_2 = -11 (1 atm) and logfO_2 = +4.7 (10 kbar) spectra, the average MORB U^{5+} spectrum, and the AD reduced end-member spectrum collected from the glass equilibrated at logfO_2 = -18 (1 atm). To calculate the proportions of each component in these

fits the relative normalised heights of all four components must be known, as the AD M_4-edge spectra were not background-normalised. The proportion of a particular component in a given spectrum (P_1) can be expressed as

$$P_1 = \frac{h_{P_1}/N}{H_{P_1}} \tag{5.20}$$

where H_{P_1} is the maximum intensity of the background-normalised spectrum of that component, h_{P_1} is the maximum intensity of the component in the fit to the non-background normalised spectrum of a mixed valence sample, and N is a normalisation factor. As the factor N is the same for all four components in a particular spectrum, and the sum of the proportions of all four components in a single fit is expected to be equal to 1, N can be cancelled to give

$$P_1 = \frac{\frac{h_{P_1}}{H_{P_1}}}{\left(\frac{h_{P_1}}{H_{P_1}} + \frac{h_{P_2}}{H_{P_2}} + \frac{h_{P_3}}{H_{P_3}} + \frac{h_{P_4}}{H_{P_4}}\right)} \tag{5.21}$$

The relative intensities of the three MORB spectral components used to fit the AD M_4-edge spectra are known, as the MORB spectra were appropriately-normalised. However, the relative intensity of the AD log$f$O$_2$ = -18 (1 atm) M_4-edge spectrum is not known because AD spectra could not be normalised (see sections 3.3.1 and 3.3.2). To calculate the proportion of each component in the four-component fits from Eq. 5.21, the normalised intensity of the AD log$f$O$_2$ = -18 (1 atm) spectrum was taken to be equal to that of the MORB log$f$O$_2$ = -11 spectrum. This assumption will have a relatively small impact on the final result as changing the assumed normalised height of the AD log$f$O$_2$ = -18 component by as much as 25 % only changes the calculated proportions of each component by < 0.05. Finally, the U^{4+}, U^{5+}, and U^{6+} proportions contributed by the three MORB line-shapes were calculated; it was not possible to breakdown the contribution of the log$f$O$_2$ = -18 (1 atm) spectrum into separate U states.

5.3.3.2 Results

A selection of the AD four component fits are shown in Fig. 5.12, which illustrates that the differences between the model fit and the recorded spectrum are largest for the most oxidised spectra. In the case of spectra of glasses equilibrated at logfO_2 = 0 and -3 the residual exhibits variation beyond that attributable to noise. As shown in Fig. 5.13, the U oxidation state proportions estimated from the M_4-edge four component fits are entirely different to both solutions obtained from the L_3-edge three-sigmoid models. Although the individual oxidation state proportions contributed by the AD logfO_2 = -18 spectrum could not be calculated this cannot explain the discrepancies between the U state proportions estimated using the two different methodologies.

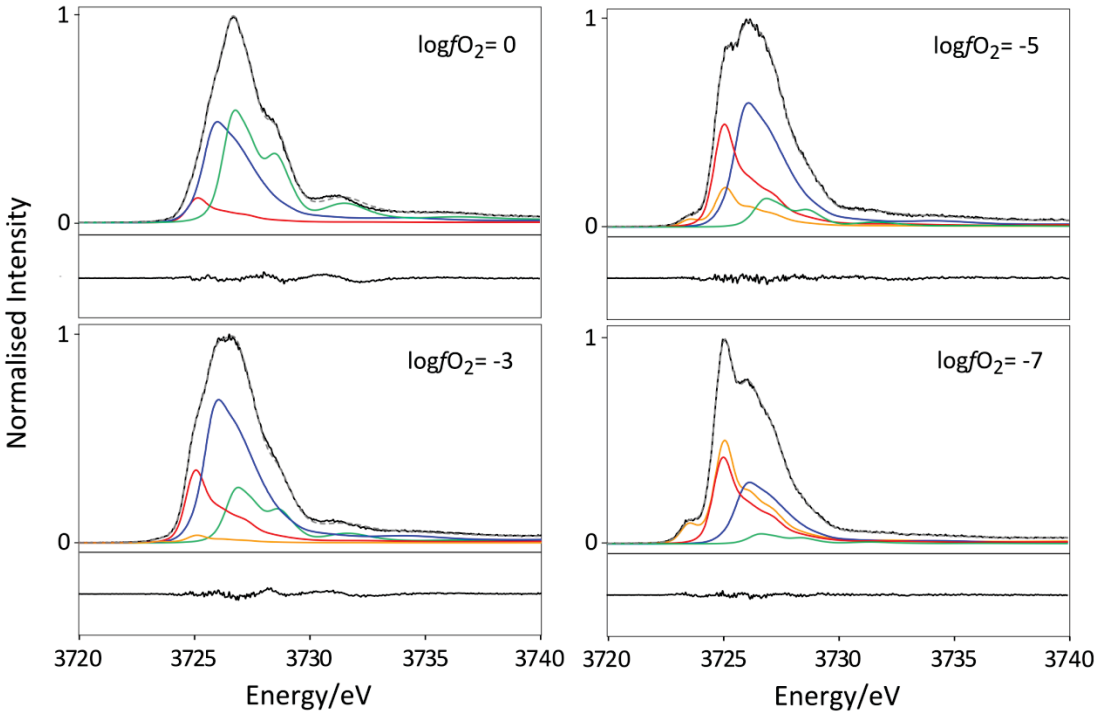


Figure 5.12: U M_4-edge XANES spectra of AD 1 atm glasses, quenched from 1400 °C and the logfO_2 values indicated, fitted (grey dashed lines) using a combination of the most reduced (logfO_2 = -18: orange) 1 atm AD spectrum, the most reduced (logfO_2 = -11, P = 1 atm: red) and oxidised (logfO_2 = +4.7, P = 10 kbar: green) MORB spectra, and the average U^{5+} line-shape determined from two-sigmoid modelling of MORB spectra. The difference between the recorded spectrum and the fit is shown below each spectrum.

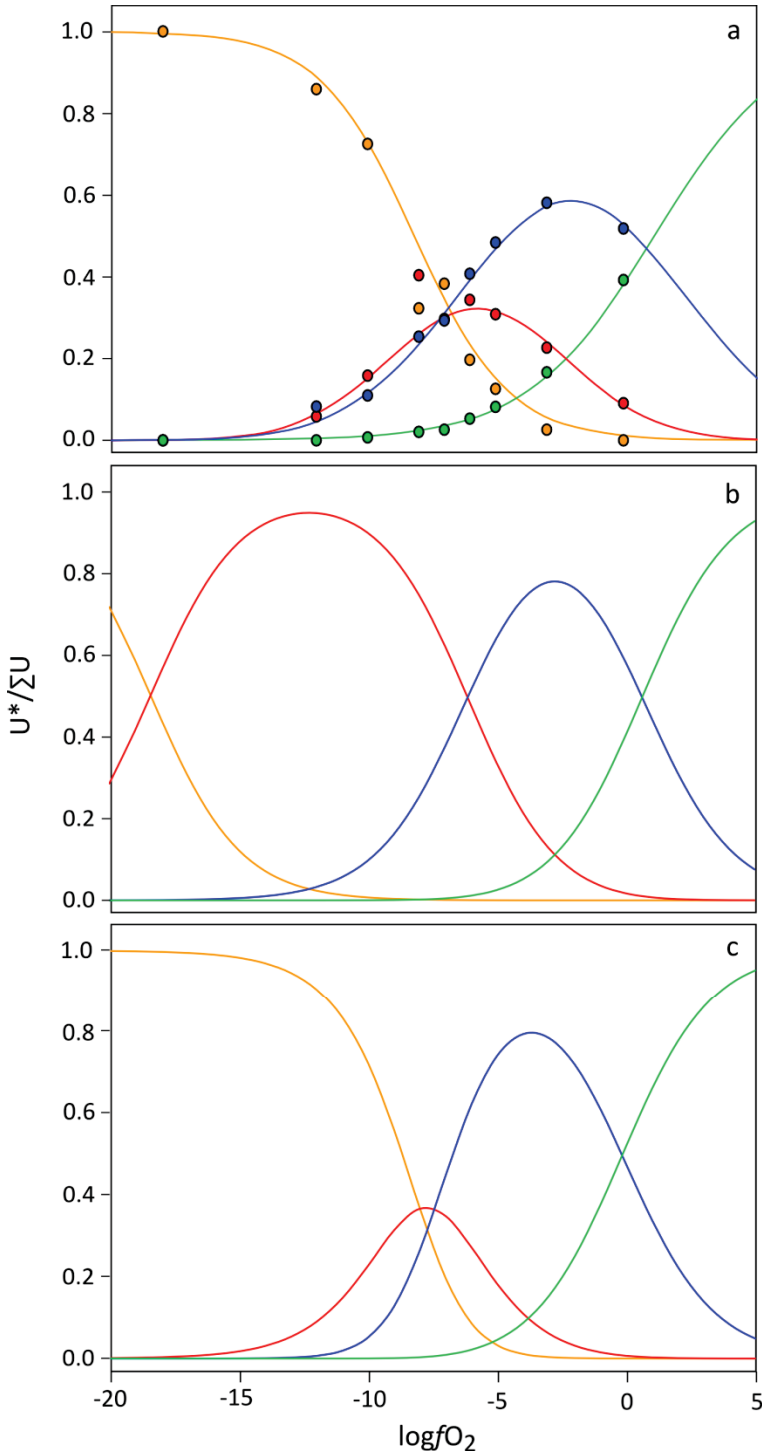


Figure 5.13: Estimated proportions of U^{4+} (red), U^{5+} (blue), U^{6+} (green), and a fourth U component (orange) in AD 1 atm glasses equilibrated at 1400 °C. Values were calculated from (a) four-component fits of AD M_4-edge XANES spectra, or from modelling of L_3-edge XANES spectral intensities using three sigmoids representing the $U^{3+}\rightarrow U^{4+}\rightarrow U^{5+}\rightarrow U^{6+}$ reactions, with the line-shape of U^{4+} (b) free to vary and (c) fixed to that of MORB glasses. For the M-edge fits (a) the fourth component (orange) is the spectrum of the AD glass equilibrated at $\log fO_2$ = -18, whilst for the three-sigmoid approach (b and c) the fourth component is defined as U^{3+} by the form of the model.

5.3.4 Discussion

If the pre-edge observed in AD M_4-edge XANES spectra is a feature of only one U state, then the recorded spectra, and four component fits to them, indicate that this state must persist in significant proportions to conditions as oxidised as $\log fO_2 = -5$. This is a surprising result if this component does indeed represent a more reduced state than U^{4+}. In addition, the four component fits to the AD M_4-edge spectra are entirely at odds with the two possible solutions derived from thermodynamic modelling of the L_3-edge spectral intensities assuming U^{3+}, U^{4+}, U^{5+}, and U^{6+}. The oxidation state values derived from the four component fits will be limited by the accuracy of the line-shapes used for each U component. However, whilst the residuals between the true spectra and model fits for oxidised spectra are sufficiently large to suggest that at least some of the U M_4-edge oxidation state line-shapes are not identical between MORB and AD glasses, this does not seem to be sufficient to explain the large discrepancies between the two different approaches. If the additional component was assigned to an even more reduced oxidation state the oxidation reaction would involve more electrons and would be expected to occur over a much smaller fO_2 range, which is inconsistent with the M_4-edge four component fits.

5.4 Conclusions

Modelling the variation of the MORB L_3- and M_4-edge XANES spectral shapes with fO_2 using the expected thermodynamic relationships for two one-electron oxidation reactions in a melt produced excellent fits to the data. The agreement between the logK′ values determined across the two datasets and the extraction of a consistent U^{5+} line-shape using a reverse approach suggests that the true solution was obtained. However, application of a similar thermodynamic model and linear combination fits to AD spectra failed to produce a consistent solution.

Chapter 6:

U L_3-edge XANES spectroscopy of silicate melts

6.1 Introduction

U^{5+} has been unambiguously identified as a significant oxidation state in both Fe-bearing and Fe-free glass compositions at geologically relevant fO_2s, with $U^{5+}/\sum U \sim 0.4$ at QFM for MORB at 1 atm (Chapter 5). To determine whether the U oxidation state equilibrium observed in the quenched glasses is representative of the original melts, *in situ* U L_3-edge XANES spectra of silicate melts at high temperatures and controlled fO_2s were recorded using a purpose built XAS furnace. *In situ* studies also allowed the effect of temperature on the U L_3-edge XANES spectra and oxidation state equilibrium to be investigated.

6.2 XAS furnace

The small one-atmosphere gas mixing furnace described in Berry *et al.* (2003a), and shown in Fig. 6.1 was used for the *in situ* experiments. The furnace can heat a sample up to temperatures of ~1500 °C in a controlled gas environment. It consists of a central alumina tube that is resistively heated using a $Pt_{0.6}Rh_{0.4}$ winding. The sample is suspended in the centre of this tube on an alumina sample rod that is locked in place by a compression O-ring seal in the furnace lid. The heating element windings are further supported and held in place by an outer alumina tube machined to fit snugly around the inner furnace tube. A piece of Pt foil wrapped around the central section of the outer furnace tube acts as a heat shield, and the whole assembly is surrounded by a nickel foam cylinder to provide insulation. The ends of the furnace tubes are centrally aligned, supported, and insulated by precisely machined pyrophyllite cylinders. In the lower pyrophyllite cylinder the furnace heating wires clamp into two Cu rods, which exit the furnace's outer aluminium casing through insulated O-ring

seals; these provided the power contacts for heating. The outer Al body of the furnace is cooled by circulating water through its base and lid.

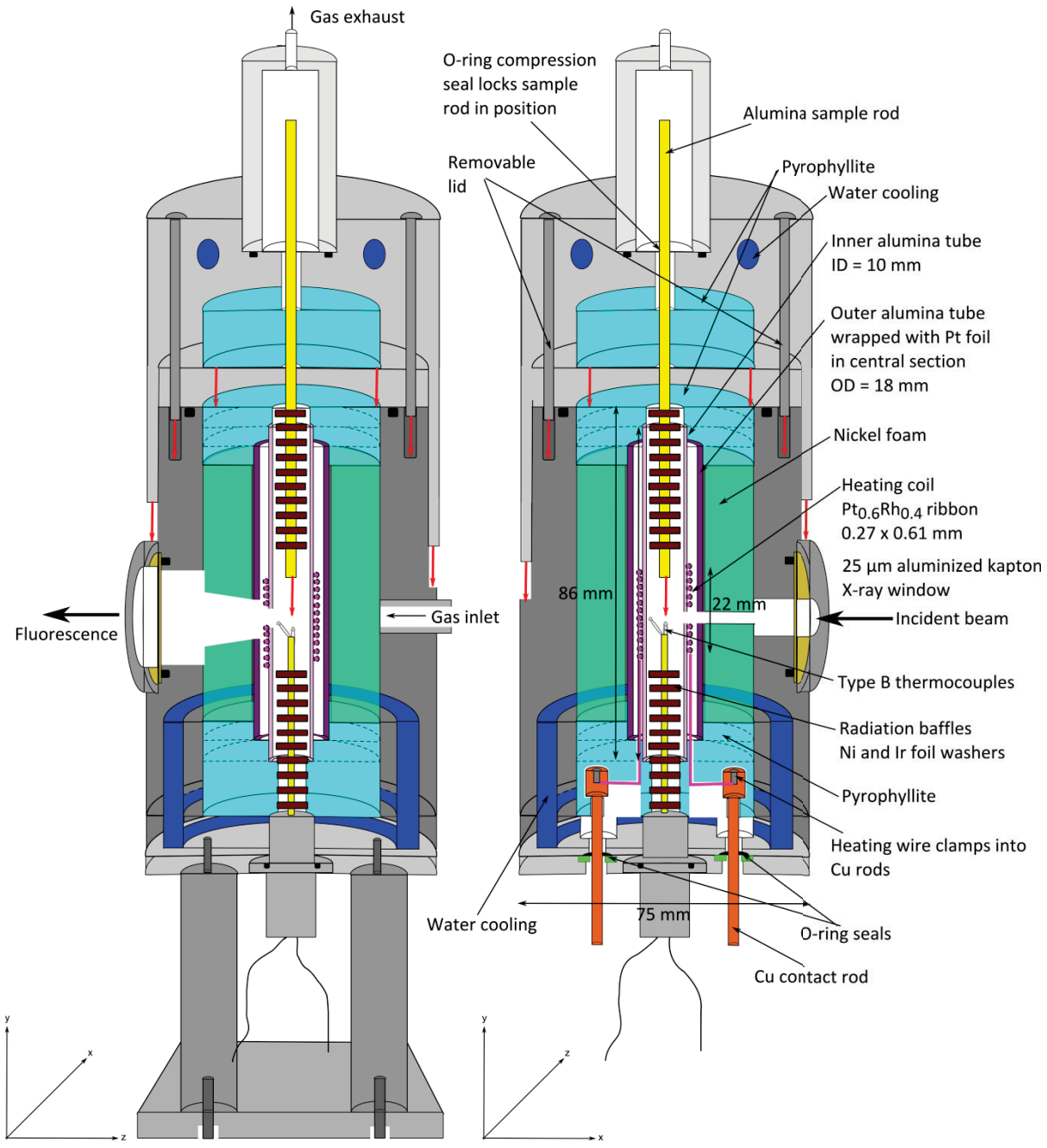


Figure 6.1: Cross sections through the controlled atmosphere XAS furnace. The sample rod is locked into the lid of the furnace that can be removed for sample changes. The illustrations show the furnace lid as it is being lifted away, whilst the red arrows indicate its position when the furnace is closed and sealed.

With dimensions of ~75 mm (diameter) × 300 mm (height) and a weight of ~2 kg the furnace is portable and light enough to be mounted on the motorised sample stages of synchrotron beamlines, Fig. 6.2. The furnace is compatible with XAS measurements in fluorescence mode with the inner alumina tube, outer supporting tube, and insulation having two holes machined at 90 ° for incident X-ray beam entry and fluorescence X-ray exit. The aluminium outer casing has two gas-tight aluminized kapton windows that are X-ray transparent and reflect heat back to the furnace interior.

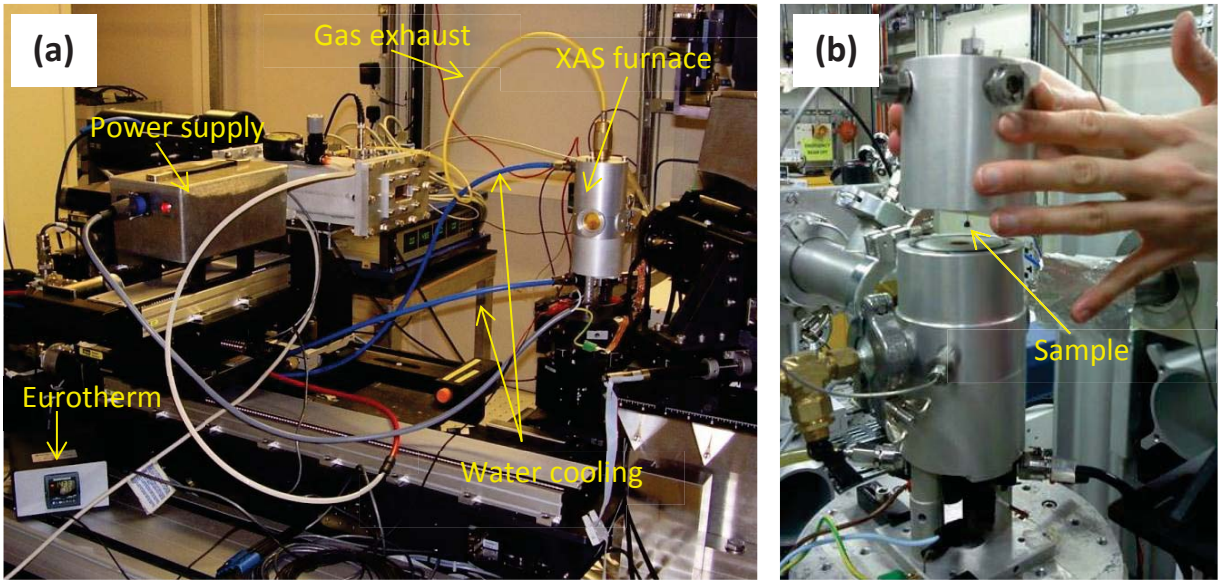


Figure 6.2: The XAS furnace (a) installed on beamline I18 at Diamond Light Source, and (b) during sample loading.

During XANES spectra acquisition the furnace temperature was measured by a Type B thermocouple located against the inside wall of the inner furnace tube just below the level of the sample/windows; at a distance of ~7 mm from the centre of the sample. This was monitored by a Eurotherm controller (model 3216) which controlled the power supplied by a step-down transformer with a maximum output of 40 V at 10 A. The offset between the temperature measured by the control thermocouple and that at the sample position was

calibrated before each beamtime, as described in Appendix A4. Gas flow rates were controlled using Celerity FC2900 CO and CO_2 calibrated MFCs with two flow rate channels for each gas, one slow (up to 10 sccm) and one fast (up to 200 sscm) (see Table 2.1 for gas flow rates). Visual monitoring of an oil bubbler connected to the furnace exhaust tube was used to confirm that the gas was flowing through the furnace. Cooling water was supplied either by an external chiller unit or plumbed directly from the beamlines own cooling system.

The need for an uninterrupted path from the kapton windows to the centre of the furnace means that all the furnace parts, including the heating element, thermocouple, and insulation are exposed to the sample gas atmosphere. The upper fO_2 value is limited by the oxidation of Ni insulating components, and the lower value by the corrosion of the Pt heating element and thermocouple arising from the absorption of C. As such, with all of its original components, the furnace can heat samples up to 1500 °C in CO-CO_2 gas atmospheres covering an fO_2 range of $\log fO_2$ = -3 to -12 (at 1400 °C). The upper fO_2 limit of the furnace has been extended to $\log fO_2$ = 0 (pure O_2) for *in situ* studies of Ce-bearing melts (Appendix A5), by exchanging the Ni foam insulation for alumina ceramic foam. However, this adaption was not used for studies of U-bearing melts because it was inappropriate to achieve highly oxidising conditions where U is volatile. The $\log fO_2$ of the furnace atmospheres were calibrated for gas mixtures of $\log fO_2 \leq$ -8 using the solubility of Fe, Ni and Co in silicate melts, as discussed in Appendix A4.

A key consideration before *in situ* XANES experiments is the absorption of the incident X-ray beam and emitted fluorescence during transit through the furnace. The absorption of X-rays of a particular energy can be expressed by the absorption/attenuation length of the material, which is the distance after which ~63 % of the incident photons have been stopped

(or the beam has dropped to 1/e). The incident X-ray beam and the resulting fluorescence from the sample must pass through the aluminized kapton windows and the furnace gas atmosphere in order to reach the sample and the detector, respectively. As shown in Table 6.1, the absorption of X-rays at the U M_4-edge is too large for the acquisition of XANES spectra using this XAS furnace.

Table 6.1: Absorption lengths for furnace window materials and gas atmospheres at the L_3- and HERFD M_4-edge X-ray energies. Calculated from Hephaestus software (Ravel and Newville, 2005).

Absorber	Path length in furnace	Absorption length		
		U M_4-edge (3725 eV)	U M_β line (3337 eV)	U L_3-edge (17172 eV)
Kapton	25 μm	117.8 μm	84.7 μm	9660 μm
Aluminium	sub-micron layer	8.4 μm	6.2 μm	690 μm
CO_2	3.75 cm	5.25 cm	3.80 cm	465 cm
CO	3.75 cm	9.84 cm	7.10 cm	859 cm

6.3 Experimental methods

In situ U L_3-edge XANES spectra of U-bearing melts were recorded at beamline I18 of Diamond Light Source. Spectra were collected in two separate sessions, in March and May 2013. The excitation energy was selected using a Si(111) double crystal monochromator. The Rh coated toroidal mirror before the crystal monochromator rejected higher order harmonics. The spectral energy resolution, a combination of the Darwin width of the monochromator (2.40 eV at 17172 eV) and the U L_3 core-hole width (7.43 eV, Krause and Oliver 1979; Hämäläinen *et al*., 1991), was ~7.8 eV. Fluorescence was recorded using a 9 element Ge detector and the X-ray beam size on the sample was ~300 × 300 μm (H × V).

Spectra were recorded over the energy range 17000-17400 eV, with a step size of 10 eV in the pre-edge region (17000-17145 eV), 0.5 eV over the white-line (17145-17190 eV), 2 eV in the near post-edge region (17190-17250 eV), and 10 eV in the far post-edge region (17250-17400 eV), with a counting time of 1 s per point, resulting in a total acquisition time of 7-9 minutes per spectrum. Spectra were recorded from MORB melts at temperatures between 1200 and 1500 °C, and from AD melts at 1400 °C, and logfO_2 values between -3 and -12 (values at 1400 °C). Between changes in fO_2 or temperature, XANES spectra were recorded sequentially until no further change in spectral shape was observed indicating that equilibrium had been reached. Finally, a further 5-10 spectra were recorded and averaged. As the glass loops had been pre-equilibrated at each fO_2 (as discussed in section 2.2.1.1) melts typically reached equilibrium within the time taken to record 1-2 spectra. As a direct comparison, XANES spectra were also collected from many of the pre-equilibrated glass loops at RT. To allow comparison between different beamtimes, including those when spectra from the quenched glasses (Chapter 4) were acquired, reference spectra were collected from several of the same glasses during each session.

6.4 Results

The *in situ* spectra were normalised using the same methodology and energy ranges as those applied to the glass spectra reported in Chapter 4. A linear base-line fitted to the pre-edge energy range, 17000-17070 eV, was subtracted followed by division by a linear function fitted in the post-edge between 17230 and 17400 eV. The effect of this edge-step normalisation on AD spectra acquired separately with either the nickel or ceramic foam insulation inside the furnace, but during the same session and at the same temperature and fO_2 conditions, is shown in Fig. 6.3. The spectra exhibit slightly different background shapes

(different gradients in their post-edge regions) meaning that a linear functional form rather than a single average value is required for consistent normalisation.

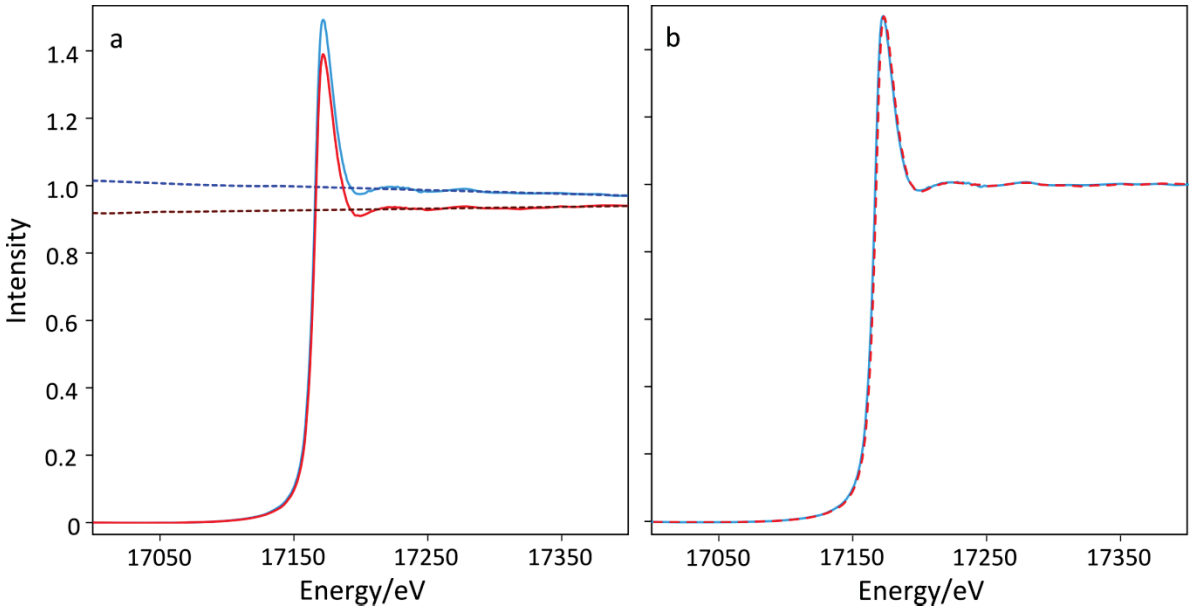


Figure 6.3: U L_3-edge XANES spectra of AD melts equilibrated at 1400 °C and logfO_2 = -5 recorded during the same session but using different furnace insulating parts (a) before and (b) after normalisation to the edge-step. Normalisation was achieved by division by a linear function (shown in a) fitted in the post-edge between 17230 and 17400 eV.

In situ spectra were not expected to exhibit beam damage, as was observed for the AD glasses (section 4.3.1), because the samples were able to constantly re-equilibrate with the imposed gas atmosphere and temperature. The data collection method in itself was sufficient to discount beam damage as the spectra recorded sequentially at a single set of conditions were sufficiently similar after equilibrium had been reached. In contrast, the beam damage previously reported for AD glasses was manifested as a decrease in the normalised spectral white-line intensity that was observable between consecutive XANES scans with similar acquisition times to those used for the melts.

The spectra collected from both MORB and AD melts varied systematically with fO_2 at all temperatures. The relative changes in spectral shape with fO_2 were analogous to those of spectra collected from the equivalent glasses (reported in Chapter 4), as shown in Fig. 6.4; the white-line shifted to higher energy, broadened, and became increasingly asymmetric as the melts became more oxidised. Spectra collected from quenched glasses (pre-equilibrated loops prior to first heating) exhibited more intense white-lines than those collected from their equivalent *in situ* melts at 1400 °C (Fig. 6.5). Spectra of MORB melts equilibrated under a constant gas mixture at a range of temperatures also exhibited a systematic decrease in white-line intensity with increasing temperature.

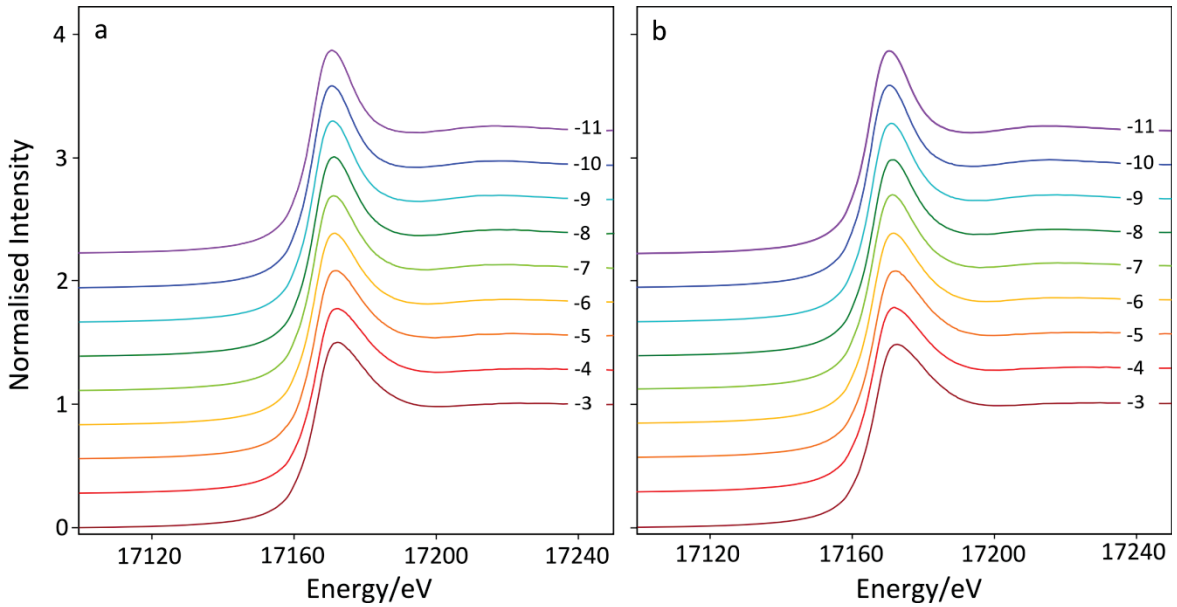


Figure 6.4: U L_3-edge XANES spectra of (a) MORB and (b) AD melts equilibrated at 1 atm, 1400 °C and the logfO_2 values indicated.

6.4.1 XANES analysis

6.4.1.1 Glasses vs. melts

As for the spectra of U-bearing glasses, the variations of spectral features with fO_2 for *in situ* melts at a particular temperature are expected to be oxidation state controlled, and thus have a sigmoidal form comprising of one or more sigmoid functions. However, due to the limited

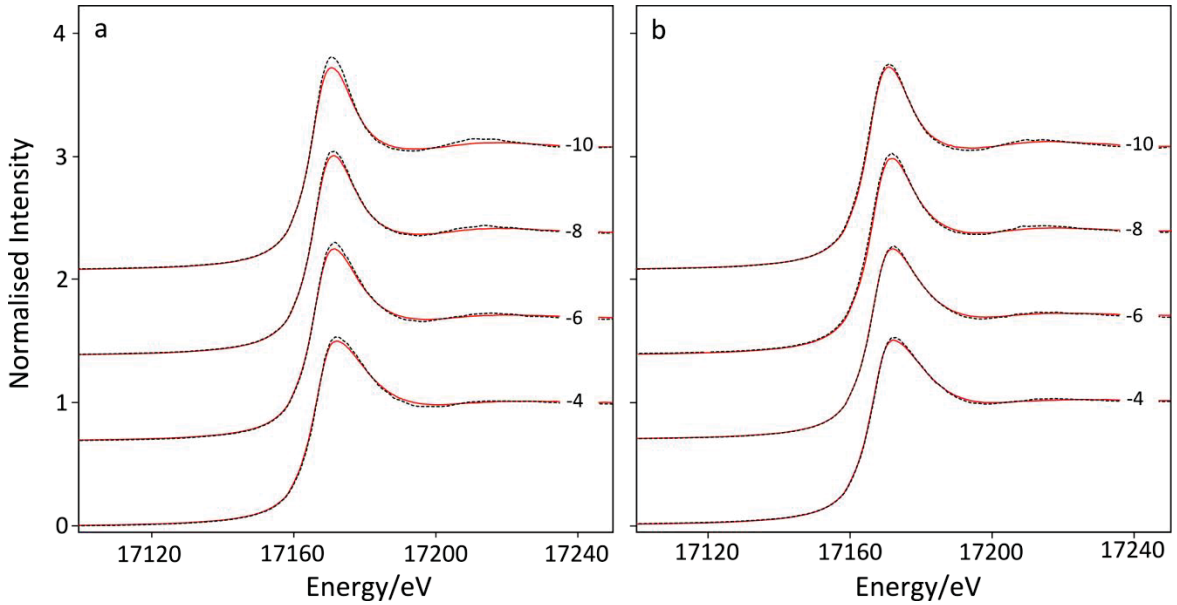


Figure 6.5: U L_3-edge XANES spectra of (a) MORB and (b) AD melts (red) and RT loops (black) equilibrated at 1 atm, 1400 °C and the logfO_2 values indicated.

---

fO_2 range of the melt data, even a single-sigmoid fit requiring only four parameters will have too little constraint on its oxidised limit to necessarily produce a robust and reliable solution. In addition, a single outlying data point will have a far greater influence on the derived fit parameters than for the glass data, particularly if this data point is amongst the most oxidised of the set. For these reasons the best approach to analysing the L_3-edge XANES spectra of the melts was by direct comparison with the spectra of equivalent glasses.

Features of AD and MORB melt spectra were compared with those of AD and MORB glasses (reported in Chapter 4). All samples discussed in this section were equilibrated at 1400 °C. The energies of all the spectra were shifted so that spectra of the calibration samples (those collected during all sessions) were aligned. This energy shift was constant for a given beamtime, thus the calibration did not change the relative variation of a particular feature within each dataset. The features selected for comparison were the maximum intensity of the white-line, the energy value at an intensity of 0.7 on the edge-rise, and the energy value at an intensity of 1.1 on the post-edge shoulder. The values of these spectral features were

determined after smoothing the raw data by recreating each spectrum using a number of Gaussians; the purpose of this was only to remove the noise from each spectrum (the same protocol as used in Chapter 4).

The variations in the maximum white-line intensities of the MORB and AD melt spectra with fO_2 are shown in Fig. 6.6. These variations are consistent with the expected sigmoidal relationship. The spectra of reduced MORB and AD melts ($\log fO_2$ = -11) have almost identical white-line intensities (dashed line in Fig. 6.6). This is in stark contrast to the large difference in MORB and AD spectral intensities for the equivalent quenched glasses, where MORB spectra exhibited a significantly more intense white-line maximum. The change in intensity between a glass and melt of equivalent composition and fO_2 are of a comparable magnitude to those observed between glasses equilibrated over several log units of fO_2.

The change in intensity between spectra of melts and glasses equilibrated at equivalent fO_2s was defined as the white-line crest intensity of the glass spectrum divided by the white-line

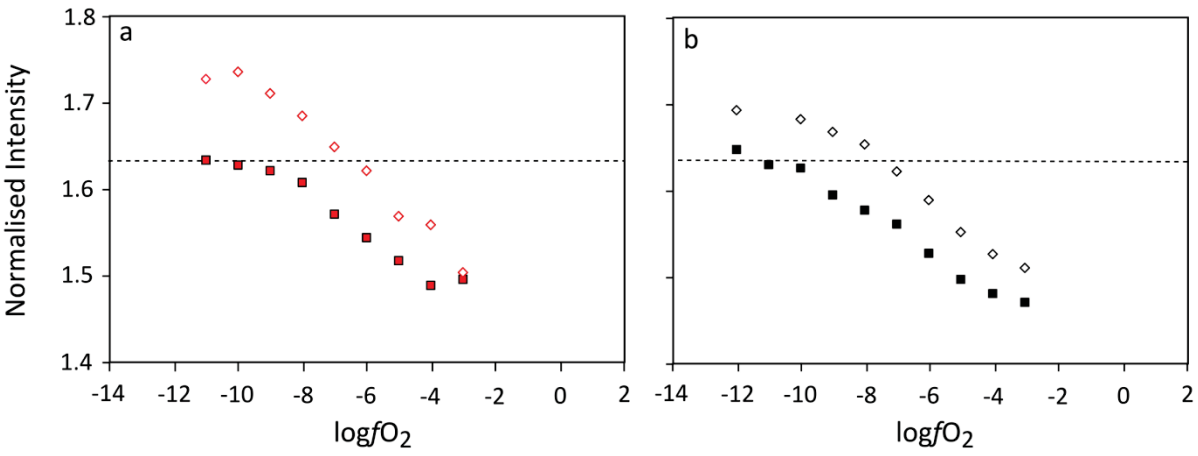


Figure 6.6: Maximum white-line intensities of U L_3-edge XANES spectra of (a) MORB (red) and (b) AD (black) melts (filled squares) equilibrated at 1400 °C as a function of fO_2. The data for equivalent glasses (unfilled diamonds) are shown for comparison. Dashed lines indicate the maximum intensity of the spectrum of the MORB melt equilibrated at $\log fO_2$ = -11.

crest intensity of the melt spectrum. Thus, a value of 1 indicates that the melt and glass had equivalent white-line intensities, whilst a value > 1 indicates that the glass white-line maximum was more intense. The relative intensity change between glass and melt spectra as a function of fO_2 are shown in Fig. 6.7. Since the melt and glass spectra were collected on separate occasions, it is not the absolute y-axis values that are of interest but the overall variation within a particular dataset. Whilst even small variations in the maximum intensity or the normalisation of a particular spectrum will have a large impact on the y-axis value in Fig. 6.7, comparison of the overall distributions suggests that the intensity offsets are not constant with fO_2 and are different for MORB and AD spectra. The MORB data exhibit a broadly negative correlation, indicating an increase in the offset between glass and melt white-line intensities with decreasing fO_2. In contrast, the variations of the AD melt-glass offsets with fO_2 exhibit a slightly "humped" profile, with a maximum at $\log fO_2 = -8$. The divergence of the MORB and AD trends at reduced fO_2s is clearly controlled by the significant differences in the white-line intensities of the glass spectra between the two compositions at these fO_2s.

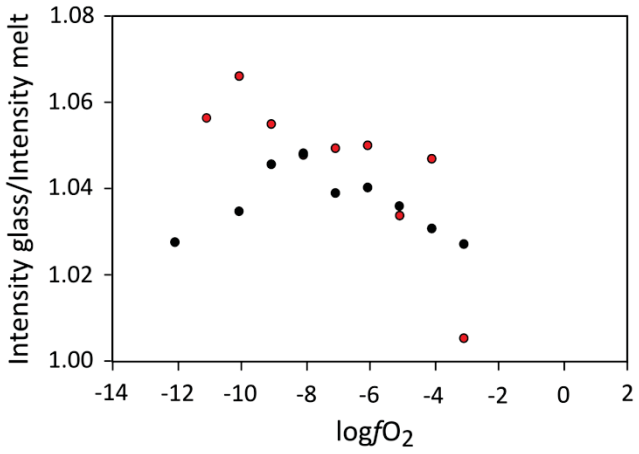


Figure 6.7: Maximum white-line intensity of U L_3-edge XANES spectra of MORB (red) and AD (black) glasses equilibrated at 1400 °C relative to those of equivalent *in situ* melts as a function of fO_2 of sample equilibration.

The variations of the spectral edge-energies as a function of fO_2 are shown in Fig. 6.8(a) and 6.8(b). The edge-energy value was taken at a normalised intensity of 0.7 as this appeared to represent the largest energy offset for a particular sample in transforming from a pre-equilibrated glass to an *in situ* melt. The total shift in the edge-energy of spectra from reduced to oxidised for the fO_2 sets ($\log fO_2$ = -3 to -11) were ~1.4 eV and ~1.3 eV, for MORB glasses and MORB melts, respectively, and ~2.1 eV and 1.65 eV for AD glasses and melts.

The energy shifts of the edge between equivalent glasses and melts (i.e. energy melt-energy glass) as a function of fO_2 are shown in Fig. 6.8(c); a y-axis value of 0 corresponds to no shift. The edge-energy shifts are relatively small, with the spread of values across the whole fO_2 range, shown as shaded regions in Fig. 6.8(c), amounting to ~0.2 eV for MORB and ~0.6 eV for AD. In comparison, the shift between the U^{4+} and U^{5+} end-member L_3-edge spectra for MORB glasses (Chapter 5) was ~2 eV. There is no systematic variation in the MORB edge-energy offsets with fO_2, and the scatter within the data is likely to represent the uncertainty associated with the edge-step values, which is controlled by the monochromator energy stability/reproducibility during the XANES data collection sessions; a scatter of ~0.2 eV is significantly smaller than one energy step of the monochromator (0.5 eV over the white-line). The greater spread of the offset values for AD spectra extends to higher values than for MORB, indicating that the edge-energy of some of the glass spectra are at lower values than their equivalent melts. The AD offsets exhibit a broadly negative trend with fO_2, such that the largest offsets between melt and glass spectra occurred for the most reduced samples.

The same approach as outlined for the edge-energy was applied to the spectral energy at a normalised height of 1.1 in the post-white-line region, as shown in Fig. 6.9. In this case MORB and AD melt-glass offsets exhibit similar degrees of spread/scatter (shaded regions in

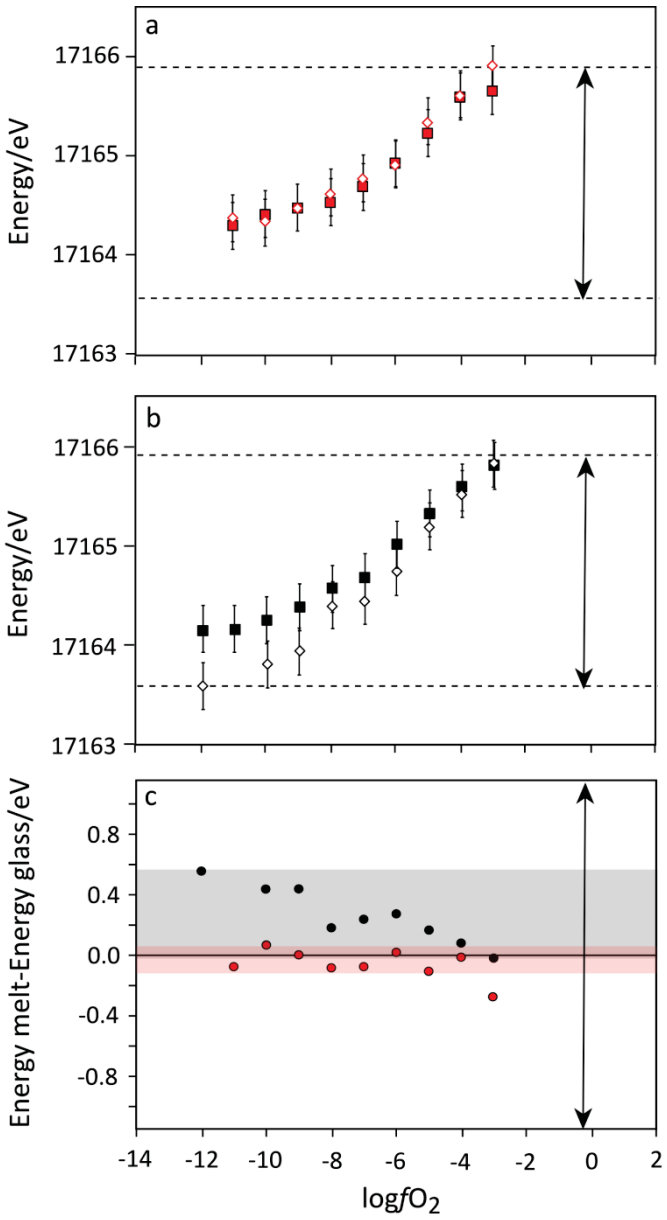


Figure 6.8: Edge-energy at a normalised intensity of 0.7 of U L_3-edge XANES spectra of (a) MORB and (b) AD melts (filled squares) and glasses (unfilled diamonds), equilibrated at 1400 °C, as a function of fO_2. Error bars represent the upper estimate of the uncertainty in energy due to the monochromator reproducibility and drift over a single session; this estimate is based on replicate spectra. Panel (c) shows the difference in edge-energies of equivalent MORB (red) and AD (black) melts and glasses as a function of fO_2 of sample equilibration. Shaded regions in (c) indicate the energy spread of MORB (red) (excluding $\log fO_2$ = -3 outlier) and AD (grey) data. Dashed lines in (a) and (b) mark the upper and lower limits of the edge-energy values, which occur for AD glasses equilibrated at $\log fO_2$ = -3 and -12, respectively. The arrows indicate the energy spread of these limits and are shown in panel (c) for a comparison of scale.

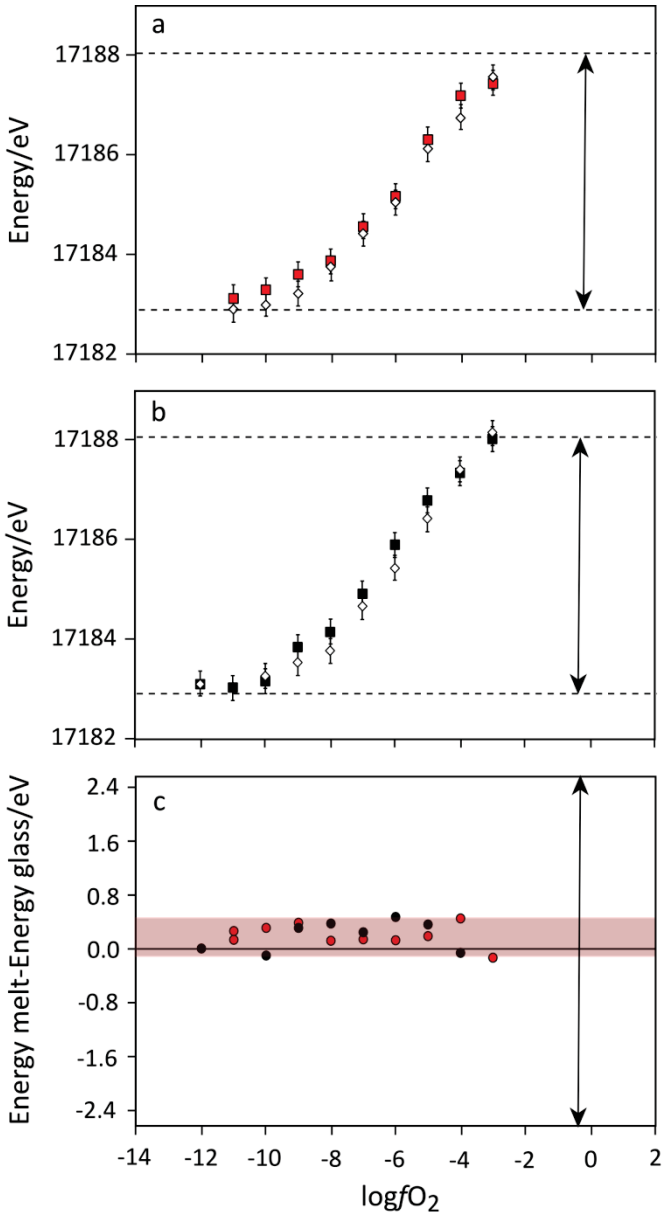


Figure 6.9: Post-white-line energy at a normalised intensity of 1.1 of U L_3-edge XANES spectra of (a) MORB and (b) AD melts (filled squares) and glasses (unfilled diamonds), equilibrated at 1400 °C, as a function of fO_2. Error bars represent the upper estimate of the uncertainty in energy due to the monochromator reproducibility and drift over a single session; this estimate is based on replicate spectra. Panel (c) shows the difference in post-white-line energies of equivalent MORB (red) and AD (black) melts and glasses as a function of fO_2 of sample equilibration. Shaded regions in (c) indicate the energy spread of MORB (red) and AD (grey) data. Dashed lines in (a) and (b) mark the upper and lower energy values, which occur for AD glasses equilibrated at $\log fO_2$ = -3 and -12, respectively. The arrows indicate the energy spread of these limits and are shown in panel (c) for a comparison of scale.

Fig. 6.9(c)), and no systematic variation with fO_2. The larger energy spread of the MORB post-edge melt-glass offsets (~0.6 eV) when compared to those of the edge-rise most likely reflects the shallower gradient of the spectral line-shapes in the post-edge relative to the steep edge-rise. A shallower gradient will be more sensitive to uncertainty in normalisation because the energy range covered by a small intensity change is larger.

6.4.1.2 Effect of temperature

In this section, MORB melts equilibrated under a particular gas atmosphere at a range of temperatures are compared to each other. Whilst the absolute fO_2 of a particular CO + CO_2 gas mixture changes significantly with temperature (e.g. for 94 % CO and 6 % CO_2, logfO_2 changes from -13.4 to -10.0 between 1200 and 1500 °C), the fO_2 only varies by ~0.3 log units relative the QFM buffer. Spectra recorded from MORB melts at ~QFM+0.2 (logfO_2 = -6 at 1400 °C) at various temperatures are shown in Fig. 6.10(a). The change in the white-line intensity with temperature over ~200 °C is comparable to that observed for a log unit change

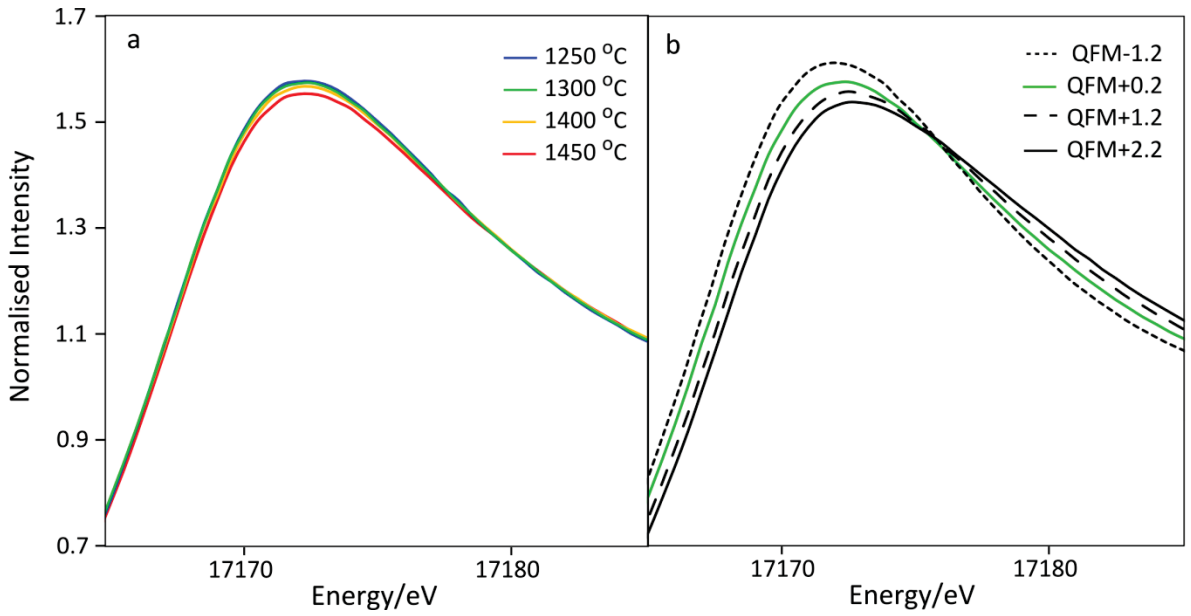


Figure 6.10: U L_3-edge XANES spectra of MORB melts equilibrated (a) at ~QFM+0.2 (logfO_2 = -6 at 1400 °C) as a function of temperature, and (b) at 1300 °C as a function of fO_2.

in fO_2 at a set temperature (Fig. 6.10(b)); the spectrum of a MORB melt equilibrated at QFM+0.2 at 1450 °C has much the same intensity as the spectrum of a melt equilibrated at QFM+1.2 at 1300 °C. However, this temperature induced intensity change is not accompanied by a significant edge-energy shift or broadening in the post white-line region, which is clearly discernible for a single log unit change in fO_2.

Temperature sets of melt spectra were quantitatively compared using the same features and methodology as for the comparison of glasses and melts in the previous section (6.4.1.1). The changes between spectral features for melts equilibrated at 1400 °C relative to all other temperatures (1200-1500 °C) are shown in Fig. 6.11 and are entirely consistent with the observations previously summarised for selected spectra in Fig. 6.10. Energy shifts of the edge-step (Fig. 6.11(a)) and post-edge shoulder (Fig. 6.11(b)) are generally very small and exhibit no systematic variation with fO_2. The melt spectral intensities decrease systematically with increasing temperature for a particular gas atmosphere, but there is no evidence of a systematic variation in the magnitudes of these changes as a function of fO_2 (Fig. 6.11(c)).

6.5 Discussion

6.5.1 Temperature

The offsets in white-line intensities between equivalent glasses and melts exhibit systematic variations with fO_2 for both MORB and AD samples, and are of a comparable magnitude to the intensity variation associated with significant changes in U oxidation state for fO_2 sets of spectra. However, a decrease in the white-line peak intensity in going from a glass to a melt, and with increasing melt temperature, is not necessarily indicative of an oxidation state change. Increasing temperature may cause changes in coordination environment or symmetry around the absorbing ion due to thermal expansion of bonds around the cation and/or changes

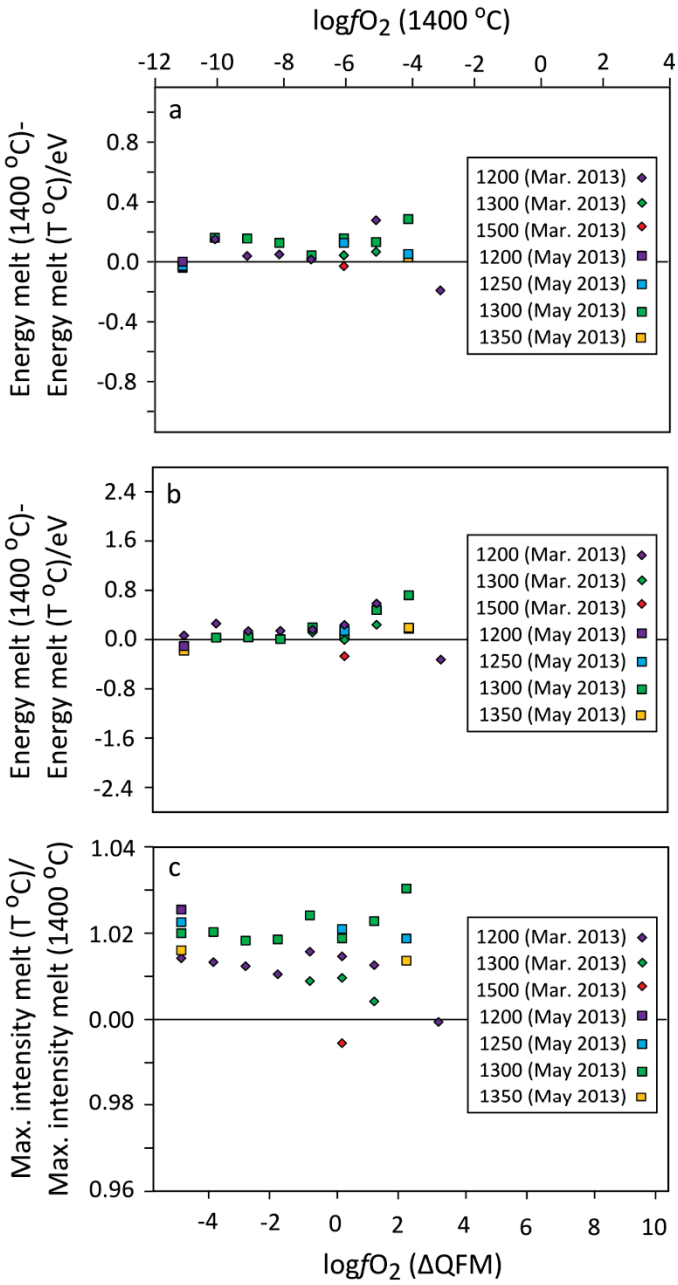


Figure 6.11: Relative changes of the (a) edge-energy at a normalised intensity of 0.7, and (b) post-white-line energy at a normalised intensity of 1.1, and (c) maximum white-line intensity of U L_3-edge XANES spectra between MORB melts equilibrated at 1400 °C (collected in March 2013) and MORB melts equilibrated at the temperatures indicated, T, under a constant gas atmosphere. X-axes show logfO_2 values corresponding to each gas mixture at 1400 °C (top) and relative to the QFM buffer (bottom), which is near constant at all temperatures for a particular gas atmosphere.

in the bulk melt network structure, which may affect the XANES spectral-shape (Wilke *et al.*, 2007; Farges *et al.*, 1996). In addition, a decrease in the intensity of the XANES maximum with increasing temperature is consistent with spectral broadening arising from increased thermal disorder. Similar thermal effects have been reported in other high temperature XANES studies of melts and crystals (Wilke *et al.*, 2007; Farges *et al.*, 1996; Özkendir and Ufuktepe, 2005). Importantly, oxidation states and chemical environments may be influenced differently by changing temperature, indeed, thermal disorder effects can even be asymmetric (or anharmoic) around a single absorbing ion with different bond types/lengths (Farges *et al.*, 1996). Thus, it is impossible to separate changes in U oxidation state from the temperature dependence of the different pure U oxidation state line-shapes using the intensity of the white-line alone.

Whilst the intensity of the white-line decreases in going from a glass to a melt and with increasing melt temperature, comparison of the post-crest region (i.e. energy at a normalised intensity of 1.1) of MORB spectra of equivalent melts and glasses does not show any significant or systematic change. Similarly, the variation of melt-glass edge-rise energies for the MORB spectra is well within the estimated energy uncertainty of the experiments. There is also no evidence of significant shifts in edge-energy as a function of melt temperature under a particular gas atmosphere. In contrast, for both MORB glass and melt fO_2 series, increasing U oxidation state is manifested as a decrease in the intensity of the white-line peak accompanied by significant shifts in edge-energy and broadening in the post-crest region. Thus, there is no indication that the temperature induced changes in MORB spectra white-line intensities, either between glasses and melts or as a function of temperature, result from a change in U redox ratios.

The lack of evidence for any electron exchange reactions between Fe and U on quenching is consistent with previous studies of redox interactions between U and Fe (Schreiber *et al.*, 1983). This has been attributed to the similarity of the electrochemical reduction potentials (i.e. -logK′) for Fe and U (Schreiber, 1987; Schreiber *et al.*, 1987). Notably, the argument for predicting redox interactions from the difference in reduction potentials does not appear to hold for Eu, which has similar logK′ values to Cr, and yet is not fully oxidised to Eu^{3+} by Fe^{3+} on quenching (Burnham *et al.*, 2014; Berry *et al.*, 2006).

For MORB melts equilibrated in CO_2 + CO atmospheres (logfO_2 = -4 to -11 at 1400 °C) the relative fO_2 change with temperature is constant for all gas mixing proportions, and hence will not affect the relationships observed for a particular fO_2 set. In addition, the $U^{4+} \rightarrow U^{5+}$ and $U^{5+} \rightarrow U^{6+}$ logK′ values determined previously for the MORB glasses equilibrated at 1400 °C (Chapter 5) indicate that the U^{4+} and U^{5+} states make up > 95 % of all the U present over the fO_2 range of the furnace data. Thus, it is primarily the $U^{4+} \rightarrow U^{5+}$ reaction that is being considered here, and the logK′ value derived for 1400 °C from MORB glasses can simply be corrected for temperature by accounting for the shift in the absolute fO_2 values. For example, in the case of cooling under a constant gas mixture from 1400 to 1200 °C:

$$\Delta \log fO_2 = -2.4 \tag{6.1}$$

Since -4logK′ is the inflexion point of the sigmoid (i.e. $U^{4+}/\sum U$ = 0.5), and the whole sigmoid (including its inflexion point) is simply shifted by ΔlogfO_2, the new logK′ value can be calculated as outlined below:

$$\log K_{A\,(1400)}{}' = \frac{-\log fO_{2,\text{inflexion (1400)}}}{4} \tag{6.2}$$

$$\log K_{A\,(1200)}{}' = \frac{-\log fO_{2,\text{inflexion (1400)}} - \Delta \log fO_2}{4} \tag{6.3}$$

$$\Delta \log K_{A\,(1200)}' = \log K_{A\,(1400)}' + 0.6 \quad (6.4)$$

This temperature dependence for $\log K_A'$ is significantly smaller than that previously reported for two Na-bearing CMAS glass compositions (ADA-1 and ADA-2), where $\log K_A'$ was estimated to change by ~1.5 between 1450 and 1250 °C (Schreiber, 1983).

Examination of the edge-rise shift between AD glasses and melts indicates a systematic variation as a function of fO_2 (Fig. 6.8(c)). For AD spectra the largest edge-energy offsets between melts and glasses occur at reduced fO_2s, with the spectra of melts shifted to slightly higher energies than their equivalent glasses. It is notable that the spectra of reduced MORB and AD melts ($\log fO_2$ = -11) are almost identical, whilst spectra collected from their RT glasses prior to first heating are significantly different, with the AD spectrum having a much lower white-line intensity and a slightly lower edge-energy than the MORB spectrum (Fig. 6.12). In previous chapters it has been shown that, in addition to the U^{4+}, U^{5+}, and U^{6+} states similar to those observed in MORBs, AD (and other Fe-free composition) glasses must contain a fourth U component. The proportion of this fourth component increases with decreasing fO_2, and is characterised by a decrease in white-line intensity and edge-energy at the L_3-edge. From the above observations it seems probable that the fourth U component is induced by the quench and thus is not present in AD melts. This interpretation would explain why the U oxidation state proportions of the CMAS glasses could not be successfully modelled from the L_3-edge data using the expected thermodynamic relationships between four U oxidation states in a melt.

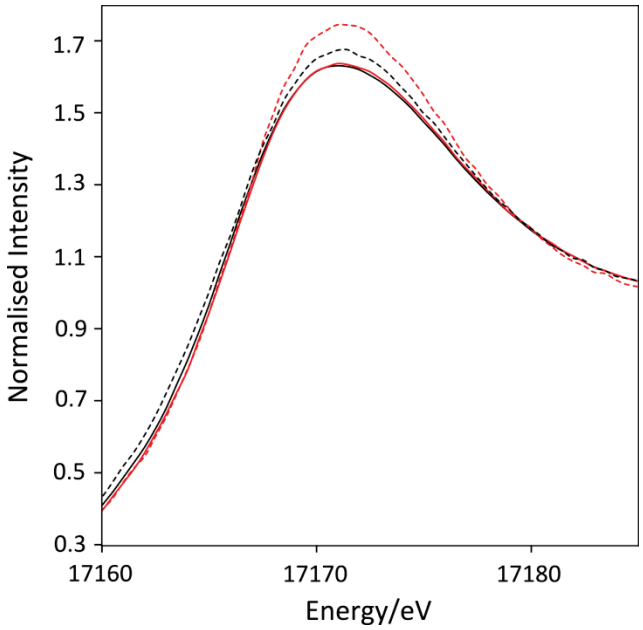


Figure 6.12: U L_3-edge XANES spectra of MORB (red) and AD (black) melts (solid lines) and RT glasses (dashed lines) equilibrated at 1400 °C and logfO_2 = -11.

The apparent change in U state in an Fe-free (and other multivalent element-free) system in going from a melt to a glass is a surprising result, as quench induced changes in redox ratios of other multivalent systems have clearly been linked to electron exchange reactions with Fe (Berry *et al.*, 2006; Burnham and Berry, 2014 and Appendix A5 of this thesis; Burnham *et al.*, in preparation: Appendix A6 of this thesis). One possibility is that some sort of electron exchange reaction or charge disproportionation is occurring between the different U oxidation states of the AD melts during quenching (e.g. $2U^{4+} \rightarrow U^{3+}+U^{5+}$). Alternatively, the additional U component in AD glasses might represent nano-particles of U-metal or a crystalline U component such as UO_2. Indeed, U^{4+} was found to be four times less soluble than U^{6+} in sodium trisilicate glasses (Veal *et al.*, 1987), and a valence dependent decrease in solubility could explain the apparent increase of the fourth component with decreasing fO_2.

For charge transfer between U ions to occur, we might expect them to be very close together in the melt. Since the U is extremely dilute in the glasses studied, this might imply some

degree of U clustering, although this is purely speculative as it is not known over what distances and by what mechanism charge transfer might occur. Similarly, for the case of the presence of a crystalline U compound, we might expect relatively short U-U distances. Farges *et al.* (1992) reported evidence for U-U second neighbours in the EXAFS spectrum of a reduced albite glass (1300 °C, logfO_2 = -13) containing only 1 wt % U, and suggested the presence of crystalline UO_2. However, no evidence of U-U next nearest neighbours was found for any other compositions of the study, which included anorthite, diopside, sodium trisilicate, and rhyolitic glasses, and a composition intermediate between the albite and sodium trisilicate end-members.

If the reduced U component in the AD glasses is a crystalline compound, it is surprising that the normalised L_3-edge XANES spectra white-line intensities decreases as this component presumably increases. A crystalline structure is expected to be associated with an increase in the white-line intensity relative to a glass, similar to that observed between a melt and a glass, due to a decrease in static disorder. In addition, whilst U M_4-edge spectra of both UO_2 and U metallic compounds exhibit similar edge-energies to the reduced AD and MORB glass spectra (i.e. similar to U^{4+}), they are not associated with a substantial pre-edge feature (Kvashnina *et al.*, 2013 and K. Kvashnina: personal communication 07/11/2013). In fact, their spectral line-shapes are very similar to the U^{4+} spectrum of the MORB glasses, although spectra collected from U metallic compounds exhibit broader spectral features.

It is possible that the pre-edge feature in M_4-edge spectra actually represents U^{4+} in a second unusual coordination environment in the AD glasses. Changes in the average coordination number between glasses and melts have been reported for other cations, including Fe and Ti (Wilke *et al*., 2007; Farges *et al*., 1996). These average changes may reflect coordination

changes across only a small fraction of the total ions present, and have been shown to be dependent on composition and oxidation state. For example, a slight increase in the amount of low coordinated (tetrahedral) Fe^{2+} has been noted in reduced alkali-silicate and haplogranitic composition melts relative to their equivalent quenched glasses. In contrast, whilst oxidised alkali-silicate compositions exhibited a similar temperature effect to reduced samples, oxidised haplogranitic compositions did not show significant coordination changes between glasses and melts (Wilke *et al.*, 2007). In the case of citing a coordination change for the U samples of this thesis, the L_3-edge spectra of all the Fe-free glass compositions are consistent with a similar quench effect to that observed for AD samples leading to the conclusion that it is the Fe in the MORB samples that is somehow preventing a quench-induced change in the U environment.

For all of the scenarios outlined above it is surprising that the XANES spectra of AD glasses continue to exhibit variations in line-shape at the most reduced fO_2s (i.e. between $\log fO_2$ = -12 and -18) if all the high temperature melts contain only U^{4+}, which is what might be expected. However, it is not known how reproducible a quench effect such as a coordination change might be across multiple experiments. In addition, without being able to reach this extremely reduced fO_2 range in the *in situ* studies it is impossible to rule out the possibility that two different processes have been superimposed in the glasses. The most reduced melts may indeed contain a fourth U oxidation state that is impossible to unravel from the additional quench effect using the XANES spectra of glasses.

6.5.2 Melt composition

Based on the premise that the fourth U component observed in reduced AD glasses ($\log fO_2 \sim$ -11) did not occur in the equivalent melts at 1400 °C (at least down to $\log fO_2$ = -12), the U

oxidation states in the AD melts are expected to vary according to a two-sigmoid relationship ($U^{4+} \rightarrow U^{5+}$ and $U^{5+} \rightarrow U^{6+}$), as was successfully applied to the MORB glasses in Chapter 5 (section 5.2). However, U^{6+} is not a significant component in the MORB melts over the fO_2 range accessible using the XAS furnace. Based on both the similarity of MORB and AD melts spectral shapes, and the fitting of AD glass M_4-edge spectra (Fig. 5.12 and 5.13), U^{6+} is likely to make up < 5 % of the total U in AD melts at $\log fO_2 \leq -6$. Thus, the intensity variation at the U^{4+} crest energy (~17172 eV) of L_3-edge spectra of MORB and AD melts equilibrated at 1400 °C as a function of $\log fO_2$ was fitted using single-sigmoid functions, with their slopes fixed to that expected for a single electron oxidation ($a/4 = 0.25$: $U^{4+} \rightarrow U^{5+}$). Only spectra where $\log fO_2$ was ≤ -6 or ≤ -5, for AD and MORB, respectively, were included to ensure that the U^{6+} proportion was minimal. The MORB and AD fits were run simultaneously with the sigmoid reduced and oxidised limits constrained to be the same for both compositions.

As shown in Fig. 6.13, both the MORB and AD data are well reproduced by the forced-slope single-sigmoid fits. The fits give a $\log K_A'$ value of 1.5(1) for MORB, which is in good agreement with that reported for two-sigmoid fits of spectra of equivalent glasses ($\log K_A' = 1.38(3)$: Chapter 5). A $\log K_A'$ value of 1.7(1) for AD melts indicates that this higher basicity melt with respect to MORB slightly favours U^{5+} ($\Lambda = 0.607$ compared to $\Lambda = 0.588$). However, this compositional effect is equivalent to a change of less than one unit in $\log fO_2$ for a constant composition. This change in $\log K'$ with composition is in good agreement with $\log K_A'$ values previously reported for two CMAS glass compositions with similar optical basicities to MORB and AD (Schreiber, 1983: FAS = 0.586 and FAD = 0.618), which are shown in Fig. 6.14.

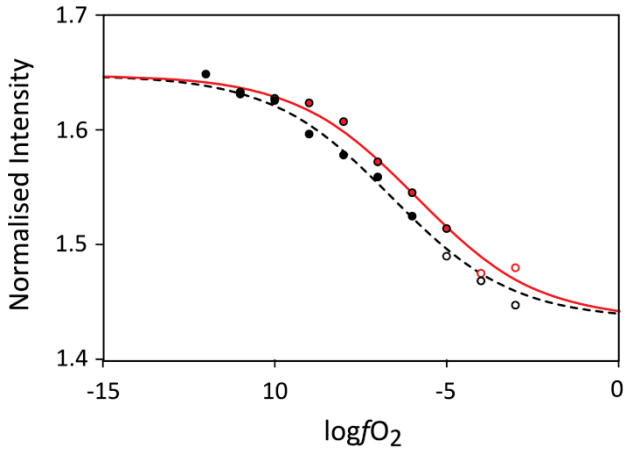


Figure 6.13: Intensity of U L_3-edge XANES spectra of MORB (red) and AD (black) 1 atm *in situ* melts, equilibrated at 1400 °C, at the U^{4+} crest energy (~17172 eV) as a function of fO_2 of melt equilibration. Plots show best-fit single-sigmoid curves. Unfilled data points were excluded to ensure that U^{6+} did not contribute to the fit parameters.

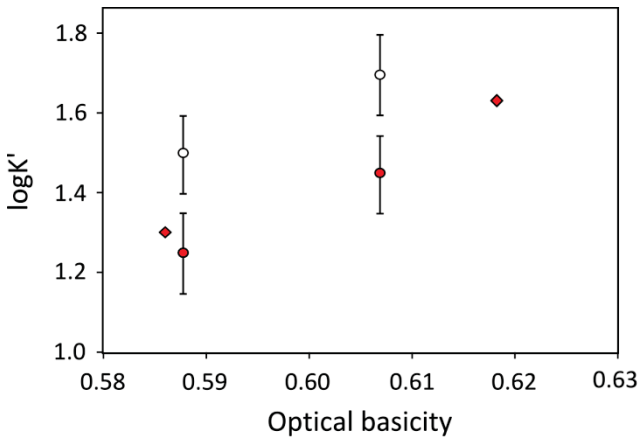


Figure 6.14: $\log K_A'$ values as a function of optical basicity for MORB (Λ = 0.588) and AD (Λ = 0.607) melts at 1400 °C (unfilled circles), and corrected to 1500 °C (red circles). These are compared to values obtained for the FAS (Λ = 0.586) and FAD (Λ = 0.618) composition glasses equilibrated at 1500 °C reported by Schreiber (1983) (red diamonds).

6.6 Conclusions

Changes in XANES spectra between MORB glasses and melts do not suggest a change in U oxidation state on quenching. In addition, when fO_2 is considered relative to the QFM buffer

there is no distinguishable change in the U oxidation state proportions in the melts as a function of temperature. In contrast, comparison of spectra of AD glasses and melts equilibrated at 1400 °C seems to indicate a quench induced change in U chemical state at reduced conditions, although it is not clear what the nature of this change is.

Chapter 7:

Geological Implications

7.1 Introduction

Widely accepted U-series models (Stracke *et al.* 2003; Spiegelman and Elliott, 1993; McKenzie, 1985 and 2000) suggest that the ^{230}Th excesses characteristic of MORBs can be generated by decompression melting in the presence of garnet, or in the spinel lherzolite stability field at pressures > 10 kbar where $D_U/D_{Th} > 1$ for clinopyroxene (Landwehr *et al.*, 2001; Wood *et al.* 1999; Blundy and Wood, 2003). Melting at lower pressure is expected to result in $D_U/D_{Th} < 1$ for clinopyroxene creating the potential for the generation of ^{238}U excesses, as has been suggested for rare small U excesses (~5 %) in MORBs (Tepley *et al.*, 2004). However, the relative change in U and Th partition coefficients with decreasing pressure caused by changing clinopyroxene chemistry is not sufficient to explain the large U excesses observed in many arc basalts (e.g. Lesser Antilles: Huang *et al.*, 2011; Mariana Arc: Avanzinelli *et al.*, 2012; Tonga-Kermadec Arc: Caulfield *et al.*, 2012) as $D_U/D_{Th} \geq$ ~0.9 (Landwehr *et al.*, 2001). As such, arc U excesses have been widely attributed to the addition of U-enriched slab derived fluids (Turner *et al.*, 2003; Turner *et al.*, 2001). If the (^{226}Ra/^{230}Th) disequilibria of arc magmas are also a slab signature then this requires mass transfer times, from slab to eruption, of less than a few thousand years (Turner *et al.*, 2001). The U partition coefficients utilised by many U-series models are based on the assumption that U occurs only as U^{4+}. However the potential for significant U^{5+} proportions at the conditions of melt generation, transport, or differentiation should be considered, as this is likely to have a large impact on the bulk partitioning behaviour of U (Lundstrom *et al.*, 1994).

7.2 U-series at MORs

The oxygen fugacity of the MOR mantle has been estimated to be in the range QFM-1 to QFM+0.2 (Bézos and Humler, 2005; Cottrell and Kelley, 2011; Lee et al. 2005; Mallmann and O'Neill, 2009). The results of this study suggest that for MORB melts at ≥ 5 kbar $U^{4+}/\sum U$ = 0.8-0.9 over this fO_2 range (Fig. 7.1). Thus, the U partition coefficients of MORB U-series melting models are likely to be slightly overestimated. In contrast, significant proportions of U^{5+}, $U^{5+}/\sum U$ ~0.4, are stabilised at the same fO_2s at 1 atm. The exact pressure dependence of this change in U^{4+}-U^{5+} equilibrium is not known and the presence of significant U^{5+} at pressures relevant to MOR magma chambers ~1-4 km (pressure ~0.5-1.5 kbar) below the seafloor (Rubin and Sinton, 2007) cannot be ruled out. However, the high incompatibility of the U-series elements means that low pressure fractional crystallisation of MORBs is not expected to have any leverage on the mantle derived U-series regardless of whether U occurs in the tetravalent or pentavalent state.

7.3 U-series at Arcs

An alternative model for the ($^{238}U/^{230}Th$) systematics of arc magmas, where partial melting at higher oxygen fugacities than in the MORB source increases the incompatibility of U relative to Th, has been proposed, (Beier *et al.*, 2010; Huang *et al.*, 2011; Reubi *et al.*, 2011; Reubi *et al.*, 2014). There is little doubt that arc lavas are more oxidised than MORBs (Kelley and Cottrell, 2009, Jenner *et al.*, 2010). However, it is not clear whether this is a reflection of melting of a more oxidised arc mantle source or results from a later differentiation process. V/Sc and V/Ga ratios of MOR and arc basalts have been used to suggest that the fO_2 of the arc mantle is equivalent to that of MORs (Lee *et al.*, 2005; Mallmann and O'Neill, 2009). In contrast, V/Yb ratios of lavas from many MOR and arc settings have been suggested to be consistent with variable oxidation of the primary arc magma source (up to ~QFM+2.5)

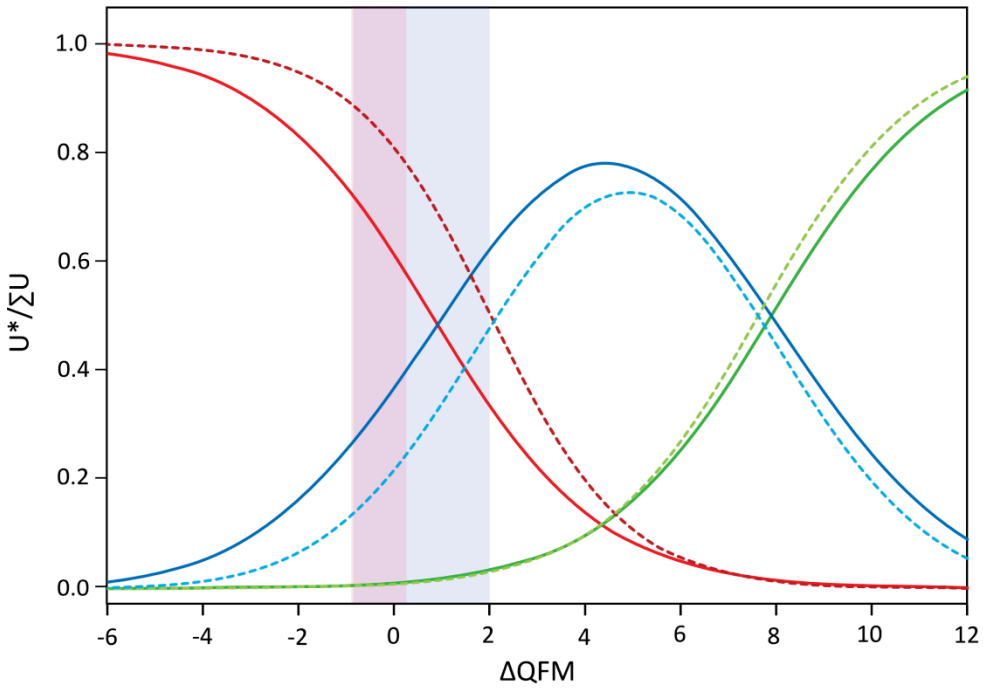


Figure 7.1: Estimated U oxidation state proportions: U^{4+} (red), U^{5+} (blue) and U^{6+} (green) of MORB melts at 1 atm (solid lines) and > 5 kbar (dashed lines). Estimated fO_2s for MOR and arc mantle/primary melts are shown as red and blue shaded regions, respectively.

(Laubier *et al.*, 2014). The $Fe^{3+}/\sum Fe$ systematics of olivine-hosted melt inclusions (Kelley and Cottrell, 2012) and application of the spinel-olivine oxybarometer to crystals in arc basalts (Evans *et al.*, 2012) have also been used to infer an oxidised mantle source (QFM +1 to QFM+1.6 and QFM+1 to QFM+4, respectively). A possible mechanism for oxidation of arc primary magmas is the addition of S^{6+} in Fe-poor supercritical slab liquids to the mantle wedge, where production of more Fe-rich magmas causes a shift of the sulphide-sulphate equilibrium to favour S^{2-}, resulting in oxidation of Fe^{2+} to Fe^{3+}. This mechanism limits oxidation of an originally reduced primary melt to QFM+2 (Klimm *et al.*, 2012). Dehydration of serpentinites in the slab or mantle wedge, where consumption of magnetite and the formation of olivine and orthopyroxene results in the reduction of Fe^{3+} and the liberation of oxidised fluids into the mantle wedge, has also been proposed (Elburg and Kamenetsky, 2007). If the fO_2 of arc lavas is a reflection of the conditions during mantle melting, the

results of this study indicate that the proportion of U^{5+} in primary melts could be very large even at the pressures of melting, and will be highly variable across the estimated logfO_2 range of arc magmas ($U^{5+}/\sum U$ increases from ~0.2 to ~0.5 between QFM and QFM+2 for pressures ≥ 5 kbar, Fig. 7.1).

7.4 Modelling U-series in arcs: Part 1

7.4.1 Methodology

The ability of oxidised mantle melting to produce U-series disequilibria comparable to those recorded from arc settings was tested using UserCalc 2.0. (Spiegelman, 2000), a web-based U-series calculator. The underlying equations and parameters of UserCalc are based on the equilibrium transport model of Spiegelmann and Elliot (1993) (extended to include the ^{231}Pa-^{235}U system), which calculates the effect of both melting and melt transport on the ($^{230}Th/^{238}U$), ($^{231}Pa/^{235}U$), and ($^{226}Ra/^{230}Th$) activity ratios. The parameters and equations of the model are discussed in detail by Spiegelman (2000). For the purpose of this study it is sufficient to know that the three U-series ratios are calculated from a spreadsheet input expressing the degree of melting, permeability, and the bulk partition coefficients (D) of the U-series elements as a function of pressure/depth. The model requires these properties in the form of continuous functions and the spreadsheet input is interpolated using cubic splines. Thus, the input values should vary smoothly to prevent artefacts from the spline routines.

The UserCalc website provides an online spreadsheet calculator that allows for a simple two-layer melting column (the user may provide their own spreadsheet for a column made up of more layers), where the user inputs the depth/length of the column, two sets of bulk U, Th, Ra, and Pa partition coefficients for above and below a chosen transition depth (e.g. the garnet-spinel transition), the length of this transition interval, and the degree of melting in

each layer (Fig. 7.2). In addition, the user may choose to change the permeability of the lower layer relative to the upper layer, for example, an increase in the permeability of the deep region might be applied for a hydrous melt. As the aim of this study is only to explore the relative effect of changing the partitioning behaviour of U on U-series models, a two-layer model is considered sufficient and only the length of the melting column, bulk partition coefficients, and transition depth were considered, the rest of the input parameters were kept as the default values, which are believed to be reasonable (Spiegelman 2000).

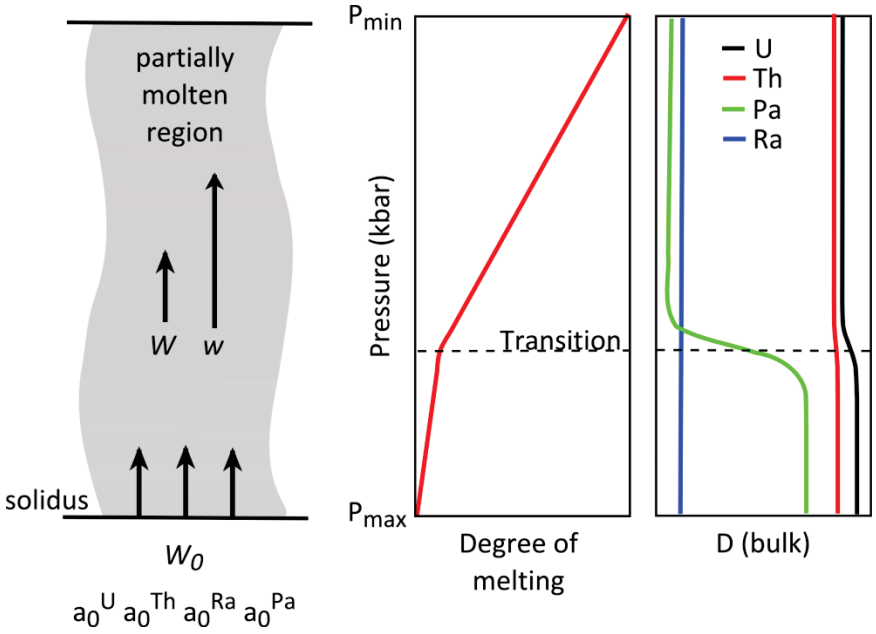


Figure 7.2: Illustration of the key parameters of the melting column model of UserCalc (Spiegelman 2000). W_0 is the initial solid upwelling rate, W is the matrix velocity, and w is the melt velocity. The input parameters include the pressure/depth at which melting is initiated (P_{max}), the pressure of the top of the melting column (P_{min}), the bulk partition coefficients (D) for the U-series elements, and the degree of melting. For the two-layer model shown the U-series element D's vary between two sets of values for above and below a user-defined transition depth (panel to the right); the degree of melting reached by the top of the transition depth and the surface (central panel) is also input by the user .

The U-series disequilibria of melts as a function of mantle upwelling rate and porosity were generated using the UserCalc model for both a 60 km (20 kbar, garnet-absent) and a 90 km (30 kbar, garnet present) melting column. The transition depth of the shallower column was set at 10 kbar (with a transition interval of 1 kbar) to reflect the change in U-Th partitioning with clinopyroxene chemistry. The longer melting column is somewhat simplified by the framework of a two-layer model, as ideally three sets of partition coefficients are required to represent the garnet lherzolite stability field in addition to the deep and shallow spinel lherzolite fields. However, for the purpose of this discussion, which is only comparative, the transition in the longer melting column was chosen to reflect an approximate garnet-spinel lherzolite transition (25 kbar) and partition coefficients appropriate for a higher pressure clinopyroxene chemistry (i.e. $D_{U^{4+}}/D_{Th} > 1$) were used in the top layer. The effect of mantle/melt oxidation was considered by systematically changing the input U bulk partition coefficients to reflect increasing U^{5+}. The mantle was assumed to be at secular equilibrium at the onset of melting.

The U, Th, Ra, and Pa partition coefficients of the major minerals present during mantle melting were chosen based on a combination of experimentally measured and lattice strain model derived values (from Blundy and Wood, 2003) and are given in Table 7.1, along with the resulting bulk partition coefficients for the chosen melting mineralogies. Since no experimental partition coefficients are available for the extremely incompatible Ra and Pa, current estimates are based on extrapolations from their most suitable proxies (Ba^{2+} for Ra^{2+}, and Nb^{5+} and Ta^{5+} for Pa^{5+}) (Blundy and Wood, 2003). As U partitioning studies have largely neglected the effect of fO_2, the partition coefficients of U^{5+} were taken to be identical to those used for Pa^{5+}. As a result, the overall bulk partition coefficient for U, given by:

$$D_U = nD_{U^{4+}} + (1-n)D_{U^{5+}}$$

where $n = U^{4+}/(U^{4+}+U^{5+})$, was essentially scaled as a function of the proportion of U^{4+} assumed, with the exception of when garnet was present in the melting mineralogy. Notably, whilst the partition coefficients for Pa and hence U^{5+} are theoretical estimates, even a large uncertainty in $D_{U^{5+}}$ (i.e. an error of 2 orders of magnitude) will have a minimal impact on the calculated U bulk partition coefficient, and hence the modelled ($^{230}Th/^{238}U$), for melting in the spinel lherzolite stability field, which will be dominated by the partitioning of U^{4+} in clinopyroxene. A scaling dependence of the U bulk partition coefficient seems reasonable based on the limited available fO_2 dependent experimental partitioning data, which found that

---

Table 7.1: Partition coefficients and mineral modes used for UserCalc in-growth melting models.

	$D_{Olivine}$	$D_{Orthopyroxene}$	$D_{Clinopyroxene}$ (P > 10 kbar)	$D_{Clinopyroxene}$ (P < 10 kbar)	D_{Garnet}
U^{4+}	6.0×10^{-5}	[1] 1.7×10^{-3}	1.8×10^{-2}	1.9×10^{-2}	[2] 2.6×10^{-2}
Th	9.5×10^{-5}	[1] 8.0×10^{-4}	1.5×10^{-2}	2.2×10^{-2}	[2] 7.9×10^{-3}
Ra	5.8×10^{-8}	2.4×10^{-6}	4.1×10^{-6}	4.1×10^{-6}	1.0×10^{-9}
Pa or U^{5+}	6.0×10^{-8}	1.7×10^{-6}	3.6×10^{-7}	3.8×10^{-7}	0.01

Mineral modes		
	60 km column*	**90 km column***
	> 10 kbar: 0.57 Ol, 0.28 Opx, 0.15 Cpx[3]	> 25kbar: 0.5 Ol, 0.2 Opx, 0.2 Cpx, 0.08 Grt[4]
	< 10 kbar: 0.57 Ol, 0.28 Opx, 0.15 Cpx[3]	< 25 kbar 0.57 Ol, 0.28 Opx, 0.15 Cpx[3]

	D_{bulk}		D_{bulk}	
	> 10 kbar	**< 10 kbar**	**> 25 kbar**	**< 25 kbar**
U^{4+}	3.21×10^{-3}	3.36×10^{-3}	6.05×10^{-3}	3.36×10^{-3}
Th	2.48×10^{-3}	3.53×10^{-3}	3.80×10^{-3}	3.53×10^{-3}
Ra	1.32×10^{-6}	1.32×10^{-6}	1.33×10^{-6}	1.32×10^{-6}
Pa or U^{5+}	5.64×10^{-7}	5.67×10^{-7}	8.00×10^{-4}	5.67×10^{-7}

* Degree of melting taken as default values of 0 at base of column, 0.05 at transition depth and 0.2 at top.

[1] Coefficients measured by Wood *et al.* (1999).

[2] Coefficients used by Stracke *et al.* (2003).

[3] Mineral/ melting modes from Beier *et al.* (2010).

[4] Mineral/melting modes from Dosseto and Turner (2013).

the value of D_{Th}/D_U for clinopyroxene doubled between logfO_2 = ~-11 (QFM-3.5) and -7.5 (QFM) at 1285 °C and 1 atm (Lundstrom *et al.*, 1994). Since the results of this study (Chapters 5 and 6) suggest that U^{6+} is not stable at such low fO_2s this change in partitioning behaviour is consistent with the conclusion that U^{5+} is highly incompatible relative to U^{4+}.

Fig. 7.3 shows an example of the output from the UserCalc program. The three U-series activity ratios are plotted in the 2D parameter space of the maximum porosity (volume fraction of melt) at the top of the column (ϕ) and the rate of solid upwelling at the base of the melting column (W_0). A small porosity implies very efficient melt extraction with the melt moving many times faster than the solid (Spiegelman and Elliot, 1993). The contours of the activity ratios exhibit two behaviours that depend on the total melt extraction time, t_c. Regions where a particular daughter-parent activity ratio is controlled primarily by upwelling velocity (region (a) of Fig. 7.3) arise when the total extraction time is short relative to the relevant daughter half-life ($t_c < 6t_{1/2}$). In contrast, regions where the activity ratio is controlled

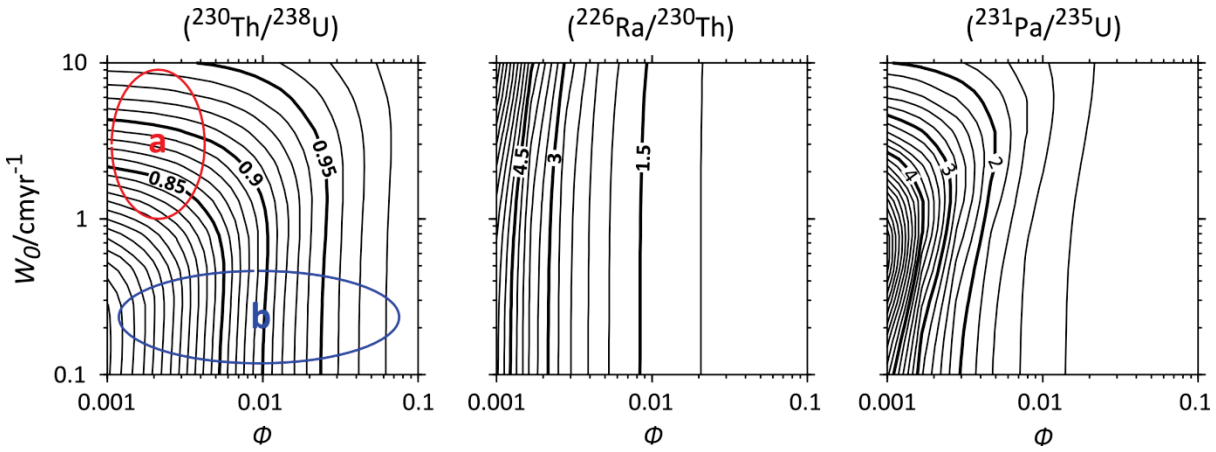


Figure 7.3: Modelling results from UserCalc 2.0 (Spiegelman, 2000). Contours of activity ratios for ($^{230}Th/^{238}U$), ($^{226}Ra/^{230}Th$), and ($^{231}Pa/^{235}U$) as a function of solid upwelling velocity at the base of the melting column (W_0) and the maximum porosity at the top of the column (ϕ), for melts initiated at 20 kbar (60 km melt column: spinel lherzolite field) assuming U^{5+} makes up 30 % of the total U. Highlighted regions correspond to when the total extraction time is short (a) or long (b) relative to the relevant daughter half-life.

by porosity (region (b) of Fig. 7.3) indicate that the melt extraction time is long relative to the daughter half-life ($t_c > 6t_{1/2}$) (Spiegelman and Elliot, 1993).

7.4.2 Results

The U-series activity ratios calculated as a function of ϕ and W_0 for varying proportions of U^{5+} during mantle melting are summarised in Tables 7.2 and 7.3; the values of ϕ and W_0 are within the range usually reported for U-series melting models (e.g. Beier *et al.*, 2010; Huang *et al.*, 2011; Dosseto and Turner, 2013). Lower porosities favour greater ($^{230}Th/^{238}U$) disequilibria for a particular column length and $U^{5+}/\sum U$. However, the sense and magnitude of disequilibria are strongly controlled by the melting mineral modes (i.e. long vs. short column) and the proportion of U^{5+} assumed. The calculated ratios vary widely from ^{230}Th excesses, to close to equilibrium, to ^{238}U excesses. Initiation of melting in the garnet stability field requires a significantly larger proportion of U^{5+} than melting of spinel lherzolite to generate any ^{238}U excess due to the high $D_{U^{5+}}/D_{Th}$ of garnet. The dependence on solid upwelling velocity is somewhat variable, however, for the high $U^{5+}/\sum U$ values required to generate large ^{238}U excesses, the largest excesses are produced at the slowest upwelling rates.

All the melting scenarios outlined in Tables 7.2 and 7.3 result in significant ^{231}Pa excesses relative to ^{235}U. With all else being equal, the magnitude of ^{231}Pa excesses decreases with increasing $U^{5+}/\sum U$, resulting in a positive correlation between ($^{230}Th/^{238}U$) and ($^{231}Pa/^{235}U$), both decreasing with increasing oxidation. Including garnet in the melting mineral mode also results in a reduction of the generated ($^{231}Pa/^{235}U$) due to the significantly more compatible nature of Pa in garnet relative to olivine or the pyroxenes (Blundy and Wood, 2003). Clearly the exact choice of mineral proportions will impact the magnitude of all the U-series activity ratios generated by changing the input bulk partition coefficients. This effect is illustrated in

Table 7.2: Calculated ($^{230}Th/^{238}U$), ($^{226}Ra/^{230}Th$), and ($^{231}Pa/^{235}U$) as a function of solid upwelling velocity (W_0) and porosity (ϕ), from the UserCalc "equilibrium transport" model of Spiegelman (2000) for a 60 km melting column (see Table 7.1) for various $U^{5+}/\sum U$.

$U^{5+}/\sum U = 0$	W_0 = 1 cm/yr			W_0 = 3 cm/yr			W_0 = 5 cm/yr		
ϕ	($^{230}Th/^{238}U$)	($^{226}Ra/^{230}Th$)	($^{231}Pa/^{235}U$)	($^{230}Th/^{238}U$)	($^{226}Ra/^{230}Th$)	($^{231}Pa/^{235}U$)	($^{230}Th/^{238}U$)	($^{226}Ra/^{230}Th$)	($^{231}Pa/^{235}U$)
0.01	0.99	1.42	1.46	1.03	1.42	1.60	1.04	1.43	1.65
0.005	1.01	1.84	2.09	1.06	1.87	2.35	1.06	1.90	2.24
0.003	1.02	2.42	3.13	1.08	2.50	3.11	1.07	2.58	2.69
0.002	1.03	3.16	4.46	1.09	3.35	3.73	1.08	3.51	3.01
0.001	1.05	5.52	7.52	1.10	6.23	4.60	1.09	6.71	3.42
$U^{5+}/\sum U = 0.1$	W_0 = 1 cm/yr			W_0 = 3 cm/yr			W_0 = 5 cm/yr		
ϕ	($^{230}Th/^{238}U$)	($^{226}Ra/^{230}Th$)	($^{231}Pa/^{235}U$)	($^{230}Th/^{238}U$)	($^{226}Ra/^{230}Th$)	($^{231}Pa/^{235}U$)	($^{230}Th/^{238}U$)	($^{226}Ra/^{230}Th$)	($^{231}Pa/^{235}U$)
0.01	0.96	1.41	1.41	0.99	1.42	1.54	1.01	1.43	1.59
0.005	0.96	1.84	1.99	1.01	1.87	2.24	1.02	1.90	2.13
0.003	0.96	2.42	2.93	1.01	2.50	2.94	1.02	2.58	2.56
0.002	0.96	3.16	4.15	1.02	3.35	3.51	1.03	3.52	2.86
0.001	0.96	5.52	6.99	1.03	6.25	4.33	1.03	6.75	3.23
$U^{5+}/\sum U = 0.3$	W_0 = 1 cm/yr			W_0 = 3 cm/yr			W_0 = 5 cm/yr		
ϕ	($^{230}Th/^{238}U$)	($^{226}Ra/^{230}Th$)	($^{231}Pa/^{235}U$)	($^{230}Th/^{238}U$)	($^{226}Ra/^{230}Th$)	($^{231}Pa/^{235}U$)	($^{230}Th/^{238}U$)	($^{226}Ra/^{230}Th$)	($^{231}Pa/^{235}U$)
0.01	0.90	1.41	1.32	0.92	1.42	1.43	0.94	1.43	1.47
0.005	0.85	1.84	1.77	0.90	1.87	1.99	0.92	1.90	1.92
0.003	0.83	2.42	2.53	0.89	2.50	2.58	0.92	2.58	2.28
0.002	0.81	3.16	3.53	0.88	3.35	3.06	0.91	3.53	2.53
0.001	0.79	5.52	5.88	0.88	6.29	3.75	0.91	6.85	2.85
$U^{5+}/\sum U = 0.5$	W_0 = 1 cm/yr			W_0 = 3 cm/yr			W_0 = 5 cm/yr		
ϕ	($^{230}Th/^{238}U$)	($^{226}Ra/^{230}Th$)	($^{231}Pa/^{235}U$)	($^{230}Th/^{238}U$)	($^{226}Ra/^{230}Th$)	($^{231}Pa/^{235}U$)	($^{230}Th/^{238}U$)	($^{226}Ra/^{230}Th$)	($^{231}Pa/^{235}U$)
0.01	0.83	1.41	1.23	0.84	1.42	1.31	0.86	1.43	1.35
0.005	0.75	1.84	1.56	0.79	1.87	1.74	0.83	1.90	1.69
0.003	0.69	2.41	2.11	0.76	2.50	2.19	0.81	2.59	1.97
0.002	0.66	3.15	2.87	0.74	3.36	2.57	0.79	3.55	2.17
0.001	0.61	5.51	4.69	0.72	6.33	3.11	0.78	6.96	2.43

Table 7.3: Calculated ($^{230}Th/^{238}U$), ($^{226}Ra/^{230}Th$), and ($^{231}Pa/^{235}U$) as a function of solid upwelling velocity (W_0) and porosity (ϕ), from the UserCalc "equilibrium transport" model of Spiegelman (2000) for a 90 km melting column (see Table 7.1) for various $U^{5+}/\sum U$.

$U^{5+}/\sum U = 0$	$W_0 = 1$ cm/yr			$W_0 = 3$ cm/yr			$W_0 = 5$ cm/yr		
ϕ	($^{230}Th/^{238}U$)	($^{226}Ra/^{230}Th$)	($^{231}Pa/^{235}U$)	($^{230}Th/^{238}U$)	($^{226}Ra/^{230}Th$)	($^{231}Pa/^{235}U$)	($^{230}Th/^{238}U$)	($^{226}Ra/^{230}Th$)	($^{231}Pa/^{235}U$)
0.010	1.07	1.29	1.40	1.09	1.29	1.46	1.09	1.29	1.49
0.005	1.12	1.59	1.85	1.15	1.59	1.99	1.13	1.60	1.93
0.003	1.17	1.98	2.53	1.18	2.00	2.53	1.15	2.02	2.26
0.002	1.20	2.48	3.37	1.20	2.52	2.95	1.17	2.56	2.49
0.001	1.25	4.00	5.16	1.23	4.19	3.54	1.18	4.46	2.77
$U^{5+}/\sum U = 0.1$	$W_0 = 1$ cm/yr			$W_0 = 3$ cm/yr			$W_0 = 5$ cm/yr		
ϕ	($^{230}Th/^{238}U$)	($^{226}Ra/^{230}Th$)	($^{231}Pa/^{235}U$)	($^{230}Th/^{238}U$)	($^{226}Ra/^{230}Th$)	($^{231}Pa/^{235}U$)	($^{230}Th/^{238}U$)	($^{226}Ra/^{230}Th$)	($^{231}Pa/^{235}U$)
0.010	1.04	1.29	1.36	1.06	1.29	1.45	1.06	1.29	1.45
0.005	1.07	1.59	1.77	1.10	1.59	2.03	1.09	1.60	1.85
0.003	1.10	1.98	2.39	1.12	2.00	2.64	1.11	2.02	2.15
0.002	1.12	2.48	3.14	1.14	2.52	3.15	1.11	2.57	2.36
0.001	1.15	4.00	4.77	1.15	4.20	3.87	1.12	4.48	2.62
$U^{5+}/\sum U = 0.3$	$W_0 = 1$ cm/yr			$W_0 = 3$ cm/yr			$W_0 = 5$ cm/yr		
ϕ	($^{230}Th/^{238}U$)	($^{226}Ra/^{230}Th$)	($^{231}Pa/^{235}U$)	($^{230}Th/^{238}U$)	($^{226}Ra/^{230}Th$)	($^{231}Pa/^{235}U$)	($^{230}Th/^{238}U$)	($^{226}Ra/^{230}Th$)	($^{231}Pa/^{235}U$)
0.010	0.98	1.29	1.28	0.99	1.29	1.32	1.00	1.29	1.35
0.005	0.97	1.58	1.60	0.99	1.59	1.71	1.00	1.60	1.67
0.003	0.91	1.98	2.08	1.00	2.00	2.10	1.01	2.02	1.92
0.002	0.96	2.48	2.68	1.00	2.52	2.42	1.01	2.57	2.09
0.001	0.96	4.00	3.98	1.00	4.22	2.86	1.01	4.53	2.30
$U^{5+}/\sum U = 0.5$	$W_0 = 1$ cm/yr			$W_0 = 3$ cm/yr			$W_0 = 5$ cm/yr		
ϕ	($^{230}Th/^{238}U$)	($^{226}Ra/^{230}Th$)	($^{231}Pa/^{235}U$)	($^{230}Th/^{238}U$)	($^{226}Ra/^{230}Th$)	($^{231}Pa/^{235}U$)	($^{230}Th/^{238}U$)	($^{226}Ra/^{230}Th$)	($^{231}Pa/^{235}U$)
0.010	0.92	1.29	1.20	0.92	1.29	1.23	0.93	1.29	1.26
0.005	0.86	1.58	1.43	0.89	1.59	1.52	0.91	1.60	1.49
0.003	0.82	1.98	1.78	0.87	2.00	1.81	0.90	2.02	1.68
0.002	0.79	2.48	2.21	0.86	2.53	2.04	0.89	2.58	1.81
0.001	0.76	4.00	3.17	0.84	4.25	2.37	0.89	4.59	1.97

Fig. 7.4 where a decrease in the percentage of orthopyroxene and increase in clinopyroxene favours larger disequilibria for all three U-series pairs at a set ϕ and W_0 (Note that disequilibria is the deviation from an activity ratio of 1, so (^{230}Th/^{238}U) = 0.6 represents a greater disequilibrium than (^{230}Th/^{238}U) = 0.7). Unsurprisingly the calculated (^{226}Ra/^{230}Th) is insensitive to oxidation. In all cases, the largest ^{231}Pa and ^{226}Ra excesses are produced at lower porosities.

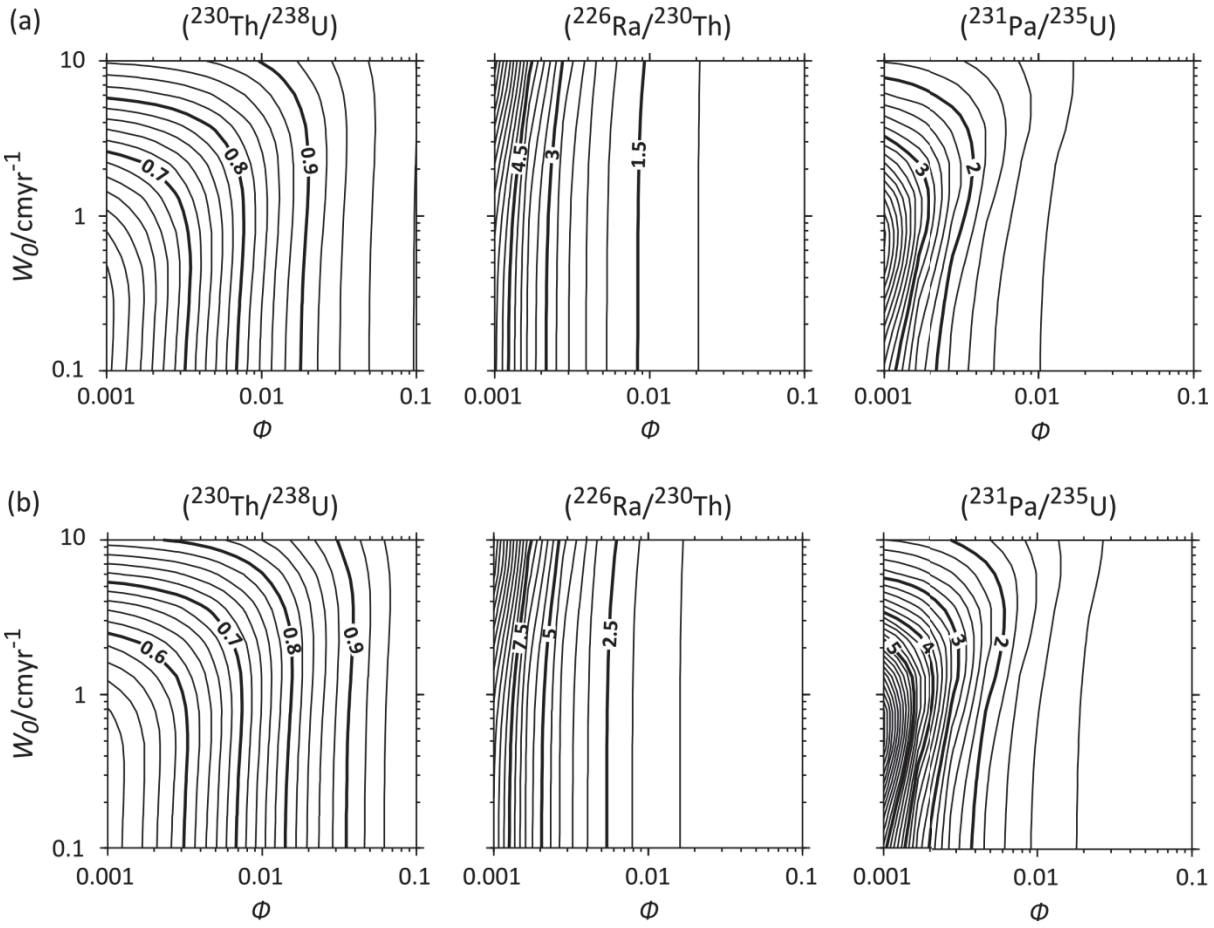


Figure 7.4: Modelling results from UserCalc 2.0 (Spiegelman, 2000). Contours of activity ratios for (^{230}Th/^{238}U), (^{226}Ra/^{230}Th), and (^{231}Pa/^{235}U) as a function of solid upwelling velocity at the base of the melting column (W_0) and the maximum porosity at the top of the column (ϕ) for melts initiated at 20 kbar (60 km melt column: spinel lherzolite field) with bulk partition coefficients based on a source with (a) 57% olivine, 28% orthopyroxene and 15% clinopyroxene or (b) 57% olivine, 13% orthopyroxene and 30% clinopyroxene, and assuming U^{5+} makes up 50 % of the total U.

7.5 Modelling U-series in arcs: Part 2

7.5.1 Methodology

UserCalc represents one end-member type of the U-series melting models (equilibrium transport). For comparison, the effect of U oxidation during mantle melting was applied to the "incremental dynamic melting model" of Stracke *et al.* (2003) (spreadsheet and detailed description of model provided with the supplementary data of the same publication). This represents a more sophisticated solution to U-series than the original dynamic melting models (McKenzie, 1985; Mckenzie 2000), as it allows for changing mineralogy, and hence U and Th partitioning behaviour, with depth and progressive melting. The model includes the effects of changing mineralogy from garnet peridotite (>75 km) to spinel lherzolite, and of changing clinopyroxene chemistry from low Ca to high Ca, which varies smoothly between depths of 75 and 33 km. It is a non-modal melting model (in contrast to UserCalc) and incorporates changes in the initial phase assemblage and proportions of phases entering the melt as a function of depth due to increasing consumption with progressive melting. The effect of radioactive decay during melt transport (i.e. through chemically isolated channels after melt-matrix separation) is also calculated based on a melt ascent velocity provided by the user.

The model is provided as a Microsoft Excel spreadsheet in to which a number of parameters have to be entered that define the initial conditions and the melting conditions. Again, as the aim here is only to determine the leverage of increasing U^{5+} on the calculated ($^{230}Th/^{238}U$) disequilibria of current U-series models, most of these parameters, including the starting mineral modes, mineral melting modes (as a function of depth), and the total amount of melt extracted (10 %) were not changed from their default values (i.e. those used by Stracke *et al.* (2003) to model melting beneath northern Iceland). In this approach, the variation of

($^{230}Th/^{238}U$) was again investigated as a function of W_0, ϕ, $U^{5+}/\sum U$, and the depth of melt initiation. Three melting depths, 90 km (30 kbar), 60 km (20 kbar), and 40 km (13.3 kbar), were considered in order to cover the main mineralogical/compositional induced changes in U-Th partitioning. The input U ($nU^{4+}+(1-n)U^{5+}$) and Th partition coefficients for olivine, orthopyroxene, low Ca clinpyroxene, high Ca clinopyroxene, and garnet were the same as those used to calculate the bulk partition coefficients for the equilibrium transport model of section 7.4 (listed in Table 7.1). The ($^{230}Th/^{238}U$) ratios reported here are those calculated before correction for radioactive decay during chemically isolated melt transport; the magnitude of which is entirely dependent on the user defined melt ascent velocity. Since dynamic melting models envision rapid melt extraction (1-10's m/yr) via channelized flow the effect of this decay on the original ($^{230}Th/^{238}U$) ratio will be small.

7.5.2 Results

The U-series activity ratios calculated as a function of ϕ and W_0 for varying proportions of U^{5+} during mantle melting are summarised in Table 7.4. The resulting variation in ($^{230}Th/^{238}U$) is similar to that predicted by the equilibrium transport model, although the maximum ^{238}U excess achievable from melting starting at depths of 90 km and 60 km are significantly smaller. This offset is due to the resulting activity ratio of the dynamic melting model being dominated by U-Th partitioning at the onset of melting. Stracke *et al.* (2003) noted that progressive melting in the spinel field does not significantly affect the U-series signature generated in the garnet field, provided at least 2-3 % of the melt was generated in this field, as virtually all U and Th is exhausted in the residue during the first few percent melting. Shallower depths of melting are therefore required to generate comparable ^{238}U excesses to those produced during equilibrium transport.

Importantly, the ϕ term has a somewhat different meaning in dynamic melting than in equilibrium transport models. The equilibrium transport model of UserCalc assumes that porosity increases from zero at the base of the melting column to the defined maximum value at the top. In contrast, the model of Stracke *et al.* (2003) (and other dynamic melting models) assumes that the residual porosity remains constant throughout melting. Thus, for dynamic melting the porosity term represents an estimate of the average value during melting. This difference is significant in terms of the magnitude of (^{230}Th/^{238}U) disequilibria achievable. Regardless of the final porosity in equilibrium transport models, the porosity at the onset of melting is effectively zero making it possible to initially generate larger disequilibria (at the base of the melting column) than dynamic melting models (Stracke *et al.*, 2003).

7.6 Discussion

It is apparent that large ^{238}U excesses relative to ^{230}Th are achievable within the framework of current U-series models if significant U^{5+} is present during partial melting. However, whilst many arc lavas exhibit ^{238}U excesses, what is perhaps most notable is their wide variation in (^{230}Th/^{238}U) compared to the relatively tight distribution of MORBs (generally ^{230}Th excesses only). The results of this study (Chapters 5 and 6) suggest that for the fO_2 range estimated for subduction zone lavas, the proportion of U^{5+} in silicate melts is highly sensitive to fO_2 (i.e. covers the steep part of the $U^{4+} \rightarrow U^{5+}$ sigmoid), creating the potential for large variation in U^{5+} during melting of the sub-arc mantle. Fig. 7.5 shows a subset of the UserCalc and dynamic melting results (W_0 = 1 cm/yr) overlain on U-series data from various arcs, which suggests that partial melting of a variably oxidised mantle wedge can produce much of the range of reported U-series activity ratios. Exceptions to this are samples exhibiting extreme ^{226}Ra excesses ((^{226}Ra/^{230}Th) > 4), and the high ^{238}U excesses and ^{231}Pa deficits of Tongan arc lavas (Bourdon *et al.*, 1999). Since in this modelling the behaviour of U converges to that of

Table 7.4: Calculated ($^{230}Th/^{238}U$), as a function of solid upwelling velocity and porosity, from the incremental "dynamic" melting model of Stracke *et al.* (2003) for varying depths of melt initiation and $U^{5+}/\sum U$.

$U^{5+}/\sum U = 0$	W_0 = 1 cm/yr			W_0 = 3 cm/yr			W_0 = 5 cm/yr		
ϕ	90 km	60 km	40 km	90 km	60 km	40 km	90 km	60 km	40 km
0.010	1.13	1.01	0.97	1.10	1.01	0.98	1.08	1.01	0.98
0.005	1.20	1.02	0.96	1.13	1.01	0.97	1.10	1.01	0.98
0.003	1.23	1.02	0.96	1.15	1.02	0.97	1.11	1.01	0.98
0.002	1.26	1.03	0.96	1.16	1.02	0.97	1.11	1.01	0.98
0.001	1.28	1.03	0.95	1.17	1.02	0.97	1.12	1.01	0.98
$U^{5+}/\sum U = 0.1$	W_0 = 1 cm/yr			W_0 = 3 cm/yr			W_0 = 5 cm/yr		
ϕ	90 km	60 km	40 km	90 km	60 km	40 km	90 km	60 km	40 km
0.010	1.09	0.98	0.94	1.07	0.99	0.96	1.05	0.99	0.97
0.005	1.14	0.98	0.92	1.09	0.99	0.95	1.07	0.99	0.96
0.003	1.16	0.97	0.91	1.10	0.98	0.94	1.08	0.99	0.96
0.002	1.18	0.97	0.90	1.11	0.98	0.94	1.08	0.99	0.96
0.001	1.20	0.97	0.90	1.12	0.98	0.94	1.08	0.99	0.95
$U^{5+}/\sum U = 0.3$	W_0 = 1 cm/yr			W_0 = 3 cm/yr			W_0 = 5 cm/yr		
ϕ	90 km	60 km	40 km	90 km	60 km	40 km	90 km	60 km	40 km
0.010	1.03	0.93	0.89	1.02	0.95	0.92	1.02	0.96	0.93
0.005	1.05	0.91	0.84	1.03	0.94	0.89	1.02	0.95	0.92
0.003	1.06	0.89	0.82	1.04	0.93	0.88	1.03	0.95	0.91
0.002	1.06	0.88	0.80	1.04	0.93	0.88	1.03	0.95	0.91
0.001	1.07	0.87	0.78	1.04	0.92	0.87	1.03	0.95	0.91
$U^{5+}/\sum U = 0.5$	W_0 = 1 cm/yr			W_0 = 3 cm/yr			W_0 = 5 cm/yr		
ϕ	90 km	60 km	40 km	90 km	60 km	40 km	90 km	60 km	40 km
0.010	0.95	0.88	0.84	0.96	0.91	0.88	0.97	0.93	0.90
0.005	0.94	0.83	0.77	0.96	0.89	0.85	0.97	0.92	0.88
0.003	0.92	0.79	0.73	0.95	0.87	0.83	0.96	0.91	0.87
0.002	0.92	0.77	0.71	0.95	0.86	0.82	0.96	0.90	0.87
0.001	0.91	0.75	0.68	0.94	0.85	0.81	0.96	0.90	0.86

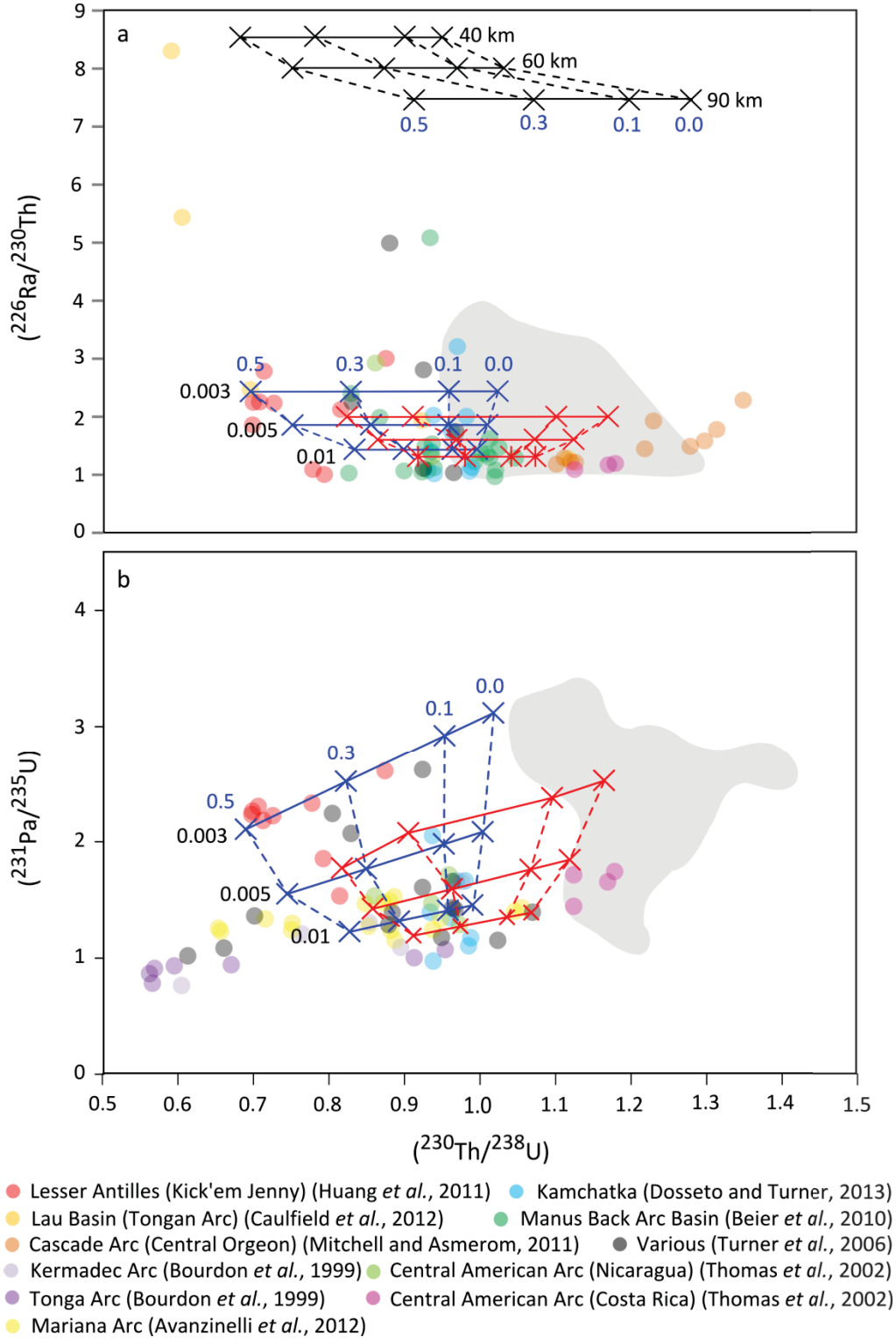


Figure 7.5: (a) ($^{226}Ra/^{230}Th$) and (b) ($^{231}Pa/^{235}U$) vs. ($^{230}Th/^{238}U$) of arc basalts and basaltic andesites and results of the UserCalc model (Spiegelman, 2000) for a 60 km (blue crosses) and 90 km (red crosses) melting column with W_0 = 1 cm/yr. Results are contoured for $U^{5+}/\sum U$ (blue numbers) and the maximum porosity, ϕ (black numbers). The ($^{230}Th/^{238}U$) values calculated using a dynamic melting model (Stracke *et al.*, 2003) with ϕ = 0.001, W_0 = 1 cm/yr, and different column lengths are also shown at the top of plot (a) (black crosses). Note that these points do not indicate ($^{226}Ra/^{230}Th$) values. Shaded regions correspond to the fields of MORB data.

Pa as the proportion of U^{5+} increases it is impossible to attribute ($^{231}Pa/^{235}U$) < 1 to mantle melting. These cases may indeed require a young U- and/or Ra-enriched slab component; however, it is possible that the preservation of these U-series signatures, which requires rapid transport from the slab to the mantle wedge to the surface, represent the exception rather than the norm.

Mantle/melt oxidation seems to be inherently linked to subduction and is likely to be directly controlled by mass transfer from the subducted plate to the mantle wedge (Kelley and Cottrell, 2009). As such, it may be difficult to prove whether the erupted U-series activity ratios are derived directly from the slab or result from oxidised melting, as similar associations between the magnitude of ^{238}U excesses and indicators of slab fluid/melt addition are expected in each case. Both theories are also consistent with the global positive correlation between ($^{231}Pa/^{235}U$) and ($^{230}Th/^{238}U$). A potential test for the oxidised melting model would be comparison of $Fe^{3+}/\sum Fe$ and ($^{238}U/^{230}Th$) from the same samples. For example, highly variable U-Th-Pa systematics from the Mariana Islands have been interpreted to be inconsistent with the oxidised melting model as the distribution of ($^{238}U/^{230}Th$) across different volcanic centres seems to require a large variation in oxygen fugacity along the arc, which seems to be at odds with the available (but extremely limited) $Fe^{3+}/\sum Fe$ data for Mariana basalts (Avanzinelli *et al.*, 2012).

Large variation in U-series systematics at some arcs may also result from secondary processes. For example, linear arrays in ($^{230}Th/^{238}U$) and ($^{231}Pa/^{235}U$) pointing towards secular equilibrium have been attributed to assimilation of old plutonic rocks in the arc crust (Reubi *et al.*, 2011). Ageing and differentiation in the crust have also been used to explain positive correlations between ($^{226}Ra/^{230}Th$) and Ba/Th and Sr/Th in arc magmas (Huang *et al.*, 2008).

Magma chamber recharge and mixing of different magma batches may have a similar leverage on U-series disequilibria. In addition, it is apparent that mineral melting modes exert a strong control on the U-series activities generated, with melting in the presence of garnet producing small-to-no U-Th disequilibrium even for a significant proportion of U^{5+}. Different U-series signatures along a single arc or at a single volcanic centre may thus reflect a range of melting depths and/or melting mineralogies/modes. Finally, there is also the possibility that not all U-series disequilibria are purely derived from melting, as cumulate-melt interaction has also been cited as a potential source of ^{226}Ra excesses (Van Orman *et al*., 2006).

7.7 Conclusions

U^{4+} partitioning is likely to dominate the behaviour of U at MORs. However, due to the (expected) high incompatibility of U^{5+} during melting of major mantle phases, even small proportions of this oxidation state could slightly reduce the bulk D_U/D_{Th} during melting at MORs. A small reduction in D_U/D_{Th} may make it significantly more difficult to generate ^{230}Th excesses in the spinel lherzolite field where D_U/D_{Th} is already close to unity. Notably, the U-series models used in this study did not produce large ^{230}Th excesses (i.e. ($^{238}U/^{230}Th$) > 1.03) except for the case of dynamic melting in the presence of garnet. However, large ^{230}Th excesses have been generated using other similar models assuming melting only in the spinel lherzolite field (Landwehr *et al.*, 2001). The ability of U-series models to produce ^{230}Th excesses by melting in the presence of clinopyroxene assuming 10-20 % U^{5+} is therefore beyond the scope of this study. The stabilisation of large proportions of U^{5+} during mantle melting over the reported fO_2 range of arc lavas can produce a wide variety of ($^{230}Th/^{238}U$) signatures that are broadly similar to those reported for many arc settings. Whether the U-series variation associated with individual volcanic centres or along a single subduction zone can be explained by an oxidised melting model remains to be tested.

Chapter 8:

Concluding remarks and future work

8.1 Conclusions

The U redox ratios of MORB glasses, which represent a three oxidation state system, have been successfully quantified by modelling the variation of U L_3- and M_4-edge XANES spectra, as a function of fO_2, as two single-electron oxidation reactions: $U^{4+} \rightarrow U^{5+}$ and $U^{5+} \rightarrow U^{6+}$. Unlike previous studies of multivalent systems, which have tended to rely on a single spectral feature that is highly sensitive to changes in fO_2, the approach of this study uses the information provided by the majority of the XANES spectral region. Simultaneous fitting of the normalised spectral intensity variations over many energy values allowed accurate logK´ values and the oxidation state end-member spectral line-shapes to be extracted from the data in a single step. Consistency between the logK´ values obtained from modelling of the L_3- and M_4-edge XANES data for the same samples illustrates the robustness of the approach, and its ability to produce the real solution even when the total variation in spectral shape is small, as is the case for the U L_3-edge XANES spectra.

The data derived from the spectra of MORB glasses for which the original melts were equilibrated for only 4 h ($\log fO_2$ = 0, -3, -5, and -7) exhibited comparable scatter from the model trends as that from glasses equilibrated between 8 and 88 h. As such, 4 h is sufficient to reach U redox equilibrium in this Fe-bearing composition at these fO_2s.

There was no evidence of beam induced changes in oxidation state during XANES acquisition for any of the MORB glasses. Further, comparison of U L_3-edge XANES spectra of MORB glasses and those collected from equivalent melts *in situ* at high temperatures did

not exhibit any evidence of a change in U oxidation state between melts and glasses. Thus, it is concluded that there is no charge transfer between U and Fe during quenching to a glass, and that the results obtained from analysis of the XANES spectra of MORB glasses are entirely representative of the original melts. Additionally, the change in U oxidation state with melt temperature is negligible when fO_2 is considered relative to the QFM solid-state buffer.

XANES spectral analysis of MORB glasses and melts indicated the presence of significant U^{5+}, in addition to U^{4+}, at geologically relevant fO_2s (~QFM-1 to QFM+2), with $U^{5+}/\sum U$ ~0.4 in MORB melts at QFM and 1 atm. In contrast, U^{6+} is only stabilised at conditions that are very oxidised relative to those estimated for the generation and differentiation of basaltic melts (≥ QFM+3). Comparison of the spectra of glasses equilibrated at 1 atm to those of glasses prepared using piston cylinder apparatus suggests that the stability field of U^{5+} is significantly supressed in favour of U^{4+} at pressures ≥ 5 kbar relative to at 1 atm. If this change is only due to the change in pressure (i.e. assuming that it is not related to the higher volatile contents or uncertainties in the buffering values of fO_2 for some piston cylinder glasses), it is consistent with the U^{5+} state having a larger molar volume than U^{4+}. In this case the change in the relative U^{4+} and U^{5+} proportions may occur at pressure significantly below 5 kbar, as this pressure value represents the upper bound defined from the available data. In contrast, the proportions of U^{5+} relative to U^{6+} were hardly affected by pressure. There was no evidence of a pressure induced change in U oxidation state between 5 and 15 kbar.

In spite of the apparent reduction in size of the U^{5+} stability field at pressures ≥ 5 kbar, this state is still likely to be present at conditions relevant to MORB generation (fO_2 ~ QFM and pressures of ~10-30 kbar) and may make up as much as 20 % of the total U in the melt. If the

offsets in U oxidation state between 1 atm and piston cylinder glasses equilibrated at fO_2s relevant to the mantle are not purely pressure induced then the proportion of U^{5+} stabilised during partial melting may be even higher. Whilst this is unlikely to affect the ability of mantle melting in the presence of garnet to generate the large ^{230}Th excesses characteristic of young MORBs from many ridge settings, it will impact models currently attributing such signatures to melting in the spinel lherzolite field.

The leverage of U^{5+} on the U-series systematics of arc basalts is strongly controlled by the assumed fO_2 of melt generation. However, if the oxidised nature of some arc magmas is derived from their mantle source, U^{5+} is expected to make up as much as 50 % of the total U present in the melt. Stabilisation of differing proportions of U^{5+} in arc melts by variably oxidised mantle wedges can produce a wide range of U-series signatures that are consistent with the highly variable nature of the available U-series data for arcs.

XANES spectra of Fe-free glasses indicated the presence of varying proportions of U^{4+}, U^{5+}, and U^{6+}, in addition to another U component; the precise identity of which remains unconfirmed. The variation of the XANES spectral line-shape of AD composition glasses with fO_2 does not follow the expected relationship for three oxidation reactions, and suggests that the four components do not represent a four oxidation state equilibrium within the original melts. This conclusion is supported by evidence for a quench induced change in U state at reduced fO_2s, which is represented by systematic lowering of the edge-energies of U L_3-edge XANES spectra between equivalent AD melts and glasses. Spectra of AD melts equilibrated at conditions as reduced as ~QFM-5.7 are consistent with the stability of the same three oxidation states as observed in the MORB glasses and melts, with U^{4+} and U^{5+} dominating at the fO_2s relevant to mantle melting.

Both U L_3- and M_4-edge XANES spectra of Fe-free glasses are affected by beam damage. The impact of beam damage on M_4-edge spectra of AD glasses was minimised by the employment of fast scan times and sample movement during XANES acquisitions. However, the rapidity of damage meant that it could not be minimised at the L_3-edge, and the magnitude of its effect on the recorded spectra of CMAS glasses needs to be considered. The changes in XANES spectral-shapes with increasing beam exposure are consistent with a beam induced oxidation of the U in the glass. This damage appears to be limited to reduced glasses that contain the fourth, seemingly quench-induced, U state. However, this state is not caused by beam damage as its proportion appears to decrease with increasing exposure to the X-ray beam.

With both quench effects and beam damage appearing to change the state of U from that originally present in Fe-free melts the oxidation state proportions of the compositional sets of CMAS glasses could not be correctly quantified. However, simplistic fits to the L_3-edge XANES spectral variation as a function of fO_2 indicated that higher basicity compositions favour higher average U oxidation states. This is also in agreement with the slightly more oxidised L_3-edge line-shapes of AD composition *in situ* melts relative to their equivalent MORB composition melts.

8.2 Future work

The exact pressure dependence of the changes in U oxidation state is not known and is a problem that requires preparation of further glasses at a series of pressures between 1 atm and 5 kbar. This pressure range extends to values too low for piston cylinders, and the temperature requirements are too high for cold-seal pressure vessels (of the original "Tuttle" design). However, apparatus such as internally heated gas pressure vessels (IHPV) (Holloway

and Wood, 1988) and Titanium–Zirconium-Molybdenum or Molybdenum-Hafnium-Carbide (TZM/MHC) pressure vessels may be able to achieve appropriate temperatures and pressures. Preparation of glasses in this pressure range may also help to resolve the role of pressure versus dissolved volatiles on the changes in the U oxidation state observed between glasses synthesised at 1 atm and using piston cylinder apparatus at equivalent fO_2s. The effect of water as a chemical component on U redox ratios could also be explored by preparing glasses with varying water contents at a single set of conditions.

The nature of the quench effect on U in Fe-free CMAS composition glasses remains to be resolved. However, modelling EXAFS spectra from these glasses could provide a preliminary means of testing some of the hypotheses outlined in section 6.5.1 of this thesis. EXAFS is a valuable technique for investigating the type, number, and distance of atoms in near-neighbour environments, and in this case may indicate the presence of U-U distances in these glasses that are sufficiently short to enable U-U charge transfer, or for the existence of U nano-particles. Preliminary EXAFS scans were recorded from selected glasses during a XANES data collection session at the microfocus beamline I18 of the DLS as a trial. However, scans were too noisy to unambiguously confirm any structure beyond the first coordination shell, and there was not sufficient time to collect repeat measurements to improve the signal-to-noise ratio. While these trial measurements were inconclusive, it is likely that a dedicated beamtime experiment on a core EXAFS beamline, such as B18 of the DLS, would produce data of a sufficient standard for EXAFS analysis.

The four-component fits of AD M_4-edge spectra (section 5.3.3) indicated that the proportion of the fourth U component was largest for glasses equilibrated at the most reduced fO_2s ($\log fO_2$ = -12 to -18). As such, these glasses are expected to be the best for EXAFS

measurements. However, EXAFS is an averaging technique and the contribution of U-U neighbours to the EXAFS spectrum will be weak if their numbers in the glasses are small and/or if the U-U distances are relatively large. In addition, the disorder in interatomic distances and bond angles of the glasses will restrict the information attainable with respect to similar studies on crystalline materials. The four component fits indicate the proportion of the unknown component in each glass spectrum relative to the spectrum of the most reduced glass; however, it is not known what proportion of the total U this state actually represents at $\log fO_2 = -18$. Thus, whilst EXAFS might be able to provide conclusive evidence for short U-U distances, an absence of evidence for U-U neighbours in the EXAFS spectra of glasses will not be sufficient to disprove their presence.

With no evidence of quench-induced changes in the U states of MORB composition glasses, which contain abundant Fe (~7.4 wt % Fe), a XANES study of sets of compositionally similar U-bearing glasses (i.e. compositions with similar values for parameterisations such as optical basicity) that contain different concentrations of Fe (from trace to wt %) would be of interest. Using HERFD M_4-edge XANES spectroscopy it would be straightforward to see if the beam sensitive U-state associated with the distinct pre-edge peak is present at any Fe concentrations (i.e. when Fe contents are lower than or comparable to U). Assuming that beam damage and quench artefacts are limited to Fe-free glasses the effect of melt composition on U redox ratios might be better explored using additional fO_2 sets of Fe-bearing glasses that cover a wide compositional range. In addition, since the degree of change in the average coordination number of Ti between melts and glasses has been shown to be dependent on quench rate, with a lower coordination number being slightly favoured by slower quench rates (Farges *et al.*, 1996), the impact of varying quench rate on the U XANES spectra of reduced CMAS (i.e. Fe-free) glasses might make an interesting study.

The methodology of thermodynamically fitting the variation of XANES spectral features of samples prepared over a large fO_2 range to determine oxidation state ratios of divalent systems in glasses and melts has been well established (Berry *et al.*, 2006; Berry and O'Neill, 2004; Burnham and Berry, 2014; Burnham *et al*., in preparation: see Appendix 6), and the spectral analysis outlined in this thesis successfully extends such an approach to a three oxidation state system (Chapter 5). Similar analyses can be extended to other complex systems (i.e. three oxidation states or more). For example, an equation for modelling a four oxidation state system has already been derived (Chapter 5: Eq. 5.19: three-sigmoid model). Vanadium is another element of geological interest that occurs in more than two oxidation states in silicate melts (V^{2+}, V^{3+}, V^{4+} and/or V^{5+}). The mineral-melt partition coefficients of V in different phases are highly sensitive to fO_2 (Mallmann and O'Neill, 2009), and the redox state of V in glasses has been suggested as a potential oxybarometer (Sutton *et al.*, 2005). Redox titrations have previously been used to determine V redox ratios in two CMAS glass compositions as a function of fO_2 (Schreiber and Balazs, 1982); these glasses have subsequently been used as "known" standards to produce V K-edge XANES calibration curves, from which the average oxidation state of V in other synthetic and natural glasses were estimated (Sutton *et al*., 2005). However, this approach assumes that the V oxidation states determined by redox titrations were accurate, and also requires that the coordination environments of the different V oxidation states is the same in the unknowns as in the two standard compositions. In addition, the average oxidation state values obtained do not necessarily allow the contribution of different V states to be distinguished (for example, it does not distinguish between V^{4+} and a 50:50 mixture of V^{3+} and V^{5+}).

The V K-edge XANES spectra of silicate glasses exhibit significant variation in spectral shape with changing oxidation state (Fig. 8.1: Sutton *et al.*, 2005). As such, the experimental

and analytical methods outlined in this thesis have the potential to quantify V oxidation state proportions in a wide range of compositions (including Fe-bearing compositions) directly from K-edge XANES spectra of fO_2 sets of glasses or melts, without the need for independently quantified standards. However, as for the U L_3-edge the cause of spectral variation at the V K-edge may be difficult to unambiguously resolve for such a complex system. In a similar approach to that used in this thesis to overcome the limitations of the L_3-edge by complimentary studies of U-bearing glasses at the M_4-edge, studies of V-bearing glasses at the L-edges, where the spectral line-shapes exhibit large variations between different oxidation states (Fig. 8.2: Schofield *et al.*, 2014), may further facilitate accurate oxidation state quantification.

Although the effect of pressure on the partitioning of U and Th in clinopyroxene has been investigated (Landwehr *et al.*, 2001), samples of these experiments were prepared in graphite lined capsules resulting in fO_2 values at least 1.3 log units below the QFM buffer (Holloway *et al.*, 1992). The results of this thesis show that it is not sufficient to assume that U^{4+} is the only significant oxidation state even during MOR mantle melting, and U-series models must

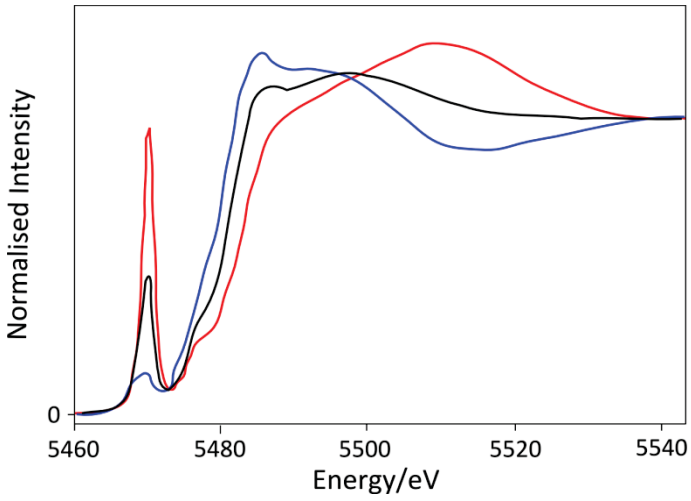


Figure 8.1: V K-edge XANES spectra of three glasses equilibrated at 1500 °C and logfO_2 = 0 (red), -6.8 (black), and -9 (blue) (Figure Source: Sutton *et al.*, 2005, Fig. 1, p. 2336).

instead be built on partition coefficients that are appropriate for the assumed fO_2 of melting. A small number of fO_2 dependent U clinopyroxene-melt partition coefficients have been reported for 1 atm experiments (Lundstrom *et al.*, 1994). However, studies combining both the effects of pressure and fO_2 on U partitioning are required

---

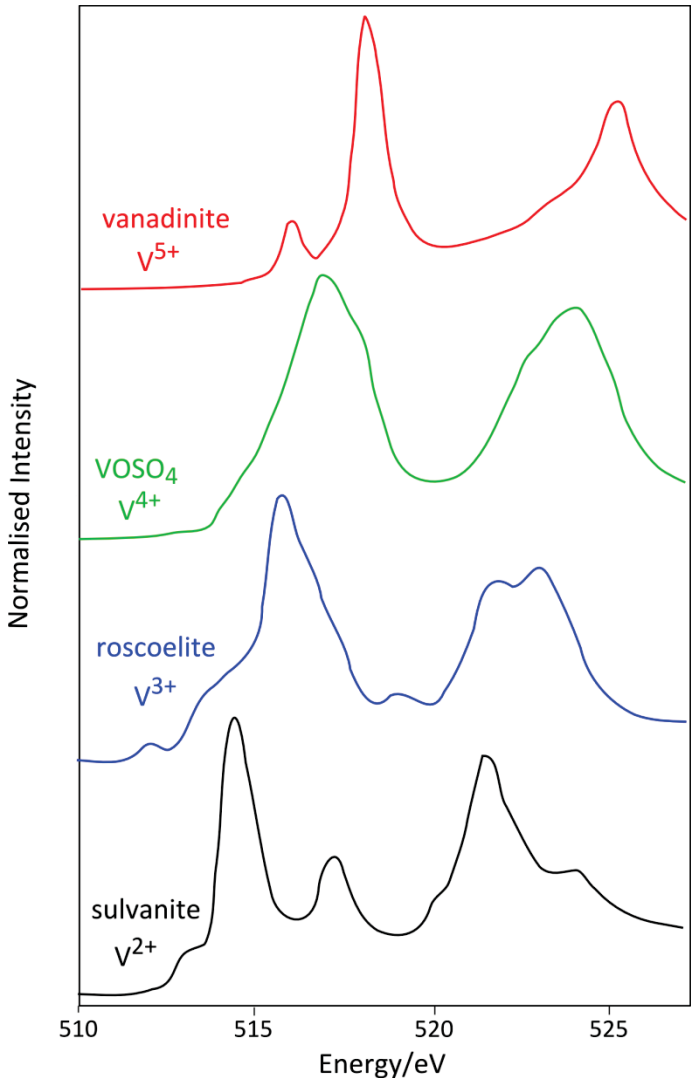


Figure 8.2: V L_2 and L_3-edge XANES spectra of vanadiniferous minerals (Figure Source: Schofield *et al.*, 2014, Fig. 1, p. 4 of article (in press)).

Acknowledgements

This PhD would not have been possible without the tireless support and expertise of the staff at Diamond Light Source. Beamline scientists Gianntonio Cibin, Steve Parry, Tina Geraki, Konstantin Ignatyev, Fred Mosselmans and Andy Dent went above and beyond the call of duty to ensure the success of our beamtimes. The technical support provided by Phil Robbins, Steve Keylock, and Adrian Marsh was also invaluable, particularly in the setting up for experiments using the XAS furnace. A special thanks to Steve Keylock for ingenious solutions to many furnace related problems and his ability to make things work just by looking at them. Also, to Tina Geraki for bringing some degree of sanity to the group when "synchrotron brain" had set in.

Our U M_4-edge experiments were entirely dependent on the assistance and specialist knowledge provided by ESRF beamline scientists Kristina Kvashnina and Pieter Glatzel. I am extremely grateful to Kristina for her contribution to data collection at the U M_4-edge, her advice and ideas on spectral normalisation and beam damage reduction, and for patiently answering my many questions.

I would like to thank Dean Scott and Guil Mallmann who prepared many of the U-bearing glasses used in the RT XANES studies of this thesis (see Appendix 1 and 2). Dean Scott and Dave Clarke also taught me how to prepare samples, and continued to provide a huge amount of assistance in my piston cylinder experiments; I am particularly grateful to Dave for preparing salt sleeves and running samples when deadlines were looming. Thanks also to Antony Burnham for providing me with a great deal of advice and lab training, and for his maintenance of the Imperial College 1 atm furnace. Antony also deserves credit for his assistance on XANES beamtimes (including filling in for the "proto-prof") and for providing

samples for Eu and Ce *in situ* experiments (Appendix 5 and 6). In addition, the laboratory work of this PhD was reliant on the help and equipment provided by Jack Nolan, Graham Nash and Barry Coles.

During the course of this PhD I have used a range of equipment and techniques at the Natural History Museum; for which I have received a large amount of technical support. John Spratt provided assistance and seemingly endless optimism and patience with my electron probe analyses. Tomasz Goral and Alex Ball dedicated much time to helping me on the confocal microscope and were accommodating in its application to my unusual sample analyses. Similarly, Anton Kearsley provided assistance and access to the SEM for an unusual application.

Simon Turner and Fang Huang provided useful discussion and insight into U-series models. I am very grateful to Simon for pointing me in the direction of accessible U-series models. Thanks also to Hugh O'Neill, for his advice relating to data analysis and experimental techniques.

This PhD was financially supported by Diamond Light Source, Imperial College, and the Natural History Museum, and I would like to thank all of them for this. I am also grateful to the NHM for access to their analytical facilities, and to Diamond and the ESRF for the beamtime awarded for this work. The Menzies Centre for Australian studies, King's College London, is gratefully acknowledged for providing financial assistance for a three months visit to the Australian National University Research School of Earth Sciences. In addition, the Mineral Physics Group of the Mineralogical Society is thanked for provision of a travel bursary to present this research at Goldschmidt 2013.

I would also like to thank my family, friends, and colleagues who have encouraged and supported me and helped to make my PhD such an enjoyable and positive experience. Especially thanks to Dan for putting up with months of writing up and long absences. Also, for providing emotional support and, most importantly, many delicious meals when they were needed most!

Finally I must thank my supervisors: Andrew Berry for his guidance and sharing of expertise throughout the project, and his liberal use of red pen; Paul Schofield for his support and endless tolerance to a never ending barrage of questions and disasters (also for using less red pen and the provision of chocolate); Fred Mosselmans for giving us in-house beamtime and supervising my time at Diamond. I am also extremely grateful for their assistance on many long, sometimes sleepless, and always entertaining XANES beamtimes.

References

Aigner-Torres, M. and Blundy, J. (2007) Laser Ablation ICPMS study of trace element partitioning between plagioclase and basaltic melts: an experimental approach. *Contributions to Mineralogy and Petr*ology, **153**, 647-667.

Arnold, T., Grossman, K., and Baumann, N. (2010) Uranium speciation in biofilms studied by laser fluorescence techniques. *Analytical and Bioanalytical Chemistry*, **396**, 1641-1653.

Arnold, T., Utsunomiya, S., Geipel, G., Ewing, R.C., Baumann, N., and Brendler, V. (2006) Absorbed U(VI) surface species on muscovite identified by laser fluorescence spectroscopy and transmission electron microscopy. *Environmental Science and Technology*, **40**, 4646-4652.

Avanzinelli, R., Prytulak, J., Skora, S., Heumann, A., Koetsier, G., and Elliott, T. (2012) Combined ^{238}U-^{230}Th and ^{235}U-^{231}Pa constraints on the transport of slab-derived material beneath the Mariana Islands. *Geochimica et Cosmochimica Acta*, **92**, 308-328.

Bali, E., Audétat, A., and Keppler, H. (2011) The mobility of U and Th in subduction zone fluids: an indicator of oxygen fugacity and fluid salinity. *Contributions to Mineralogy and Petrol*ogy, **161**, 597-613

Batanova, V.G. and Savelieva, G.N. (2009) Melt migration in the mantle beneath spreading zones and formation of replacive dunites: a review. *Russian Geology and Geophysics*, **50**, 763-778.

Beattie, P. (1993a) The generation of uranium series disequilibria by partial melting of spinel peridotite: constraints from partitioning studies. *Earth and Planetary Science Lett*ers, **117**, 379-391.

Beattie, P. (1993b) Uranium-thorium disequilibria and partitioning on melting of garnet peridotite. *Nature*, **363**, 63-65.

Becker, H., Jochum, K.P., and Carlson, R.W. (2000) Trace element fractionation during dehydration of eclogites from high-pressure terranes and the implications for element fluxes in subduction zones. *Chemical Geology*, **163**, 65-99.

Beier, C., Turner, S.P., Sinton, J.M., and Gill, J.B. (2010) Influence of subducted components on back-arc melting dynamics in the Manus Basin. *Geochemistry Geophysics, Geosystems*, **11**, doi:10.1029/2010GC003037.

Belai, N., Frisch, M., Ilton, E.S., Ravel, B., and Cahill, L. (2008) Pentavalent uranium oxide reduction of $[UO_2]^{2+}$ under hydrothermal reaction conditions. *Inorganic Chem*istry, **47**, 10135-10140.

Belonoshko, A. and Saxena, S.K. (1991) A molecular dynamics study of the pressure-volume-temperature properties of supercritical fluids: II. CO_2, CH_4, CO, O_2, and H_2. *Geochimica et Cosmochimica Acta*, **55**, 3191-3208.

Berry, A.J. and O'Neill, H.St.C. (2004) A XANES determination of the oxidation state of chromium in silicate glasses. *American Mineralogist*, **89**, 790-798.

Berry, A.J., O'Neill, H.St.C., Scott, D.R., Foran, G.J., and Shelley, J.M.G. (2006) The effect of composition on Cr^{2+}/Cr^{3+} in silicate melts. *American Mineralogist*, **91**, 1901-1908.

Berry, A.J., O'Neill, H.St.C., Jayasuriya, D., Campbell, S.J., and Foran, G.J. (2003b) XANES calibrations for the oxidation state of iron in a silicate glass. *American Mineralogist*, **88**, 967-977.

Berry, A.J., Shelley, J.M.G., Foran, G.J., O'Neill, H.St.C., and Scott, D.R. (2003a) A furnace design for XANES spectroscopy of silicate melts under controlled oxygen fugacities and temperatures to 1773 K. *Journal of Synchrotron Radiation*, **10**, 332-336.

Bézos, A. and Humler, E. (2005) The $Fe^{3+}/\Sigma Fe$ ratios of MORB glasses and their implications for mantle melting. *Geochimica et Cosmochimica Acta*, **69**, 711-725.

Blundy, J. and Wood, B. (1994) Prediction of crystal-melt partition coefficients from elastic moduli. *Nature*, **372**, 452-453.

Blundy, J. and Wood, B. (2003) Mineral-melt partitioning of Uranium, Thorium and their daughters. *Reviews in Mineralogy and Geochem*istry, **52**, 59-123.

Borisov, A. and Jones, J.H. (1999) An evaluation of Re, as an alternative to Pt, for the 1 bar loop technique: an experimental study at 1400 °C. *American Min*eralogist, **84**, 1528-1534.

Botcharnikov, R.E., Koepke, J., Holtz, F., McCammon, C., and Wilke, M. (2005) The effect of water activity on the oxidation and structural state of Fe in a ferro-basaltic melt. *Geochimica et Cosmochimica Acta*, **69**, 5071-5085.

Bourdon, B., Turner, S., and Allègre, C. (1999) Melting dynamics beneath the Tonga-Kermadec island arc inferred from ^{231}Pa-^{235}U systematics. *Science*, **286**, 2491-2493.

Bourdon, B., Turner, S., Henderson, G.M., and Lundstrom, C.C. (2003) Introduction to U-series geochemistry. *Reviews in Mineralogy and Geochem*istry, **52**, 1-21.

Brown, Jr., G.E., Calas, *G.,* Waychunas, G.A., and Petiau, J. (1988) X-ray absorption spectroscopy and its applications in mineralogy and geochemistry, in Hawthorne, F.C. (Ed.), Spectroscopic methods in mineralogy and geology, Reviews in Mineralogy, **18**, Mineralogical Society of America, 431-512.

Burnham, A.D. (2012) Zircon as a recorder of the oxygen fugacity of magmas. PhD Thesis, Imperial College London, UK.

Burnham, A.D. and Berry, A.J. (2012) An experimental study of trace element partitioning between zircon and melt as a function of oxygen fugacity. *Geochimica et Cosmochimica Acta*, **95**, 196-212.

Burnham, A.D. and Berry, A.J. (2014) The effect of oxygen fugacity, melt compoisition, temperature and pressure on the oxidation state of cerium in silicate melts. *Chemical Geology*, **366**, 52-60.

Burnham, A.D., Berry, A.J., Halse, H.R., Cibin, G., and Mosselmans, J.F.W. (2014) The oxidation state of europium in silicate melts as a function of oxygen fugacity, composition and temperature. (in preparation).

Calas, G., Brown, Jr., G.B., Waychunas, G.A., and Petiau, J. (1987) X-ray absorption spectroscopic studies of silicate glasses and minerals. *Physics and Chemistry of Minerals*, **15**, 19-29.

Campbell, J.L. and Papp, T. (2001) Widths of the atomic K-N7 levels. *Atomic Data and Nuclear Data Tables*, **77**, 1-56.

Caulfield, J., Turner, S., Arculus, R., Dale, C., Jenner, F., Pearce, J., Macpherson, C., and Handley, H. (2012) Mantle flow, volatiles, slab-surface temperature and melting dynamics in the north Tonga arc-Lau back-arc basin. *Journal of Geophysical Research*, **117**, doi:10.1029/2012JB009526.

Chase, M. W. Jr. (1998) NIST-JANAF Thermochemical Tables. Washington DC, USA: National Institute of Standards and Technology.

Cooper, K.M., Goldstein, S.J., Sims, K.W.W., and Murrell, M.T. (2003) Uranium-series chronology of Gorda Ridge volcanism. *Earth and Planetary Science Letters*, **206**, 459-475.

Cottrell, E. and Kelley, K.A. (2011) The oxidation state of Fe in MORB glasses and the oxygen fugacity of the upper mantle. *Earth and Planetary Science Letters*, **305**, 270-282.

Cramer, S.P., Tench, O., Yocum, M., and George, G.N. (1988) A 13 element Ge detector for fluorescence EXAFS. *Nuclear Instruments and Methods in Physics Research*, A**266**, 586-591.

Davidson, J., Turner, S., Handley, H., Macpherson, C., and Dosseto, A. (2007) Amphibole "sponge" in arc crust. *Geology*, **35**, 787-790.

Dent, A.J., Cibin, G., Ramos, S., Smith, A.D., Scott, S.M., Varandas, L., Pearson, M.R., Krumpa, N.A., Jones, C.P., and Robbins, P.E. (2009) B18: A core XAS spectroscopy

beamline for Diamond. *Journal of Physics: Conference Series*, **190**, doi:10.1088/1742-6596/190/1/012039.

de Groot, F.M.F., Krisch, M.H., and Vogel, J. (2002) Spectral sharpening of the Pt L edges by high-resolution X-ray emission. *Physical Review B*, **66**, doi:10.1103/PhysRevB.66.195112.

Deines, P., Nafziger, R.H., Ulmer, G.C., and Woermann, E. (1974) Temperature-oxygen fugacity tables for selected gas mixtures in the system C-H-O at one atmosphere total pressure. *Bulletin of the Earth and Mineral Sciences Experiment Station No.* **88**. The Pennsylvania State University, University Park, Pennsylvania, 1-129.

Dosseto, A. and Turner, S. (2013) Reappraisal of uranium-series isotope data in Kamchatka lavas, implications for continental arc magma genesis. *Geological Society Special Publication*, **385**, 103-116.

Duffy, J.A. (1993) A review of optical basicity and its applications to oxidic systems, *Geochimica et Cosmochimica Acta*, **57**, 3961-3970.

Duffy, J.A. and Ingram, M.D. (1976) An interpretation of glass chemistry in terms of the optical basicity concept. *Journal of Non-Crystalline Solids*, **21**, 373-410.

Elburg, M.A. and Kamenetsky, V.S. (2007) Dehydration processes determine fO_2 of arc and intraplate magmas. *Geochimica et Cosmochimica Acta*, **71**, A252.

Elkins, L.J., Sims, K.W.W., Prytulak, J., Elliot, T., Mattielli, N., Blichert-Toft, J., Blusztajn, J., Dunbar, N., Devey, C., Mertz, D.F., Schilling, J.-G., and Murrell, M. (2011) Understanding melt generation beneath the slow-spreading Kolbeinsey Ridge using ^{238}U, ^{230}Th, and ^{231}Pa excesses. *Geochimica et Cosmochimica Acta*, **75**, 6300-6329.

Elkins, L.J. (2009) Basalt petrogenesis beneath slow- and ultraslow spreading Arctic mid-ocean ridges. PhD Thesis, Massachusetts Institute of Technology and Wood Oceanographic Institution.

Evans, K.A., Elburg, M.A., and Kamenetsky, V.S. (2012) Oxidation state of subarc mantle. *Geology*, **40**, 783-786.

Fabbrizio, A., Schmidt, M.W., Günther, D., and Eikenberg, J. (2009) Experimental determination of Ra mineral/melt partitioning for feldspars and ^{226}Ra-disequilibrium crystallization ages of plagioclase and alkali-feldspar. *Earth and Planetary Science Letters*, **280**, 137-148.

Falloon, T.J. and Green, D.H. (1987) Anhydrous partial melting of MORB pyrolite and other peridotite compositions at 10 kbar implications for the origin of primitive MORB glasses. *Mineralogy and Petrology*, **37**, 181-219.

Farges, F., Ponader, C.W., Calas, G., and Brown, Jr., G.E. (1992) Structural environments of incompatible elements in silicate glass/melt systems: II. U^{IV}, U^{V}, U^{VI}. *Geochimica et Cosmochimica Acta*, **56**, 4205-4220.

Fuggle, J.C. and Alvarado, S.F. (1980) Core-level lifetimes as determined by X-ray photoelectron spectroscopy measurements. *Physical Review A*, **22**, 1615-1624.

Glatzel, P., de Groot, F.M.F., and Bergmann, U. (2009). Hard X-ray photon-in photon-out spectroscopy. *Synchrotron Radiation News*, **22**, 12-16.

Glatzel, P., Weng, T.-C., Kvashnina, K., Swarbrick, J., Sikora, M., Gallo, E., Smolentsev, N., and Mori, R.A. (2013) Reflections on hard X-ray photon-in/photon-out spectroscopy for electronic structure studies. *Journal of Electron Spectroscopy and Related Phenomena*, **188**, 17-25.

Grossman, K., Arnold, T., Ikeda-Ohno, A., Steudtner, R., Geipel, G., and Bernhard, G. (2009a) Fluorescence properties of a uranyl(V)-carbonate species $[U(V)O_2(CO_3)_3]^{5-}$ at low temperature. *Spectrochimica Acta Part A: Molecular and Bimolecular Spectroscopy*, **72**, 449-453.

Grossman, K., Arnold, T., Krawczyk-Bärsch, E., Diessner, S., Wobus, A., and Krawietz, R. (2007) Identification of fluorescent U(V) and U(VI) microparticles in a multispecies biofilm

by confocal scanning microscopy and fluorescence spectroscopy. *Environmental Science and Technology*, **41**, 6498-6504.

Grossman, K., Arnold, T., Steudtner, R., Weiss, S., and Bernhard, G. (2009b) Visualizing different uranium oxidation states during the surface alteration of uraninite and uranium tetrachloride. *Naturwissenschaften*, **96**, 963-974.

Guillot, B. and Sator, N. (2011) Carbon dioxide in silicate melts: A molecular dynamics simulation study. *Geochimica et Comsochimica Acta*, **75**, 1829-1857.

Hämäläinen, K., Siddons, D.P., Hastings, J.B., and Berman, L.E. (1991) Elimination of the inner-shell lifetime broadening in X-ray absorption spectroscopy. *Physical Review Lett*ers, **67**, 2850-2853.

Heald, S. M. (1988) Design of an EXAFS experiment, in Koningsberger, D. C. and Prins, R. (Ed.), X-ray Absorption: Principles, Applications, Techniques of EXAFS, SEXAFS, and XANES, John Wiley & Sons: New York, 87-118.

Hermann, J. and Rubatto, D. (2009) Accessory phase control on the trace element signature of sediment melts in subduction zones. *Chemical Geology*, **265**, 512-526.

Holland, T.J.B. and Powell, R. (1998) An internally consistent thermodynamic data set for phases of petrological interest. *Journal of Metamorphic Geology*, **16**, 309-343.

Holloway, J.R., Pan, V., and Gudmundsson, G. (1992) High-pressure fluid-absent melting experiments in the presence of graphite: oxygen fugacity, ferric/ferrous ratio and dissolved CO_2. *European Journal of Mineralogy*, **4**, 105-114.

Holloway, J.R. and Wood, B.J. (1988) Simulating the Earth: Experimental Geochemistry, Harper Collins Academic, London, UK.

Holzheid, A., Palme, H., and Chakraborty, S. (1997) The activities of NiO, CoO and FeO in silicate melts. *Chemical Geology*, **139**, 21-38.

Hu, Z., Kaindl, G., and Meyer, G. (1998) Chemical shifts in the X-ray absorption near-edge structure spectra of UBr_n (n = 3, 4, 5) and $CsLiUX_6$ (X = F, Cl, Br, I). *Journal of Alloys and Compounds*, **274**, 38-41.

Huang, F., Gao, L., and Lundstrom, C.C. (2008) The effect of assimilation, fractional crystallization, and ageing on U-series disequilibria in subduction zone lavas. *Geochimica et Comsochimica Acta*, **72**, 4136-4145.

Huang, F., Lundstrom, C.C., Sigurdsson, H., and Zhang, Z. (2011) U-series disequilibria in Kick'em Jenny submarine volcano lavas: A new view of time-scales of magmatism in convergent margins. *Geochimica et Cosmochimica Acta*, **75**, 195-212.

Hudson, E.A., Rehr, J.J., and Bucher, J.J. (1995) Multiple-scattering calculations of the uranium L_3-edge X-ray absorption near-edge structure. *Physical Review B*, **52**, 13815-13826.

Idriss, H. (2010) Surface reactions of uranium oxide powder, thin films and single crystals. *Surface Science Reports*, **65**, 67-109.

Ilton, E.S. and Bagus, P.S. (2011) XPS determnation of uranium oxidation states. *Surface and Interface Analysis*, **43**, 1549-1560.

Iwamori, H. (1994) ^{238}U-^{230}Th-^{226}Ra and ^{235}U-^{231}Pa disequilibria produced by mantle melting with porous and channel flows. *Earth and Planetary Science Letters*, **125**, 1-16.

Jenner, F.E., O'Neill, H.St.C., Arculus, R.J., and Mavrogenes, J.A. (2010) The magnetite crisis in the evolution of arc-related magmas and the initial concentration of Au, Ag and Cu. *Journal of Petrology*, **51**, 2445-2464.

Jull, M., Kelemen, P.B., and Sims, K. (2002) Consequences of diffuse and channelled porous melt migration on uranium series disequilibria. *Geochimica et Comsochimica Acta*, **66**, 4133-4148.

Kalkowski, G., Kaindl, G., Brewer, W.D., and Krone, W. (1987) Near-edge X-ray-absorption fine structure in uranium compounds. *Physical Review B*, **35**, 2667-2677.

Karner, J.M., Papike, J.J., Sutton, S.R., Burger, P.V., Shearer, C.K., Le, L., Newville, M., and Choi, Y. (2010) Partitioning of Eu between augite and a highly spiked martian basalt composition as a function of oxygen fugacity (IW-1 to QFM): Determination of Eu^{2+}/Eu^{3+} ratios by XANES. *American Mineralogist,* **95**, 410-413.

Kelemen, P.B., Shimizu, N., and Salters, V.J.M. (1995) Extraction of mid-ocean-ridge basalt from the upwelling mantle by focused flow of melt in dunite channels. *Nature*, **375**, 747-753.
Kelley, K.A. and Cottrell, E. (2009) Water and the oxidation state of subduction zone magmas. *Science*, **325**, 605-607.

Kelley, K.A. and Cottrell, E. (2012) The influence of magmatic differentiation on the oxidation state of Fe in a basaltic arc magma. *Earth and Planetary Science Letters*, **329-330**, 109-121.

Kirishima, A., Kimura, T., Tochiyama, O., and Yoshida, Z. (2003) Luminescence study of tetravalent uranium in aqueous solution. *Chemical Communications*, **7**, 910-911.

Klemme, S. and O'Neill, H.St.C. (1997) The reaction $MgCr_2O_4 + SiO_2 = Cr_2O_3 + MgSiO_3$ and the free energy of formation of magnesiochromite ($MgCr_2O_4$). *Contributions to Mineralogy and Petrology*, **130**, 59-65.

Klimm, K., Kohn, S.C., and Botcharnikov, R.E. (2012) The dissolution mechanism of sulphur in hydrous silicate melts. II: Solubility and speciation of sulphur in hydrous silicate melts as a function of fO_2. *Chemical Geology*, **322-323**, 250-267.

Knoll, G.F. (2010) Radiation detection and measurement (4th Ed.), Hoboken, N.J. : Wiley.

Kohn, S.C. (2000) The dissolution mechanisms of water in silicate melts; a synthesis of recent data. *Mineralogical Magazine*, **64**, 389-408.

Kosog, B., La Pierre, H.S., Denecke, M.A., Heinemann, F.W., and Meyer, K. (2012) Oxidation state delineation via U L_{III}-edge XANES in a series of isostructural uranium coordination complexes. *Inorganic Chemistry*, **51**, 7940-7944.

Krause, M.O. and Oliver, J.H. (1979). Natural widths of atomic K and L levels, Kα X-ray lines and several KLL Auger lines. *Journal of Physical and Chemical Reference Data*, **8**, 329-338.

Kress, V.C. and Carmichael, I.S.E. (1991) The compressibility of silicate liquids containing Fe_2O_3 and the effect of composition, temperature, oxygen fugacity and pressure on their redox states. *Contributions to Mineralogy and Petrology*, **108**, 82-92.

Kvashnina, K.O., Butorin, S.M., Martin, P., and Glatzel, P. (2013) Chemical state of complex uranium oxides. *Physical Review Letters*, **111**, doi: 10.1103/PhysRevLett.111.253002.

Kvashnina, K.O. and Butorin, S.M. (2014) Role of resonant inelastic X-ray scattering in high-resolution core-level spectroscopy of actinide materials. *Journal of Electron Spectroscopy and Related Phenomena*, (in press) doi: 10.1016/j.elspec.2014.01.016.

Landwehr, D., Blundy, J., Chamorro-Perez, E.M., Hill, E., and Wood, B. (2001) U-series disequilibria generated by partial melting of spinel lherzolite. *Earth and Planetary Science Letters*, **188**, 329-348.

Lange, R. A. and Carmichael, I.S.E. (1989) Ferric-ferrous equilibria in Na_2O-FeO-Fe_2O_3-SiO_2 melts: Effects of analytical techniques on derived partial molar volumes. *Geochimica et Comsmochimica Acta*, **53**, 2195-2204.

Laubier, M., Grove, T.L., and Langmuir, C.H. (2014) Trace element mineral/melt partitioning for basaltic and basaltic andesitic melts: an experimental and laser ICP-MS study with application to the oxidation state of mantle source regions. *Earth and Planetary Science Letters*, **392**, 265-278.

Lauer, H.V. Jr. and Morris, R.V. (1977) Redox equilibria of multivalent ions in silicate glasses. *Journal of the American Ceramic Society*, **60**, 443-451.

Lebouteiller, A. and Courtine, P (1998) Improvement of a bulk optical basicity table for oxidic systems. *Journal of Solid State Chemistry*, **137**, 94-103.

Lee, C.-T.A., Leeman, W.P., Canil, D., and Li, Z.-X.A. (2005) Similar V/Sc systematics in MORB and arc basalts: Implications for the oxygen fugacities of their mantle source regions. *Journal of Petrology*, **46**, 2313-2336.

Liu, X., O'Neill, H. St. C., and Berry, A.J. (2006) The effects of small amounts of H_2O, CO_2 and Na_2O on the partial melting of spinel lherzolite in the system CaO-MgO-Al_2O_3-SiO_2 ± H_2O ± CO_2 ± Na_2O at 1.1 GPa. *Journal of Petrology*, **47**, 409-434.

Lundstrom, C. (2000) Models of U-series disequilibria generation in MORB: the effects of two scales of melt porosity. *Physics of the Earth and Planetary Interiors*, **121**, 189-204.

Lundstrom, C.C. (2003) Uranium-series Disequilibria in Mid-ocean Ridge Basalts: Observations and Models of Basalt Genesis. *Reviews in Mineralogy and Geochem*istry, **52**, 175-214.

Lundstrom, C.C., Shaw, H.F., Ryerson, F.J., Phinner, D.L., Gill, J.B., and Williams, Q. (1994) Compositional controls on the partitioning of U, Th, Ba, Pb, Sr and Zr between clinopyroxene and haplobasaltic melts: implications for uranium series disequilibria in basalts. *Earth and Planetary Science Letters*, **128**, 407-423.

Mallmann, G. and O'Neill, H. St., C. (2007) The effect of oxygen fugacity on the partitioning of Re between crystals and silicate melt during mantle melting. *Geochimica et Comoschimica Acta*, **71**, 2837-2857.

Mallmann, G. and O'Neill, H.St.C. (2009) The crystal/melt partitioning of V during mantle melting as a function of oxygen fugacity compared with some other elements (Al, P, Ca, Sc, Ti, Cr, Fe, Ga, Y, Zr and Nb). *Journal of Petro*logy, **50**, 1765-1794.

McKenzie, D. (1985) ^{230}Th-^{238}U disequilibrium and the melting processes beneath ridge axes. *Earth and Planetary Science Letters*, **72**, 149-157.

McKenzie, D. (2000) Constraints on melt generation and transport from U-series activity ratios. *Chemical Geology*, **162**, 81-94.

Miller, S.A., Burnett, D.S., Asimow, P.D., Phinney, D.L., and Hutcheon, I.D. (2007) Experimental study of radium partitioning between anorthite and melt at 1 atm. *American Mineralogist*, **92**, 1535-1538.

Mitchell, E.C. and Asmerom, Y. (2011) U-series isotope systematic of mafic magmas from central Oregon: Implications for fluid involvement and melting processes in the Cascade arc. *Earth and Planetary Science Letters*, **312**, 378-389.

Mosselmans, J.F.W., Quinn, P.D., Dent, A.J., Cavill, S.A., Moreno, S.D., Peach, A., Leicester, P.J., Keylock, S.J., Gregory, S.R., Atkinson, K.D., and Rosell, J.R. (2009) I18-the microfocus spectroscopy beamline at the Diamond Light Source. *Journal of Synchrotron Radiation*, **16**, 818-824.

Mottana, A. (2004) X-ray absorption spectroscopy in mineralogy: theory and experiment in the XANES region, in Beran, A. and Libowitzky, E. (Ed.), Spectroscopic methods in mineralogy, Notes in Mineralogy, **6**, European Mineralogical Union, 465-552.

Mysen, B.O. and Virgo, D. (1980) Solubility mechanisms of carbon dioxide in silicate melts: a Raman spectroscopic study. *American Mineralogist,* **65**, 885-899.

Mysen, B.O. and Virgo, D. (1985) Iron-bearing silicate melts: relations between pressure and redox equilibria. *Physics and Chemistry of Minerals,* **12**, 191-200.

Mysen, B.O., Virgo, D., and Seifert, F.A. (1982) The structure of silicate melts: implications for chemical and physical properties of natural magma. *Reviews of Geophysics and Space Physics*, **20**, 353-383.

Newville, M. (2004) Fundamentals of EXAFS. Consortium for Advanced Radiation Sources, University of Chicago (USA) [http://xafs. org].

Ni, H. and Keppler, H. (2013) Carbon in silicate melts. *Reviews in Mineralogy and Geochem*istry, **75**, 251-287.

Olivero, J.J. and Longbothum, R.L. (1977) Empirical fits to the Voigt line width: A brief review. *Journal of Quantitative Spectroscopy and Radiative Transfer*, **17**, 233-236.

O'Neill, H.St.C. (1987) Quartz-fayalite-iron and quartz-fayalite-magnetite equilibria and the free energy of formation of fayalite (Fe_2SiO_4) and magnetite (Fe_3O_4). *American Mineralogist*, **72**, 67-75.

O'Neill, H.St.C., Berry, A.J., McCammon, C.C., Jayasuriya, K.D., Campbell, S.J., and Foran, G. (2006) An experimental determination of the effect of pressure on the $Fe^{3+}/\sum Fe$ ratio of an anhydrous silicate melt to 3.0 GPa. *American Mineralogist*, **91**, 404-412.

O'Neill, H.St.C. and Eggins, S.M. (2002) The effect of melt composition on trace element partitioning: an experimental investigation of the activity coefficients of FeO, NiO, CoO, MoO_2 and MoO_3 in silicate melts. *Chemical Geology*, **186**, 151-181.

O'Neill, H.St.C. and Mavrogenes, J.A. (2002) The sulphide capacity and the sulphur content at sulphide saturation of silicate melts at 1400 ^{0}C and 1 bar. *Journal of Petrology,* **43**, 1049-1087.

O'Neill, H.St.C. and Nell, J. (1997) Gibbs free energies of formation of RuO_2, IrO_2, and OsO_2: A high temperature electrochemical and calorimetric study. *Geochimica et Comoschimica Acta*, **61**, 5279-5293.

O'Neill, H.St.C. and Pownceby, M.I. (1993) Thermodynamic data from redox reactions at high temperatures. I. An experimental and theoretical assessment of the electrochemical method using stabilized zirconia electrolytes, with revised values for Fe-"FeO", Co-CoO, Ni-NiO and Cu-Cu_2O oxygen buffers, and new data for the W-WO_2 buffer. *Contributions to Mineralogy and Petrology,* **114**, 296-314.

Onuma, N., Higuchi, H., Wakita, H., Nagasawa, H. (1968) Trace element partition between two pyroxenes and the host lava. *Earth and Planetary Science Letters*, **5**, 47-51.

Özkendir, O.M. and Ufuktepe, Y. (2005) Temperature dependent change of the MnS K-edge. *Journal of Optoelectronics and Advanced Materials*, **7**, 2655-2660.

Peach, C.L. and Mathez, E.A. (1993) Sulfide melt-silicate melt distribution coefficients for nickel and iron and implications for the distribution of other chalcophile elements. *Geochimica et Cosmochimica Acta*, **57**, 3013-3021.

Petiau, J., Calas, G., Petitmaire, D., Bianconi, A., Benfatto, M., and Marcelli, A. (1986). Delocalized versus localized unoccupied 5f states and the uranium site structure in uranium oxides and glasses probed by X-ray absorption near-edge structure. *Physical Revie*w B, **34**, 7350-7361.

Pickett, D.A. and Murrell, M.T. (1997) Observations of $^{231}Pa/^{235}U$ disequilibrium in volcanic rocks. *Earth and Planetary Science Letters*, **148**, 259–271.

Pireaux, J.J., Thibaut, R.E., and Tenret-Noel, C. (1977) Shake-up satellites in the X-ray photoelectron spectra of uranium oxides and fluorides. A band structure scheme for uranium dioxide, UO_2. *Chemical Physics*, **22**, 113-120.

Polovov, I.B., Volkovich, V.A., Charnock, J.M., Kralj, B., Lewin, R.G., Kinoshita, H., May, I., and Sharrad, C.A. (2008) In situ spectroscopy and spectroelectrochemistry of uranium in high-temperature alkali chloride molten salts. *Inorganic Chem*istry, **47**, 7474-7482.

Pownceby, M.I. and O'Neill, H.St.C. (1994) Thermodynamic data from redox reactions at high temperatures. IV. Calibration of the Re-ReO_2 oxygen buffer from EMF and NiO + Ni-Pd redox sensor measurements. *Contributions to Mineralogy and Petrology*, **118**, 130-137.

Rabedeau, T. (2010) SSRL XAS Beam Lines-Soft X-ray, SSRL SMB summer school [PowerPoint slides]. Retrieved from http://www-conf.slac.stanford.edu/smbxas-ss/2010/talks/Rabedeau_02.pdf (viewed 12 June 2013).

Ravel, B. and Newville, M. (2005) Athena, Artemis, and Hephaestus. *Journal of Synchrotron Radiation*, **12**, 537-541.

Reed, S.J.B. (2005) Electron microprobe analysis and scanning electron microscopy in geology (2nd Ed.), Cambridge University Press.

Reubi, O., Bourdon, B., Dungan, M.A., Koornneef, J.M., Sellés, D, Langmuir, C.H., and Aciego, S. (2011) Assimilation of the plutonic roots of the Andean arc controls variations in U-series disequilibria at Volcan Llaima, Chile. *Earth and Planetary Science Letters*, **303**, 37-47.

Reubi, O., Sims, K.W.W., and Bourdon, B. (2014) ^{238}U-^{230}Th equilibrium in arc magmas and implications for the time scales of mantle metasomatism. *Earth and Planetary Science Letters*, **391**, 146-158.

Rubin, K.H. and Sinton, J.M. (2007) Inferences on mid-ocean ridge thermal and magmatic structure from MORB compositions. *Earth and Planetary Science Letters*, **260**, 257-276.

Rubin, K.H., van der Zander, I., Smith, M.C., and Bergmanis, E.C. (2005) Minimum speed limit for ocean ridge magmatism from ^{210}Pb-^{226}Ra-^{230}Th disequilibria. *Nature*, **437**, 534-538.

Russo, C.J., Rubin, K.H., and Graham, D.W. (2009) Mantle melting and magma supply to the Southeast Indian Ridge: The role of lithology and melting conditions from U-series disequilibria. *Earth and Planetary Science Letters*, **278**, 55-66.

Salters, V.J.M. and Longhi, J. (1999) Trace element partitioning during the initial stages of melting beneath mid-ocean ridges. *Earth and Planetary Science Letters*, **166**, 15-30.

Salters, V.J.M., Longhi, J.E., and Bizimis, M. (2002) Near mantle solidus trace element partitioning at pressures up to 3.4 GPa. *Geochemistry Geophysics Geosystems*, **3**, doi:10.1029/2001GC000148.

Schelter, E.J., Wu, R., Veauthier, J.M., Bauer, E.D., Booth, C.H., Thomson, R.K., Graves, C.R., John, K.D., Scott, B.L., Thompson, J.D., Morris, D.E., and Kiplinger, J.L. (2010) Comparative study of F-element electronic structure across a series of multimetallic actinide and lanthanoid-actinide complexes possessing redox-active bridging ligands. *Inorganic Chemistry*, **49**, 1995-2007.

Schmitt, A. K. (2007) Ion microprobe analysis of (^{231}Pa)/(^{235}U) and an appraisal of protactinium partitioning in igneous zircon. *American Mineralogist*, **92**, 691-694.

Schnetzler, C.C. and Philpotts, J.A. (1970) Partition coefficients of rare-earth elements between igneous matrix material and rock-forming mineral phenocrysts-II. *Geochimica et Cosmochimica Acta*, **34**, 331-340.

Schofield, P.F., Smith, A.D., Scholl, A., Doran, A., Covey-Crump, S.J., Young, A.T., and Ohldag, H. (2014) Chemical and oxidation-state imaging of mineralogical intergrowths: The application of X-ray photo-emission electron microscopy (XPEEM). *Coordination Chemistry Reviews*, doi: 10.1016/j.ccr.2014.02.006.

Schreiber, H. D. (1977) Redox states of Ti, Zr, Hf, Cr and Eu in basaltic magmas: an experimental study. *Proceedings of the 8th Lunar and Planetary Science Conference*, 1785-1807.

Schreiber, H.D. (1983). The chemistry of uranium in glass-forming aluminosilicate melts. *Journal of Less Common Metals*, **91**, 129-147.

Schreiber, H.D. (1987). An electrochemical series of redox couples in silicate melts: a review and applications to geochemistry. *Journal of Geophysical Research*, **92**, 9225-9232.

Schreiber, H.D., Balazs, G.B., and Kozak, S.J. (1983) Chemistry of uranium in glass-forming melts: redox interaction of uranium with chromium and iron in aluminosilicates. *Journal of the American Ceramic Society*, **66**, 340-346.

Schreiber, H.D., Merkel, R.C., Schreiber V.L., and Balazs, B. (1987) Mutual interactions of redox couples via electron exchange in silicate melts: models for geochemical melt systems. *Journal of Geophysical Research*, **92**, 9233-9245.

Sims, K.W.W., Goldstein, S.J., Blichert-Toft, J., Perfit, M.R., Keleman, P., Fornari, D.J., Michael, P., Murrell, M.T., Hart, S.R., DePaolo, D.J., Layne, G., Ball, L., Jull, M., and Bender, J. (2002) Chemical and isotopic constraints on the generation and transport of magma beneath the East Pacific Rise. *Geochimica et Cosmochimica Acta*, **66**, 3481-3504.

Soldatov, A.V., Ivanchenko, T.S., Longa, S.D., Kotani, A., Iwamoto, Y., and Bianconi, A. (1994) Crystal-structure effects in the Ce L_3-edge X-ray absorption spectrum of CeO_2:

Multiple-scattering resonances and many-body final states. *Physical Review B*, **50**, 5074-5080.

Soldatov, A.V., Lamoen, D., Konstantinović, M.J., Van den Berghe, S., Scheinost, A.C., and Verwerft, M. (2007) Local structure and oxidation state of uranium in some ternary oxides: X-ray absorption analysis. *Journal of Solid State Chemistry*, **180**, 53-60.

Spiegelman, M. (2000) UseCalc: A web-based uranium series calculator for magma migration problems. *Geochemistry Geophysics Geosystems*, **1**, 1016, doi:10.1029/1999GC000030.

Spiegelman, M. and Elliot, T. (1993) Consequences of melt transport for uranium series disequilibrium in young lavas. *Earth and Planetary Science Letters*, **118**, 1-20.

Standish, J.J. and Sims, K.W.W. (2010) Young off-axis volcanism along the ultraslow-spreading Southwest Indian Ridge. *Nature Geoscience*, **3**, 286-292.

Stern, E. A. (1988) Theory of EXAFS, in Koningsberger, D. C. and Prins, R. (Ed.), X-ray Absorption: Principles, Applications, Techniques of EXAFS, SEXAFS, and XANES, Ed. Koningsberger, D. C. and Prins, R., John Wiley & Sons: New York, 3-52.

Steudtner, R., Arnold, A., Grossman, K., Geipel, G., and Brendler, V. (2006) Luminescence spectrum of uranyl(V) in 2-propanol perchlorate solution. *Inorganic Chemistry Communications*, **9**, 939-941.

Stracke, A., Zindler, A., Salters, V.J.M., McKenzie, D., and Grönvold, K. (2003) The dynamics of melting beneath Theistareykir, northern Iceland. *Geochemistry Geophysics Geosystems*, **4**, doi:10.1029/2002GC000347.

Sugawara, T. (1999) Experimental techniques to minimize Fe and Na losses in one atmosphere gas mixing furnace. *Journal of Mineralogy, Petrology and Economic Geology*, **94**, 425-441.

Sutton, S.R., Karner, J., Papike, J., Delaney, J.S., Shearer, C., Newville, M., Eng, P., Rivers, M., and Dyar, M.D. (2005) Vanadium K edge XANES of synthetic and natural basaltic

glasses and application to microscale oxygen barometry. *Geochimica et Cosmochimica Acta*, **69**, 2333-2348.

Swarbrick, J.C., Skyllberg, U., Karlsson, T., and Glatzel, P. (2009) High energy resolution X-ray absorption spectroscopy of environmentally relevant Lead(II) compounds. *Inorganic Chemistry*, **48**, 10748-10756.

Takahashi, Y., Sakami, H., and Nomura, M. (2002) Determination of the oxidation state of cerium in rocks by Ce L_{III}-edge X-ray absorption near-edge structure spectroscopy. *Analytica Chimica Acta*, **468**, 345-354.

Tepley, F.J. III, Lundstrom, C.C., Sims, K.W.W., and Hékinian, R. (2004) U-series disequilibria in MORB from the Garrett Transform and implications for mantle melting. *Earth and Planetary Science Letters*, **223**, 79-97.

Thomas, R.B., Hirschmann, M.M., Cheng, H., Reagan, M.K., and Edwards, R.L. (2002) (^{231}Pa/^{235}U)-(^{230}Th/^{238}U) of young mafic volcanic rocks from Nicaragua and Costa Rica and the influence of flux melting of U-series systematics of arc lavas. *Geochimica et Cosmochimica Acta*, **66**, 4287-4309.

Thompson, A. (2009) X-ray data booklet, Lawrence Berkeley National Laboratory, University of California, Berkeley [http://xdb.lbl.gov/].

Turner, S., Regelous, M., Hawkesworth, C., and Rostami, K. (2006) Partial melting processes above subducting plates: Constraints from ^{231}Pa-^{235}U disequilibria. *Geochimica et Cosmochimica Acta*, **70**, 480-503.

Turner, S., Bourdon, B., and Gill, J. (2003) Insights into magma genesis at convergent margins from U-series isotopes. *Reviews in Mineralogy and Geochem*istry, **52**, 255-315.

Turner, S., Evans, P., and Hawkesworth, C. (2001) Ultrafast source-to-surface movement of melt at island arcs from ^{226}Ra-^{230}Th systematics. *Science*, **292**, 1363-1366.

Ulmer, P. and Luth, R.W. (1991) The graphite-COH fluid equilibrium in P, T, fO_2 space. *Contributions to Mineralogy and Petrology*, **106**, 265-272.

Van Orman, J.A., Saal, A.E., Bourdon, B., and Hauri, E.H. (2006) Diffusive fractionation of U-series radionuclides during mantle melting and shallow-level melt-cumulate interaction. *Geochimica et Cosmochimica Acta*, **70**, 4797-4812.

Veal, B.W., Mundy, J.N., and Lam, D.J. (1987) Actinides in silicate glasses, in Freeman, A.J. and Lander, G.H. (Ed.), Handbook of the Physics and Chemistry of The Actinides, Elsevier, 271-309.

Volpe, A.M. and Goldstein, S.J. (1993) ^{226}Ra-^{230}Th disequilibrium in axial and off axial mid-ocean ridge basalts. *Geochimica et Cosmochimica. Acta*, **57**, 1233-1241.

Walter M.J. and Presnall, D.C. (1994) Melting behavior of simplified lherzolite in the system CaO-MgO-Al_2O_3-SiO_2-Na_2O from 7 to 35 kbar. *Journal of Petrology*, **35**, 329-359.

Wildner, M., Andrut, M., and Rudowicz, C.Z. (2004) Optical absorption spectroscopy in geosciences. Part 1: Basic concepts of crystal field theory, in Beran, A. and Libowitzky, E. (Ed.), Spectroscopic methods in mineralogy, Notes in Mineralogy, **6**, European Mineralogical Union, 93-143.

Wilke, M., Farges, F., Partzsch, G.M., Schmidt, C., and Behrens, H. (2007) Speciation of Fe in silicate glasses and melts by in-situ XANES spectroscopy. *American Mineralogist*, **92**, 44-56.

Wilke, M., Partzsch, G.M., Bernhardt, R., and Lattard, D. (2004) Determination of the iron oxidation state in basaltic glasses using XANES at the K-edge. *Chemical Geology*, **213**, 71-87.

Willmott, P. (2011) An Introduction to Synchrotron Radiation: Techniques and Applications, John Wiley & Sons, Ltd, Chichester, UK.

Wojdyr, M. (2010) Fityk: a general-purpose peak fitting program. *Journal of Applied Crystallography*, **43**, 1126-1128.

Wood, B.J., Blundy, J.D., and Robinson, A.C. (1999) The role of clinopyroxene in generating U-series disequilibrium during mantle melting. *Geochimica et Cosmochimica Acta*, **63**, 1613-1620.

Zhang. G.L., Zeng, Z.G., Beier, C., Yin, X.B., and Turner, S. (2010) Generation and evolution of magma beneath the East Pacific Rise: Constraints from U-series disequilibrium and plagioclase-hosted melt inclusions. *Journal of Volcanology and Geothermal Research*, **193**, 1-17.

Table A1.1: List of piston cylinder experiments.

Exp. no.	Comp.	fO_2 buffer	T (° C)	P (kbar)	Assembly	Capsule	Exp. time	Notes	Metal and oxide
C4290	MORB	C-CO_2	1500	15	1/2"	4 mm	24	100 % carbonated	NA
C4291	MORB	C-CO_2	1400	10	1/2"	4 mm	24	100 % carbonated	NA
C4292	MORB	C-CO_2	1400	5	1/2"	4 mm	failed	100 % carbonated	NA
C4293	MORB	C-CO_2	1400	8.5	1/2"	4 mm	failed	100 % carbonated	NA
C4294	MORB	C-CO_2	1500	20	1/2"	4 mm	24	100 % carbonated	NA
C4295	MORB	C-CO_2	1500	10	1/2"	4 mm	failed	100 % carbonated	NA
C4296	MORB	C-CO_2	1500	12.5	1/2"	4 mm	24	100 % carbonated	NA
C4297	MORB	C-CO_2	1400	7.5	1/2"	4 mm	failed	10% carbonated + 90% decarbonated	NA
C4298	MORB	C-CO_2	1500	10	1/2"	4 mm	failed	10% carbonated + 90% decarbonated	NA
C4301	MORB	C-CO_2	1400	7.5	1/2"	4 mm	failed	10% carbonated + 90% decarbonated	NA
C4303	MORB	Ru-RuO_2	1400	7.5	1/2"	4 mm	failed	100 % decarbonated	Yes
C4304	MORB	Ru-RuO_2	1500	15	1/2"	4 mm	12	100 % decarbonated	Yes
C4305	MORB	Ru-RuO_2	1500	20	1/2"	4 mm	8	100 % decarbonated	Yes
C4308	MORB	Ru-RuO_2	1400	10	1/2"	4 mm	8	100 % decarbonated	Yes
C4309	MORB	Ru-RuO_2	1500	12.5	1/2"	4 mm	8	100 % decarbonated	Yes
C4310	MORB	Ru-RuO_2	1500	25	1/2"	4 mm	7	100 % decarbonated	Yes
C4311	MORB	Pt-PtO_2	1400	10	1/2"	2.7 mm	12	100 % decarbonated	NA
C4313	MORB	Pt-PtO_2	1500	15	1/2"	2.7 mm	12	100 % decarbonated	NA
C4314	MORB	C-CO_2	1400	7.5	5/8"	3.5 mm	12	10% carbonated + 90% pre-equilibrated glass reground ($\log fO_2 = -8$)	NA
C4317	MORB	Pt-PtO_2	1500	12.5	1/2"	2.7 mm	12	100 % decarbonated	NA
D1490	MORB	Pt-PtO2	1400	7.5	5/8”	2.7 mm	24	100 % decarbonated	NA

Exp. no.	Comp.	fO_2 buffer	T (° C)	P (kbar)	Assembly	Capsule	Exp. time	Notes	Metal and oxide
C4318	MORB	C-CO_2	1400	5	5/8"	3.5 mm	12	10% carbonated + 90% pre-equilibrated glass reground ($\log fO_2 = -8$)	NA
D1491	MORB	Ru-RuO_2	1400	7.5	5/8"	2.7 mm	24	100 % decarbonated	Yes
D1492	MORB	Pt-PtO_2	1400	5	5/8"	2.7 mm	24	100 % decarbonated	NA
D1493	MORB	Ru-RuO_2	1400	5	5/8"	2.7 mm	24	100 % decarbonated	Yes
Samples prepared by Guil Mallmann (ANU)									
D1251	AD	Pt-PtO_2	1400	5	1/2"	2.7 mm	24		NA
D1259	AD	Pt-PtO_2	1400	15	1/2"	2.3 mm	24		NA
C4012	AD	Ir-IrO_2	1400	5	1/2"	2.7 mm	24		Yes
D1235	AD	Ir-IrO_2	1400	10	1/2"	2.3 mm	23		Yes
C4011	AD	Ir-IrO_2	1400	15	1/2"	2.7 mm	24		Yes
D1244	AD	C-CO_2	1400	5	1/2"	2.7 mm	24		NA
D1257	AD	C-CO_2	1400	15	1/2"	3.5 mm	24		NA
D1236	AD	Ru-RuO_2	1400	15	1/2"	2.3 mm	23		Yes
D1243	AD	Re-ReO_2	1400	5	1/2"	2.3 mm	24		No ReO_2
D1254	AD	Re-ReO_2	1400	5	1/2"	2.7 mm	24		No ReO_2
D1242	AD	Re-ReO_2	1400	15	1/2"	2.7 mm	25		No ReO_2
D1253	AD	Re-ReO_2	1400	15	1/2"	2.7 mm	24		No ReO_2

PM208_1,2,3,4,5,6, PM224_1, and J29: MORB and AD10 kbar series equilibrated at C-CO_2, Re-ReO_2, Ru-RuO_2, and Pt-PtO_2 were prepared by Dean Scott (ANU).

Appendix 2:

EPMA data

A2.1 Comments on EPMA data for 1 atm glasses

EPMA data for all of the 1atm MORB composition glasses prepared for RT XANES studies (Table A2.1) give compositional totals of > 98.5% and indicate that none of the melts lost significant Fe, with the exception of the sample prepared at $\log fO_2 = -12$ (FeO = 4.9(1) wt %), which is excluded from the XANES studies described in this thesis. CMAS 1 atm glasses (Table A2.3) exhibit more variable totals with some falling as low as ~95.5%. These low totals are not associated with a particular glass composition, and the variation between glasses prepared in a single experiment (i.e. in the same furnace atmosphere) is commonly 1-2 wt %. Repeat measurements of some of the CMAS glasses that yielded the lowest totals gave much higher values close to 100 wt % (see Table A2.5). The low totals of the original analyses are therefore most likely due to technical difficulties associated with measuring samples in these mounts and do not reflect sample contamination.

EPMA totals for the AD composition glasses prepared for *in situ* XANES studies (Table A2.4) are excellent, whilst totals for the MORB *in situ* glasses (Table A2.2) are slightly lower (although still > 97.5% except for one sample with 97.2%). However, the EPMA data were collected over many different sessions, and the deviations of these compositional totals from 100% are well correlated with the sessions and the times in a given session at which the glasses were analysed. For example, the lowest totals for the MORB glasses are for those analysed at the end of a sequence set to run overnight.

Table A2.1: Compositions determined by EPMA of MORB glasses prepared for room-temperature XANES studies. 1 atm glasses and selected 10 kbar glasses (see Table A1.1) were prepared by Dean Scott at the RSES, ANU. Values in parentheses indicate one standard deviation. Dashes indicate that the element was below the detection limit and blank spaces indicate that the element was not included on the measurement list.

	P6/11/03_4	B23/11/10_1	PM224_2	PM30/10_6	PM224_3	P6/11/03_3	PM33/10_1,2	P6/11/03_2	PM31/10_6	P6/11/03_1	P6/11/03_7	PM31/10_4	PM224_4	P6/11/03_6
Composition	MORB	MORB	MORB	MORB	MORB	MORB	MORB	MORB	MORB	MORB	MORB	MORB	MORB	MORB
Pressure	1 atm	1 atm	1 atm	1 atm	1 atm	1 atm	1 atm	1 atm	1 atm	1 atm	1 atm	1 atm	1 atm	1 atm
logfO_2	0	-0.7	-1	-2	-2	-3	-4	-5	-6	-7	-8	-9	-9	-10
Analyses	12	11	10	12	10	12	12	12	12	12	12	12	12	12
SiO_2	51.5 (3)	51.2 (5)	50.9 (1)	51.8 (4)	50.9 (1)	51.6 (5)	52.3 (1)	51.4 (2)	52.7 (1)	51.7 (3)	51.2 (3)	51.2 (7)	51.1 (1)	51.5 (4)
Al_2O_3	15.6 (1)	15.5 (1)	15.3 (1)	15.7 (1)	15.36 (6)	15.7 (1)	15.90 (6)	15.78 (6)	15.99 (6)	15.8 (1)	15.7 (1)	15.8 (2)	15.5 (1)	15.7 (1)
MgO	8.07 (5)	8.03 (7)	8.09 (3)	8.13 (6)	8.10 (3)	8.14 (7)	8.18 (3)	8.16 (4)	8.24 (3)	8.15 (5)	8.09 (6)	8.1 (1)	8.15 (3)	8.11 (6)
CaO	12.20 (7)	12.0 (2)	12.09 (4)	12.03 (6)	12.04 (5)	12.21 (7)	12.07 (6)	12.26 (7)	12.49 (5)	12.27 (4)	12.15 (8)	12.3 (3)	12.1 (1)	12.2 (1)]
FeO	9.92 (3)	9.8 (2)	9.80 (4)	9.76 (2)	9.65 (6)	9.90 (5)	9.30 (5)	9.70 (3)	8.29 (2)	9.50 (5)	9.84 (7)	9.0 (2)	9.79 (6)	9.83 (2)
TiO_2	1.26 (2)	1.25 (2)	1.26 (2)	1.27 (2)	1.27 (3)	1.25 (3)	1.26 (2)	1.25 (2)	1.30 (2)	1.27 (2)	1.26 (2)	1.3 (4)	1.26 (3)	1.24 (2)
Na_2O			0.16 (1)		0.18 (1)								0.12 (1)	
K_2O			-		-								-	
Cl			-		-								-	
P_2O_5			-		-								-	
UO_2	0.27 (3)	0.21 (4)	0.19 (5)	0.16 (2)	0.2 (4)	0.40 (1)	0.24 (1)	0.42 (1)	0.35 (2)	0.44 (2)	0.48 (1)	0.43 (2)	0.46 (4)	0.42 (2)
ThO_2	0.51 (1)	-	0.53 (3)	-	0.50 (3)	0.51 (1)	0.52 (2)	0.51 (2)	-	0.52 (1)	0.51 (1)	-	0.51 (4)	0.52 (2)
$Fe^{3+}/\sum Fe$*	0.74	0.68	0.65	0.54	0.54	0.43	0.32	0.23	0.16	0.11	0.07	0.05	0.05	0.03
Basicity [(1)]	0.586	0.586	0.588	0.586	0.588	0.588	0.586	0.589	0.586	0.589	0.590	0.589	0.590	0.590
Basicity [(2)]	0.576	0.577	0.578	0.579	0.580	0.582	0.582	0.586	0.584	0.587	0.589	0.588	0.590	0.589
Total[c]	100.0	98.8	99.0	99.4	98.9	100.4	100.4	100.1	99.9	100.2	99.9	98.7	99.6	100.2

* Calculated using Kress and Carmichael (1991)

(1) Calculated using Duffy (1993) assuming basicity of Fe^{3+} to be equal to that of Fe^{2+}

(2) Calculated using Duffy (1993) assuming basicity of Fe^{3+} to be equal to that of Al^{3+}

[c] EPMA totals corrected for Fe_2O_3 contents based on calculated $Fe^{3+}/\sum Fe$

	AD3_3	PM224_5	P6/11/03_5	C4290	C4291	C4294	C4296	C4304*Ru	C4305*Ru	C4308*Ru	C4309*Ru	C4310*Ru	C4311*Pt
Composition	MORB	MORB	MORB	MORB	MORB	MORB	MORB	MORB	MORB	MORB	MORB	MORB	MORB
Pressure	1 atm	1 atm	1 atm	15 kbar	10 kbar	20 kbar	12.5 kbar	15 kbar	20 kbar	10 kbar	12.5 kbar	25 kbar	10 kbar
logfO_2	-11	-11	-12	-7.2	-7.7	-6.8	-7.4	-0.3	-0.1	-0.4	-0.3	0.1	4.7
Analyses	6	12	13	10	10	10	12	14	12	12	12	10	12
SiO_2	51.7 (4)	51.1 (1)	52.8 (6)	50.6 (2)	51.0 (1)	50.3 (4)	51.2 (3)	49.2 (2)	48.9 (3)	48.5 (2)	48.7 (3)	49.3 (2)	49.8 (3)
Al_2O_3	16.1 (1)	15.50 (6)	16.0 (2)	15.4 (1)	15.6 (1)	15.3 (1)	15.5 (1)	15.11 (6)	15.0 (1)	15.11 (6)	15.26 (4)	14.83 (9)	14.92 (8)
MgO	8.33 (3)	8.15 (2)	8.3 (1)	7.98 (5)	8.08 (2)	7.94 (5)	8.09 (3)	7.60 (3)	7.4 (1)	7.57 (4)	7.58 (4)	7.61 (4)	7.78 (4)
CaO	12.2 (1)	12.06 (7)	12.4 (2)	12.09	12.17	11.97 (6)	12.09 (6)	11.46 (7)	11.4 (1)	11.46 (7)	11.42 (8)	11.65 (2)	11.75 (3)
FeO	8.53 (7)	9.76 (6)	4.9 (1)	9.87 (4)	9.8 (5)	9.29 (6)	9.77 (5)	9.24 (6)	9.1 (1)	9.37 (6)	9.30 (4)	9.35 (8)	9.76 (5)
TiO_2	1.31 (3)	1.25 (2)	1.28 (2)	1.33 (2)	1.33 (3)	1.31 (3)	1.35 (2)	1.15 (1)	1.14 (1)	1.20 (1)	1.16 (1)	1.16 (3)	1.32 (2)
Na_2O	-	0.13 (1)		0.11 (1)	0.11 (1)	0.11 (1)	0.12 (1)					0.12 (1)	0.25 (2)
K_2O	-	-		-	-	-	-	-	-	-	-	-	-
Cl	-	-		-	-	-	-					0.89 (1)	0.27 (1)
P_2O_5	-	-		-	-	-	-					-	-
UO_2	0.41 (1)	0.42 (1)	0.95 (4)	0.41 (4)	0.44 (3)	0.43 (6)	0.42 (4)	0.40 (1)	0.40 (2)	0.41 (1)	0.40 (1)	0.38 (6)	0.41 (4)
ThO_2	-	0.50 (4)	0.53 (2)	-	-	-	-	-	-	-	-	-	-
$Fe^{3+}/\sum Fe$*	0.02	0.02	0.01	0.06	0.06	0.06	0.06	0.59	0.57	0.62	0.61	0.55	0.94
Basicity [(1)]	0.588	0.591	0.579	0.591	0.591	0.590	0.590	0.586	0.586	0.587	0.586	0.587	0.586
Basicity [(2)]	0.587	0.590	0.579	0.590	0.590	0.589	0.589	0.578	0.578	0.578	0.578	0.579	0.573
Total[c]	98.6	98.9	97.2	97.9	98.6	96.7	98.6	94.8	93.9	94.3	94.5	95.9	97.3

* Calculated using Kress and Carmichael (1991)

[(1)] Calculated using Duffy (1993) assuming basicity of Fe^{3+} to be equal to that of Fe^{2+}

[(2)] Calculated using Duffy (1993) assuming basicity of Fe^{3+} to be equal to that of Al^{3+}

[c] EPMA totals corrected for Fe_2O_3 contents based on calculated $Fe^{3+}/\sum Fe$

*[Pt] The fO_2 inside the piston cylinder capsule was buffered by Pt-PtO_2 powder and EPMA gave Pt = 0.44(5) wt % for C4311.

*[Ru] The fO_2 inside the piston cylinder capsule was buffered by Ru-RuO_2 powder. However, no evidence of Ru was observed in the full WDS spectra (for LLIF, LPET and LTAP crystals) of these glasses.

	C4313*Pt	C4314	C4317*Pt	C4318	D1490*Pt	D1491*Ru	D1492*Pt	D1493*Ru	PM208_4	PM208_5	PM208_6	PM224_1
Composition	MORB	MORB	MORB	MORB	MORB	MORB	MORB	MORB	MORB	MORB	MORB	MORB
Pressure	15 kbar	7.5 kbar	12.5 kbar	5 kbar	7.5 kbar	7.5 kbar	5 kbar	5 kbar	10 kbar	10 kbar	10 kbar	10 kbar
logfO_2	5.2	-7.9	4.9	-8.2	4.4	-0.5	4.1	-0.6	-7.7	-3.9	-0.4	4.7
Analyses	10	10	12	10	10	12	10	10	10	12	10	10
SiO_2	50.0 (2)	50.6 (4)	49.3 (4)	51.5 (3)	50.0 (3)	49.8 (1)	50.1 (5)	49.4 (2)	50.8 (3)	51.40 (7)	50.4 (1)	49.7 (4)
Al_2O_3	15.0 (1)	15.2 (1)	14.8 (1)	15.6 (1)	15.0 (1)	15.0 (1)	15.1 (1)	14.8 (1)	15.53 (6)	15.65 (5)	15.28 (7)	15.13 (8)
MgO	7.83 (3)	7.88 (4)	7.96 (7)	8.08 (5)	7.71 (5)	7.67 (3)	7.87 (4)	7.62 (3)	8.2 (2)	8.08 (2)	8.07 (2)	8.0 (1)
CaO	11.75 (6)	12.03 (9)	11.68 (6)	12.05 (5)	11.88 (7)	11.67 (7)	11.8 (1)	11.65 (9)	12.1 (1)	10.31 (6)	11.94 (7)	11.92 (4)
FeO	9.74 (4)	9.09 (5)	9.65 (6)	9.80 (7)	9.82 (5)	9.37 (7)	9.75 (5)	9.36 (7)	9.8 (1)	9.08 (3)	9.62 (3)	9.8 (1)
TiO_2	1.32 (2)	1.33 (2)	1.30 (3)	1.33 (2)	1.31 (3)	1.18 (3)	1.31 (2)	1.18 (2)	1.25 (3)	1.27 (2)	1.21 (2)	1.26 (2)
Na_2O	0.28 (1)	0.14 (1)	0.24 (1)	0.11 (1)	0.24 (1)	0.11 (1)	0.25 (1)	0.11 (1)	0.15 (1)	-	0.16 (1)	0.28 (1)
K_2O	-	-	-	-	-	-	-	-	-	-	-	-
Cl	0.31 (1)	-	0.25 (1)	-	0.26 (1)	0.79 (1)	0.24 (1)	0.66 (1)	-	-	0.37 (1)	-
P_2O_5	-	-	-	-	-	-	-	-	-	-	-	-
UO_2	0.43 (5)	0.42 (4)	0.43 (4)	0.40 (4)	0.44 (4)	0.39 (4)	0.44 (4)	0.39 (4)	0.43 (5)	0.46 (5)	0.42 (5)	0.44 (4)
ThO_2	-	-	-	-	-	-	-	-	-	-	-	0.50 (4)
$Fe^{3+}/\sum Fe$*	0.94	0.06	0.94	0.06	0.94	0.63	0.95	0.68	0.06	0.25	0.62	0.94
Basicity [(1)]	0.586	0.589	0.587	0.59	0.586	0.586	0.586	0.586	0.591	0.582	0.588	0.587
Basicity [(2)]	0.573	0.588	0.573	0.589	0.573	0.578	0.573	0.577	0.590	0.579	0.579	0.574
Total[c]	97.7	96.8	96.6	98.9	97.7	96.6	97.9	95.9	98.3	96.5	98.1	98.1

* Calculated using Kress and Carmichael (1991)

(1) Calculated using Duffy (1993) assuming basicity of Fe^{3+} to be equal to that of Fe^{2+}

(2) Calculated using Duffy (1993) assuming basicity of Fe^{3+} to be equal to that of Al^{3+}

[c] EPMA totals corrected for Fe_2O_3 contents based on calculated $Fe^{3+}/\sum Fe$

*[Pt] The fO_2 inside the piston cylinder capsule was buffered by Pt-PtO_2 powder and EPMA gave Pt = 0.89(6) wt % for C4313, 0.63(5) wt % for C4317, 0.13(3) wt % for D1490, and 0.14(6) wt % for D1492.

*[Ru] The fO_2 inside the piston cylinder capsule was buffered by Ru-RuO_2 powder. However, no evidence of Ru was observed in the full WDS spectra (for LLIF, LPET and LTAP crystals) of these glasses.

Table A2.2: Compositions determined by EPMA of MORB glasses prepared for *in situ* XANES studies using the XAS furnace. Values in parentheses indicate one standard deviation. Dashes indicate that the element was below the detection limit and blank spaces indicate that the element was not included on the measurement list.

	IC090412	IC050313	IC210213	IC250213	IC180213	IC260213	IC220213	IC230213	IC270213
Composition	MORB	MORB	MORB	MORB	MORB	MORB	MORB	MORB	MORB
Pressure	1 atm	1 atm	1 atm	1 atm	1 atm	1 atm	1 atm	1 atm	1 atm
logfO_2	-3	-4	-5	-6	-7	-8	-9	-10	-11
Analyses	10	12	5	12	5	12	5	5	10
SiO_2	51.7 (9)	51.1 (3)	50.5 (3)	51.8 (1)	51.6 (2)	51.2 (2)	49.4 (4)	49.4 (3)	52.1 (1)
Al_2O_3	15.86 (5)	15.5 (1)	15.82 (7)	15.77 (5)	16.08 (3)	15.48 (7)	15.6 (1)	15.52 (4)	15.84 (6)
MgO	8.03 (3)	8.01 (6)	8.04 (4)	8.12 (5)	8.16 (3)	8.05 (5)	7.94 (1)	7.94 (3)	8.20 (4)
CaO	12.1 (1)	12.18 (8)	12.11 (5)	12.34 (4)	12.4 (1)	12.16 (9)	12.00 (6)	12.00 (3)	12.4 (1)
FeO	9.82 (4)	9.77 (4)	9.11 (5)	8.62 (6)	6.72 (9)	9.78 (4)	9.63 (2)	9.30 (3)	7.93 (1)
TiO_2	1.33 (1)	1.33 (2)	1.35 (2)	1.33 (2)	1.37 (2)	1.33 (3)	1.33 (3)	1.32 (2)	1.34 (3)
Na_2O		-	0.33 (2)	0.39 (4)	0.90 (2)	0.23 (1)	0.64 (3)	0.57 (1)	0.34 (1)
K_2O	-	-	0.19 (1)	0.10 (1)	0.63 (3)	-	0.54 (3)	0.68 (3)	0.37 (3)
Cl		-	-	-	-	-	-	-	-
P_2O_5	-	-	-	-	-	-	-	-	-
UO_2	0.22 (1)	0.39 (3)	0.35 (1)	0.39 (4)	0.48 (1)	0.40 (3)	0.48 (1)	0.49 (2)	0.43 (4)
ThO_2	-	-	-	-	-	-	-	-	-
$Fe^{3+}/\sum Fe$*	0.43	0.32	0.23	0.16	0.11	0.07	0.05	0.03	0.02
Basicity [(1)]	0.587	0.589	0.590	0.588	0.589	0.591	0.595	0.595	0.588
Basicity [(2)]	0.581	0.584	0.587	0.586	0.588	0.590	0.594	0.594	0.588
Total[c]	99.1	98.3	97.8	98.9	98.3	98.6	97.6	97.2	99.0

* Calculated using Kress and Carmichael (1991)

[(1)] Calculated using Duffy (1993) assuming basicity of Fe^{3+} to be equal to that of Fe^{2+}

[(2)] Calculated using Duffy (1993) assuming basicity of Fe^{3+} to be equal to that of Al^{3+}

[c] EPMA totals corrected for Fe_2O_3 contents based on calculated $Fe^{3+}/\sum Fe$

Table A2.3: Compositions determined by EPMA of CMAS glasses prepared for room temperature XANES studies. 1 atm and selected 10 kbar glasses (see Table A1.1) were prepared by Dean Scott at the RSES, ANU. The remaining AD piston cylinder glasses were prepared by Guil Mallmann at the RSES, ANU. Note that C-7A = CMAS-7A. Values in parentheses indicate one standard deviation. Basicity values calculated from Duffy (1993). Dashes indicate that the element was below the detection limit and blank spaces indicate that the element was not included on the measurement list.

	d8/10/08_5	d27/8/02_1	d28/8/02_4	AD3_1	c13/1/03_5	d22/7/02_1	c15/1/03_2	d23/7/02_4	d11/10/08A_2	d7/8/02_1	d16/1/03_5	d8/8/02_4	d2/9/02_5	c10/1/03_1
Composition	AD	AD	AD	AD	AD	AD	AD	AD	AD	AD	AD	AD	AD	AD
Pressure	1 atm	1 atm	1 atm	1 atm	1 atm	1 atm	1 atm	1 atm	1 atm	1 atm	1 atm	1 atm	1 atm	1 atm
logfO_2	0	-0.7	-2	-3	-4	-5	-6	-7	-8	-9	-10	-12	-14	-16
Analyses	5	5	5	6	5	6	7	5	5	5	5	5	5	5
SiO_2	49.0 (3)	49.3 (2)	47.7 (4)	49.3 (2)	48.1 (8)	50.0 (1)	49.5 (6)	49.2 (2)	49.7 (2)	48.7 (1)	48.0 (4)	49.1 (2)	49.3 (1)	48.8 (1)
Al_2O_3	14.6 91)	14.81 (5)	14.30 (8)	15.2 (1)	14.5 (2)	15.07 (5)	14.9 (2)	14.9 (1)	15.00 (8)	14.77 (8)	14.5 (1)	14.64 (7)	14.93 (4)	14.76 (4)
MgO	10.44 (3)	10.72 (5)	10.43 (4)	10.87 (5)	10.52 (7)	10.76 (5)	10.80 (7)	10.80 (2)	10.75 (3)	10.76 (2)	10.55 (7)	10.66 (6)	10.64 (2)	10.64 (4)
CaO	22.92 (6)	23.33 (7)	22.7 (1)	23.4 (1)	23.0 (1)	23.36 (8)	23.2 (1)	23.55 (7)	23.49 (8)	22.52 (8)	22.82 (5)	23.21 (6)	23.10 (4)	23.4 (1)
FeO	-	-	-	-	-	-	-	-	-	-	-	-	0.14 (1)	-
TiO_2	-	-	-	-	-	-	-	-	-	-	-	-	-	-
Na_2O	0.18 (1)	0.20 (1)	0.20 (1)	0.15 (1)	0.11 (1)	0.22 (1)	0.13 (1)	0.17 (1)	-	0.13 (1)	-	-	-	-
K_2O	-	-	-	-	-	-	-	-	-	-	-	-	-	-
Cl	-	-	-	-	-	-	-	-	-	-	-	-	-	-
P_2O_5	-	-	-	-	-	-	-	-	-	-	-	-	-	-
UO_2	0.38 (2)	0.24 (1)	0.21 (1)	0.27 (1)	0.37 (1)	0.36 (1)	0.40 (2)	0.38 (1)	0.57 (1)	0.37 (1)	0.40 (1)	0.38 (2)	0.38 (1)	0.41 (2)
ThO_2	-	-	-	-	-	-	-	-	-	-	-	-	-	-
Total	97.6	98.6	95.5	99.3	96.5	99.8	98.9	99.1	99.6	97.3	96.3	98.0	98.6	98.0
Basicity	0.606	0.607	0.607	0.607	0.607	0.606	0.606	0.608	0.606	0.606	0.607	0.606	0.606	0.607

	c24/4/03_6	d8/10/08_6	d27/8/02_6	d28/8/02_5	c13/1/03_2	d22/7/02_6	c15/1/03_4	d23/7/02_3	d11/10/08A_3	d7/8/02_6	d16/1/03_1	d8/8/02_3	d2/9/02_3
Composition	AD	C-7A	C-7A	C-7A	C-7A	C-7A	C-7A	C-7A	C-7A	C-7A	C-7A	C-7A	C-7A
Pressure	1 atm	1 atm	1 atm	1 atm	1 atm	1 atm	1 atm	1 atm	1 atm	1 atm	1 atm	1 atm	1 atm
logfO_2	-18	0	-0.7	-2	-4	-5	-6	-7	-8	-9	-10	-12	-14
Analyses	6	4	5	5	5	6	5	5	5	5	4	5	5
SiO_2	47.9 (1)	55.1 (2)	54.6 (3)	53.1 (6)	53.5 (3)	54.5 (4)	54.4 (4)	54.5 (3)	55.0 (2)	54.0 (1)	54.2 (6)	54.3 (3)	54.3 (1)
Al_2O_3	15.07 (3)	15.40 (5)	15.25 (8)	15.0 (1)	15.06 (8)	15.4 (1)	15.2 (1)	15.30 (8)	15.43 (4)	15.28 (7)	15.3 (1)	15.18 (8)	15.44 (5)
MgO	10.67 (2)	12.37 (4)	12.32 (3)	12.14 (5)	12.15 (4)	12.36 (4)	12.17 (8)	12.41 (2)	12.47 (3)	12.35 (6)	12.31 (4)	12.32 (3)	12.34 (2)
CaO	22.94 (6)	15.66 (7)	15.53 (7)	15.28 (6)	15.42 (8)	15.25 (6)	15.69 (8)	15.7 (2)	15.86 (4)	15.06 (6)	15.5 (1)	15.52 (7)	15.40 (5)
FeO	-	-	-	-	-	-	-	-	-	-	-	-	0.25 (1)
TiO_2	-	-	-	-	-	-	-	-	-	-	-	-	-
Na_2O	-	0.14 (1)	0.21 (1)	0.19 (1)	0.13 (1)	0.32 (1)	0.17 (1)	0.32 (1)	0.16 (1)	0.31 (1)	0.14 (1)	0.14 (1)	-
K_2O	-	-	-	-	-	-	-	-	-	-	-	-	0.10 (1)
Cl	-	-	-	-	-	-	-	-	-	-	-	-	-
P_2O_5	-	-	-	-	-	-	-	-	-	-	-	-	-
UO_2	0.38 (2)	0.26 (2)	0.18 (1)	0.17 (1)	0.38 (1)	0.34 (1)	0.39 (1)	0.41 (1)	0.42 (1)	0.40 (1)	0.44 (1)	0.42 (1)	0.39 (1)
ThO_2	-	-	-	-	-	-	-	-	-	-	-	-	-
Total	96.9	98.9	98.1	95.9	96.7	98.2	98.0	98.6	99.3	97.5	97.9	97.9	98.2
Basicity	0.607	0.582	0.582	0.583	0.583	0.582	0.583	0.584	0.583	0.582	0.583	0.583	0.583

	c10/1/03_5	c24/4/03_5	d8/10/08_2	d27/8/02_3	d28/8/02_2	c13/1/03_3	d22/7/02_3	c15/1/03_1	d23/7/02_5	d11/10/08B_1	d7/8/02_3	d16/1/03_6	d8/8/02_6
Composition	C-7A	C-7A	En	En	En	En	En	En	En	En	En	En	En
Pressure	1 atm	1 atm	1 atm	1 atm	1 atm	1 atm	1 atm	1 atm	1 atm	1 atm	1 atm	1 atm	1 atm
logfO_2	-16	-18	0	-0.7	-2	-4	-5	-6	-7	-8	-9	-10	-12
Analyses	5	9	4	5	5	5	6	7	5	5	5	4	5
SiO_2	53.1 (6)	51.0 (1)	53.3(9)	53.1 (3)	52.0 (4)	52.4 (4)	53.4 (3)	53.9 (6)	53.7 (1)	53.2 (2)	52.1 (4)	53.2 (2)	53.3 (4)
Al_2O_3	15.1 (1)	16.4 (1)	9.2 (1)	8.99 (5)	8.90 (5)	9.02 (2)	9.07 (8)	9.2 (1)	9.14 (7)	9.10 (2)	8.90 (5)	9.00 (6)	9.03 (6)
MgO	12.24 (8)	12.71 (4)	20.6 (2)	21.27 (7)	21.15 (7)	20.77 (8)	21.4 (1)	21.3 (1)	21.83 (5)	20.75 (4)	21.5 (1)	21.50 (8)	21.48 (7)
CaO	15.43 (8)	16.2 (1)	14.6 (2)	14.3 (1)	14.0 (1)	14.3 (1)	14.26 (8)	14.4 (1)	14.44 (5)	14.7 (1)	13.78 (7)	14.09 (8)	14.3 (1)
FeO	-	-	-	-	-	-	-	-	-	-	-	-	-
TiO_2	-	-	-	-	-	-	-	-	-	-	-	-	-
Na_2O	-	-	0.16 (1)	0.20 (1)	0.20 (1)	0.10 (1)	0.26 (1)	0.13 (1)	0.21 (1)	0.11 (1)	0.16 (1)	-	-
K_2O	-	-	-	-	-	-	-	-	-	-	-	-	-
Cl	-	-	-	-	-	-	-	-	-	-	-	-	-
P_2O_5	-	-	-	-	-	-	-	-	-	-	-	-	-
UO_2	0.43 (2)	0.42 (1)	0.28 (2)	0.21 (2)	0.14 (1)	0.38 (1)	0.36 (1)	0.41 (1)	0.40 (1)	0.41 (1)	0.38 (1)	0.41 (1)	0.40 (1)
ThO_2	-	-	-	-	-	-	-	-	-	-	-	-	-
Total	96.3	96.8	98.3	98.1	96.5	97.0	98.8	99.4	99.8	98.3	96.8	98.2	98.6
Basicity	0.583	0.589	0.595	0.595	0.596	0.595	0.595	0.594	0.596	0.595	0.596	0.595	0.595

	d2/9/02_2	c10/1/03_3	c24/4/03_1	d8/10/08_1	d27/8/02_5	d28/8/02_6	c13/1/03_4	d22/7/02_5	c15/1/03_6	d23/7/02_2	d11/10/08B_3	d7/8/02_5	d16/1/03_4
Composition	En	En	En	Fo	Fo	Fo	Fo	Fo	Fo	Fo	Fo	Fo	Fo
Pressure	1 atm	1 atm	1 atm	1 atm	1 atm	1 atm	1 atm	1 atm	1 atm	1 atm	1 atm	1 atm	1 atm
logfO_2	-14	-16	-18	0	-0.7	-2	-4	-5	-6	-7	-8	-9	-10
Analyses	5	5	5	4	5	5	5	6	7	5	5	5	4
SiO_2	53.3 (1)	52.6 (3)	52.6 (1)	48.8 (1)	48.0 (1)	47.1 (2)	47.1 (6)	48.5 (3)	48.6 (4)	48.7 (2)	47.9 (2)	47.9 (2)	47.0 (3)
Al_2O_3	9.26 (6)	9.14 (5)	9.60 (5)	12.72 (3)	12.44 92)	12.29 (4)	12.2 (1)	12.6 (1)	12.8 (2)	12.65 (8)	12.44 (7)	12.53 (7)	12.28 (6)
MgO	21.59 (4)	20.56 (4)	20.60 (4)	17.65 (5)	17.37 (2)	17.25 (5)	17.1 (1)	17.4 (1)	17.7 (3)	17.67 (6)	17.31 (3)	17.50 (5)	17.24 (6)
CaO	14.24 (5)	14.58 (8)	14.4 (1)	19.97 (5)	19.73 (7)	19.51 (6)	19.5 (2)	19.7 (3)	20.0 (1)	20.17 (6)	20.09 (5)	19.2 (1)	19.37 (6)
FeO	0.22 (1)	-	-	-	-	-	-	-	-	-	-	-	-
TiO_2	-	-	-	-	-	-	-	-	-	-	-	-	-
Na_2O	-	-	-	0.11 (1)	0.14 (1)	0.15 (1)	-	0.15 (1)	-	0.14 (1)	-	-	-
K_2O	-	-	-	-	-	-	-	-	-	-	-	-	-
Cl	-	-	-	-	-	-	-	-	-	-	-	-	-
P_2O_5	-	-	-	-	-	-	-	-	-	-	-	-	-
UO_2	0.39 (1)	0.43 (1)	0.40 (1)	0.34 (1)	0.27 (1)	0.24 (1)	0.40 (1)	0.38 (1)	0.41 (2)	0.40 (1)	0.40 (1)	0.40 (1)	0.41 (1)
ThO_2	-	-	-	-	-	-	-	-	-	-	-	-	-
Total	99.1	97.3	97.6	99.6	98.0	96.6	96.5	98.8	99.6	99.7	98.2	97.6	96.4
Basicity	0.595	0.595	0.594	0.610	0.610	0.611	0.610	0.609	0.610	0.611	0.611	0.609	0.610

	d8/8/02_2	d2/9/02_1	c10/1/03_2	c10/1/03_7	c24/4/03_2	d8/10/08_3	d27/8/02_4	d28/8/02_1	c13/1/03_1	d22/7/02_4	c15/1/03_5	d23/7/02_1	d11/10/08A_1
Composition	Fo	Fo	Fo	Fo	Fo	Qz	Qz	Qz	Qz	Qz	Qz	Qz	Qz
Pressure	1 atm	1 atm	1 atm	1 atm	1 atm	1 atm	1 atm	1 atm	1 atm	1 atm	1 atm	1 atm	1 atm
logfO_2	-12	-14	-16	-16	-18	0	-0.7	-2	-4	-5	-6	-7	-8
Analyses	5	5	5	5	5	4	5	4	5	6	7	5	5
SiO_2	48.2 (3)	49.1 (1)	47.5 (2)	47.5 (3)	47.2 (2)	64.8 (3)	65.6 (4)	64.7 (8)	64.9 (2)	66.5 (2)	65.8 (5)	66.8 (1)	65.8 (3)
Al_2O_3	12.38 (7)	12.72 (6)	12.39 (7)	12.42 (5)	12.78 (40	9.91 (7)	9.5 (1)	9.42 (4)	9.79 (3)	9.61 (3)	10.0 (2)	9.7 (1)	9.96 (8)
MgO	17.38 (4)	17.11 (2)	17.27 (5)	17.27 (5)	17.24 (8)	7.16 (2)	6.89 (4)	6.82 (5)	7.05 (3)	6.87 (3)	7.2 (1)	6.93 (4)	7.17 (5)
CaO	19.67 (5)	19.62 (6)	19.70 (7)	19.63 (7)	19.4 (1)	15.6 (1)	15.03 (5)	14.8 (1)	15.43 (7)	15.00 (7)	15.5 (2)	15.17 (5)	15.7 (1)
FeO	-	0.19 (1)	-	-	-	-	-	-	-	-	-	-	-
TiO_2	-	-	-	-	-	-	-	-	-	-	-	-	-
Na_2O	-	-	-	-	-	0.10 (1)	0.22 (1)	0.16 (1)	-	0.29 (1)	0.13 (1)	0.35 (1)	0.16 (1)
K_2O	-	-	-	-	-	-	-	-	-	-	-	-	-
Cl	-	-	-	-	-	-	-	-	-	-	-	-	-
P_2O_5	-	-	-	-	-	-	-	-	-	-	-	-	-
UO_2	0.38 (1)	0.39 (1)	0.42 (2)	0.42 (1)	0.39 (1)	0.34 (6)	0.19 (4)	0.15 (4)	0.40 (2)	0.38 (3)	0.45 (3)	0.43 (1)	0.44 (1)
ThO_2	-	-	-	-	-	-	-	-	-	-	-	-	-
Total	98.1	99.2	97.3	97.3	97.0	98.0	97.5	96.1	97.6	98.8	99.2	99.4	99.3
Basicity	0.609	0.608	0.610	0.610	0.610	0.561	0.558	0.558	0.560	0.558	0.560	0.558	0.560

	d7/8/02_4	d16/1/03_3	d8/8/02_1	d2/9/02_4	c10/1/03_6	c24/4/03_3	d8/10/08_4	d27/8/02_2	d28/8/02_3	c13/1/03_6	d22/7/02_2	c15/1/03_3	d23/7/02_6
Composition	Qz	Qz	Qz	Qz	Qz	Qz	Wo	Wo	Wo	Wo	Wo	Wo	Wo
Pressure	1 atm	1 atm	1 atm	1 atm	1 atm	1 atm	1 atm	1 atm	1 atm	1 atm	1 atm	1 atm	1 atm
logfO_2	-9	-10	-12	-14	-16	-18	0	-0.7	-2	-4	-5	-6	-7
Analyses	5	4	5	5	5	6	4	5	5	5	6	5	5
SiO_2	65.2 (2)	64.8 (3)	65.8 (6)	65.4 (4)	63.5 (8)	62 (1)	50.0 (4)	49.5 (2)	48.7 (4)	49.3 (6)	50.6 (4)	50.5 (3)	50.5 (1)
Al_2O_3	9.34 (5)	9.50 (5)	9.40 (8)	9.42 (7)	10.0 (1)	10.1 (5)	6.3 (1)	5.87 (2)	5.80 (5)	5.6 (1)	6.07 (7)	6.13 (8)	6.04 (4)
MgO	6.76 (2)	6.89 (3)	6.85 (4)	6.82 (2)	7.01 (8)	7.2 (7)	4.53 (5)	4.24 (1)	4.20 (1)	4.0 (8)	4.32 (2)	4.42 (3)	4.34 (3)
CaO	14.45 (7)	14.98 (8)	14.9 (1)	14.6 (1)	15.1 (2)	16 (1)	37.1 (3)	37.4 (1)	37.0 (2)	38 (2)	37.5 (4)	37.5 (1)	38.2 (1)
FeO	-	-	-	0.29 (1)	-	-	-	-	-	-	-	-	-
TiO_2	-	-	-	-	-	-	-	-	-	-	-	-	-
Na_2O	0.39 (2)	0.19 (1)	0.24 (1)	0.11 (1)	-	-	-	0.11 (1)	0.11 (1)	-	0.11 (1)	-	-
K_2O	-	-	0.10 (1)	0.30 (1)	-	-	-	-	-	-	-	-	-
Cl	-	-	-	-	-	-	-	-	-	-	-	-	-
P_2O_5	-	-	-	-	-	-	-	-	-	-	-	-	-
UO_2	0.41 (1)	0.44 (1)	0.40 (4)	0.46 (1)	0.47 (1)	0.44 (2)	0.51 (1)	0.53 (1)	0.36 (1)	0.37 (8)	0.40 (1)	0.40 (1)	0.38 (1)
ThO_2	-	-	-	-	-	-	-	-	-	-	-	-	-
Total	96.6	96.8	97.6	97.5	96.2	95.7	98.6	97.7	96.1	97.3	99.0	99.0	99.5
Basicity	0.557	0.559	0.558	0.558	0.560	0.563	0.633	0.634	0.635	0.636	0.633	0.633	0.634

	d11/10/08B_2	d7/8/02_2	d16/1/03_2	d8/8/02_5	d2/9/02_6	c10/1/03_4	c24/4/03_4	d1251*Pt	J29	d1259*Pt	c4012*Ir	d1235*Ir	c4011*Ir
Composition	Wo	Wo	Wo	Wo	Wo	Wo	Wo	AD	AD	AD	AD	AD	AD
Pressure	1 atm	1 atm	1 atm	1 atm	1 atm	1 atm	1 atm	5 kbar	10 kbar	15 kbar	5 kbar	10 kbar	15 kbar
logfO_2	-8	-9	-10	-12	-14	-16	-18	4.1	4.7	5.2	1.7	1.9	2.0
Analyses	4	5	4	5	5	5	5	20	6	12	15	13	12
SiO_2	49.5 (4)	49.1 (5)	49.4 (5)	49.6 (4)	50.0 (2)	48.3 (6)	47.6 (3)	49.0 (3)	48.8 (1)	48.9 (2)	48.9 (1)	48.4 (1)	48.6 (1)
Al_2O_3	6.16 (4)	5.91 (6)	5.98 (2)	5.92 (7)	5.97 (2)	6.10 (6)	6.56 (5)	14.6 (1)	14.8 (1)	14.65 (6)	14.66 (6)	14.4 (1)	14.54 (4)
MgO	4.45 (4)	4.29 (2)	4.30 (2)	4.29 (3)	4.35 (2)	4.41 (3)	4.55 (1)	10.6 (1)	10.75 (2)	10.27 (5)	10.40 (4)	10.41 (5)	10.24 (7)
CaO	37.7 (1)	36.8 (2)	37.32 (7)	37.4 (2)	37.1 (2)	36.4 (1)	36.5 (2)	23.7 (2)	23.31 (3)	22.3 (1)	22.7 (1)	23.5 (1)	22.3 (1)
FeO	-	-	-	-	0.14 (1)	-	-	0.10 (1)	-	-	-	-	0.10 (3)
TiO_2	-	-	-	-	-	-	-	-	-	-	-	-	-
Na_2O	-	-	-	-	-	-	-	0.23 (1)	0.33 (2)	0.23 (1)	0.18 (1)	0.19 (1)	0.18 (1)
K_2O	-	-	-	-	-	-	-	-	0.11 (2)	-	-	-	-
Cl	-	-	-	-	-	-	-	-	-	0.11 (1)	0.83 (1)	1.02 (2)	0.79 (1)
P_2O_5	-	-	-	-	-	-	-	-	-	-	-	-	-
UO_2	0.41 (2)	0.36 (1)	0.40 (2)	0.38 (1)	0.36 (2)	0.41 (1)	0.41 (1)	0.86 (4)	0.41 (1)	0.89 (4)	0.90 (5)	0.85 (4)	0.87 (3)
ThO_2	-	-	-	-	-	-	-		-	-			
Total	98.3	96.6	97.4	97.6	98.0	95.7	95.6	99.1	98.5	97.4	98.6	98.8	97.6
Basicity	0.635	0.633	0.634	0.634	0.633	0.634	0.636	0.608	0.609	0.604	0.605	0.608	0.605

*[Pt] The fO_2 inside the piston cylinder capsule was buffered by Pt-PtO_2 powder and EPMA gave Pt = 0.16(4) wt % for d1251 and 0.8(1) wt % for d1259.

*[Ir] The fO_2 inside the piston cylinder capsule was buffered by Ir-IrO_2 powder. However, Ir was below the limit of detection (~1000 ppm) for all samples.

	PM2/08_1	d1236*Ru	d1243*Re	d1254*Re	PM2/08_2	d1242*Re	d1253*Re	d1244	PM2/08_3	d1257
Composition	AD	AD	AD	AD	AD	AD	AD	AD	AD	AD
Pressure	10 kbar	15 kbar	5 kbar	5 kbar	10 kbar	15 kbar	15 kbar	5 kbar	10 kbar	15 kbar
logfO_2	-0.4	-0.3	-4.2	-4.2	-3.9	-3.8	-3.8	-8.2	-7.7	-7.2
Analyses	5	10	17	12	5	24	12	10		12
SiO_2	47.0 (3)	47.9 (1)	50.8 (2)	50.4 (1)	47.7 (3)	48.5 (1)	47.7 (2)	48.7 (2)		48.9 (2)
Al_2O_3	14.61 (7)	14.55 (7)	15.40 (7)	15.2 (1)	14.77 (6)	14.49 (8)	14.41 (7)	14.7 (1)		14.69 (5)
MgO	10.2 (1)	10.27 (5)	10.72 (8)	10.50 (5)	10.05 (5)	10.86 (5)	10.00 (6)	10.52 (7)		10.4 (1)
CaO	21.8 (1)	23.1 (1)	19.0 (1)	18.1 (1)	18.7 (2)	20.2 (1)	19.5 (1)	23.1 (1)		22.6 (1)
FeO	-	-	-	-	-	-	-	-		-
TiO_2	-	-	-	-	-	-	-	-		-
Na_2O	0.17 (1)	0.19 (1)	-	-	-	-	-	0.21 (1)		0.19 (1)
K_2O	-	-	-	-	-	-	-	-		-
Cl	0.21 (1)	0.87 (2)	-	-	-	-	-	-		-
P_2O_5	-	-	-	-	-	-	-	-		-
UO_2	0.53 (1)	0.76 (4)	0.88 (3)	0.91 (4)	0.54 (1)	0.84 (4)	0.85 (3)	0.81 (3)		0.87 (4)
ThO_2	-				-					
Total	94.5	97.6	96.8	95.1	91.8	94.9	92.5	98.0		97.7
Basicity	0.606	0.608	0.593	0.591	0.595	0.600	0.598	0.607		0.605

*Re The fO_2 inside the piston cylinder capsule was buffered by Re-ReO_2 powder and EPMA gave Re = 2.8(2) wt % for d1243, 2.00(8) wt % for d1254, 3.02(8) wt % for d1242, and 3.84(7) wt % for d1253.

*Ru The fO_2 inside the piston cylinder capsule was buffered by Ru-RuO_2 powder. However, no evidence of Ru was observed in the full WDS spectra (for LLIF, LPET and LTAP crystals) of these glasses.

Table A2.4: Compositions determined by EPMA of AD glasses prepared for *in situ* XANES studies using the XAS furnace. Values in parentheses indicate one standard deviation. Basicity values calculated from Duffy (1993). Dashes indicate that the element was below the detection limit and blank spaces indicate that the element was not included on the measurement list.

	IC090412	IC040313	IC140412	IC110412	IC160412	IC120412	IC150213	IC130412	IC280213	IC210412
Composition	AD	AD	AD	AD	AD	AD	AD	AD	AD	AD
Pressure	1 atm	1 atm	1 atm	1 atm	1 atm	1 atm	1 atm	1 atm	1 atm	1 atm
logfO_2	-3	-4	-5	-6	-7	-8	-9	-10	-11	-12
Analyses	10	12	10	10	5	10	5	10	12	5
SiO_2	50.4 (1)	49.8 (3)	49.7 (2)	50.28 (8)	49.1 (1)	50.0 (1)	48.3 (4)	49.7 (1)	49.6 (2)	48.6 (4)
Al_2O_3	15.1 (1)	14.9 (1)	15.07 (5)	15.18 (8)	15.09 (6)	15.20 (6)	14.8 (1)	15.06 (4)	14.8 (1)	15.1 (1)
MgO	10.55 (6)	10.53 (4)	10.49 (4)	10.61 (3)	10.60 (3)	10.61 (3)	10.40 (4)	10.52 (3)	10.54 (5)	10.57 (2)
CaO	23.69 (6)	23.6 (1)	23.59 (6)	23.64 (6)	23.51 (7)	23.61 (5)	23.1 (1)	23.65 (6)	23.6 (1)	23.5 (7)
FeO	-	-	-	-	-	-	-	-	-	-
TiO_2	-	-	-	-	-	-	-	-	-	-
Na_2O		-			-		0.82 (3)		-	-
K_2O	-	-	-	-	-	-	0.99 (2)	-	0.10 (1)	-
Cl		-			-		-		-	-
P_2O_5	-	-	-	-	-	-	-	0.13 (2)	-	-
UO_2	0.32 (1)	0.44 (6)	0.43 (1)	0.45 (2)	0.42 (1)	0.46 (1)	0.58 (1)	0.46 (1)	0.44 (4)	0.43 (1)
ThO_2	-	-	-	-	-	-	-	-	-	-
Total	100.1	99.3	99.3	100.2	98.7	99.9	99.0	99.5	99.1	98.2
Basicity	0.605	0.606	0.606	0.606	0.607	0.606	0.608	0.606	0.606	0.608

Table A2.5: Summary of EPMA compositional totals obtained from initial and repeat analyses of selected CMAS 1 atm glasses. Values in parentheses indicate one standard deviation.

Sample	Original Total (Table A2.3)	Repeat Analyses	Repeat Total
d28/8/02_1	96.1	3	99.9 (5)
d28/8/02_2	96.5	3	100.7 (3)
d28/8/02_3	96.1	3	100.2 (3)
d28/8/02_4	95.5	3	100.1 (1)
d28/8/02_5	95.9	3	100.5 (4)
d28/8/02_6	96.6	3	100.5 (4)
c13/1/03_1	97.6	3	100.4 (2)
c13/1/03_2	96.7	3	100.5 (1)
c13/1/03_3	97	3	100.8 (4)
c13/1/03_4	96.5	3	100.8 (4)
c13/1/03_5	96.5	3	100.8 (1)
c13/1/03_6	97.3	3	100.4 (4)

Appendix 3:

An assessment of the oxidation state line-shape extraction method using Cr K-edge XANES spectra of glasses

A3.1 Introduction

The reliability of extracting the unknown XANES spectrum of an oxidation state end-member using the XANES spectra collected from a series of mixed valence samples was investigated by applying the same methodology as used for the U M_4-edge XANES spectra in Chapter 3 of this thesis to an independently quantified set of Cr^{2+}/Cr^{3+} mixed valence glasses. Cr K-edge XANES spectra of a series of AD+En composition glasses collected and previously analysed by Berry and O'Neill (2004) were used to extract the "oxidation-state end-member" line-shapes and, thereby, quantify Cr redox ratios in the glasses. The spectra utilised in this appendix were not collected as part of the work for this thesis, however, by applying the line-shape extraction approach to a system that has already been characterised by other well-established analytical techniques (Berry and O'Neill, 2004) this analysis method is tested and evaluated.

A3.2 Cr^{3+} line-shape extraction

A3.2.1 Part 1

A3.2.1.1 Methodology

The spectra utilised in this appendix were collected from glasses quenched from melts equilibrated over a range of logfO_2s (logfO_2 = -16.1 to -0.7) at 1400 °C and 1 atm (Berry and O'Neill, 2004). In this sample set the pure Cr^{2+} XANES spectrum has been directly measured from highly reduced glasses. However, although spectra of the most oxidised glasses are

likely to be close to 100 % Cr^{3+}, a pure Cr^{3+} end-member does not exist as Cr^{6+} and Cr-spinel are also present. To extract a Cr^{3+} line-shape from intermediate logfO_2 spectra the logfO_2 = -13.8 spectrum was taken as the Cr^{2+} end-member (identical spectral shape to logfO_2 = -16.1). Extraction of a Cr^{3+} line-shape from mixed Cr^{2+}/Cr^{3+} spectra does not require a true Cr^{2+} end-member, only that the "end-member" line-shape has a larger proportion of Cr^{2+} than the intermediate spectra it is used to fit, and that it is made up of only two Cr components (i.e. Cr^{2+} and Cr^{3+}). Intermediate logfO_2 spectra were then fitted using the Cr^{2+} line-shape and adding a number of Gaussian to produce a good fit to the data over the spectral energy range (~5980-6018 eV). Initially, the Gaussians were constrained to have a positive height, but did not have constrained widths, although peaks that were clearly ftting noise (i.e. very narrow peaks) were removed and re-fitted. Five Gaussians were required in most cases, although four was adequate for the most reduced samples spectra. Using this approach the sum of the additional Gaussians is expected to represent the Cr^{3+} component. The contribution from the Cr^{2+} end-member spectrum was allowed to vary in intensity but not in shape; the effect of allowing small shifts in end-member energy was also considered. To quantify the Cr oxidation state proportions in each glass the spectra were finally fitted using a combination of the original Cr^{2+} end-member spectrum and the average of the extracted "Cr^{3+}" line-shapes.

A3.2.1.1 Results

The extracted Cr^{3+} line-shapes are shown in Fig. A3.1, and are generally very similar for glasses equilibrated at different fO_2s between logfO_2 = -10 and -6. This is consistent with the assumption that only two Cr components were present in the glasses. Line-shapes could not be extracted from the spectra of the most oxidised glasses; this is attributed to the relatively small contribution of Cr^{2+} and the presence of Cr^{6+} and/or Cr-spinel. The Cr^{2+} proportions estimated from the resulting two end-member fits are compared with those of Berry and

O'Neill (2004) in Fig. A3.2. The linear combination fits increasingly underestimate the amount of Cr^{2+} with increasing fO_2, by up to as much as 10 %.

Inappropraite normalisation of XANES spectra could result in errors in the oxidation state proportions estimated. All the spectra were normalised to the intensity of the white-line crest, which leads to the inbuilt assumption in linear combination fitting that the Cr^{2+} and Cr^{3+} end-member spectra have the same normalised intensity. This is not the case, as normalising spectra to their intensity above the edge indicates that the Cr^{3+} crest is more intense than that of Cr^{2+}. However, this correction factor is not large enough to make a significant difference to the estimated Cr oxidation state proportions, and cannot expain the discrepancies between the two models.

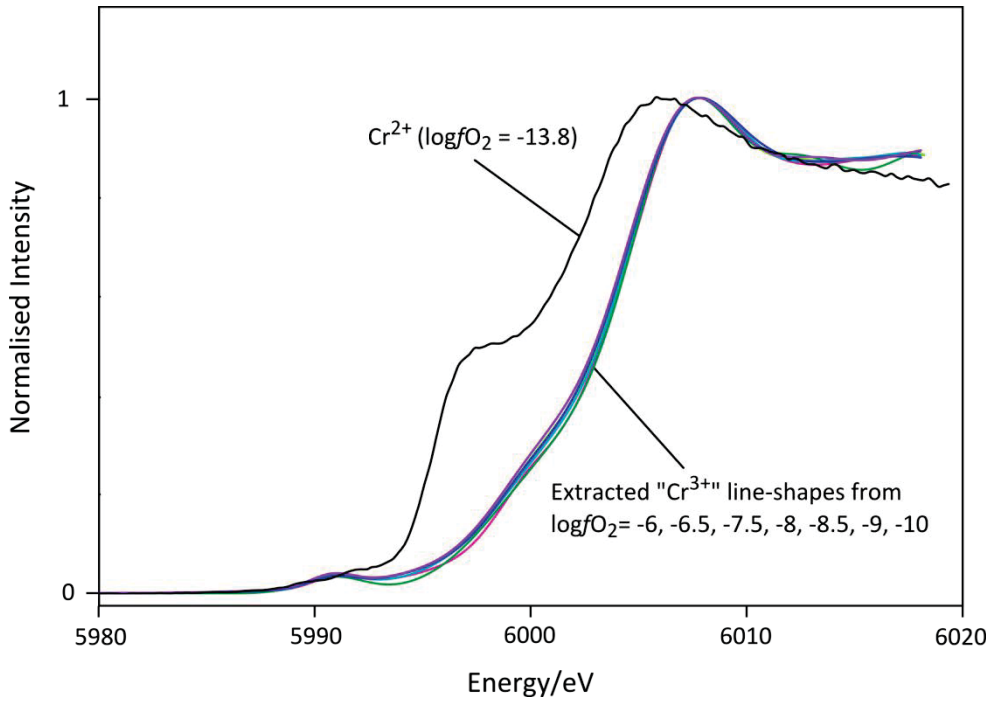


Figure A3.1: Cr K-edge spectrum of AD+En composition glass equilibrated at logfO_2 = -13.75, which represents 100 % Cr^{2+} , and "Cr^{3+}" line-shapes extracted from spectra of AD+En glasses equilibrated at various intermediate fO_2s. Spectra were fitted using a combination of logfO_2 = -13.8 spectrum and 4-5 Gaussians to produce the missing "Cr^{3+}" component.

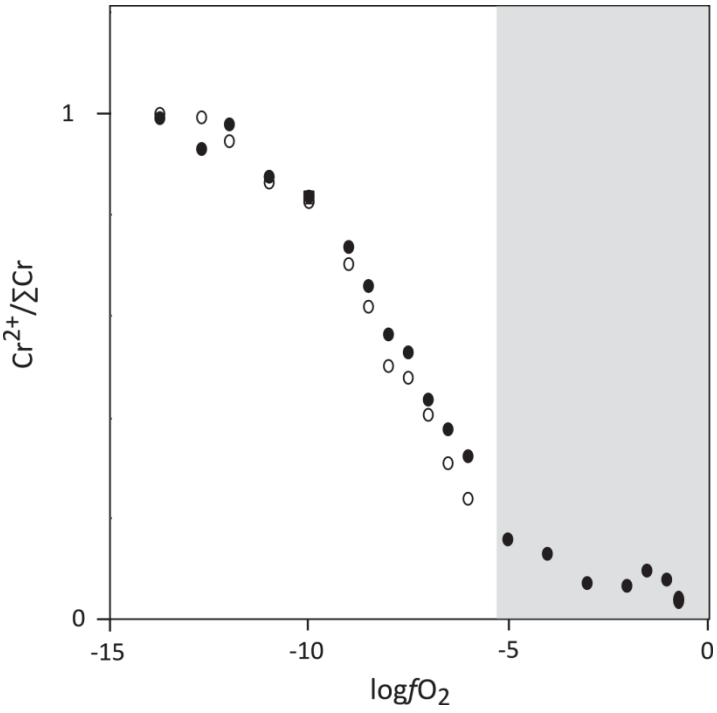


Figure A3.2: Comparison of the Cr^{2+} proportions in AD+En glasses reported by Berry and O'Neill (2004) (filled) to those derived from end-member linear combination fits (unfilled), where the Cr^{3+} line-shape was extracted using Gaussians of no fixed width. The shaded region corresponds to glasses containing other Cr incorporating phases (spinel) and/or oxidation states (Cr^{6+}), in addition to the Cr^{2+} and Cr^{3+} in the glass.

A3.2.2 Part 2

A3.2.2.1 Methodology

Given that the XANES spectral features are in fact limited by the energy resolution of the experiment (a combination of the core-hole width and beamline optics), the fitting method was repeated with the widths of the additional Gaussians fixed to the spectral energy resolution of 2.4 eV (Berry and O'Neill, 2004). This methodology makes it impossible to choose a fixed number of Gaussians to add to the fit, as peaks are narrow, and a large number (20-30) may be required to produce a good fit over the whole spectral energy range. As such, Gaussians with a full width at half maximu (FWHM) of 2.4 eV were simply added

to the Cr^{2+} fit of the mixed valence spectrum until they stopped improving the quality of the fit.

A3.2.2.2 Results

The new extracted "Cr^{3+}" line-shapes are shown in Fig. A3.3, and are very similar for spectra where $\log fO_2 \leq -6$. This approach also allowed missing component line-shapes to be extracted for the most oxidised samples, which vary sysetmatically in shape with the fO_2 of sample equilibration. A shift of the components white-line to higher energies occurred in samples containing Cr-spinel, whilst a change in shape and intensity of the pre-edge is associated with the presence of Cr^{6+} in the most oxidised glasses. Cr oxidation state proportions derived from linear combination fits using the average extracted Cr^{3+} line-shape ($\log fO_2 \leq -6$ only) are in excellent agreement with those reported by Berry & O'Neill (2004) (Fig. A3.4).

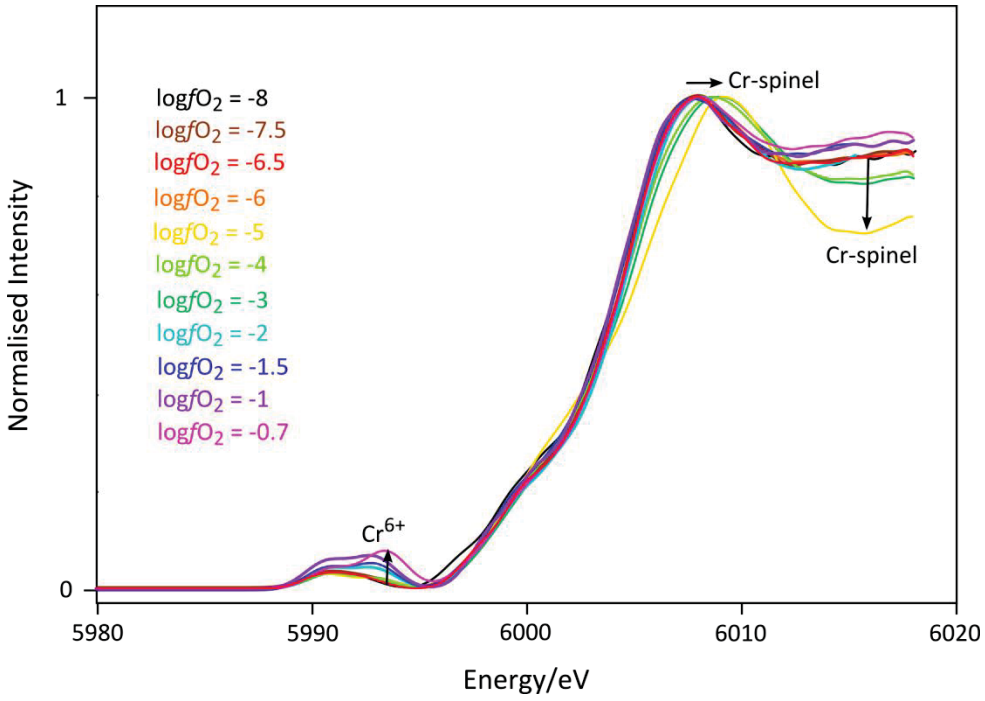


Figure A3.3: "Cr^{3+}" line-shapes extracted from the Cr K-edge XANES spectra of AD+En glasses equilibrated at the fO_2s indicated. Spectra were fitted using a combination of the $\log fO_2 = -13.8$ spectrum and many Gaussians, with FWHM = 2.4 eV, to produce the missing "Cr^{3+}" component.

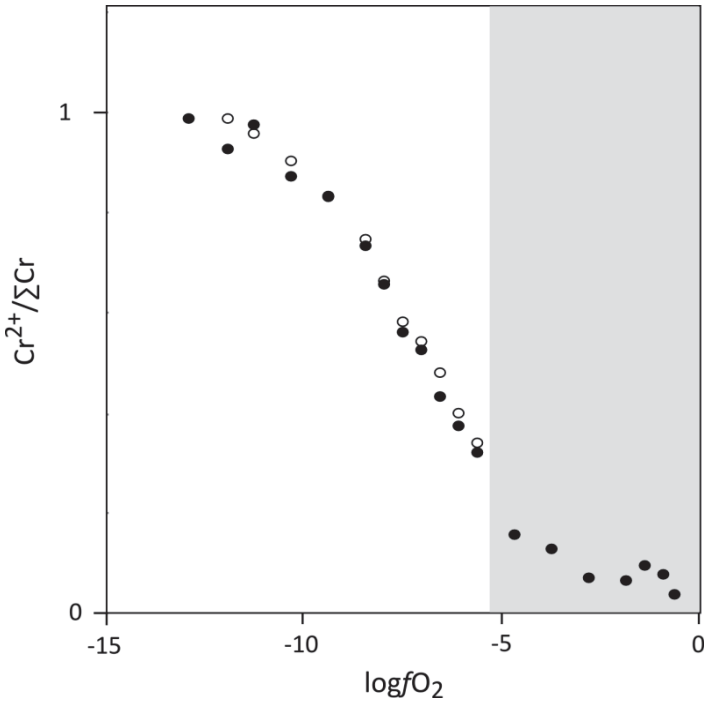


Figure A3.4: Comparison of the Cr^{2+} proportions in AD+En glasses reported by Berry and O'Neill (2004) (filled) to those derived from end-member linear combination fits (unfilled), where the Cr^{3+} line-shape was extracted using Gaussians with FWHM = 2.4 eV. The shaded region corresponds to glasses containing other Cr incorporating phases (spinel) and/or oxidation states (Cr^{6+}), in addition to the Cr^{2+} and Cr^{3+} in the glass.

A3.3 Cr^{2+} line-shape extraction

A3.3.1 Methodology

As a further test of the above procedure, the same methodology was applied to the Cr data in reverse; that is, a "Cr^{2+}" line-shape was extracted using a Cr^{3+} end-member. Two Cr^{3+} end-member line-shapes were trialled: (1) the extracted 100 % Cr^{3+} spectrum of section A3.2.2, and (2) the spectrum collected from the most oxidised glass that contained only Cr^{2+} and Cr^{3+} (logfO_2 = -6). The previously extracted Cr^{2+} line-shape is know to be close to the true end-member spectrum due to the excellent agreement between Cr redox ratios determined from linear combination fits of mixed valence spectra using this line-shape and those reported by Berry and O'Neill (2004).

A3.3.2 Results

Applying the line-shape extraction method using Gaussians of unconstrained widths could not produce a consistent "Cr^{2+}" line-shape between the intermediate spectra. Therefore only line-shapes extracted using Gaussians constrained by the experimental energy resolution (FWHM = 2.4 eV) are shown in Fig. A3.5. The line-shapes are reasonably consistent across the fO_2 set, and between the two choices of the Cr^{3+} end-member. However, they are entirely different to the original spectra from which they were produced, particularly in the post-edge region, where the fluorescence intensity drops off sharply to almost zero at ~6006 eV.

A3.4 Discussion

Clearly the missing component extracted in the absence of a Cr^{2+} spectrum (section A3.3) is not the true Cr^{2+} XANES spectrum (Fig. A3.5). This results from the extraction method, which will effectively extract the minimum possible missing component or the part of the spectrum that cannot be fitted by the known end-member line-shape (i.e. so that the residual of the fit when it only includes the known end-member will have values ≥ 0 at all energies). Successful extraction of the true (or close to true) oxidation state end-member spectrum by this method, both using Gaussians of constrained and unconstrained widths, will depend on the known oxidation state end-member spectrum having a unique spectral feature. For example, fortuitously Cr^{2+} has a strong shoulder (Fig. A3.1: 5997 eV) on its edge rise, whilst at the same energy the intensity of the Cr^{3+} spectrum is almost zero. Thus, the intensities of mixed valence spectra at this energy are almost entirely due to the contribution of Cr^{2+}; it is this that allows an accurate Cr^{3+} spectral shape to be extracted. Conversely, the Cr^{3+} end-member has no such feature (i.e. a feature where Cr^{3+} has a high intensity and Cr^{2+} has very little intensity) so the true Cr^{2+} spectrum cannot be extracted by reversal of the method. Inspite of this, linear combination fits using the extracted Cr^{2+} component and the 100 % Cr^{3+}

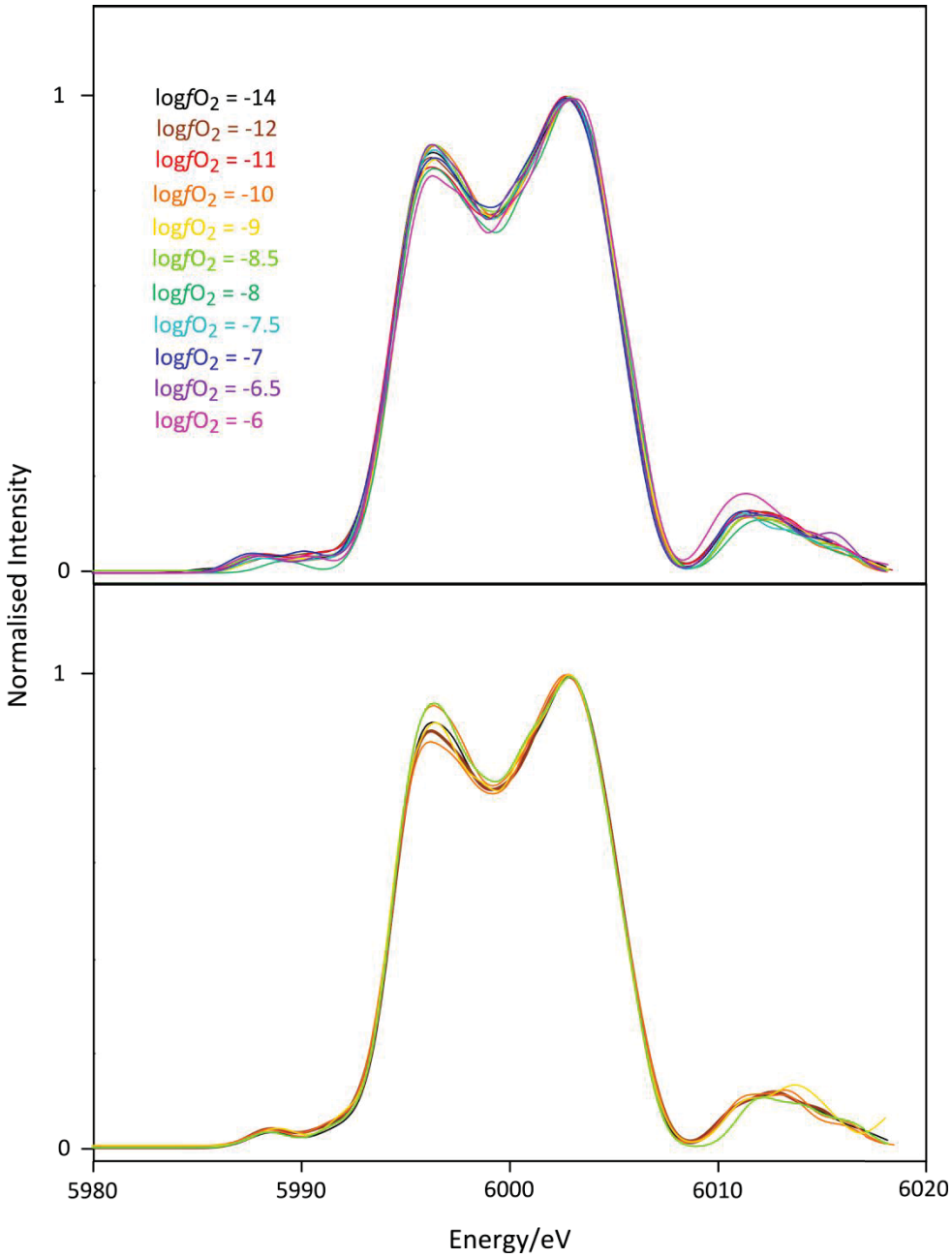


Figure A3.5: "Cr^{2+}" line-shapes extracted from the Cr K-edge XANES spectra of AD+En glasses equilibrated at the fO_2s indicated. Spectra were fitted using a combination of (a) the logfO_2 = -6 spectrum or (b) the estimated Cr^{3+} spectrum (section A3.2.2), and many Gaussians, with FWHM = 2.4 eV, to produce the missing "Cr^{2+}" component.

---

line-shape still reveal something about the oxidation state proportions in the glasses, as its contibution to each fit will be proportional to the amount of Cr^{2+} actually present. In fact, in the case of this two state system, Cr redox ratios can still be accurately quantified, as the

variation of the maximum intensity, *I*, of the Cr^{2+} component with logfO_2 is systematic and can be fitted using the expected sigmoidal relationship:

$$I = \frac{b}{(1 + 10^{(0.25\log fO_2 + \log K')})} + c \qquad \text{(A3.1)}$$

where *b* and *c* are constants that define the reduced and oxidised limits of the sigmoid. The value of *c* can be set equal to zero if we known that the Cr^{3+} line-shape is the true end-member spectrum (Fig. A3.6). The fit shown in Fig. A3.6 gives a logK′ value of 1.84 (2) identical to that of Berry and O'Neill (1.844 (16)). However, similar fits to the variation of components in mixed spectra consisting of three oxidation state line-shapes, where the true line-shape of the intermediate oxidation state is unknown (i.e. as for the MORB U M_4-edge spectra of Chapter 3), will not produce the true logK′ values.

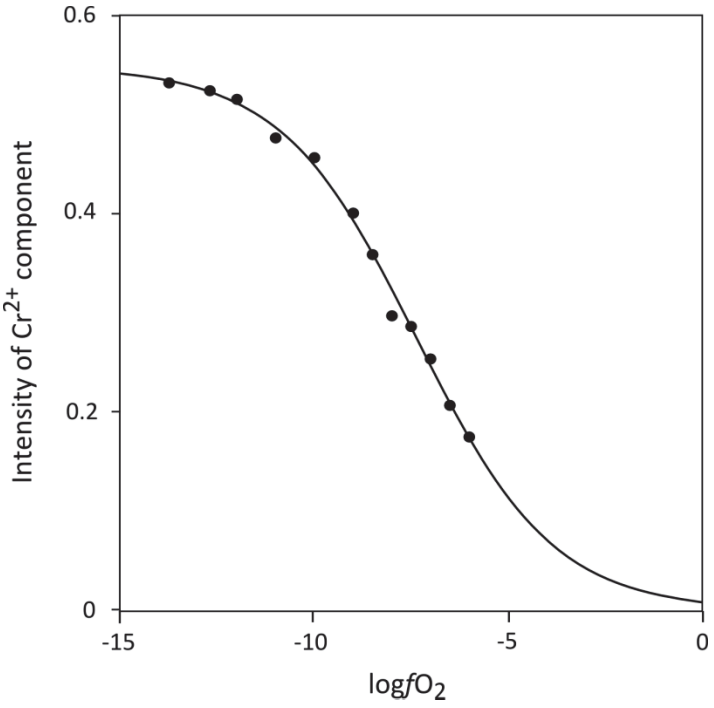


Figure A3.6: Intensity variation of the Cr^{2+} component in linear combination fits using the average "Cr^{2+}" line-shape extracted in section A3.3, and the corresponding single sigmoid fit (with *a*/4 = 0.25 and an oxidised limit of zero).

Appendix 4:

Calibration of the XAS furnace

A4.1 Temperature

Preparation for beamtime included temperature and fO_2 calibrations of the XAS furnace. The furnace Eurotherm controller was connected to a type B (Pt/Rh) thermocouple located against the inside wall of the furnace. The temperature difference between that measured by the control thermocouple and at the sample position was determined by inserting a second thermocouple down the sample rod so that its tip was aligned with the centre of the furnace windows. A temperature calibration plot is shown in Fig. A4.1.

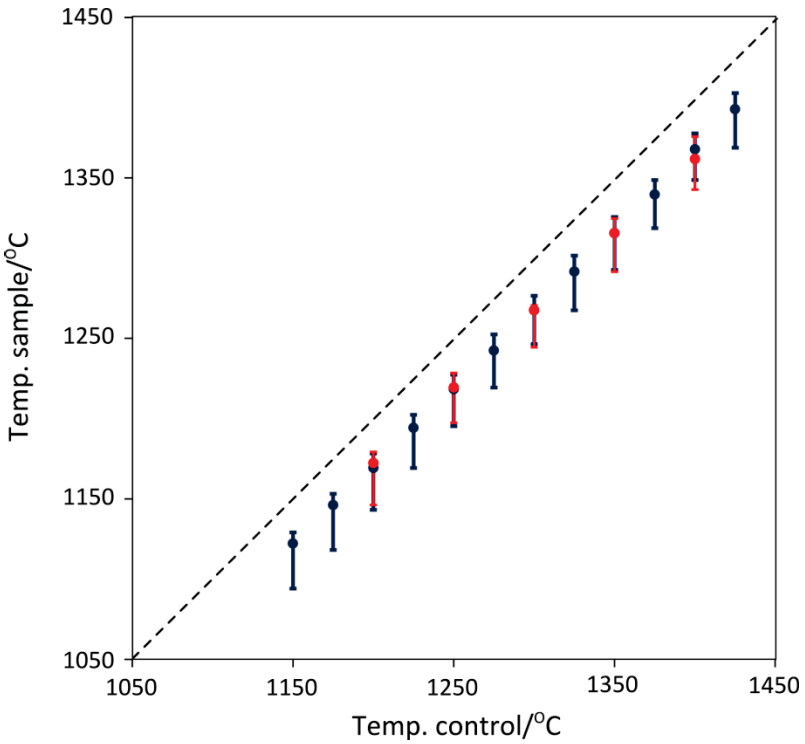


Figure A4.1: Relationship between temperature measured by control thermocouple connected to eurotherm and temperature measured at sample position by a second calibration thermocouple (dashed line: Temp. control = Temp. sample). The data points represent the temperature when the sample thermocouple is aligned with the centre of the furnace window, whilst negative and positive error bars are the temperatures measured when the thermocouple was aligned with the top and base of the window (gradient over ~8mm vertical distance), respectively. Red points are repeat measurements.

A4.2 Oxygen fugacity

To confirm that the fO_2 matched that desired when different gas mixtures were passed through the furnace, the fO_2 dependent solubility's of iron, nickel and cobalt in an anorthite-diopside eutectic melt composition were used. For example, for Ni (treatment of Fe and Co is completely analogous), the oxidation of metallic Ni is given by:

$$\mathrm{Ni} + \frac{1}{2}\mathrm{O_2} \leftrightarrows \mathrm{NiO} \tag{A4.1}$$

The equilibrium constant, K, for this reaction can be expressed as:

$$\log \mathrm{K}^{\mathrm{Ni-NiO(l)}} = -\frac{1}{2}\log f\mathrm{O_2} + \log X_{\mathrm{NiO}} + \log \gamma_{\mathrm{NiO}} \tag{A4.2}$$

where X_{NiO} is the mole fraction of NiO dissolved in the silicate melt, and γ_{NiO} is the corresponding activity coefficient of NiO. Using this, and the thermodynamic relation:

$$\Delta \mathrm{G} = -\mathrm{RT}\ln \mathrm{K} \tag{A4.3}$$

the fO_2 of a system can be calculated provided γ_{NiO} and ΔG are known. Using the ΔG expressions of Holzheid & Chakraborty (1997) and the γ data of O'Neill & Eggins (2002) the NiO, CoO, or FeO content of a melt of anorthite-diopside eutectic (AD) composition can be related to fO_2. For example, in the case of Ni:

$$\Delta \mathrm{G}^{\mathrm{Ni-NiO}} = -185092 + 99.844 \cdot \mathrm{T} - 4.898 \cdot \mathrm{T} \cdot \ln \mathrm{T} \tag{A4.4}$$

$$\ln \mathrm{K} = \frac{185092}{\mathrm{RT}} + \frac{4.898 \cdot \ln \mathrm{T} - 99.844}{\mathrm{R}} \tag{A4.5}$$

$$-\frac{1}{2}\ln f\mathrm{O_2} + \ln X_{\mathrm{NiO}} + \ln \gamma_{\mathrm{NiO}} = \frac{185092}{\mathrm{RT}} + \frac{4.898 \cdot \ln \mathrm{T} - 99.844}{\mathrm{R}} \tag{A4.6}$$

$$-\frac{1}{2}\log f\mathrm{O_2} + \log X_{\mathrm{NiO}} + \log \gamma_{\mathrm{NiO}} = \frac{9668}{\mathrm{T}} + 0.589 \cdot \log \mathrm{T} - 5.215 \tag{A4.7}$$

$$\log f\mathrm{O_2} = 2\left(-\frac{9668}{\mathrm{T}} - 0.589 \cdot \log \mathrm{T} + 5.616 + \log X_{\mathrm{NiO}}\right) \tag{A4.8}$$

Analogously for Fe and Co:

$$\log f\mathrm{O}_2 = 2\left(-\frac{12751.1}{\mathrm{T}} - 1.019 \cdot \log \mathrm{T} + 6.172 + \log X_{\mathrm{FeO}}\right) \quad \text{(A4.9)}$$

$$\log f\mathrm{O}_2 = 2\left(-\frac{9806.6}{\mathrm{T}} - 0.682 \cdot \log \mathrm{T} + 4.822 + \log \mathrm{X}_{\mathrm{CoO}}\right) \quad \text{(A4.10)}$$

Fe, Ni, and Co loops of AD mix were equilibrated at a range of fO_2s at 1400 °C. The compositions of the resulting glasses were determined using a Cameca SX-100 electron probe in WDS mode with an accelerating voltage of 20 keV and a beam current of 20 nA. The standards used were forsterite (Mg Kα), corundum (Al Kα), fayalite (Fe Kα), wollastonite (Ca Kα, Si Kα), Co metal (Co Kα), and Ni metal or NiO_2 (Ni, Kα). The fO_2 of melt equilibration was calculated using the measured $X_{metal\ oxide}$, and compared to that expected based on the input gas mixture. All compositions and fO_2s are given in Table A4.1.

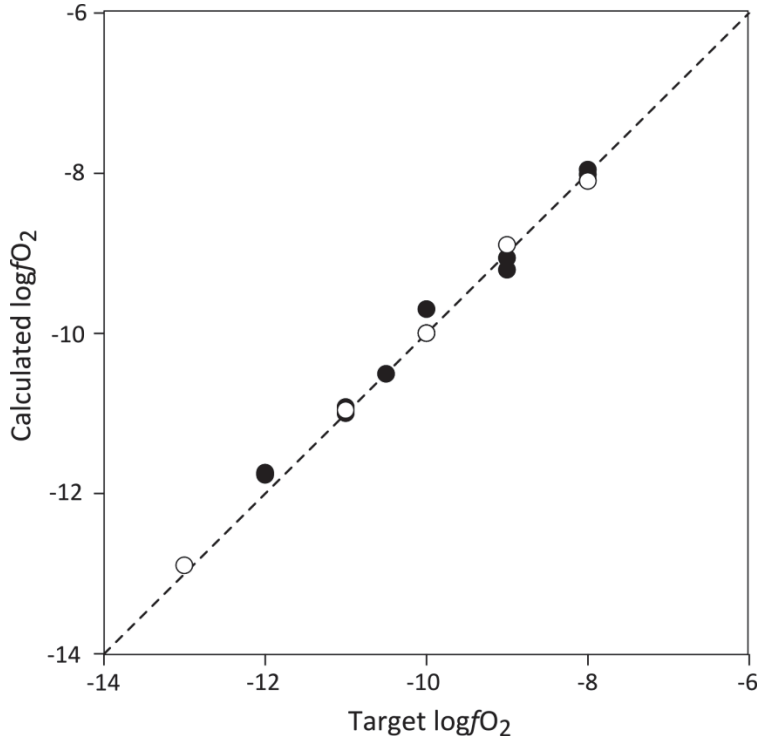


Figure A4.2: Comparison between the fO_2 of imposed gas mixture and that calculated from solubility of Fe, Ni, or Co in anorthite-diopside eutectic melt at 1400 °C for the Imperial College sample preparation furnace (unfilled points) and the *in situ* XAS furnace (filled points) (dashed line: target logfO_2 = calculated logfO_2). The calculated uncertainties (see Table A4.1) are smaller than the data points.

Table A4.1: Composition of anorthite-diopside eutectic glass in equilibrium with Co, Ni, or Fe determined by EPMA. Gas flow-rates are given as a percentage of the maximum flow rate on the channel (set 1) or as actual flow rates (set 2) with the MFC channel used indicated in brackets (i.e. 200 represents the 200 sccm channel for the relevant gas). Values in parentheses indicate one standard deviation for compositional analyses and the resulting uncertainty in fO_2 for "Calculated $\log fO_2$".

Sample	Loop	Target $\log fO_2$	Gas mix/channels	Run time/hr	Analyses	SiO_2	Al_2O_3	MgO	CaO	Metal oxide	Total	Calculated $\log fO_2$
MFCs set 1, XAS furnace-Nickel foam												
S020911	Fe	-12	20 % x 10 SCCM CO_2 50 % x 200 SCCM CO	8	13	47.20 (7)	13.71 (7)	9.52 (5)	21.46 (7)	8.46 (3)	100.4	-11.77 (1)
S120911	Co	-12	20 % x 10 SCCM CO_2 50 % x 200 SCCM CO	8	22	51.9 (5)	14.95 (9)	10.34 (4)	23.4 (2)	0.31 (3)	100.9	-11.74 (5)
S130911	Co	-11	60 % x 10 SCCM CO_2 47 % x 200 SCCM CO	8	32	50.7 (8)	15.04 (9)	10.30 (4)	23.7 (2)	0.69 (3)	100.4	-11.00 (4)
S140911	Co	-10.5	4.7 % x 200 SCCM CO_2 41.5 % x 200 SCCM CO	7.5	22	51.1 (4)	14.8 (1)	10.23 (4)	23.1 (1)	1.21 (6)	100.4	-10.51 (4)
S260811	Ni	-10	6.7 % x 200 SCCM CO_2 33.4 % x 200 SCCM CO	9	22	51.4 (5)	15.0 (1)	10.46 (9)	23.5 (1)	0.16 (3)	100.5	-10.0 (2)
S110711	Ni	-9	20 % x 200 SCCM CO_2 31 % x 200 SCCM CO	7.5	23	51.2 (3)	15.1 (1)	10.52 (7)	23.5 (2)	0.36 (3)	100.7	-9.21 (7)
S290811	Ni	-8	27 % x 200 SCCM CO_2 13 % x 200 SCCMCO	8	34	50.6 (8)	14.78 (8)	10.20 (3)	23.2 (2)	1.3 (1)	100.7	-8.09 (7)
MFCs set 1, IC furnace												
IC100611	Fe	-13	6 % x 200 SCCM CO_2 47 % x 200 SCCM CO	64	12	50.0 (2)	14.9 (1)	10.12 (7)	22.8 (1)	2.32 (2)	100.1	-12.90 (1)
IC170611	Ni	-10	6.7 % x 200 SCCM CO_2 33.4 % x 200 SCCM CO	44	22	50.8 (5)	15.1 (2)	10.55 (8)	23.6 (1)	0.15 (2)	100.2	-10.0 (1)

Sample	Loop	Target logfO_2	Gas mix/channels	Run time/hr	Analyses	SiO_2	Al_2O_3	MgO	CaO	Metal oxide	Total	Calculated logfO_2
IC270611	Ni	-9	20 % x 200 SCCM CO_2 31 % x 200 SCCM CO	24	34	50.7 (4)	15.0 (1)	10.5 (2)	23.4 (2)	0.5 (1)	100.2	-8.9 (2)
IC280611	Ni	-8	27 % x 200 SCCM CO_2 13 % x 200 SCCM CO	24	34	50.3 (5)	14.9 (1)	10.5 (1)	23.2 (1)	1.3 (2)	100.2	-8.1 (1)
IC090911	Co	-11	60 % x 10 SCCM CO_2 47 % x 200 SCCM CO	24	30	50.3 (4)	15.2 (1)	10.51 (6)	23.5 (2)	0.72 (3)	100.2	-10.96 (4)
IC290611	Co	-10	6.7 % x 200 SCCM CO_2 33.4 % x 200 SCCM CO	24	12	49.9 (6)	14.8 (1)	10.0 (2)	22.6 (2)	2.16 (4)	99.5	-10.00 (2)
MFCs set 2, XAS furnace-Nickel foam												
S250113	Co	-11	6 (20) SCCM CO_2 94 (200) SCCM CO	7	22	49.2 (7)	15.2 (1)	10.61 (5)	23.6 (2)	0.75 (4)	99.4	-10.92 (5)
S270113	Ni	-10	13.4 (20) SCCM CO_2 66.8 (200) SCCM CO	6.5	21	49.5 (5)	15.2 (1)	10.65 (3)	23.7 (3)	0.21 (5)	99.3	-9.7 (2)
S300113	Ni	-9	40 (200) SCCM CO_2 62 (200) SCCM CO	6.5	24	49.3 (6)	15.2 (1)	10.62 (4)	23.7 (3)	0.42 (4)	99.2	-9.06 (9)
S310113	Ni	-8	54 (200) SCCM CO_2 26 (200) SCCM CO	6	22	48.8 (6)	15.1 (1)	10.50 (5)	23.5 (3)	1.4 (1)	99.3	-8.02 (6)
S010213	Ni	-8	39.5 (200) SCCM CO_2 19 (20) SCCM CO	6	22	48.8 (7)	15.1 (1)	10.55 (5)	23.4 (3)	1.5 (1)	99.4	-7.96 (6)
MFCs set 2, XAS furnace-Ceramic foam												
S060213	Ni	-9	40 (200) SCCM CO_2 62 (200) SCCM CO	6	22	49.6 (6)	15.17 (8)	10.61 (4)	23.6 (6)	0.48 (7)	99.5	-9.0 (1)
S070213	Ni	-10	13.4 (20) SCCM CO_2 66.8 (200) SCCM CO	6	16	49.5 (6)	15.3 (1)	10.65 (3)	23.8 (1)	0.21 (7)	99.5	-9.7 (3)
S080213	Co	-11	6 (20) SCCM CO_2 94 (200) SCCM CO	6	18	49.2 (6)	15.2 (1)	10.59 (3)	23.7 (1)	0.67 (3)	99.4	-11.01 (4)

Appendix 5:

Ce L_3-edge XANES spectroscopy of silicate glasses and melts

A5.1 Introduction

Ce L_3-edge XANES spectra have previously been collected from Ce-bearing glasses (i.e. at RT) quenched from a series of Fe-free and Fe-bearing melts equilibrated at 1 atm, 1400 °C, and various fO_2s ($\log fO_2$ = 0 to -16) (Burnham and Berry, 2014). This work showed that both Ce^{3+} and Ce^{4+} were present in the Fe-free glasses equilibrated at oxidising conditions, with Ce^{4+}/Ce^{3+} = ~0.2 at $\log fO_2$ = 0. However, spectra of Fe-bearing glasses exhibited no evidence of Ce^{4+}, even for highly oxidised glasses. This was interpreted to be an artefact of the quench due to the electron exchange reaction $Fe^{2+} + Ce^{4+} \rightarrow Fe^{3+} + Ce^{3+}$. The work undertaken as part of this thesis, and outlined below, extends the study of Ce oxidation states to even more oxidised Fe-bearing glasses than those previously reported, and to high-temperature Fe-bearing melts *in situ*.

A5.2 Methods

For *in situ* studies MORB composition glasses (see Table 2.2 in Chapter 2 of this thesis) suspended on Pt and Re (for $\log fO_2 \leq -8$) loops were prepared from oxide mixes doped with 0.5 wt % CeO_2. In addition, Ce-doped MORB glasses were prepared at 10 kbar and 1400 °C buffered by Ir-IrO_2 ($\log fO_2$ = +1.9) and Pt-PtO_2 ($\log fO_2$ = +4.7) using a piston cylinder apparatus.

Ce L_3-edge XANES spectra of glasses and *in situ* melts at 1400 °C were recorded at B18 of Diamond Light Source; details in Dent *et al.* (2009). *In situ* XANES spectra were collected using a modified version of the XAS furnace of Berry *et al.* (2003), with its upper fO_2 limit

extended to logfO_2 = 0 (pure O_2). The fO_2 conditions inside the furnace were controlled using the gas mixing ratios given in Table 2.1. For the most oxidised conditions (logfO_2 > -3) gas mixtures of O_2/CO_2 were used; CO_2 was used instead of Ar as the X-ray absorption length of Ar is only 1.9 cm at the energy of the Ce L_3-edge; compared to 19.0 cm for CO_2 and 21.9 cm for O_2. The excitation energy was selected using an Si(111) monochromator, resulting in a spectral energy resolution of 3.57 eV (a combination of the Darwin width of the monochromator, 0.80 eV, and Ce L_3 core-hole width, 3.48 eV (Krause and Oliver, 1979)). Harmonic rejection was achieved using a pair of Pt coated mirrors. The beam size on the sample was ~0.7 × 1 mm (V × H), and the fluorescence was recorded using a 4 element Si drift detector.

Ce spectra were recorded between 5600 and 5980 eV with a step size of 0.2 eV with a total acquisition time of ~8 minutes. After each change in condition spectra were recorded sequentially until three to six spectra with no detectable change between them had been collected to ensure the sample had reached equilibrium. Replicate spectra indicated a monochromator drift of < 0.2 eV during the data collection session.

A5.3 Results

All spectra recorded after equilibrium had been achieved at a single condition were averaged to improve the signal-to-noise ratio. Spectra were normalised by subtracting a linear base-line fitted to the pre-edge energy range between 5600 and 5675 eV, and dividing by a linear function fitted in the post-edge between 5800 and 5980 eV.

Figure A5.1(a) shows that the spectrum of the MORB glass equilibrated at 10 kbar and logfO_2 = +1.9 is very similar to that of a glass equilibrated logfO_2 = 0 and 1 atm, with a single

white-line peak at 5726 eV. However, the spectrum of the MORB glass equilibrated at 10 kbar and logfO_2 = +4.7 has a very different line-shape; the peak at 5726 eV is almost half as intense as that of the logfO_2 = +1.9 spectrum, and an additional peak is present at 5738 eV. *In situ* spectra of MORB melts equilibrated at 1400 °C and logfO_2 ≤ -3 (Fig. A5.1(b)) are similar to those recorded from MORB glasses (with the exception of the glass prepared at logfO_2 = +4.7). However, the spectra of more oxidised melts have a distinct shoulder at 5738 eV that increases in intensity with increasing fO_2. Growth of this shoulder is accompanied by a decrease in the intensity of the white-line peak at 5726 eV.

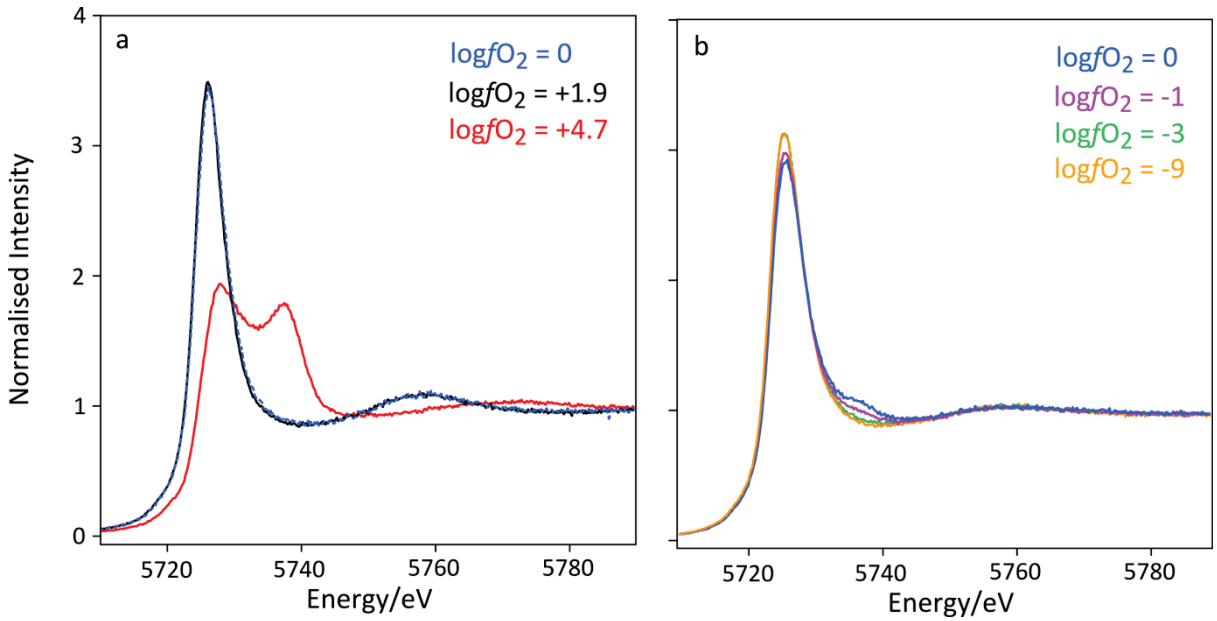


Figure A5.1: Ce L_3-edge XANES spectra of MORB (a) glasses and (b) melts equilibrated at 1400 °C and the fO_2s indicated.

A5.4 Discussion and Conclusions

Based on a simple comparison between previously reported Ce L_3-edge XANES spectra of Fe-free silicate glasses (Fig. A5.2: Burnham and Berry, 2014), for which Ce redox ratios have been quantified, and the spectra of this study, the line-shape of the MORB glass equilibrated

at logfO_2 = +1.9 is consistent with the presence of Ce^{3+} only. In contrast, the spectrum of the glass equilibrated at logfO_2 = +4.7 requires Ce^{4+} to make up at least 50 % of the total Ce present. The variation of $Ce^{4+}/\sum Ce$ between 0 and ~0.5 over less than three log units of fO_2 is not consistent with the theoretical thermodynamic relationship for a one-electron oxidation reaction in a melt. In addition, the change in shape of the most oxidised MORB melts spectra is consistent with the stabilisation of Ce^{4+} in Fe-bearing melts at highly oxidising conditions. These results support the conclusion that the electron exchange reaction $Ce^{4+} + Fe^{2+} \rightarrow Ce^{3+} + Fe^{3+}$ occurs during quenching of the MORB samples under all fO_2 conditions in which Fe^{2+} is present. Thus, Ce^{4+} was preserved in the glass equilibrated at the most oxidising conditions (logfO_2 = +4.7, 10 kbar) because the original melt did not contain sufficient Fe^{2+} to reduce the Ce^{4+}.

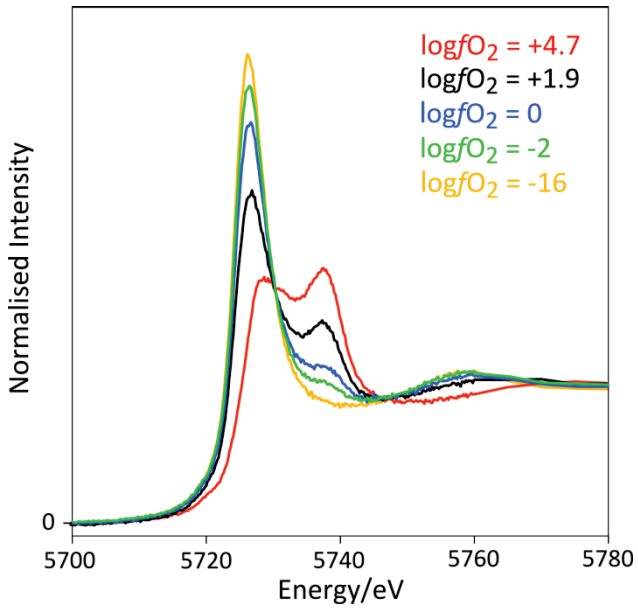


Figure A5.2: Ce L_3-edge XANES spectra of AD glasses equilibrated at 1400 °C and the fO_2s indicated (Burnham and Berry, 2014).

Appendix 6:

Eu L_3-edge XANES spectroscopy of silicate melts

A6.1 Introduction

In addition to the *in situ* XANES study of Ce-bearing melts outlined in Appendix 5, complimentary XANES studies of the oxidation state of Eu in high temperature melts were carried out. The first part of this appendix provides a brief summary of the methods and results for experiments undertaken specifically as part of this PhD project, which are an extension of the studies of Eu-bearing silicate glasses reported in the PhD thesis of Burnham (2012). The results of these *in situ* studies are expected to be published along with previous work on Eu glasses, and the submitted paper is provided in the second part of this appendix.

A6.2 Experimental methods

For *in situ* XANES studies an AD composition glass furnace loop was prepared by pasting an oxide mixture doped with 0.5 wt % Eu_2O_3 onto a Pt loop and heating to 1400 °C under a CO/CO_2 gas mixture. Two loops of MORB glass were prepared; one on Pt and one on Re (for $\log fO_2 \leq -8$). The exact fO_2s of sample preparation are not important as the same loops were used for all *in situ* measurements by allowing the glass to re-equilibrate with each change in temperature or gas atmosphere during XANES data collection.

In situ Eu L_3-edge XANES spectra of melts were recorded using a specialist XAS furnace at I18 and B18 of Diamond Light Source (DLS); details in Mosselmans *et al*. (2009) and Dent *et al.* (2009), respectively. The excitation energy was selected using an Si(111) monochromator, resulting in a spectral energy resolution of 4.05 eV (a combination of the beam divergence, ~0.35 eV, Darwin width of the monochromator, 0.98 eV, and Eu L_3 core-

hole width, 3.91 eV (Krause and Oliver, 1979)). Harmonics were removed by Rh coated KB mirrors (I18) or a pair of Pt coated harmonic rejection mirrors (B18). The beam size (V × H) was 40 × 70 μm at I18 and 0.7 x 0.8 mm at B18. The photon flux was ~10^{11} photons/s at the sample. Fluorescence was recorded using 9 element Ge (I18) or 4 element Si drift (B18) detector. The distance between the detector and the sample was adjusted to ensure that the total count rate was within the linear range of the detector.

Eu spectra were recorded between 6880-7100 eV with a step size of 5 eV between 6880-6950, 0.4 eV between 6950-7000 eV, and 5 eV between 7000-7100 eV, resulting in a total acquisition time of ~5 minutes at I18 and ~13 minutes at B18. Spectra were recorded from MORB and AD melts at temperatures between 1250 and 1450 °C. The fO_2 of melt equilibration was controlled by CO-CO_2 gas mixtures giving logfO_2 values between -3 and -12 at 1400 °C (Table 2.1in Chapter 2 of this thesis). After each change in condition spectra were recorded sequentially until at least three spectra with no detectable change between them had been collected to ensure that the sample had reached equilibrium. Spectra recorded at a single set of conditions after equilibrium had been reached were averaged. To allow comparison of data between the two sessions a number of the same sample conditions were recorded on both occasions.

A6.3 Results

For all spectra a horizontal baseline was subtracted followed by normalisation to the average fluorescence intensity above the edge between 7060 and 7090 eV. Spectra vary systematically in shape as a function of fO_2. As shown in Fig. A6.1, a white-line peak at ~6982 eV dominates the spectra of the most oxidised melts; this peak shrinks and a white-line peak at ~6974 eV grows with decreasing fO_2. These peaks are assigned to the $2p_{3/2} \rightarrow 5d$

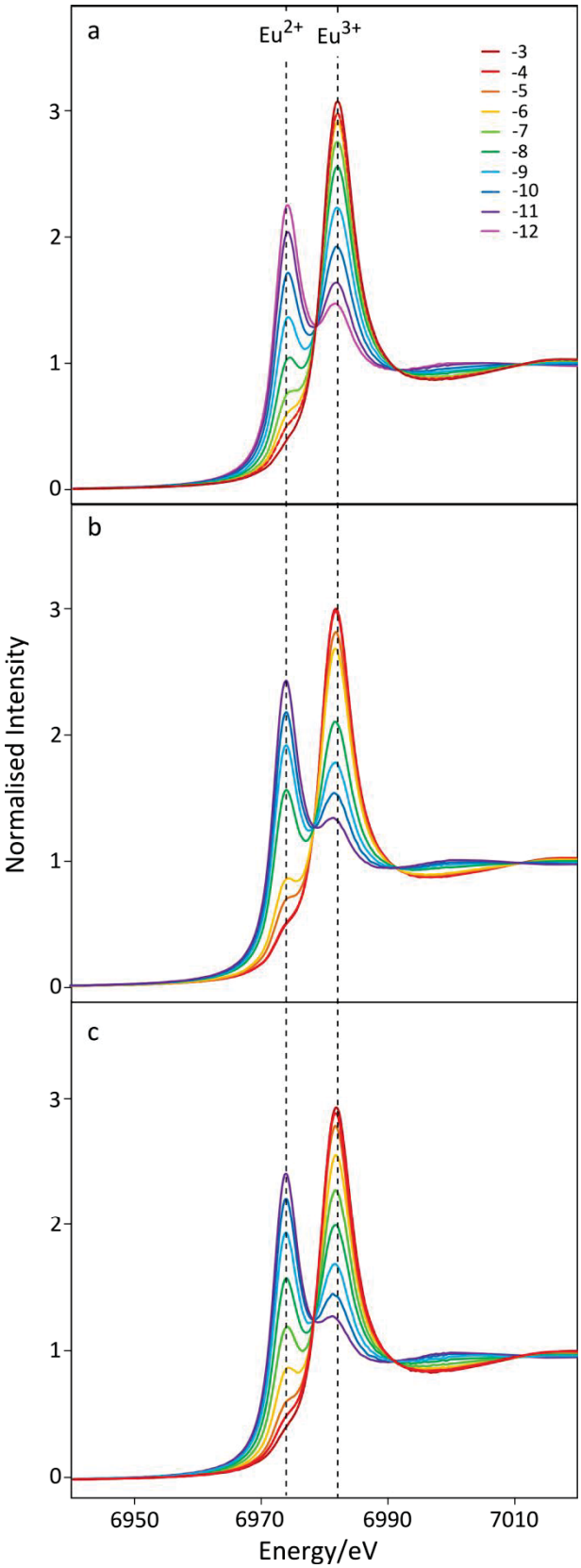


Figure A6.1: Eu L_3-edge XANES spectra of (a) AD melts at 1400 °C, (b) MORB melts at 1400 °C, and (c) MORB melts at 1250 °C equilibrated at a the logfO_2s indicated. Note that the logfO_2s indicated refer to the fO_2 of the imposed gas mixture at 1400 °C.

transitions in Eu^{2+} and Eu^{3+}, and their normalised-intensities are sigmoidally correlated with fO_2. The variation of the Eu^{2+} and Eu^{3+} white-line crest intensities can be well fitted using the expected thermodynamic relationship for a one electron oxidation reaction (Fig. A6.2).

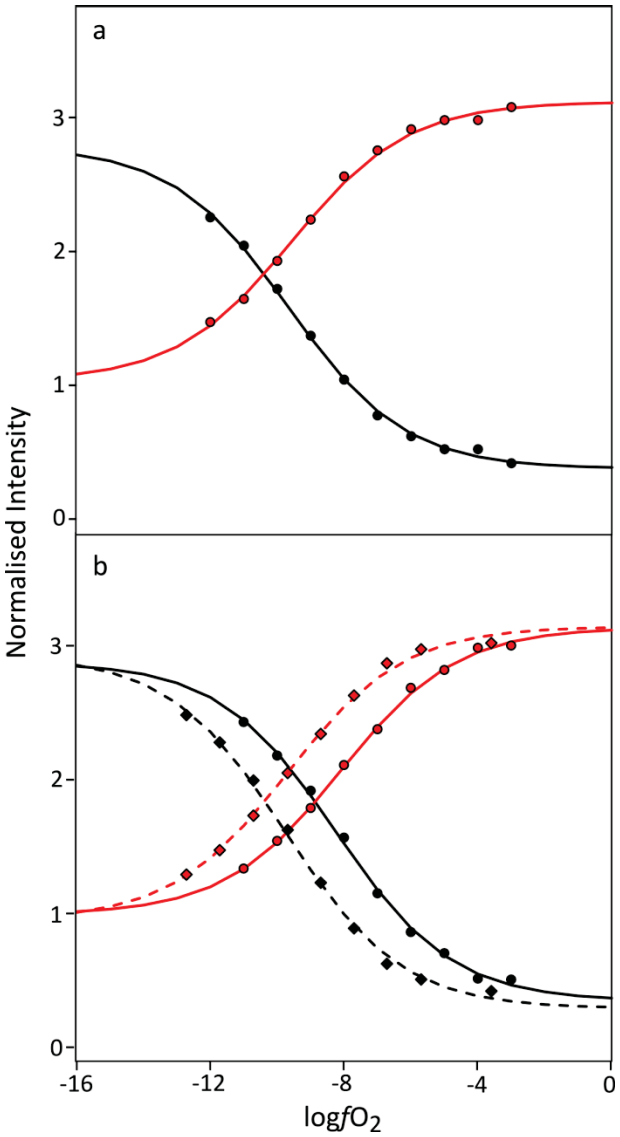


Figure A6.2: Normalised-intensities of Eu^{2+} (black) and Eu^{3+} (red) white line peaks in the Eu L_3-edge XANES spectra of (a) AD melts equilibrated at 1400 °C and (b) MORB melts equilibrated at 1400 °C (solid lines) and 1250 °C (dashed lines), as a function of fO_2.

The oxidation state of europium in silicate melts as a function of oxygen fugacity, composition and temperature

A. D. Burnham[1*], A. J. Berry[1,2,3], H. R. Halse[1,2,4], P. F. Schofield[2], G. Cibin[4] and J. F. W. Mosselmans[4]

[1]Department of Earth Science and Engineering, Imperial College London, South Kensington, SW7 2AZ, U.K.

[2]Department of Earth Sciences, Natural History Museum, Cromwell Road, London, SW7 5BD, U.K.

[3]Research School of Earth Sciences, Australian National University, Canberra, ACT 2601, Australia.

[4]Diamond Light Source, Harwell Science and Innovation Campus, Didcot, OX11 0DE, U.K.

*(present address) School of Earth Sciences, Wills Memorial Building, Queen's Road, Bristol, BS8 1RJ, UK.

Corresponding author: A. D. Burnham (a.burnham08@alumni.imperial.ac.uk)

Abstract

Eu L_{III}-edge X-ray absorption near edge structure (XANES) spectra were recorded for a series of synthetic glasses and melts equilibrated over a range of oxygen fugacities (fO_2s, from -14 to +6 in logarithmic units relative to the quartz-fayalite-magnetite, QFM, buffer) and temperatures (1250 – 1500 °C). $Eu^{3+}/\Sigma Eu$ (where $\Sigma Eu = Eu^{2+} + Eu^{3+}$) was determined from the spectra with a precision of ±0.015. $Eu^{3+}/\Sigma Eu$ varies systematically with fO_2 from 0 to 1 over the range studied, increases with decreasing melt polymerisation and temperature, and can be described by the empirical equation: $Eu^{3+}/\sum Eu = \frac{1}{1+10^{-0.25\log fO_2 + \frac{6750}{T} + 14.4\Lambda - 10.4}}$, where Λ is the optical basicity of the melt and T is in K. $Eu^{3+}/\Sigma Eu$ in glasses and melts equilibrated at the same conditions are in excellent agreement for Fe-free systems; however, in Fe-bearing compositions the reaction $Eu^{2+} + Fe^{3+} = Eu^{3+} + Fe^{2+}$ occurs during quenching to a glass. The high temperature value of $Eu^{3+}/\Sigma Eu$ is not preserved on cooling and *in situ* measurements are essential for determining $Eu^{3+}/\Sigma Eu$ in natural melts.

Highlights

- Eu^{2+}/Eu^{3+} in melts can be predicted using a simple equation
- Eu^{2+}/Eu^{3+} in a natural melt is not preserved on quenching to a glass
- $Eu^{2+} + Fe^{3+} = Eu^{3+} + Fe^{2+}$

Keywords: XANES, redox, rare earth element, silicate glass, oxygen fugacity, *in situ*, Eu/Eu*

Introduction

Europium is the only rare earth element (REE) that can occur in significant proportions of an oxidation state other than REE^{3+} in natural silicate melts (e.g. Drake, 1975). The oxidation state of Eu is of geochemical interest because Eu^{2+} and Eu^{3+} partition differently and thus the behaviour of Eu in a magma depends on the oxygen fugacity (fO_2) and the phase(s) crystallising. Chondrite-normalised REE patterns with anomalous Eu concentrations, quantified as $Eu/Eu^* = Eu/\sqrt{[Sm \times Gd]}$, are frequently observed and are attributed to the redox-variability of Eu. Experimental studies have calibrated the fO_2-dependency of Eu partitioning between feldspars and melt and shown $D_{Eu^{2+}}$ (where D_i is the ratio of the weight fraction of i in the crystal to that in the melt) to be an order of magnitude greater than $D_{Eu^{3+}}$ (Drake, 1975; McKay et al., 1994; Wilke and Behrens, 1999; Aigner-Torres et al., 2007).

Conversely, Eu^{2+} is far less compatible than REE^{3+} in pyroxenes (McKay et al., 1994; Wadhwa, 2001; see Eby 1995 for exceptions). The resulting positive or negative Eu anomalies can provide an indication of crystal fractionation (e.g. Brophy and Basu, 1990; Hoskin et al., 2000). Alternately, these anomalies could be used to estimate the fO_2 at which a sample crystallised. For example, the partitioning of Eu between pyroxene and melt as a function of fO_2 has potential as an oxybarometer, particularly for meteoritic samples (McKay et al., 1994; Shearer et al., 2006; Karner et al., 2010). Anomalous concentrations of Eu are also commonly exhibited by zircon and similarly could record the fO_2 of crystallisation (Hoskin and Schaltegger, 2003; Burnham and Berry, 2012; Trail et al., 2012).

Partitioning between feldspar, or other minerals, and melt allows the oxidation state ratio of Eu in the melt to be estimated, because the observed D_{Eu} can be modelled to be an average of D_{Sr} (a proxy for $D_{Eu^{2+}}$) and D_{Gd} or D_{Sm} (a proxy for $D_{Eu^{3+}}$) weighted by the relative proportions of Eu^{2+} and Eu^{3+} in the melt (e.g. McKay et al., 1994). However, such experiments ideally require melts with a compositionally invariant phase on the liquidus and thus cannot fully address the roles of composition and temperature, as neither can be varied freely. Spectroscopic determinations of Eu^{3+}/Eu^{2+}, or $Eu^{3+}/\sum Eu$ where $\sum Eu = Eu^{2+} + Eu^{3+}$, are not subject to this constraint.

^{151}Eu (47.8% natural abundance) Mössbauer spectroscopy has been used to determine $Eu^{3+}/\sum Eu$ in silicate glasses (Virgo et al., 1981; Nemov et al., 2007), though the limited applications and the long spectral acquisition times (several days) have probably hampered greater uptake of this technique. $Eu^{3+}/\sum Eu$ can also be determined by electron paramagnetic resonance (EPR) spectroscopy (Eu^{2+} is EPR active), however, the method is restricted to Fe-free compositions since the resonances of other paramagnetic ions will overlap with the Eu signal (Schreiber, 1977; Morris et al., 1974a, 1974b).

Eu L_{III}-edge X-ray absorption near edge structure (XANES) spectroscopy has been used to provide information on the oxidation state ratio and coordination environment of Eu in aqueous solutions, silicate melts and minerals (Antonio et al., 1997; Cicconi et al., 2012; Karner et al., 2010; Mayanovic et al. 2007; Rakovan et al., 2001; Shearer et al., 2011). Eu^{2+} spectra are characterised by an intense peak (white line) at 6974 eV and Eu^{3+} spectra by a white line at 6982 eV (Shimizugawa et al., 1999; Rakovan et al., 2001; Takahashi et al., 2005). The peaks are assigned to the $2p_{3/2} \rightarrow 5d$ transitions of Eu^{2+} and Eu^{3+} (Rakovan et al., 2001; Takahashi et al., 2005). The ~8 eV difference in energy between these features is large compared to the core hole width of 3.91 eV (Krause and Oliver, 1979), and hence for mixed valence systems the two peaks are well resolved and the relative contributions from each oxidation state can be determined. This resolution makes quantification of redox ratios potentially easier than for many other elements (e.g. Berry and O'Neill, 2004; Sutton et al., 2005). For example, $Eu^{3+}/\sum Eu$ has been determined with a precision of 0.01 for a sample of apatite containing only 700 ppm Eu (Rakovan et al. 2001).

In order to use Eu anomalies in minerals as an oxybarometer it is necessary to understand the separate effects of fO_2, melt composition, and temperature on $Eu^{3+}/\sum Eu$ in magmas. The work of Morris et al. (1974a, 1974b) represents the most comprehensive study to date of the controls on the oxidation state ratio of Eu in glasses, covering temperatures from 1415 to 1650 °C, 12 log units of fO_2 and over 20 compositions in the system CMAS; they found that Eu^{3+} was stabilised by high fO_2s, melt compositions with high Ca/Mg ratios, and low temperatures.

Here we use XANES spectroscopy to determine $Eu^{3+}/\sum Eu$ for a range of silicate glasses and melts, thereby extending the work of Morris et al. (1974a, 1974b) to other melt compositions and to lower temperatures. Oxidation states present in a melt may not be preserved in a glass, even with rapid quenching, due to electron exchange reactions (Berry et al. 2006) and an X-ray absorption spectroscopy furnace (Berry et al., 2003) was used to make the first *in situ* measurements of $Eu^{3+}/\sum Eu$ in silicate melts. Pressure may also affect Eu^{3+}/Eu although this variable will not be addressed here.

Experimental

Eleven glass compositions in the system SiO_2-Al_2O_3-MgO-CaO, a ZrO_2-bearing glass and a synthetic MORB, all with 0.5 wt% Eu_2O_3, were prepared at a range of fO_2s ($\log fO_2$s from -18 to 0, equivalent to QFM–11.7 to QFM+6.3, where QFM is the quartz-fayalite-magnetite fO_2 buffer) and temperatures (1300-1500 °C) at atmospheric pressure. The compositions were selected to span a range of major element oxide components, and consequently compositional and structural parameters, with the aim of being able to predict the redox behaviour of Eu in other compositions. The same compositions were used in a study of $Ce^{4+}/\sum Ce$ (Burnham and Berry, 2014). Some samples contained 0.5 wt% CeO_2 in addition to Eu to test for interactions between these two elements. Reagent-grade powders of SiO_2, Al_2O_3, MgO, ZrO_2, CeO_2 and Eu_2O_3 dried at 1000 °C, and Fe_2O_3 and $CaCO_3$ dried at 300 °C were mixed under acetone using an agate mortar and pestle for >30 min. For experiments at $\log fO_2 = -16$ and below ($\log fO_2$ values are for 1400 °C unless otherwise stated) the resulting powder was pressed into pellets and loaded into wells drilled in a graphite block, as described in O'Neill and Berry (2006). For other experiments, the powder was mixed with polyethylene oxide and water to form a paste, which was mounted onto wire loops. Multiple loops, containing different compositions, were suspended from a "chandelier". For Fe-free compositions at $\log fO_2 \geq -12$, the loops and chandelier were made of Pt, and at $\log fO_2 = -13$ and -14 the loops were made of Re and the chandelier of ceramic. For MORB the loops were made of Re for $\log fO_2 \leq -8$ and Pt at higher fO_2s, with chandeliers as above. MORB samples could not be prepared below IW-1 (where IW is the iron-wüstite fO_2 buffer) due to the precipitation of Fe metal. The graphite block or chandelier was held at the end of an alumina rod in the hot zone of a 1 atm vertical gas mixing furnace. The fO_2 was controlled using a gas atmosphere regulated by Celerity FC2900 mass flow controllers; $\log fO_2$s from 0 to -2 were obtained using O_2 diluted with Ar, -3 using CO_2, -4 to -14 using mixtures of CO and CO_2 (Chase 1998), -16 using CO in equilibrium with graphite, and < -16 using CO diluted with Ar in equilibrium with graphite. Similar total flow rates were used at all fO_2s for temperature reproducibility. The fO_2 of the gas mixes were verified for $\log fO_2$ values <-10 from the solubility of Fe in the anorthite-diopside (AD) eutectic composition (O'Neill and Eggins, 2002) and at higher values using a SIRO2 solid state sensor, and found to be within ±0.1 of the target value. The accuracy of the imposed temperature is ± 1°C. Samples were equilibrated for >20 h except for a time-series of the AD+qz composition (8, 16, 24 and 42 h at $\log fO_2 = -12$). Glasses prepared at 1300 °C were equilibrated for 42 h because of the lower temperature and slower expected diffusion rates. Most samples were quenched in water to give glasses. Samples for *in situ* experiments were quenched in the bottom of the furnace to limit shattering due to thermal shock.

The glass samples were mounted in epoxy, exposed and polished, and examined optically and using a scanning electron microscope. Major element compositions were determined using a Cameca SX-100 electron probe (accelerating voltage 20 kV, current 20 nA). No interferences occur between the elements present.

Eu L_{III}-edge XANES spectra were recorded at BM29 of the European Synchrotron Radiation Facility (ESRF) and B18 and I18 of Diamond Light Source (DLS); beamline details in Filipponi et al. (2000), Dent et al. (2009) and Mosselmans et al. (2009), respectively. Glasses were studied at BM29 and B18, and melts at B18 and I18. In all cases the excitation energy was selected using a Si(111) monochromator, resulting in a spectral energy resolution of less than 4.05 eV (a combination of the beam divergence, which was no more than 0.35 eV, the Darwin width of the monochromator, 0.98 eV, and the Eu L_{III} core-hole width of 3.91 eV; Krause and Oliver, 1979). High energy harmonics were removed by Pt coated Si mirrors (collimating and focusing) at BM29 and B18 and Rh coated KB mirrors at I18. Fluorescence was recorded using 13 (BM29) and 9 (I18 and B18) element Ge detectors and a four element Si drift detector (B18 *in situ* experiments); the distance between the detector and the sample, or the number of photons on the sample, were adjusted to ensure that the total incoming count rate was within the linear range of the detector. Spectra of glasses were recorded from 6777-7221 eV at a step size of ~5 eV for the baseline (6777-6947 eV), 0.2 eV for the edge and ~5 eV above the edge (7011-7221 eV), with minor differences between sessions. Scan durations were 20 min. Spectra of melts were recorded *in situ* using the furnace described in Berry et al. (2003) from 6880-7100 eV with a step size of 5 eV from 6880-6950 eV, 0.4 eV from 6950-7000 eV, and 5 eV above 7000 eV. The re-equilibration of the sample in response to a change in temperature and/or fO_2 was monitored by the sequential acquisition of spectra (each taking 5 min at I18 and 13 min at B18); once no further spectral change was detectable, a further four spectra were recorded and averaged. This resulted in total spectral acquisition times of ~ 10-80 min. The beam size was set to 0.2 x 3.0 mm by slits at BM29 and focussed to 0.3 x 0.3 mm for glasses at B18, 0.7 x 0.8 mm for melts at B18, and 40 x 70 μm at I18 (all V x H). The photon flux (s^{-1}) was ~10^{10} at BM29 and ~10^{11} at both B18 and I18. The possibility of beam-induced changes in the Eu oxidation state was investigated at B18 by setting the monochromator to the energy of one of the peaks in the white line, opening the experimental shutter and monitoring the fluorescence as a function of time (at 700 ms intervals). This was done for both the Eu^{2+} and the Eu^{3+} peaks (always testing on a part of the sample not previously exposed to the X-ray beam) of samples prepared at $\log fO_2$ = -16, -10 and 0. The energy was calibrated at BM29 by defining the first peak in the transmission spectrum of Eu_2O_3 in BN to be at 6982.9 eV. The spectra recorded at B18 and I18 were energy corrected to those from BM29 using the spectrum of AD equilibrated at 1400 °C and $\log fO_2$ = -3. Spectra were compared after subtraction of a constant baseline and normalisation to the average intensity above 7600 eV, excluding the Fe absorption edge at ~ 7112 eV in the MORB samples.

Results

All glasses are homogeneous and vary in colour from yellow-green (reduced) to colourless (oxidised) for the Fe-free samples, and from green (reduced) to dark brown (oxidised) for MORB. The compositions determined by electron probe microanalysis (EPMA) are given in Table 1.

Representative normalised Eu L_{III}-edge XANES spectra of the quenched glasses (AD) and *in situ* melts (MORB) are shown in Fig. 1. Spectra obtained from MORB encountered the Fe *K*-edge in the far post-edge region (~7115 eV) but otherwise were similar to those of the Fe-free compositions. Samples (glass and melt) equilibrated under reducing conditions show a peak at 6974.2 eV, those equilibrated under oxidising conditions show a peak at 6982.4 eV, and samples equilibrated at intermediate fO_2s have both peaks. PseudoVoigt functions fitted to these peaks have essentially identical energies, line widths, and Lorentz fractions for both the quenched and *in situ* samples. At a given fO_2 the heights of the peaks in the spectra of the

glasses generally differ from those observed *in situ*. For AD there is an approximately linear relationship between the height of the Eu^{3+} peak in the glass and melt (Fig. 2); the peak is more intense in the glass than *in situ* at low fO_2s, but less intense at high fO_2s. The spectra are most similar at logfO_2 = -9. For MORB, at any fO_2 the Eu^{3+} peak in the melt is always more intense than in the glass. A direct comparison of the spectra obtained by the two experimental approaches is shown in Fig. 3.

Spectra of samples containing Ce are indistinguishable from those only containing Eu at the same fO_2 (AD and AD+wo at logfO_2 = 0 and -2). The series of AD+qz glasses held at 1400 °C and logfO_2 = -12 for 8, 16, 24 and 42 h yielded identical spectra (noting that the starting material has $Eu^{3+}/\sum Eu$ = 1), indicating that all other samples should have achieved equilibrium with the imposed conditions. For the *in situ* experiments samples equilibrated after a change in fO_2 in ~ 20 min, reflecting the fact that only the near-surface of the melt droplet (one absorption length ~50 μm) contributes to the fluorescence signal, and after a change in temperature in less than 5 min (a single scan).

For the AD glass prepared at logfO_2 = -16, the fluorescence signal at the energy of the Eu^{2+} peak decreased during exposure to the beam by ~5%, while the signal at the energy at the Eu^{3+} peak increased by ~9%, over a period of ~20 s before reaching a steady state after ~1 min (Fig. 4); moreover, the fluorescence intensity of these peaks did not return to the original values if the shutter was closed for tens of seconds and then reopened. Conversely, for the AD glass prepared at logfO_2 = 0, the height of the Eu^{2+} peak increased by ~8% and that of the Eu^{3+} peak decreased by ~5% on a similar timescale. For the AD glass prepared at logfO_2 = -10 no change in signal intensity was observed for either peak. Attenuation of the beam and defocusing to reduce the photon flux density did not appreciably change the extent of beam damage. The timescale over which the damage occurs is such that even spectra recorded in quick-EXAFS mode (in which an entire spectrum can be recorded in tens of seconds) would be affected. The fluorescence signal at the Eu^{2+} and Eu^{3+} peaks was constant with time for spectra recorded for AD melts *in situ* and there is no evidence of beam damage. MORB was not tested for beam damage.

XANES analysis

For the reaction $Eu^{2+}O + n/4O_2 = Eu^{3+}O_{1.5}$ it follows that $Eu^{3+}/\Sigma Eu$ should vary with fO_2 according to the sigmoidal relationship:

$$Eu^{3+}/\sum Eu = \frac{1}{1+10^{-(0.25\, n \log fO_2 + \log K')}} \quad (1)$$

where n relates to the stoichiometric number of electrons involved in the redox reaction (i.e. n = 1) and logK' is a modified equilibrium constant (see Berry and O'Neill, 2004). Equation 1 can be modified to describe any spectral feature (e.g. peak height, peak area, centroid energy) that varies with fO_2:

$$\text{feature} = \frac{a}{1+10^{-(0.25\, n \log fO_2 + \log K')}} + c \quad (2)$$

where a and c are constants. For a feature that has a positive sigmoidal dependence on logfO_2 (similar to $Eu^{3+}/\Sigma Eu$) a+c corresponds to the maximum value of the feature and c to the minimum value or zero offset. For a feature with a negative sigmoidal dependence on logfO_2 (similar to $Eu^{2+}/\Sigma Eu$) c corresponds to the maximum value and a+c to the zero offset. The intensities (heights) of the Eu^{2+} (6974.2 eV) and Eu^{3+} (6982.4 eV) peaks for all samples are given in Table 2. The data for the AD, AD+wo, and AD+qz glasses prepared at 1400 °C (the largest data sets) were fitted to Equation 2; the values of n for the fits to the Eu^{2+} peak height data were 1.02(7), 1.00(7) and 1.01(5) respectively, and those for the fits to the Eu^{3+} peak height data were 1.07(8), 1.18(8) and 1.05(6) respectively. These values are in good agreement with the expected value of 1.0. The data for all compositions and temperatures

were therefore fitted to Equation 2 with n fixed at 1. The parameters obtained from these fits (minimum of three data required) are given in Table 3 and the fits are illustrated for AD and MORB glasses and melts in Fig. 5. Substituting Equation 2 into Equation 1 allowed $Eu^{3+}/\sum Eu$ to be calculated from the height of each peak using the best fit values of a and c; these $Eu^{3+}/\sum Eu$ values are reported in Table 2. Replicate analyses of a sample gave values of $Eu^{3+}/\sum Eu$ that agreed within 0.02 on average. The values of a and c indicate that the maximum heights of the Eu^{3+} and Eu^{2+} peaks in glasses (excluding MORB) are almost independent of composition (2.55(8) for Eu^{2+} and 2.91(10) for Eu^{3+}). Therefore, these average values of a and c (respectively -2.09 and 2.55 for Eu^{2+} and 1.87 and 1.04 for Eu^{3+}) were used to convert peak heights into $Eu^{3+}/\sum Eu$ for Fe-free glasses where the data were insufficient to determine these coefficients independently. The average coefficients for MORB melt at 1250 and 1400 °C were used for MORB glass and MORB melt at other temperatures. The average of the coefficients for AD melt at 1300 and 1400 °C were used for AD melt at 1350 and 1450 °C. The resulting values of logK' (averages determined from Eu^{2+} and Eu^{3+} peaks) are given in Table 4.

Three alternate approaches to quantifying $Eu^{3+}/\sum Eu$ were considered. 1) Extraction of individual peak areas by fitting the XANES region with a combination of arithmetic functions (e.g. pseudoVoigts for the white line and an arctangent for the absorption edge) introduces uncertainty because the absorption edge arises from multiple electronic transitions and assumptions need to be made about how these are modelled. These assumptions result in values of the fO_2 coefficient, n, ranging from 0.73 to 0.98 for the AD glass series, in contrast to the result obtained by the peak heights approach, which requires no assumed shape for the various components of the XANES spectrum. 2) Fitting spectra to linear combinations of the spectra of reference compounds (e.g. EuO and Eu_2O_3) is potentially compromised by differences in the Eu coordination environment(s) between the glass and crystalline compounds in which Eu occurs at high concentrations. 3) Linear mixing of spectral end-members, as used by Burnham and Berry (2014) for quantifying $Ce^{4+}/\Sigma Ce$ from XANES spectra. For AD glass, using the spectra of samples prepared at logfO_2 = -20 and 0 as the Eu^{2+} and Eu^{3+} end-members, this gave log$K$' = 2.38(4), which is within error of the values reported in Tables 3 and 4 (determined from the peak heights). Such agreement is unsurprising given the observed constancy of the white line peak shapes and their intensities relative to the edge step. This method was not pursued further because it cannot be applied to the spectra of melts due to the limited fO_2 range of the XANES furnace, which prevents the acquisition of end-member spectra.

Discussion

For AD the values of logK' determined from the Eu^{2+} and Eu^{3+} peaks for both the glasses and *in situ* melts are identical, within error, despite the differences in the spectra. These differences are unlikely to be due to the effect of temperature (spectral broadening) because the line shapes (half width and Lorentz fraction) of the two sets of spectra are indistinguishable. Applying the fit parameters determined for AD melt to AD glass results in estimates of $Eu^{3+}/\sum Eu$ = 0.07 and 0.95 at infinitely low and high fO_2s respectively. These values are consistent with the observed time-resolved changes in the Eu^{2+} and Eu^{3+} peak intensities at logfO_2 = -16 and 0, which correspond to a change in $Eu^{2+}/\sum Eu$ of ~0.05 and ~0.08 respectively. The linear relationship between the *in situ* and glass peaks (Fig. 2) indicates that the empirical approach can negate the effects of beam damage, because the mathematical transformation required to map one dataset onto the other only requires a and c to vary, while log$K$' remains constant. Thus, $Eu^{3+}/\sum Eu$ and log$K$' can be determined for glasses of Fe-free compositions despite the presence of (minor) beam damage, provided there

are sufficient data to fit to Equation (2). The 'end-member' Eu^{2+} and Eu^{3+} spectra do not vary significantly with composition, implying similar coordination environments, and thus although the mechanism of the beam damage is unknown, we assume it will affect all Fe-free glass compositions similarly. Photo-oxidation of Eu during exposure to an X-ray beam has been documented by Shimizugawa et al. (1999), though on a much longer timescale than observed in our case (30 min to 1 h). The possibility of rapid beam-induced changes in $Eu^{3+}/\sum Eu$ means that such effects may have been overlooked by previous workers. The absence of beam damage in the melts is probably because they are in contact with a buffering gas, i.e. the redox state after beam damage is able to re-equilibrate as a result of diffusion and dynamic interaction with the imposed fO_2, which is not possible for a glass that is no longer in equilibrium with the formation conditions.

Melt composition

The $Eu^{3+}/\sum Eu$ values as a function of fO_2 for three compositions, and the corresponding fits to Equation 1, are shown in Fig. 6. This, and the range of log*K*' values given in Table 4, indicate that composition exerts a strong control on the oxidation state of Eu; the inflexion point of the sigmoid ($Eu^{3+}/\sum Eu = 0.5$) shifts by six log units in fO_2 for the range of compositions studied.

Correlations between log*K*' and NBO/T (Mills, 1993) and optical basicity (Duffy, 1993; Lebouteiller and Courtine, 1998) are shown in Fig. 7 ($R^2 = 0.93$ and 0.91, respectively). Weaker correlations exist with the mole fractions of SiO_2 (positive) and CaO (negative); there is no correlation with MgO. This suggests that the control on the oxidation state of Eu is chemical rather than structural, as is the case for Ce (Burnham and Berry, 2014), given that MgO and CaO both have equal weightings when calculating NBO/T. The results for Eu corroborate the observation that, for a given fO_2, cations of higher charge are stabilised by melts with high optical basicities (e.g. high CaO); thus reduced species will be favoured by melts rich in Si and Al; (Berry et al., 2006). From the fits shown in Fig. 7, log*K*' for the oxidation of Eu^{2+} to Eu^{3+} at 1400 °C can be predicted by the equations:

$$\log K' = 14.0(1.5)\Lambda - 6.1(9) \quad (3)$$

(where Λ is the optical basicity) and:

$$\log K' = 1.1(1)(\mathrm{NBO/T}) + 1.2(1) \quad (4)$$

which give values within ~15% relative of those determined directly by XANES. Using these relationships log*K*' and hence $Eu^{3+}/\sum Eu$ at 1400 °C can be predicted for any composition.

The log*K*' value of MORB glass (2.63(15)) differs significantly from that of MORB melt (2.05(15)). The difference between the glass and melt values corresponds to a $\Delta Eu^{3+}/\Sigma Eu$ of 0.17 at QFM. If *n* was not constrained in the fit of the MORB data to Equation 2 then log*K*' = 3.14(3) and *n* = 1.29(17) (average of Eu^{2+} and Eu^{3+} values), which is in even worse agreement with the melt, though more realistic maximum peak heights are predicted. In contrast, the glass and melt values of log*K*' for AD are in excellent agreement, at both 1300 and 1400 °C. Although beam damage in the MORB glass was not investigated, the discrepancy is not attributed to this phenomenon. As seen in Fig. 5a, the asymptotes of the peak heights for AD differ between the glass and melt due to beam damage, whereas for MORB they are almost indistinguishable at high fO_2s (for which the sigmoids are better constrained than at low fO_2s); end-member Eu^{2+} and Eu^{3+} spectra are similar for glass and melt (Fig. 5b), but the spectra of samples prepared at intermediate fO_2s are different. Moreover, the observed non-linear relationship between the Eu^{3+} peak heights for glass and melt contrasts with the linear correlation observed for AD. This difference between peak heights, log*K*', and hence the oxidation state ratio of Eu in MORB at magmatic conditions

and that preserved in a glass at room temperature can be explained by a transfer of electrons between Fe and Eu during cooling: $Fe^{3+} + Eu^{2+} = Fe^{2+} + Eu^{3+}$. Such a reaction also explains why a better fit to the glass data is found when *n* is unconstrained. The unexpectedly high rate of change of peak height as a function of logfO_2 and the different values of log*K*' for glass and melt are evident in Fig. 5b. In contrast to the glasses, the *in situ* data are consistent with the thermodynamics of the redox reaction. The efficiency of the Eu^{2+}-Fe^{3+} interaction is determined by the concentrations of the two ions (Fig. 8), calculated using the concentrations of Eu and Fe given in Table 1, $Eu^{3+}/\sum Eu$ in the melt give by log*K*' = 2.05 and in the glass by log*K*' = 3.12 (*n* = 1.29), and $Fe^{3+}/\sum Fe$ in the melt given by log*K*' = 0.721 (calculated from data in Berry et al., 2008). At low fO_2s $Eu^{2+}_{(melt)} = Eu^{2+}_{(glass)}$ since $Fe^{3+}/\sum Fe = 0$. As Fe^{3+} increases, the difference between Eu^{2+} in the melt and glass (ΔEu^{2+}) increases, reaching a maximum at log$fO_2 \sim -8$. If the charge transfer reaction went to completion we would expect no Eu^{2+} above log$fO_2 \sim -10$, where $Eu^{2+} = Fe^{3+}$. The fact that Eu^{2+} occurs in glasses where Fe^{3+} is in excess suggests that the difference in energy between the two configurations ($Eu^{2+} + Fe^{3+}$ and $Eu^{3+} + Fe^{2+}$) is small. A similar charge transfer reaction has been observed in melts containing Cr and Fe where the reaction $Cr^{2+} + Fe^{3+} = Cr^{3+} + Fe^{2+}$ occurs on cooling such that Cr^{2+} does not exist in any glass with significant concentrations of Fe^{3+} (Berry et al., 2003). Ce also undergoes a charge transfer reaction with Fe, $Ce^{4+} + Fe^{2+} = Ce^{3+} + Fe^{3+}$ (Schreiber et al., 1980; Burnham and Berry, 2014). When two redox-variable elements occur in a melt temperature dependent exchange reactions arise from differences in the relative values of log*K*' for each redox reaction (Schreiber et al., 1978) and, presumably, a Boltzmann population of the two states. The differences between the relative values of log*K*' may also change with temperature if there is a change in the coordination environment of one of the species. Ce and Eu do not interact in the present study because the extent to which Eu^{2+} and Ce^{4+} coexist is so low that no detectable charge transfer would be expected (Schreiber et al., 1980; Burnham and Berry, 2012; Burnham and Berry, 2014.). Ti occurs at concentrations of several wt% in many natural systems and for conditions below the IW buffer where Ti^{3+} is stable (Schreiber, 1977), the possibility of charge transfer reactions with Ti must also be considered (Sutton et al., 2005).

Temperature

At a given value of fO_2 Eu^{3+} is favoured at lower temperatures (Fig. 5c). The temperature dependencies of log*K*' for the AD and MORB compositions are shown in Fig. 9a. The slopes of the fits to the data are the same within error: $6850(300)/K^{-1}$ for AD (glass and *in situ* combined) and $6480(160)/K^{-1}$ for MORB (*in situ*). The slope indicates that an increase in temperature of 100 °C (at constant fO_2) has the same effect on $Eu^{3+}/\sum Eu$ as an increase in fO_2 of 1 log unit. However, natural systems do not exist at constant absolute values of fO_2 but at approximately constant values relative to mineral assemblages such as QFM. The fO_2 is defined by the oxidation state ratio of the most abundant redox variable element (usually Fe), which will control the redox state of trace elements. The fO_2 at which $Eu^{3+}/\sum Eu = 0.5$ as a function of temperature was determined for AD and MORB using Equation 1 and the fits in Fig. 9a, and is shown in Fig. 9b. This demonstrates that the fO_2 required to maintain $Eu^{3+}/\sum Eu = 0.5$ in these melts has an almost constant offset from IW and QFM, which implies that the oxidation state of Eu will be independent of temperature when either of these assemblages buffers the system. This result is consistent with the average dependence of log*K*' on temperature for Fe^{3+}/Fe^{2+} of $6460/K^{-1}$ determined from the data of Kress of Carmichael (1991). (Of course, these melt compositions are not liquid over the entire temperature range illustrated, but the extrapolation demonstrates the principle, which is expected to apply to any melt composition.)

General expression for $Eu^{3+}/\Sigma Eu$

Combining the observed temperature and compositional dependencies of logK' allows $Eu^{3+}/\Sigma Eu$ to be predicted for any melt composition, temperature and fO_2. The relationships determined in the present study,

$$\log K' = 6670/T + 14.0\Lambda - 10.1 \quad (5a)$$

$$Eu^{3+}/\sum Eu = \frac{1}{1+10^{-0.25\log fO_2 - \frac{6670}{T} - 14.0\Lambda + 10.1}} \quad (5b)$$

and

$$\log K' = 6670/T + 1.1NBO/T - 2.6 \quad (6a)$$

$$Eu^{3+}/\sum Eu = \frac{1}{1+10^{-0.25\log fO_2 - \frac{6670}{T} - 1.1NBO/T + 2.6}} \quad (6b)$$

where T is in K, reproduce the experimental values of $Eu^{3+}/\Sigma Eu$ (except for MORB glass) with an average deviation of 0.04 (Equation 5b) and 0.05 (Equation 6b). This deviation is larger than the uncertainty of the measurements and suggests that Λ and NBO/T may not perfectly describe the melt. It should be noted that a study of 21 compositions (Morris et al., 1974b, excluding the two compositions in the system anorthite-forsterite, for which the data are inconsistently reported) suggested that neither optical basicity nor NBO/T allows logK' to be predicted within the uncertainty of the measurements. Fig. 7 demonstrates that the compositional dependence varies between different binary mixing lines. Thus, while a general correlation is discernible, the data scatter considerably about the best fit line. These uncertainties must be borne in mind when extrapolating to melt compositions not studied (e.g. alkali-rich magmas). Therefore, Equations 5 and 6 should be used with caution until further work is carried out to test the compositional dependence further.

Comparison to previous work

The data presented represent the most well determined values of logK' available, owing to the large number of fO_2 values investigated for each composition. The data are exceedingly well fit by the thermodynamically expected sigmoidal function. The same cannot always be said for data found in the literature, and without this valuable check on data quality it is difficult to assess their reliability. Of spectroscopic measurements, the data of Schreiber are well-constrained by seven data points over a wide fO_2 range; those of Morris et al. (1974a, 1974b) are mostly values of $Eu^{3+}/\Sigma Eu$ at single fO_2s. Cicconi et al. (2012) studied three Fe-free compositions at multiple fO_2s, but the data are fit poorly using Equation 1 and the limited number of fO_2s per composition (three or four) makes it difficult to identify outliers. The values of logK' for AD at 1400 °C are 2.46(2) and 2.87(6) when excluding the samples prepared at IW-2 and IW respectively; the former is in reasonable agreement with the present study. Some partitioning data (Aigner-Torres et al., 2007; Blundy, 1997; Burnham and Berry, 2012; McKay et al., 1994; Sun et al., 1974) can be fit using Equation 2 by selecting reasonable approximations to $D_{Eu^{2+}}$ and $D_{Eu^{3+}}$ (e.g. D_{Sr} and D_{Gd} respectively) as a and $a+c$. As these partitioning data are derived from measurements of three elements in minerals and glass, a large number of potential sources of errors are involved. The Eu partitioning data of Wilke and Behrens (1999) can be fit to a sigmoid without recourse to estimates of $D_{Eu^{2+}}$ and $D_{Eu^{3+}}$.

Previous data relating to the effect of temperature are scarce; despite the limited temperature range studied by Schreiber (1977), 1500 – 1550 °C, and the large uncertainties in the data of Morris et al. (1974a, 1974b), whose diopside glass data scatter considerably as a function of 1/T, the data presented in the present study are consistent with previous observation, albeit with higher precision.

Expanding this test to include the samples studied in the EPR spectroscopic studies of Morris et al (1974a, 1974b) and Schreiber (1977), the average deviation is worse, with average deviations of the predicted log$K$' from the observed value of 0.26 (Equation 5a) and 0.38 (Equation 6a). If the Eu anomaly of a mineral were to be used to calculate its fO_2 of crystallisation, the former would result in a misdetermination by 1 log unit on average. Consideration of partitioning data experiments (Aigner-Torres et al., 2007; Blundy, 1997; McKay et al., 1994; Sun et al., 1974; Wilke and Behrens, 1999) similarly shows mixed success. In these studies, if $Eu^{3+}/\sum Eu$ was not stated it could be calculated as the proportion required to weight the averages of D_{Sr} (a proxy for Eu^{2+}) and D_{Gd} (a proxy for Eu^{3+}) to give the observed values of D_{Eu}; $Eu^{3+}/\sum Eu$ estimated in this way was then converted into a value of log$K$' using Equation 1. Equation 5a reproduced the log$K$' of Blundy (1997) within 0.15, the 1180 °C and 1220 °C data of Aigner-Torres within 0.05 and the 750 °C and 850 °C data of Wilke and Behrens (1999) within 0.26 on average (considered acceptable given the large extrapolation from the conditions of the present study). However, the log$K$' of McKay et al (1994) and Sun et al. (1974) differ by 0.91 and 0.46 from the calculated values. The reliability of the literature data is not known. Inter-laboratory differences between the temperature- and fO_2-calibrations of the furnaces used, and systematic analytical errors may explain some of the discrepant literature data, but it seems possible that the role of melt composition may not be as simple as the relationship observed in the present study.

An equation based solely on the data for MORB *in situ* is

$$Eu^{3+}/\sum Eu \text{ in MORB} = \frac{1}{1+10^{-0.25\log fO_2 - \frac{6480}{T} + 1.82}} \quad (7)$$

The mean deviation between the values predicted using this equation and those determined experimentally is 0.01, for all fO_2s and temperatures. The equation should predict $Eu^{3+}/\sum Eu$ in natural basalts with a high degree of accuracy given the small compositional differences between a typical basalt and the composition used in this study and the temperature range of the calibration.

Conclusions

The widespread occurrence of Eu anomalies in minerals and rocks is generally regarded as evidence of Eu depletion due to the uptake and removal of Eu^{2+} by plagioclase fractionation, however, the anomalies could also arise from variable $Eu^{3+}/\sum Eu$ (thus reducing the activity of Eu^{3+} relative to the other REE^{3+}) and thus may record the fO_2. This paper presents quantitative results that describe the dependence of $Eu^{3+}/\sum Eu$ on fO_2, temperature and melt composition, which will aid the interpretation of Eu/Eu* in igneous rocks. $Eu^{3+}/\sum Eu$ shows the expected sigmoidal dependence on logfO_2, and has a similar temperature dependence to $Fe^{3+}/\sum Fe$, which as a major element should control the redox state of the crystallising magma. Melt composition can be parameterised by optical basicity (Duffy, 1993) or NBO/T (Mills, 1993) and affects $Eu^{3+}/\sum Eu$ strongly, although neither parameterisation is a perfect descriptor and further work is required. Pressure was not investigated in the present study but by analogy to Ce (Burnham and Berry, 2014) is unlikely to be of significance at crustal pressures. The change in $Eu^{3+}/\sum Eu$ during the quench of Fe-bearing melts means that spectroscopic examination of glasses containing Fe^{3+} at greater than or similar concentrations to Eu^{2+} will give an incorrect estimate of the Eu oxidation state ratio, which cannot be linked to Eu/Eu* of a glass or mineral.

For volcanic rocks, matrix glass and melt inclusions can be used to determine mineral/melt partition coefficients for Eu, Gd and Sr, from which $Eu^{3+}/\sum Eu$ can be estimated. The major element composition of the glass can be used to predict log$K$' as a function of temperature (Equation 5a). Because the Eu^{3+}/Eu^{2+} equilibrium has a similar temperature dependence to

the QFM buffer, the estimated $Eu^{3+}/\sum Eu$ can be combined with the predicted log$K$' to give the fO_2 relative to QFM without relying on an estimate of the temperature of crystallisation. This has considerable potential as an oxybarometer; previous studies have typically relied on experimentally reproducing a particular mineral/melt combination, which is a time-consuming approach that is only applicable to a limited range of samples/conditions (e.g. McKay et al., 1994; Wadhwa, 2001; Shearer et al., 2006; Karner et al., 2010; Burnham and Berry 2012). In plutonic rocks, although melt composition is less well constrained, the sequential saturation of the melt in a range of accessory minerals that readily incorporate the REE could provide information about fO_2 changes in the later stages of crystallisation. In zircon, fO_2 is also recorded by the Ce anomaly (Hoskin and Schaltegger, 2003; Burnham and Berry, 2012); the fO_2 at which a zircon grew could be used to predict $D_{Eu}^{zircon/melt}$ and hence the Eu anomaly of the magma calculated, which in turn could be used to identify the extent of plagioclase fractionation. This would discriminate between zircons from highly reduced magmas and those whose Eu anomalies are inherited from the REE pattern of their parental magma; such information could prove useful when applied to Hadean zircon populations, as there is considerable speculation about when oxidation occurred in Earth's history (Kasting et al., 1993; Berry et al., 2008).

Acknowledgements:

Beamtime awards SP3771, SP6300, SP7452 and NT5576 (DLS) and EC-657 (ESRF) are gratefully acknowledged. We thank Hugh O'Neill and Jonathan Paul for their help with collecting some of the XANES spectra, and John Spratt for assistance with the electron probe analyses. A.D.B. thanks Imperial College London for the award of a Janet Watson Scholarship and A.J.B thanks the Australian Research Council for the award of a Future Fellowship.

References

Aigner-Torres, M., Blundy, J., Ulmer, P., Pettke, T., 2007. Laser ablation ICPMS study of trace element partitioning between plagioclase and basaltic melts: an experimental approach. Contrib. Mineral. Petrol. 153, 647-667.

Antonio, M.R., Soderholm, L., Song, I., 1997. Design of spectroelectrochemical cell for in situ X-ray absorption fine structure measurements of bulk solution species. J. Appl. Electrochem. 27, 784-792.

Berry, A.J., Danyushevsky, L.V., O'Neill, H.St C., Newville, M., Sutton, S.R., 2008. Oxidation state of iron in komatiitic melt inclusions indicates hot Archaean mantle. Nature 455, 960-963.

Berry, A.J., O'Neill, H.St C., 2004. A XANES determination of the oxidation state of chromium in silicate glasses. Am. Mineral. 89, 790-798.

Berry, A.J., O'Neill, H.St C., Scott, D.R., Foran, G.J., Shelley, J.M.G., 2006. The effect of composition on Cr^{2+}/Cr^{3+} in silicate melts. Am. Mineral. 91, 1901-1908.

Berry, A.J., Shelley, J.M.G., Foran, G.J., O'Neill, H.St C., Scott, D.R., 2003. A furnace design for XANES spectroscopy of silicate melts under controlled oxygen fugacities and temperatures to 1773 K. J. Synchrotron Radiat. 10, 332-336.

Blundy, J., 1997. Experimental study of a Kiglapait marginal rock and implications for trace element partitioning in layered intrusions. Chem. Geol. 141, 73-92.

Brophy, J.G., Basu, A., 1990. Europium anomalies in mare basalts as a consequence of mafic cumulate fractionation from an initial lunar magma. Proc. 20th Lunar Planet. Sci. Conf. 25-30.

Burnham, A.D., Berry, A.J., 2012. An experimental study of trace element partitioning between zircon and melt as a function of oxygen fugacity. Geochim. Cosmochim. Acta 95, 196-212.

Burnham, A.D., Berry, A.J., 2014. The effect of oxygen fugacity, melt composition, temperature and pressure on the oxidation state of cerium in silicate melts. Chem. Geol. 366, 52-60.

Cicconi, M.R., Giuli, G., Paris, E., Ertel-Ingrisch, W., Ulmer, P., Dingwell, D.B., 2012. Europium oxidation state and local structure in silicate glasses. Am. Mineral. 97, 918-929.

Dent, A.J., Cibin, G., Ramos, S., Smith, A.D., Scott, S.M., Varandas, L., Pearson, M.R., Krumpa, N.A., Jones, C.P., Robbins, P.E., 2009. B18: A core XAS spectroscopy beamline for Diamond. J. Phys.: Conference Series 190, 012039.

Drake, M.J., 1975. The oxidation state of europium as an indicator of oxygen fugacity. Geochim. Cosmochim. Acta 39, 55-64.

Duffy, J.A., 1993. A review of optical basicity and its applications to oxidic systems. Geochim. Cosmochim. Acta 57, 3961-3970.

Eby, G.N., 1975. Abundance and distribution of the rare-earth elements and yttrium in the rocks and minerals of the Oka carbonatite complex, Quebec. Geochim. Cosmochim. Acta 39, 597-620.

Filipponi, A., Borowski, M., Bowron, D.T., Ansell, S., di Cicco, A., de Panfilis, S. & Itiè, J-P., 2000. An experimental station for advanced research on condensed matter under extreme conditions at the European Synchrotron Radiation Facility - BM29 beamline. Rev. Sci. Instrum. 71, 2422-2432.

Hoskin, P.W.O., Kinny, P.D., Wyborn, D., Chappell, B.W., 2000. Identifying accessory mineral saturation during differentiation in granitoid magmas: an integrated approach. J. Petrol. 41, 1365-1396.

Hoskin, P.W.O., Schaltegger, U., 2003. The composition of zircon and igenous and metamorphic petrogenesis, in: Hanchar, J.M., Hoskin, P.W.O. (Eds.), Reviews in Mineralogy and Geochemistry Volume 53: Zircon. Mineralogical Society of America, Washington, DC, pp. 27-62.

Karner, J.M., Papike, J.J., Sutton, S.R., Burger, P.V., Shearer, C.K., Le, L., Newville, M., Choi, Y., 2010. Partitioning of Eu between augite and a highly spiked martian basalt composition as a function of oxygen fugacity, IW-1 to QFM: determination of Eu^{2+}/Eu^{3+} ratios by XANES. Am. Mineral. 95, 410-413.

Kasting, J.F., Eggler, D.H., Raeburn, S.P., 1993. Mantle redox evolution and the oxidation state of the Archean atmosphere. J. Geol. 101, 245-257.

Krause, M.O., Oliver, J.H., 1979. Natural widths of atomic K and L levels, Kα X-ray lines and several KLL Auger lines. J. Phys. Chem. Ref. Data 8, 329-338.

Kress, V.C., Carmichael, I.S.E., 1991. The compressibility of silicate liquids containing Fe_2O_3 and the effect of composition, temperature, oxygen fugacity and pressure on their redox states. Contrib. Mineral. Petrol. 108, 82-92.

Lebouteiller, A., Courtine, P. (1998). Improvement of a bulk optical basicity table for oxidic systems. J. Solid State Chem. 137, 94-103.

Mayanovic, R.A., Anderson, A.J., Bassett, W.A., Chou, I-M., 2007. Synchrotron x-ray spectroscopy of Eu/HNO_3 aqueous solutions at high temperatures and pressures and Nb-bearing silicate melt phases coexisting with hydrothermal fluids using a modified hydrothermal diamond anvil cell and rail assembly. Rev. Sci. Instrum. 78, 053904.

McKay, G., Le, L., Wagstaff, J., Crozaz, G., 1994. Experimental partitioning of rare earth elements and strontium: constraints on petrogenesis and redox conditions during crystallization of Antarctic angrite Lewis Cliff 86010. Geochim. Cosmochim. Acta 58, 2911-2919.

Mills, K.C., 1993. The influence of structure on the physico-chemical properties of slags. ISIJ International 33, 148-155.

Morris, R.V., Haskin, L.A., Biggar, G.A., O'Hara, M.J., 1974a. Measurement of the effects of temperature and partial pressure of oxygen on the oxidation states of europium in silicate glasses. Geochim. Cosmochim. Acta 38, 1447-1459.

Morris, R.V., Haskin, L.A., NASA JSC, 1974b. EPR measurement of the effect of glass composition on the oxidation states of europium. Geochim. Cosmochim. Acta 38, 1435-1445.

Mosselmans J.F., Quinn P.D., Dent A.J., Cavill S.A., Moreno S.D., Peach A., Leicester P.J., Keylock S.J., Gregory S.R., Atkinson K.D., Rosell J.R., 2009. I18 – the microfocus spectroscopy beamline at the Diamond Light Source. J. Synchrotron Radiat. 16, 818-824.

Nemov, S.A., Marchenko, A.V., Seregin, S.S., Tomil'tsev, E.A., 2007. Europium(II) in glasses of the Al_2O_3-SiO_2-MnO-Eu_2O_3 system. Glass Phys. Chem. 33, 658-660.

O'Neill, H.St C., 1987. Quartz-fayalite-iron and quartz-fayalite-magnetite equilibria and the free energy of formation of fayalite (Fe_2SiO_4) and magnetite (Fe_3O_4). Am. Mineral. 72, 67-75.

O'Neill, H.St C., Berry, A.J., 2006. Activity coefficients at low dilution of CrO, NiO and CoO in melts in the system CaO–MgO–Al_2O_3–SiO_2 at 1400°C: Using the thermodynamic behaviour of transition metal oxides in silicate melts to probe their structure. Chem. Geol. 231, 77-89.

O'Neill, H.St C., Eggins, S.M., 2002. The effect of melt composition on trace element partitioning: an experimental investigation of the activity coefficients of FeO, NiO, CoO, MoO_2 and MoO_3 in silicate melts. Chem. Geol. 186, 151-181.

O'Neill, H.St C., Pownceby, M.I., 1993. Thermodynamic data from redox reactions at high temperatures. I. An experimental and theoretical assessment of the electrochemical method using stabilized zirconia electrolytes, with revised values for the Fe-"FeO", Co-CoO, Ni-NiO and Cu-Cu_2O oxygen buffers, and new data for the W-WO_2 buffer. Contrib. Mineral. Petrol. 114, 296-314.

Rakovan, J., Newville, M., Sutton, S., 2001. Evidence of heterovalent europium in zoned Llallagua apatite using wavelength dispersive XANES. Am. Mineral. 86, 697-700.

Schreiber, H.D., 1977. Redox states of Ti, Zr, Hf, Cr, and Eu in basaltic magmas: an experimental study. Proc. 8th Lunar Sci. Conf., 1785-1807.

Schreiber, H.D., Lauer, H.V., Thanyasiri, T., 1980. The redox state of cerium in basaltic magmas: an experimental study of iron-cerium interactions in silicate melts. Geochim. Cosmochim. Acta 44, 1599-1612.

Schreiber, H.D., Thanyasiri, T., Lach, J.J., Legere, R.A., 1978. Redox equilibria of Ti, Cr, and Eu in silicate melts: Reduction potentials and mutual interactions. Phys. Chem. Glasses 19, 126-139.

Shearer, C.K., Papike, J.J., Burger, P.V., Sutton, S.R., McCubbin, F.M., Newville, M., 2011. Direct determination of europium valence state by XANES in extraterrestrial merrillite: implications for REE crystal chemistry and martian magmatism. Am. Mineral. 96, 1418-1421.

Shearer, C.K., Papike, J.J., Karner, J.M., 2006. Pyroxene europium valence oxybarometer: effects of pyroxene composition, melt composition, and crystallization kinetics. Am. Mineral. 91, 1565-1573.

Shimizugawa, Y., Umesaki, N., Qiu, J., Hirao, K., 1999. Local structure around europium ions doped in borate glasses. J. Synchrotron Radiat. 6, 624-626.

Sun, C-O., Williams, R.J., Sun, S-S., 1974. Distribution coefficients of Eu and Sr for plagioclase-liquid and clinopyroxene-liquid equilibria in oceanic ridge basalt: an experimental study. Geochim. Cosmochim. Acta 38, 1415-1433.

Sutton, S.R., Karner, J., Papike, J., Delaney, J.S., Shearer, C., Newville, M., Eng, P., Rivers, M., Dyar, M.D., 2005. Vanadium K edge XANES of synthetic and natural basaltic glasses and application to microscale oxygen barometry. Geochim. Cosmochim. Acta 69, 2333-2348.

Takahashi, Y., Kolonin, G. R., Shironosova, G. P., Kupriyanova, I. I., Uruga, T., Shimizu, H., 2005. Determination of the Eu(II)/Eu(III) ratios in minerals by X-ray absorption near-edge structure (XANES) and its application to hydrothermal deposits. Mineral. Mag. 69, 179-190.

Trail, D., Watson, E.B., Tailby, N.D., 2012. Ce and Eu anomalies in zircon as proxies for the oxidation state of magmas. Geochim. Cosmochim. Acta 97, 70-87.

Virgo, D., Seifert, F., Mysen, B.O., 1981. The oxidation state of europium in albite and alkali-earth silicate glasses. Carnegie Inst. Wash. Yearb. 80, 313-316.

Wadhwa, M., 2001. Redox state of Mars' upper mantle and crust from Eu anomalies in shergottite pyroxenes. Science 291, 1527-1530.

Weill, D.F., McKay, G.A., 1975. The partitioning of Mg, Fe, Sr, Ce, Sm, Eu, and Yb in lunar igneous systems and a possible origin of KREEP by equilibrium partial melting. Proc. 6th Lunar Sci. Conf., 1143-1158.

Wilke, M., Behrens, H., 1999. The dependence of the partitioning of iron and europium between plagioclase and hydrous tonalitic melt on oxygen fugacity. Contrib. Mineral. Petrol. 137, 102-114.

Figure Captions

Fig. 1. Eu L_{III}-edge XANES spectra of a) AD glasses and b) MORB melt (in situ) equilibrated at 1400 °C and the logfO2 values indicated (QFM = -6.3). Spectra are offset for clarity. The dotted lines indicate peaks characteristic of Eu^{2+} (6974.2 eV) and Eu^{3+} (6982.4 eV).

Fig. 2. Heights of the Eu^{3+} peak at 6982.4 eV for glasses and in situ for AD (solid symbols) and MORB (open symbols). The line is the best fit to the AD data and has a gradient of ~0.9.

Fig. 3. Eu L_{III}-edge XANES spectra of a) AD and b) MORB melts recorded in situ at 1400 °C and the logfO_2 values indicated (solid lines) and glasses quenched from the same conditions (dashed lines). Pairs of spectra are offset for clarity. The dotted lines indicate peaks characteristic of Eu^{2+} (6974.2 eV) and Eu^{3+} (6982.4 eV).

Fig. 4. Fluorescence intensity as a function of time for AD glass prepared at 1400 °C and log fO_2 = -16. The first two peaks are for an excitation energy of 6974 eV (Eu^{2+}) and the second two are for an excitation energy of 6982 eV (Eu^{3+}). Each peak corresponds to a different position on the sample and the gaps between the peaks to periods when the shutter was closed. The insets are enlarged views of the first 55 s of the first and third segments.

Fig. 5. Heights of the Eu^{2+} (circles) and Eu^{3+} (squares) white line peaks as a function of fO_2 at 1400 °C for a) AD and b) MORB determined from glasses (solid symbols) and melts (open symbols). c) Peak heights for MORB melt at 1250 °C (grey symbols) and 1400 °C. The solid lines and dashed lines are the fits to Equation 2 with n = 1. The vertical dotted lines indicate the IW (logfO_2 = -9.7) and QFM (logfO_2 = -6.3) buffers at 1400 °C (O'Neill and Pownceby, 1993; O'Neill, 1987).

Fig. 6. $Eu^{3+}/\sum Eu$ as a function of fO_2 for selected glass compositions (AD – open squares; AD+wo – open circles; AD+qz – solid circles) and the corresponding fits to Equation 1. The precision, estimated from replicate measurements and the difference between values determined by the Eu^{2+} and Eu^{3+} peaks (Table 2) is ±0.015. The accuracy, estimated form the deviation of each point from the curve is ±0.020. The dotted lines indicate the IW and QFM buffers at 1400 °C.

Fig. 7. logK' as a function of a) NBO/T and b) optical basicity, at 1400 °C for MORB melt (open symbol), MORB glass (star) and other compositions (solid symbols). Small data points (grey) are from Schreiber (1977) and Morris et al. (1974a, 1974b), corrected using the temperature-dependence of the Eu^{2+}-Eu^{3+} equilibrium. The lines are the best fit to the data obtained in the present study (excluding MORB glass). The error in the independent variable is less than the size of the points.

Fig. 8. Concentrations (atomic ppm) of Eu^{2+} in MORB melt (solid line) and glass (dashed line), the difference between the two (dotted line) and the calculated concentration of Fe^{3+} in the melt (heavy line) as a function of fO_2 at 1400 °C. The dotted lines indicate the IW and QFM buffers at 1400 °C.

Fig. 9. a) logK' as a function of reciprocal temperature for AD (circles) and MORB (squares) determined from in situ melts (solid symbols) and quenched glasses (open symbols). The lines are the best fits to the data (combined glass and in situ data for AD; in situ data for MORB). Error bars are the same size as the data points. b) The fO_2 at which AD (dotted line) and MORB (dashed line) have $Eu^{3+}/\sum Eu = 0.5$ as a function of temperature, relative to the IW and QFM buffers (O'Neill and Pownceby, 1993; O'Neill, 1987).

Table 1. Glass compositions (wt % oxide) determined by EPMA, and melt parameterisations Λ (optical basicity, Duffy 1993; Lebouteiller and Courtine 1998) and NBO/T (Mills, 1993). Sample nomenclature follows Berry et al. (2006) with the addition of the Zr-glass; errors are 1 s.d.

	SiO_2	Al_2O_3	FeO[a]	MgO	CaO	Eu_2O_3	ZrO_2	Total	Λ	NBO/T
AD	51.21(39)	15.41(16)	-	10.41(12)	23.90(17)	0.61(5)	-	101.5(5)	0.604(4)	0.924(10)
AD+fo	48.62(15)	13.18(9)	-	16.49(5)	20.77(5)	0.49(2)	-	99.5(2)	0.610(2)	1.218(5)
AD+wo	49.95(10)	9.58(3)	-	6.55(3)	33.35(10)	0.63(2)	-	100.1(1)	0.625(1)	1.301(4)
AD+en	52.85(19)	10.85(3)	-	18.81(6)	17.17(7)	0.52(1)	-	100.2(2)	0.598(2)	1.220(5)
AD+qz	63.21(15)	11.11(5)	-	7.79(3)	17.18(6)	0.53(2)	-	99.8(2)	0.568(1)	0.615(3)
MORB	52.88(16)	12.32(6)	9.84(6)	7.85(3)	16.04(4)	0.53(2)	-	99.5(2)	0.597(2)	0.886(3)
CAS-4[b]	66.78(54)	19.98(25)	-	-	10.40(9)	0.55(2)	-	97.8(6)	0.536(4)	-0.014(4)
MAS-1[b]	60.30(39)	18.23(27)	-	20.04(15)	0.07(1)	0.65(2)	-	99.5(5)	0.551(3)	0.470(7)
Longhi1[b]	63.48(22)	7.20(5)	-	13.19(7)	16.12(9)	0.50(2)	-	100.6(3)	0.573(2)	0.909(5)
Longhi2[b]	50.41(33)	13.52(14)	-	5.25(5)	31.39(9)	0.56(1)	-	101.2(4)	0.617(3)	1.010(7)
Longhi5[b]	68.20(16)	16.64(9)	-	8.71(4)	5.52(4)	0.65(2)	-	99.8(2)	0.537(1)	0.207(2)
Osborn4[b]	46.05(28)	14.49(9)	-	10.47(7)	29.52(12)	0.61(1)	-	101.2(3)	0.627(3)	1.226(8)
Zr-glass	52.23(25)	12.79(12)	-	8.94(7)	19.50(11)	0.51(2)	6.34(8)	100.3(3)	0.589(3)	0.758(6)[c]

'-' below detection limits or not analysed.

[a] All Fe expressed as FeO and treated as such for calculation of Λ and NBO/T .

[b] Compositions contain 0.1(1) wt% Na_2O.

[c]Zr treated as a network former.

Table 2. Intensities (heights) of the Eu^{2+} (6974.2 eV) and Eu^{3+} (6982.4 eV) peaks in the Eu L_{III}-edge XANES spectra of all samples (1σ determined from replicate measurements, where available) and $Eu^{3+}/\sum Eu$ corresponding to each peak height evaluated using Equations (1) and (2) and the best fit coefficients reported in Table 3. Where the coefficients could not be evaluated: the average values of the other Fe-free compositions were used for Longhi1 and Zr-glass, the average of the AD melt values at 1300 and 1400 °C for AD melt at 1350 and 1450 °C, and the average of the MORB melt values at 1250 and 1400 °C for MORB melts at 1350 and 1450 °C. The average difference between the two calculated values of $Eu^{3+}/\sum Eu$ is 0.02(2). The error associated with $Eu^{3+}/\sum Eu$ arising from the fit to Equation 2 is ±0.02 for both peaks. The logfO_2 of QFM (the quartz-fayalite-magnetite buffer) is -7.3 at 1300 °C, -6.3 at 1400 °C, and -5.4 at 1500 °C (O'Neill, 1987).

			Peak Height		$Eu^{3+}/\sum Eu$	
Composition	Temp (°C)	logfO_2	Eu^{2+}	Eu^{3+}	Eu^{2+} peak	Eu^{3+} peak
Glasses						
AD	1300	0.0	0.55	2.88	1.00	1.00
		-7.1	0.82	2.66	0.87	0.88
		-10.1	1.41	2.13	0.57	0.59
		-12.0	1.96	1.62	0.30	0.31
		-13.1	2.18	1.43	0.19	0.20
AD	1400	0.0	0.52(1)	2.90(1)	1.00(0)	0.99(0)
		-2.0	0.56	2.85	0.98	0.97
		-3.1	0.57	2.85	0.97	0.97
		-4.0	0.55	2.87	0.98	0.98
		-6.0	0.77	2.70	0.87	0.89
		-7.0	0.91(1)	2.58(5)	0.81(0)	0.82(3)
		-8.0	1.10	2.39	0.71	0.72
		-9.0	1.37	2.19	0.58	0.60
		-9.5	1.78	1.80	0.37	0.39
		-10.0	1.57(15)	1.94(11)	0.48(7)	0.47(6)
		-10.5	1.83	1.73	0.35	0.36
		-11.0	1.97	1.62	0.28	0.30
		-12.0	2.15	1.46	0.19	0.21
		-13.0	2.36	1.25	0.09	0.10
		-14.0	2.45(1)	1.17(1)	0.04(1)	0.05(1)
		-16.1	2.41(8)	1.18(8)	0.03(4)	0.02(4)

		-18.0	2.49	1.13	0.02	0.03
		-20.0	2.49	1.12	0.02	0.02
AD	1500	0.0	0.52	2.89	0.97	0.97
		-5.0	0.65	2.80	0.91	0.93
		-8.0	1.39	2.12	0.56	0.60
		-11.0	2.14	1.34	0.20	0.22
AD+fo	1400	-4.0	0.54	2.87	0.94	0.94
		-7.0	0.69	2.71	0.87	0.86
		-9.0	1.29	2.20	0.59	0.59
		-10.0	1.51	2.05	0.49	0.51
		-12.0	2.17	1.43	0.18	0.19
		-14.0	2.41	1.19	0.07	0.06
		-18.0	2.54	1.09	0.01	0.01
		-20.0	2.51(5)	1.11(0)	0.02(2)	0.02(0)
AD+wo	1400	0.0	0.47(1)	2.91(2)	1.01(0)	1.01(1)
		-2.0	0.50	2.86	0.99	0.98
		-3.1	0.53	2.84	0.98	0.97
		-4.0	0.49	2.88	1.00	0.99
		-5.0	0.58	2.79	0.95	0.94
		-6.0	0.63	2.74	0.93	0.91
		-7.0	0.85	2.62	0.82	0.85
		-8.0	0.84	2.58	0.82	0.82
		-9.0	1.03	2.42	0.72	0.73
		-9.5	1.15	2.30	0.66	0.67
		-10.0	1.27	2.16	0.60	0.59
		-10.5	1.44	2.04	0.52	0.52
		-11.0	1.60	1.88	0.43	0.43
		-12.0	1.88	1.59	0.29	0.27
		-13.0	2.16	1.37	0.15	0.14
		-16.1	2.42	1.14	0.02	0.02
		-18.0	2.37	1.20	0.04	0.05
		-20.0	2.42	1.14	0.02	0.02
AD+en	1400	-4.0	0.50	2.92	0.95	0.96
		-7.0	0.84	2.60	0.80	0.79
		-9.0	1.39	2.15	0.55	0.56
		-10.0	1.69	1.87	0.41	0.42
		-12.0	2.18	1.42	0.19	0.19
		-13.0	2.42	1.19	0.08	0.07
		-14.0	2.42	1.20	0.08	0.08
		-18.0	2.56	1.08	0.01	0.02
AD+qz	1400	0.0	0.53	2.84	0.99	0.98
		-3.1	0.62	2.78	0.94	0.95
		-4.0	0.55	2.83	0.98	0.97
		-5.0	0.77	2.63	0.87	0.87
		-6.0	0.91	2.51	0.81	0.80
		-7.0	1.14	2.34	0.70	0.71

		-8.0	1.40	2.10	0.58	0.58
		-9.0	1.69(1)	1.87(2)	0.44(1)	0.45(1)
		-9.5	1.85	1.73	0.36	0.37
		-10.0	1.98	1.60	0.30	0.30
		-10.5	2.10	1.51	0.25	0.25
		-11.0	2.21	1.40	0.19	0.19
		-12.0	2.37	1.26	0.12	0.12
		-13.0	2.53	1.10	0.04	0.03
		-16.1	2.61	1.06	0.00	0.01
		-18.0	2.60	1.08	0.01	0.02
		-20.0	2.57	1.08	0.02	0.02
MORB	1400	0.0	0.31	3.02	0.99	0.99
		-2.0	0.34	3.00	0.99	0.98
		-3.1	0.32	2.97	0.99	0.97
		-4.0	0.31	3.02	0.99	0.99
		-5.0	0.44	2.98	0.96	0.97
		-6.0	0.50	2.90	0.94	0.94
		-7.0	0.63	2.71	0.90	0.87
		-8.0	0.89	2.58	0.83	0.82
		-9.0	1.29	2.15	0.72	0.67
		-10.0	1.74	1.79	0.60	0.53
		-11.0	2.20	1.47	0.47	0.41
CAS-4	1400	-3.1	1.10	2.43	0.69	0.76
		-9.0	2.57	1.22	-0.01	0.09
		-13.0	2.59	1.02	-0.02	-0.02
		-16.1	2.63	1.11	-0.04	0.03
MAS-1	1400	-3.1	0.73	2.73	0.86	0.85
		-9.0	2.24	1.41	0.16	0.17
		-13.0	2.60	1.02	-0.01	-0.04
		-16.1	2.53	1.22	0.02	0.06
Longhi1	1400	-3.1	0.59	2.82	0.94	0.95
		-9.0	1.42	1.84	0.55	0.43
Longhi2	1400	-3.1	0.54	2.84	0.98	0.99
		-9.0	1.12	2.30	0.68	0.70
		-13.0	2.20	1.36	0.13	0.20
		-16.1	2.34	1.06	0.06	0.04
Longhi5	1400	-3.1	0.86	2.60	0.81	0.86
		-9.0	2.45	1.30	0.12	0.16
		-13.0	2.66	1.03	0.03	0.02
		-16.1	2.74	1.01	-0.01	0.00
Osborn4	1400	-3.1	0.50	2.87	0.98	0.98
		-9.0	1.09	2.36	0.68	0.71
		-13.0	2.21	1.36	0.12	0.17
		-16.1	2.32	1.12	0.07	0.05
Zr-glass	1400	0.0	0.52	2.85	0.97	0.97
		-9.0	1.60	1.93	0.46	0.48

Melts						
AD	1300	-3.4	0.33	3.01	0.98	0.99
		-9.1	1.01	2.44	0.71	0.73
		-12.1	2.01	1.54	0.30	0.32
	1350	-11.5	1.99	1.56	0.30	0.31
	1400	-3.1	0.38	2.95	0.98	0.98
		-4.0	0.48	2.86	0.94	0.93
		-5.0	0.48	2.86	0.94	0.93
		-6.0	0.57	2.8	0.90	0.90
		-7.0	0.73	2.64	0.83	0.82
		-8.0	0.99	2.46	0.72	0.73
		-9.0	1.3	2.14	0.59	0.58
		-10.0	1.64	1.85	0.44	0.43
		-11.0	1.95	1.58	0.31	0.29
		-12.0	2.16	1.41	0.22	0.21
	1450	-10.5	1.94	1.58	0.32	0.32
MORB	1250	-3.6	0.40(1)	2.87(8)	0.95(1)	0.95(4)
		-5.7	0.50(6)	2.77(11)	0.91(2)	0.90(5)
		-6.7	0.53(4)	2.75(9)	0.90(2)	0.89(4)
		-7.7	0.83	2.46	0.78	0.75
		-8.7	1.14	2.18	0.65	0.62
		-9.7	1.52(1)	1.95(3)	0.50(1)	0.50(1)
		-10.7	1.87(2)	1.64(2)	0.37(1)	0.35(1)
		-11.7	2.15(4)	1.40(1)	0.26(1)	0.24(1)
		-12.7	2.33(2)	1.22(1)	0.18(1)	0.15(1)
	1300	-11.1	2.14	1.43	0.25	0.25
	1350	-3.2	0.42	2.91	0.95	0.97
		-10.5	2.12	1.45	0.26	0.26
	1400	-3.1	0.44(2)	2.83(7)	0.94	0.93
		-4.0	0.47	2.86	0.93	0.95
		-5.0	0.65	2.7	0.86	0.87
		-6.0	0.81	2.57	0.80	0.80
		-7.0	1.07	2.21	0.69	0.63
		-8.0	1.48	2.02	0.52	0.53
		-9.0	1.82	1.71	0.38	0.38
		-10.0	2.07	1.47	0.28	0.26
		-11.0	2.31	1.27	0.18	0.16
	1450	-2.9	0.46	2.87	0.93	0.95
		-9.5	2.07	1.47	0.28	0.27

Table 3. Coefficients obtained from fitting the heights of the Eu^{2+} and Eu^{3} peaks in the XANES spectra of samples prepared over a range of fO_2s (at 1400 °C unless indicated) to Equation 2 with $n = 1$.

	a	*c*	log*K'*
Glasses			
AD (1300)			
Eu^{2+} peak	-2.00(5)	2.56(5)	2.63(4)
Eu^{3+} peak	1.81(4)	1.07(4)	2.66(4)
AD			
Eu^{2+} peak	-2.03(4)	2.54(4)	2.37(3)
Eu^{3+} peak	1.83(3)	1.08(2)	2.37(3)
AD (1500)			
Eu^{2+} peak	-2.09(22)	2.56(23)	2.13(14)
Eu^{3+} peak	2.06(13)	0.89(14)	2.19(11)
AD+fo			
Eu^{2+} peak	-2.14(6)	2.55(4)	2.45(5)
Eu^{3+} peak	1.90(7)	1.08(2)	2.44(5)
AD+wo			
Eu^{2+} peak	-1.97(4)	2.46(4)	2.64(3)
Eu^{3+} peak	1.78(3)	1.11(2)	2.63(3)
AD+en			
Eu^{2+} peak	-2.19(3)	2.59(2)	2.34(2)
Eu^{3+} peak	1.96(6)	1.05(3)	2.35(5)
AD+qz			
Eu^{2+} peak	-2.12(3)	2.62(2)	2.13(2)
Eu^{3+} peak	1.83(3)	1.04(1)	2.15(2)
MORB			
Eu^{2+} peak	-3.59(24)	3.87(24)	2.68(5)
Eu^{3+} peak	2.71(21)	0.35(22)	2.58(7)
CAS-4			
Eu^{2+} peak	-	-	-
Eu^{3+} peak	1.81(41)	1.05(6)	1.25(39)
MAS-1			
Eu^{2+} peak	-2.17(10)	2.59(5)	1.53(15)
Eu^{3+} peak	1.91(42)	1.10(12)	1.52(46)
Longhi2			
Eu^{2+} peak	-1.96(11)	2.46(9)	2.56(10)
Eu^{3+} peak	1.87(2)	0.99(2)	2.62(2)

Longhi5			
Eu^{2+} peak	-2.30(9)	2.72(3)	1.38(10)
Eu^{3+} peak	1.86(0)	1.00(0)	1.54(0)
Osborn4			
Eu^{2+} peak	-1.99(13)	2.45(11)	2.56(12)
Eu^{3+} peak	1.87(5)	1.03(3)	2.61(6)
Melts			
AD (1300)			
Eu^{2+} peak	-2.46	2.76	2.66
Eu^{3+} peak	2.20	0.83	2.70
AD			
Eu^{2+} peak	-2.32(7)	2.66(7)	2.41(4)
Eu^{3+} peak	2.01(5)	0.99(5)	2.39(4)
MORB (1250)			
Eu^{2+} peak	-2.53(9)	2.80(10)	2.47(5)
Eu^{3+} peak	2.08(5)	0.90(6)	2.43(5)
MORB			
Eu^{2+} peak	-2.43(6)	2.74(7)	2.06(4)
Eu^{3+} peak	2.02(6)	0.95(7)	2.04(6)

"-" fit poorly constrained

Table 4. log*K*' for the oxidation of Eu in each composition and at various temperatures (average of values from each peak height). All values are for 1400 °C except where indicated; values derived from *in situ* measurements are denoted by asterisks. Uncertainties (1σ precision) were determined from the fit to the data using Equation 2 (in three cases the sigmoids were only constrained by a single value and consequently the precision cannot be assessed).

Composition	log*K*'
AD (1300)	2.64(1)
AD (1300)*	2.68
AD (1350)*	2.51
AD	2.36(2)
AD*	2.40(1)
AD (1450)*	2.30
AD (1500)	2.16(3)
AD+fo	2.45(3)
AD+wo	2.64(2)
AD+en	2.34(2)
AD+qz	2.14(1)
MORB(1250)*	2.45(2)
MORB(1300)*	2.30
MORB(1350)*	2.17(0)
MORB	2.63(1)
MORB*	2.05(1)
MORB(1450)*	1.95(1)
CAS-4	1.15(5)
MAS-1	1.52(8)
Longhi1	2.22(4)
Longhi2	2.59(2)
Longhi5	1.46(1)
Osborn4	2.58(4)
Zr-glass	2.19(4)

Figure 1

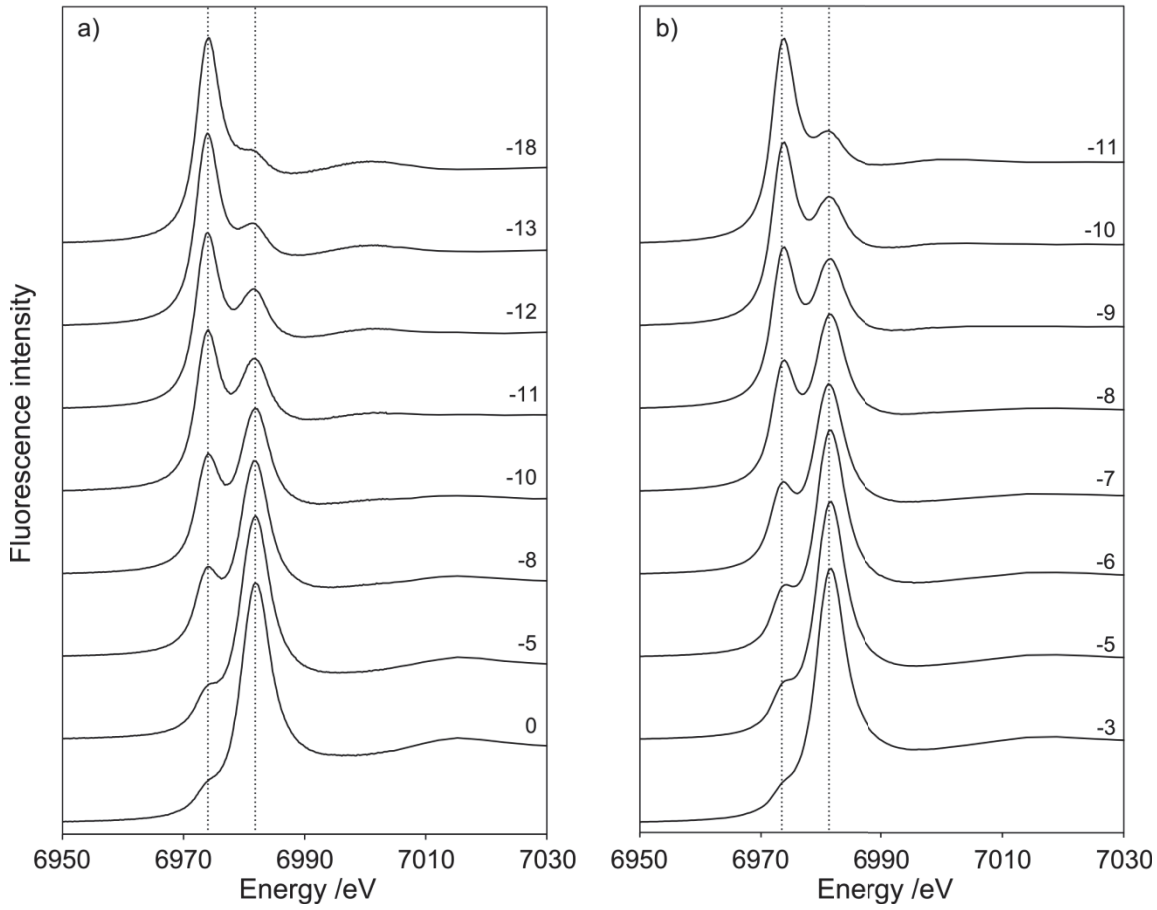


Figure 2

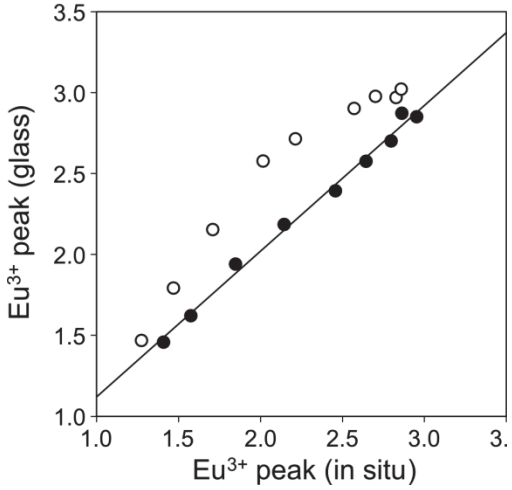


Figure 3

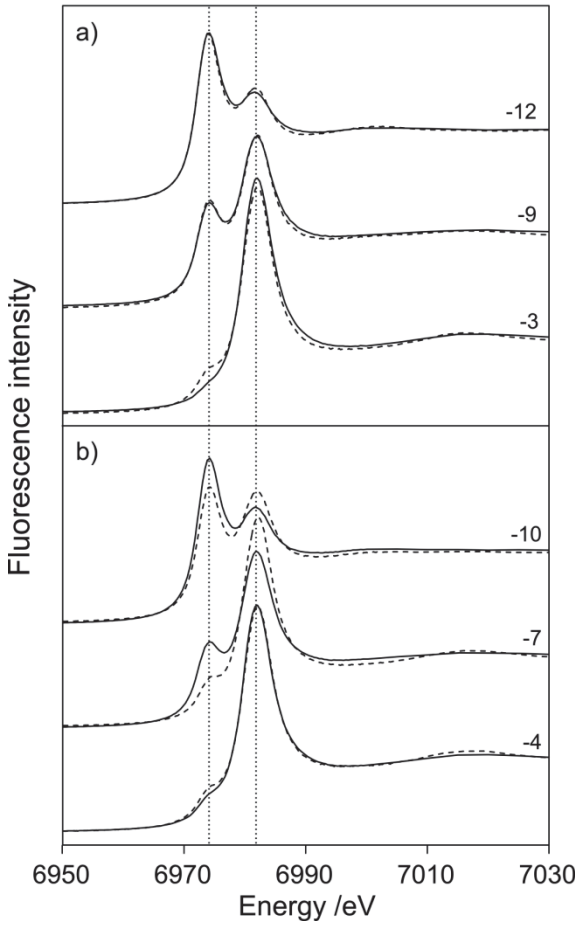


Figure 4

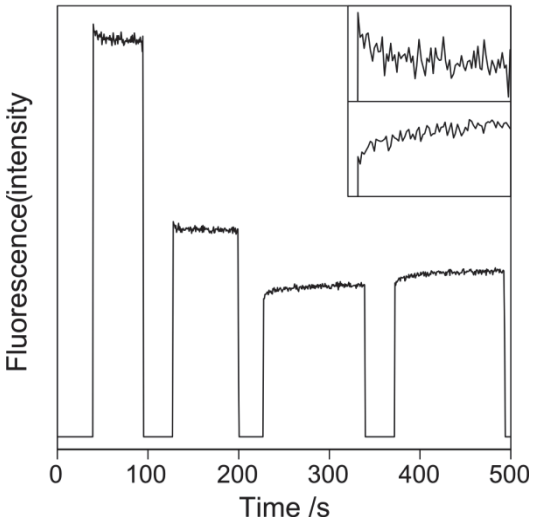


Figure 5

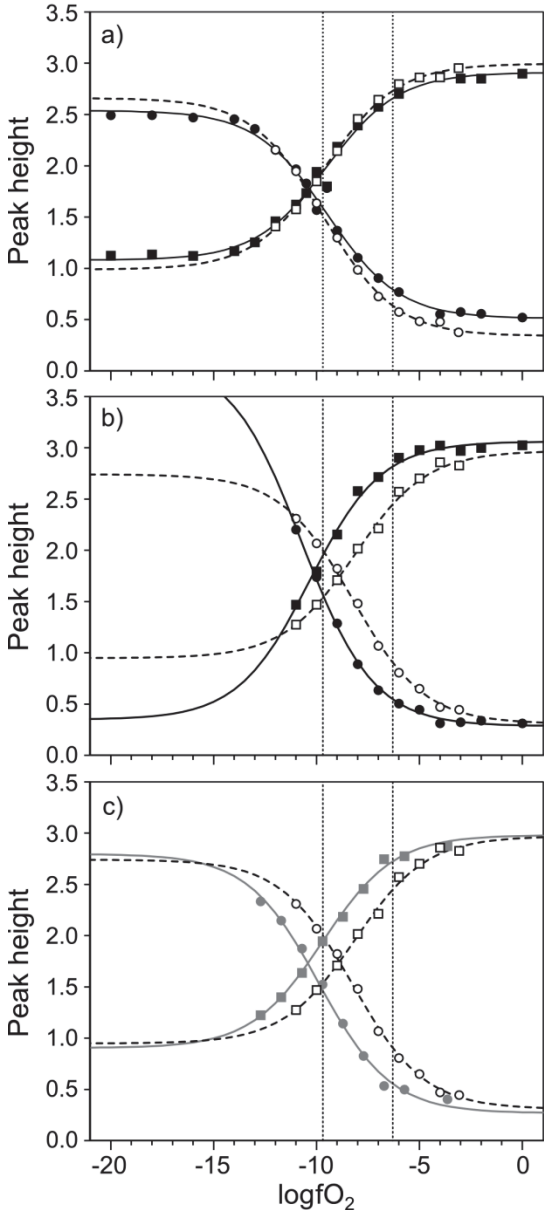

a)
b)
c)
Peak height
Peak height
Peak height
3.5
3.0
2.5
2.0
1.5
1.0
0.5
0.0
-20
-15
-10
-5
0
logfO2

Figure 6

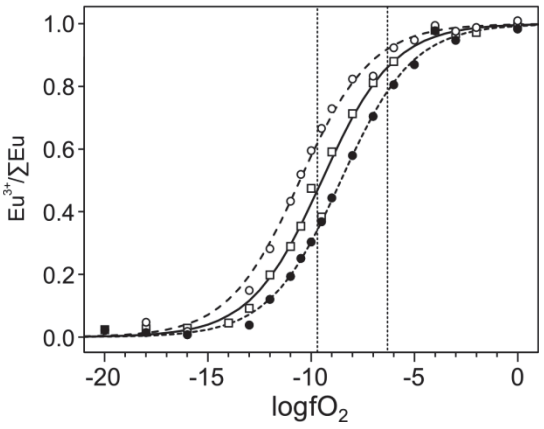


Figure 7

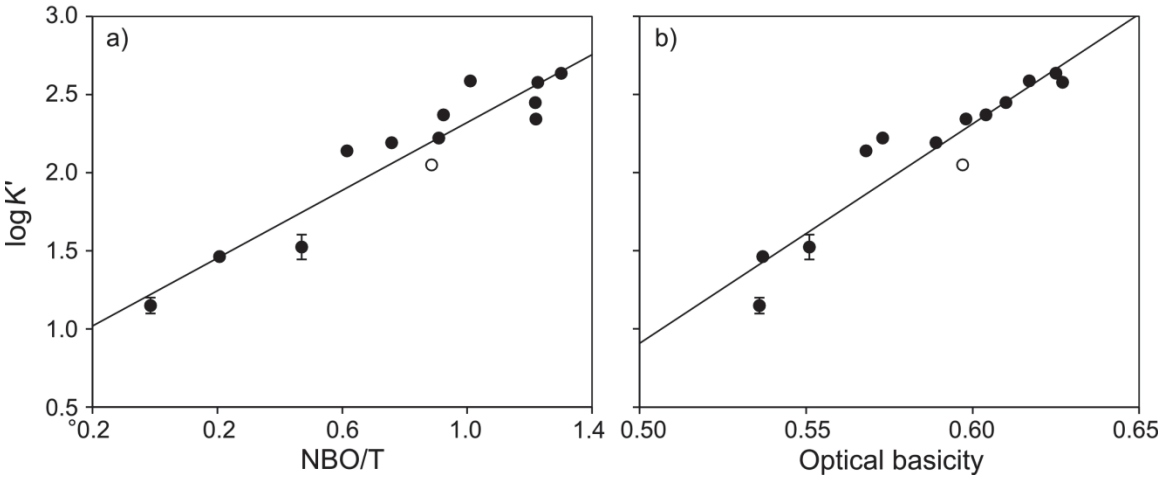


Figure 8

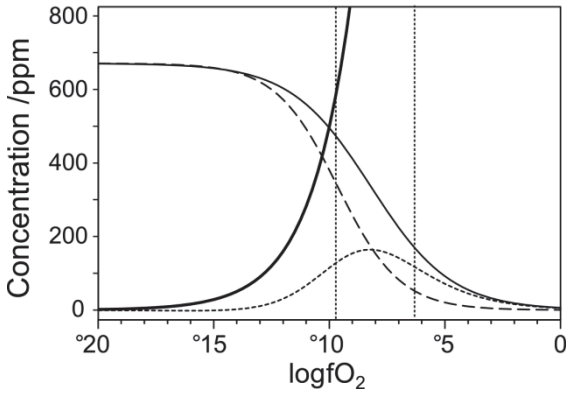
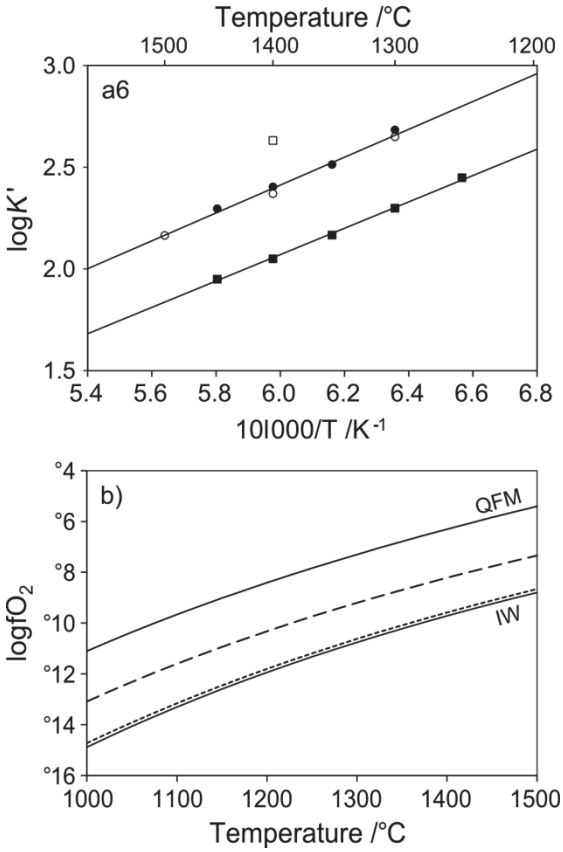


Figure 9



Appendix 7:

Confocal laser scanning microscopy of U-bearing glasses

A7.1 Introduction

It has been reported that U^{4+}, U^{5+}, and U^{6+} phases emit characteristic fluorescence signals when excited by certain ultraviolet-visible wavelengths (e.g. Kirishima *et al.*, 2003; Arnold *et al.*, 2006; Steudtner *et al.*, 2006; Grossman *et al.*, 2007, 2009a and 2009b). Laser-induced fluorescence of U-bearing samples can thus probe oxidation state, and has been used to directly observe U redox reactions during alteration of mineral surfaces (Grossman *et al.*, 2009b), and in biofilms (Grossmann *et al.*, 2007; Arnold *et al.*, 2010). Confocal laser scanning microscopy (CLSM) was used to measure the fluorescence intensity emitted by U-bearing anorthite-diopside eutectic (AD) composition glasses when irradiated by a laser. The aim was to determine the relationship between fluorescence and the fO_2 of sample equilibration, and thus attempt U oxidation state quantification.

A7.2 Methods

Samples were 1 atm AD glasses doped with ~0.4 wt % UO_2 equilibrated at 1400 °C and a range of fO_2s ($\log fO_2$ = -10 to 0 at 1 atm, and $\log fO_2$ = +4.7 at 10 kbar). Full sample preparation details are discussed in chapter 2 of this thesis. Glasses were mounted in epoxy and polished down to a 1 micron finish.

The only known excitation wavelength for U^{4+} is 245 nm (Kirishima *et al.*, 2003), and the optimal excitation wavelengths of U^{5+} and U^{6+} are 255 nm and 266 nm, respectively (Steudtner *et al.*, 2006; Grossman *et al.*, 2009a and 2009b). However, these wavelengths are not achievable on a CLSM system (Grossmann *et al.*, 2007). Measurements were carried out

with a Nikon A1-Si laser scanning confocal microscope. Initially the glasses were irradiated using three excitation wavelengths provided by the confocal system lasers: 405 nm, 488 nm and 561 nm. Sequential scanning mode was used, such that the sample was scanned by each laser separately. Only fluorescence within the wavelength collection window of each laser was recorded: 425-475 nm, 500-550 nm, and 570-620 nm for the 405 nm, 488 nm, and 561 nm lasers, respectively.

Preliminary measurements did not show any evidence of fluorescence above background when the samples were irradiated using the 408 nm laser, thus it was not included in the final measurements. Using the 488 nm and 561 nm lasers two three-dimensional stacks of fluorescence images were acquired about the sample surface (xyz scanning). Mounted glasses were placed one-by-one under the objective lens of the CLSM with a cover slip positioned on top of the sample. The microscope was optically focused onto the glass surface using a 40× oil immersion objective lens with a numerical aperture of 1.3. The pinhole size was 33.4 μm giving a theoretical x-y resolution of 0.12 μm and a z resolution of 0.76 μm. A depth (z) step-size of 0.25 μm was used to collect the fluorescence intensity from a series of x-y planes from 10 μm above to 10 μm below the optical surface (a total of 81 z slices). Images were recorded with a pixel size of 0.31 μm over a field of view of 1024 × 1024 pixels. The dwell time for each pixel was 2.3 μs, and each line was scanned twice and averaged to reduce noise. The output was a series of 12 bit fluorescence brightness images, as shown in Fig. A7.1. The laser powers were selected to avoid detector saturation when measuring the most fluorescent glasses and were kept constant throughout data collection. Repeat measurements were taken at several different positions on the surface of the same glass.

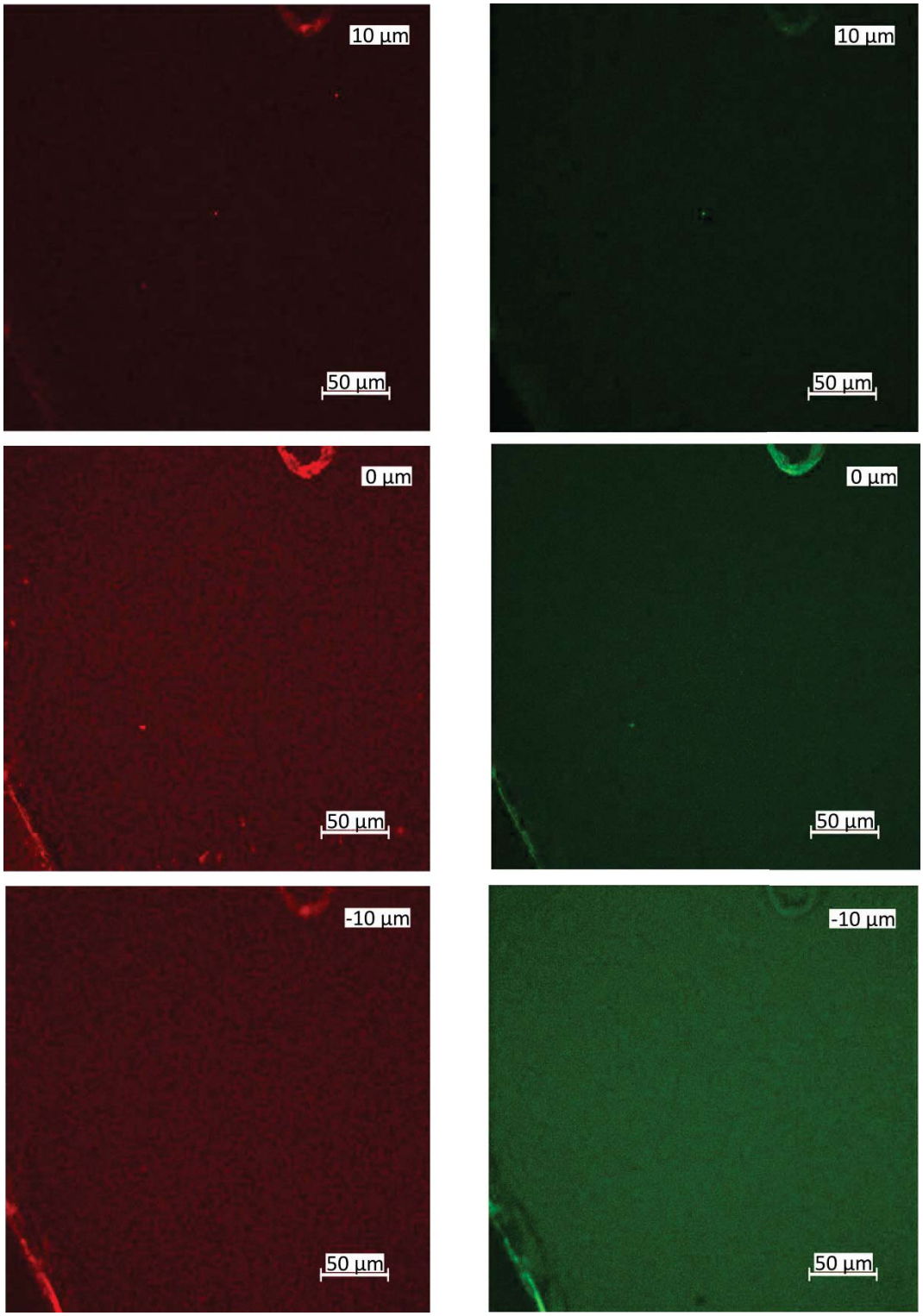


Figure A7.1: A sample of the z stack CLSM images acquired from around the surface of a AD composition glass, equilibrated at 1400 °C, 10 kbar, and logfO_2 = +4.7, using excitation wavelengths of 561 nm (left column: red) and 488 nm (right column: green). Values in the top right corners indicate the position of the microscope stage relative to that at the optically assigned surface. The brighter the image the higher the flourescence intensity (the saturation, brightness, and contrast settings of the images shown have been optimised for illustrative purposes; quantitative analyses were performed using the original images).

A7.3 Results

The fluorescence intensity at both excitation wavelengths was quantified by selecting a region of interest in the images of the glass surface that was free of any cracks, dirt, or other fluorescence anomalies, and taking the average pixel brightness over that region separately at each depth; the results of this analysis are shown in Fig A7.2. At an excitation wavelength of 488 nm the most oxidised glasses generally exhibit a larger fluorescence signal (collected between 500 and 550 nm) relative to reduced glasses (green lines in Fig. A7.2). However, the fluorescence brightness of oxidised glasses is strongly controlled by the depth of the focal plane, with fluorescence decreasing as the sample stage was moved up (positive depth values), which corresponds to the focal plane moving down below the sample surface. In contrast, reduced glasses show almost no variation in fluorescence as a function of depth. For an excitation wavelength of 561 nm the fluorescence intensity variation (collected for wavelengths between 570 and 620 nm) as a function of depth exhibits "humped" profiles for all of the glasses, with no systematic change in profile shapes as a function of fO_2 (red and yellow lines in Fig A7.2).

A7.4 Analysis

The values of fluorescence intensity obtained from the glass images are highly variable over the 20 μm depth range. This means that a comparison of the fluorescence intensity, both at different points on the same sample and across different samples will be highly sensitive to any uncertainty associated with focusing on the sample surface, which was achieved by eye. Given the similarity in shape of the fluorescence-depth profiles across the whole sample set when using the 561 nm laser (red and yellow lines in Fig A7.2), it seems reasonable to take the fluorescence intensity values in the planes corresponding to the maxima of these profiles

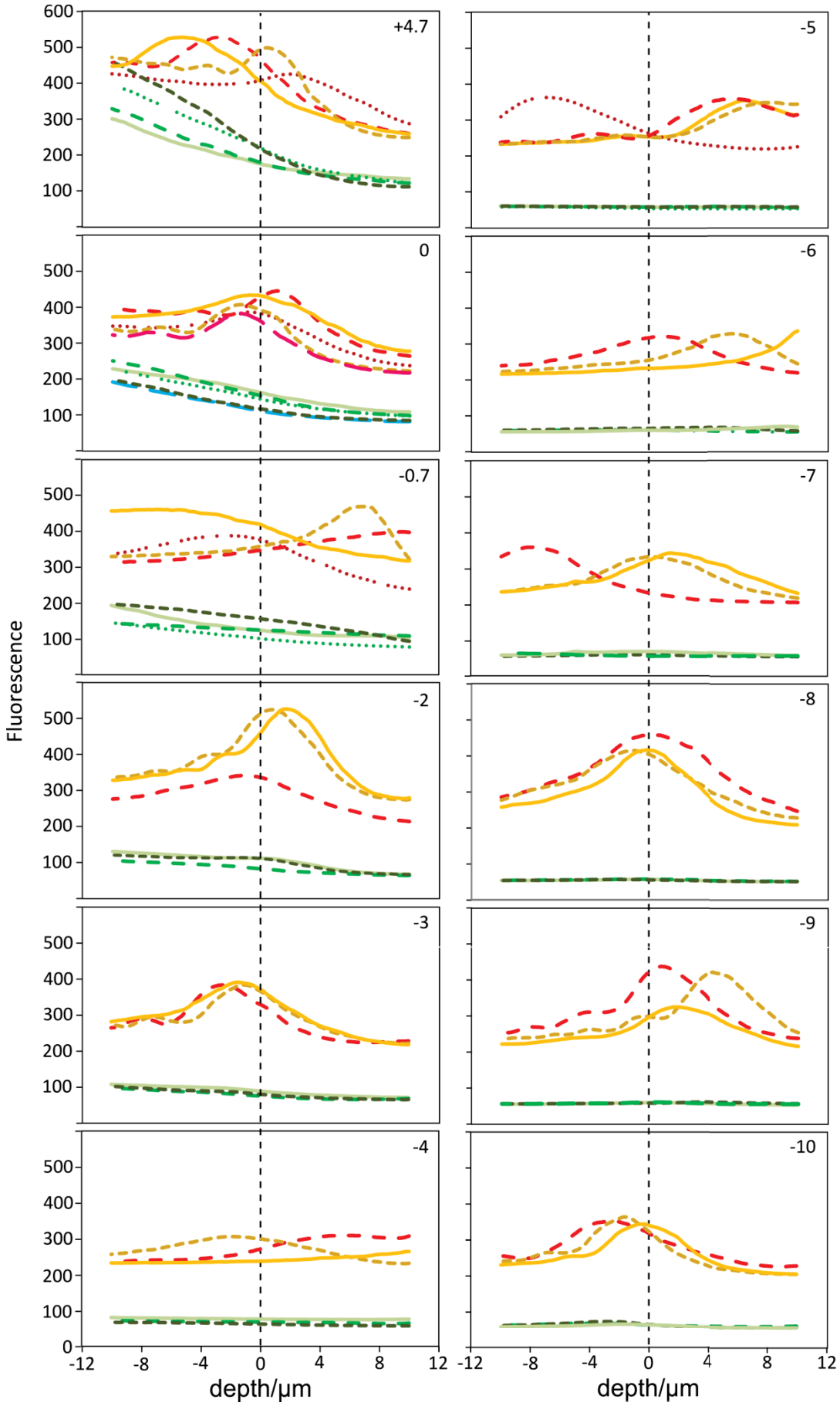


Figure A7.2: Average pixel brightness of CLSM images of AD glasses, equilibrated at the fO_2s indicated, as a function of stage position (optical surface = 0 μm) for the 561 nm (red and yellow) and 488 nm (green) lasers.

as the "sample surface" for comparative purposes. These at least seem to represent a surface that can be consistently located across the sample set.

The fluorescence intensities as a function of the fO_2 of sample equilibration for both excitation wavelengths are shown in Fig. A7.3. Values plotted in Fig. A7.3 represent the averages obtained from all measurements in the "surface" plane of a particular sample. As already stated this corresponds to the x-y plane of maximum fluorescence when using the 561 nm laser for excitation; those few depth profiles that did not exhibit a distinct maximum were excluded from averaging. The error bars in Fig. A7.3 represents the total variation in fluorescence intensity between repeat measurements of a single sample. The fluorescence intensity recorded when using the 561 nm laser for excitation (Fig. A7.3(a)) is often highly variable across measurements of a single sample. Whilst the most oxidised glass does exhibit the largest average fluorescence at this excitation wavelength, there is a high degree of

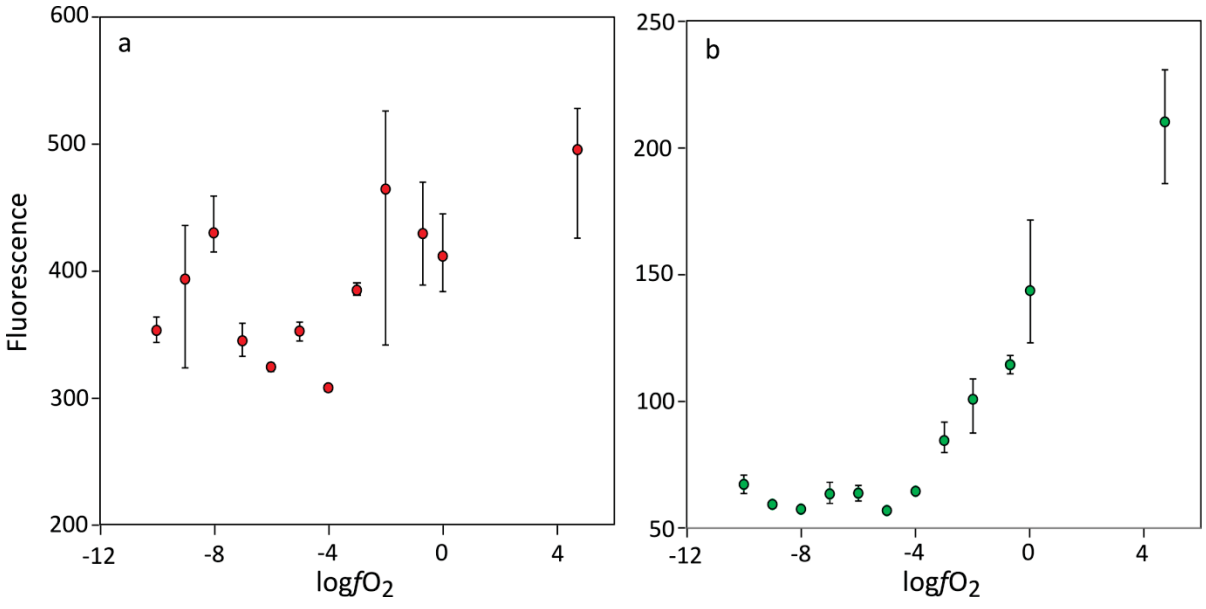


Figure A7.3: Average pixel brightness (representing fluorescence intensity) of CLSM images of AD glasses in the assigned "surface" x-y plane (defined as the depth of maximum fluorescence for an excitation wavelength of 561 nm) as a function of the fO_2 of sample equilibration for an excitation wavelength of (a) 561 nm and (b) 488 nm. Error bars represent the total variation from repeat measurments of the same sample

uncertainty and scatter within the data. In contrast, the fluorescence recorded when using the 488 nm laser (Fig. A7.3(b)) is strongly positively correlated with fO_2, although the uncertainty associated with the most oxidised glasses is large.

The fluorescence intensity contributed by a particular U oxidation state is expected to be proportional to the amount of U in the glass. Thus, the average fluorescence intensity values of Fig A7.3 were normalised by subtracting a horizontal baseline to remove the background signal and dividing the resulting intensity values by the U concentrations of the glasses (determined by EPMA: Table A2.3). The "background" (baseline) fluorescence was determined by averaging the fluorescence values obtained from the most reduced glasses equilibrated between $\log fO_2$ = -5 and -10. The results of this normalisation are plotted in Fig A7.4, which shows similar relationships for both excitation wavelengths to those summarised above for Fig. A7.3.

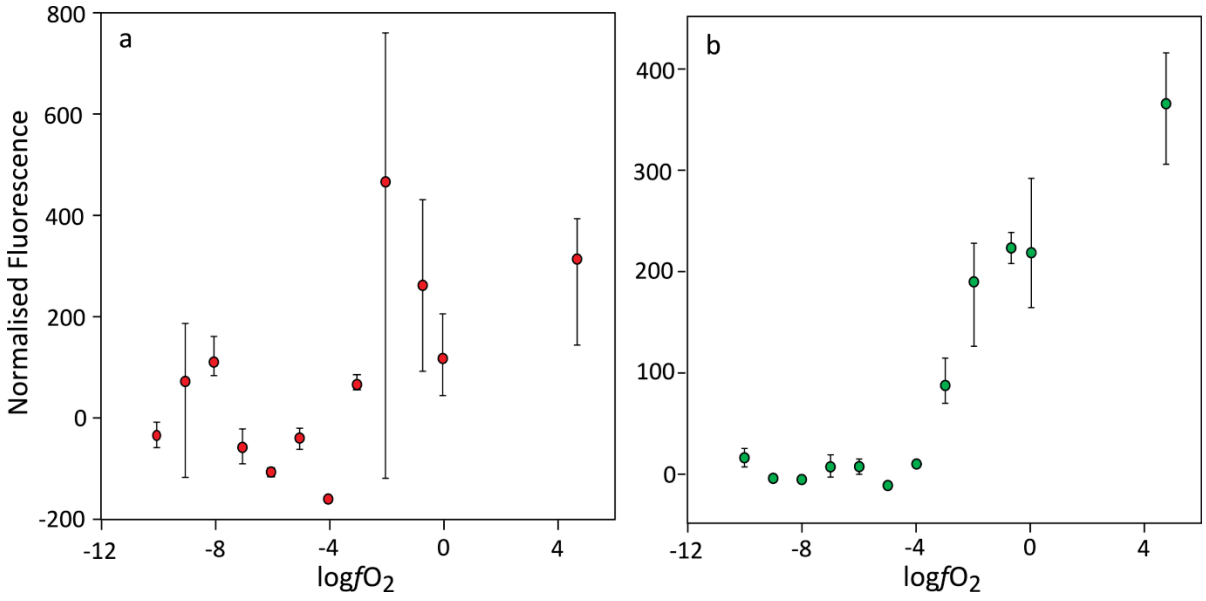


Figure A7.4: Average pixel brightness (representing fluorescence intensity) of CLSM images, normalised to the total U concentrations, of AD glasses in the assigned "surface" x-y plane as a function of the fO_2 of sample equilibration for an excitation wavelength of (a) 561 nm and (b) 488 nm. Error bars represent the total variation for repeat measurments of the same sample

A7.5 Discussion

An excitation wavelength of 408 nm has previously been used for CLSM and laser-induced fluorescence studies of U redox reactions, with U^{5+} and U^{6+} exhibiting fluorescence over different characteristic wavelengths (Grossman *et al.*, 2009a and 2009b; Arnold et al., 2010). U^{5+} fluorescence was reported in the range 415-475 nm, which corresponds to the excitation wavelength and fluorescence detection window of the 408 laser of the CLSM system used in this study of AD glasses. However, no variation in the fluorescence of the glasses as a function of fO_2 or depth is observed at this excitation wavelength. Notably, Grossman *et al*. (2009b) did not report significant fluorescence over the wavelength range attributed to U^{5+} for U_3O_8 despite its assignment as a U^{5+} compound ($2 \times U^{5+} + 1 \times U^{6+}$: Kvashnina *et al*., 2013). Similarly, whilst a fluorescence signal has been reported for uranyl(U^{5+})-carbonate species at low temperatures, room-temperature studies showed no fluorescence at all (Grossman *et al.*, 2009a).

U^{6+} associated fluorescence has been reported for an excitation wavelength of 408 nm in the range 480-560 nm (Grossman *et al.*, 2007 and 2009b; Arnold *et al.*, 2010). However, the CLSM system used in this study did not allow fluorescence detection at these wavelengths in conjunction with the 408 nm laser in sequential scanning mode. Nevertheless, significant and systematic fluorescence was detected in this wavelength range when oxidised samples were irradiated using the 488 nm laser. The occurrence of a fluorescence signal above background only for glasses prepared at $\log fO_2 \geq -3$, and the strong positive correlation between fluorescence intensity and fO_2 for these glasses is consistent with a U^{6+} signal.

Luminescence of U^{4+} has previously been reported for an excitation wavelength of 245 nm (Kirishima *et al.*, 2003). However, no evidence of U^{4+} fluorescence emission has been

reported at any other wavelengths (Kirishima *et al*., 2003; Grossman et al., 2009b). This is entirely consistent with the results of this study for AD glasses, as reduced glasses did not exhibit a fluorescence signal under any of the three laser wavelengths.

As the variation in the fluorescence intensity generated when the AD glasses were irradiated at 488 nm is thought to result from varying proportions of the U^{6+} state only, it is expected to exhibit a sigmoidal relationship with logfO_2. As such, a single-sigmoid was fitted to the average fluorescence intensity data with a slope forced to that expected for a one electron oxidation reaction (i.e. $U^{5+} \rightarrow U^{6+}$: $a/4 = 0.25$, see section 4.3.2 of Chapter 4 of this thesis for a full discussion); the 10 kbar data point at logfO_2 = +4.7 was not included during fitting, and the reduced limit of the sigmoid was forced to have a value of zero. The resulting fit is shown in Fig. A7.5 and gives a logK' value of 0.2(3), which predicts $U^{6+}/\sum U$ = 0.45-0.75 at logfO_2 = 0.

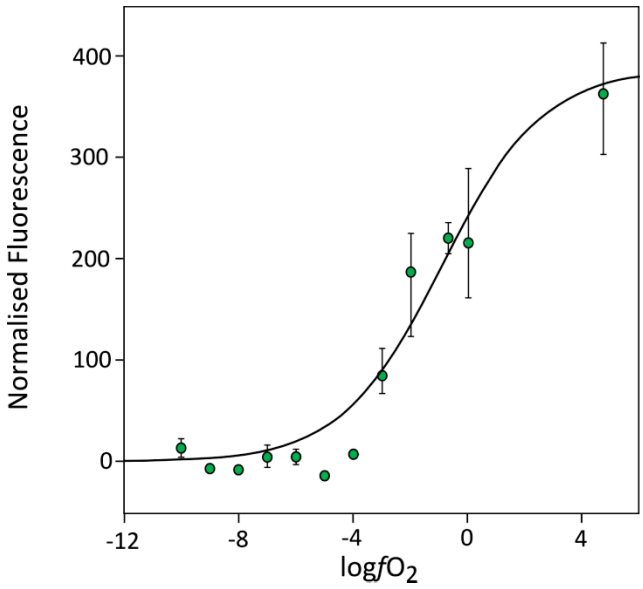


Figure A7.5: Average pixel brightness (representing fluorescence intensity) of CLSM images, normalised to the total U concentrations, of AD glasses in the assigned "surface" x-y plane as a function of the fO_2 of sample equilibration for an excitation wavelength of 488 nm. Error bars represent the total variation for repeat measurments of the same sample. A single-sigmoid fit to the data with its slope forced to that expected for a one-electron oxidation reaction (i.e. $a/4 = 0.25$) and its reduced limit forced to a value of zero is shown.

The cause of the large variations in the fluorescence intensities measured from a single sample for both excitation wavelengths is unclear. For excitation at 488 nm uncertainty may partially result from the strong depth dependence of the fluorescence intensity over only a few microns about the optically assigned surface. The methodology outlined above relies on the assumption that we are able to consistently assign the sample surface across all the glasses, as the analysis is entirely comparative. In addition, variations in the fluorescence intensity across a single sample may result from previous exposure of the glasses to X-rays during XANES measurements. The effect of previous X-ray exposure was clearly observed in the resin surrounding the glasses, which exhibited distinct X-ray beam paths where the fluorescence intensity was considerably reduced.

A7.6 Conclusions

The fluorescence of AD glasses at wavelengths between 500-550 nm when irradiated with a 488 nm laser is consistent with fluorescence of the U^{6+} oxidation state only, with no evidence of any contribution from U^{5+}, U^{4+} or other U states. Sample fluorescence at excitation wavelengths of 408 nm and 561 nm did not seem to be highly sensitive to any particular U oxidation state over the detected fluorescence wavelengths. However, whilst comparison of the fluorescence intensity across the sample set provides some indication of the variation in the proportion of U^{6+}, this approach is associated with a large uncertainty and it is not suitable for accurate quantification of U^{6+} in the glasses.